

## University of Southampton Research Repository ePrints Soton

Copyright © and Moral Rights for this thesis are retained by the author and/or other copyright owners. A copy can be downloaded for personal non-commercial research or study, without prior permission or charge. This thesis cannot be reproduced or quoted extensively from without first obtaining permission in writing from the copyright holder/s. The content must not be changed in any way or sold commercially in any format or medium without the formal permission of the copyright holders.

When referring to this work, full bibliographic details including the author, title, awarding institution and date of the thesis must be given e.g.

AUTHOR (year of submission) "Full thesis title", University of Southampton, name of the University School or Department, PhD Thesis, pagination

**UNIVERSITY OF SOUTHAMPTON**  
**FACULTY OF ENGINEERING & THE ENVIRONMENT**  
School of Engineering Sciences

**Metal Oxide and Silicate Nanotubes: Synthesis and  
Hydrogen Storage Applications**

by

**Rachel Diane White**

Thesis for the degree of Doctor of Philosophy

October 2012





UNIVERSITY OF SOUTHAMPTON

ABSTRACT

FACULTY OF ENGINEERING AND THE ENVIRONMENT

SCHOOL OF ENGINEERING SCIENCES

Doctor of Philosophy

METAL OXIDE AND SILICATE NANOTUBES: SYNTHESIS AND HYDROGEN  
STORAGE APPLICATIONS

by Rachel Diane White

In the past two decades, an appreciation of the extraordinary properties of nanotubular materials has led to the discovery and investigation of many different nanotubes. A wide variety of nanotubes can be synthesised using scalable hydrothermal techniques, but understanding of the synthesis mechanisms is often limited. This research is concerned with manipulating the synthesis conditions of metal oxide and silicate nanotubes in order to improve understanding of the underlying synthesis mechanism, and investigating the properties of the nanotubes as hydrogen storage materials.

This thesis presents experimental results for the syntheses of aluminium silicate, nickel silicate and vanadium oxide multiwalled nanotubes under controlled hydrothermal conditions. A novel synthesis method at 220 °C, pH 2 was developed for  $\text{Al}_2\text{Si}_2\text{O}_5(\text{OH})_4$  nanotubes through substitution of a mole fraction of  $\text{SiO}_2$  with  $\text{GeO}_2$  in the precursor  $\text{SiO}_2 + \text{Al}(\text{OH})_3$  suspension. An ideal Ni/Si molar ratio of 1.5 was demonstrated in the synthesis of  $\text{Ni}_3\text{Si}_2\text{O}_5(\text{OH})_4$  nanotubes at 195 °C. It was shown that increasing the concentration of NaOH widens the length distribution and increases the average length of the nanotubes. Variable temperature experiments with vanadium oxide nanostructures revealed a low temperature route for the synthesis of flexible elongated  $\text{VO}_x$  nanosheets under reflux (90 °C) in an ethylenediamine-water mixture. The hydrothermal experiments revealed important details about the nanotube formation mechanisms, including the scrolling mode of nanosheets into nanotubes, which occurs in a specific crystallographic direction relative to the nanosheet growth axis.

Subsequent investigations into the room temperature stability of  $\text{Al}_2\text{Si}_2\text{O}_5(\text{OH})_4$  nanotubes under aqueous acidic and alkaline conditions revealed significant dissolution within 10 days in  $1 \text{ mol dm}^{-3}$  NaOH,  $\text{H}_2\text{SO}_4$  and HCl solutions, initiated at the inner surface. The effect of acid or alkali concentration on the initial dissolution rate was measured, and the dissolution mechanism discussed. Acid treatment was shown to be an effective method for increasing nanotube surface area.

Investigations into the hydrogen adsorption properties of metal oxide nanotubes revealed weak adsorption of hydrogen at 77 – 298 K up to 150 bars (15 MPa) pressure. Temperature-corrected adsorption isotherms for adsorbing  $\text{H}_2\text{Ti}_n\text{O}_{2n+1}$  (titanate),  $\text{Ge-Al}_2\text{GeO}_3(\text{OH})_4$  and  $\text{Ni}_3\text{Si}_2\text{O}_5(\text{OH})_4$  nanotubes were compared with  $\text{M}_3[\text{Fe}(\text{CN})_6]_2$  Prussian-blue analogues, and dimensions of the adsorbed hydrogen layer were derived using the Langmuir-Freundlich model.



# Contents

<b>Abstract</b>	<b>i</b>
<b>Contents</b>	<b>iii</b>
<b>List of Tables</b>	<b>ix</b>
<b>List of Figures</b>	<b>xi</b>
<b>Declaration of Authorship</b>	<b>xix</b>
<b>Acknowledgements</b>	<b>xxi</b>
<b>List of Abbreviations</b>	<b>xxiii</b>
<b>Chapter 1: Introduction</b>	<b>1</b>
1.1. Background and Motivation	1
1.2. Aims and Objectives	4
1.3. Thesis Outline	5
<b>Chapter 2: Literature Review</b>	<b>7</b>
2.1. Synthesis of metal oxide nanotubes	7
2.1.1. Comparison of different synthetic strategies	7
2.1.2. Hydrothermal synthesis methods for metal oxide nanotubes	8
2.2. Structure of metal oxide nanotubes	13
2.2.1. Crystal structures of metal oxide nanotubes	13
2.2.2. Morphology and Porosity	16
2.3. Mechanisms of nanotube formation	18
2.3.1. Growth of metal oxide nanosheets	19
2.3.2. Scrolling of nanosheets into nanotubes	24
2.4. Properties of metal oxide nanotubes	29
2.4.1. Thermal stability of nanotubes	29
2.4.2. Solution stability of nanotubes and hydrothermal transformation	30
2.4.3. Electrical and mechanical properties	32

2.4.4.	Chemical properties and surface functionalisation	32
2.5.	Inorganic nanotubes as hydrogen storage materials	35
2.5.1.	Outline of current hydrogen storage methods, aims and challenges	35
2.5.2.	Techniques for measuring hydrogen storage	36
2.5.3.	PCT isotherms for hydrogen adsorption	37
2.5.4.	Current progress in hydrogen storage materials	40
2.5.5.	Feasibility of meeting the DOE targets	43
2.5.6.	Hydrogen storage in inorganic nanotubes	44
<b>Chapter 3: Experimental Methodology</b>		<b>49</b>
3.1.	Hydrothermal synthesis procedures	49
3.1.1.	Germanium-doped aluminosilicates	49
3.1.2.	Single- and double-walled germanium-imogolite nanotubes	50
3.1.3.	Nickel silicates	51
3.1.4.	Vanadium oxide nanotubes	51
3.1.5.	Low temperature synthesis of vanadium oxides	52
3.2.	Stability experiments for natural halloysite	52
3.2.1.	Reagents	53
3.2.2.	Long term stability studies of halloysite	53
3.2.3.	Preparation of solids for sample characterisation	53
3.2.4.	Preparation of solution for colorimetric analysis	53
3.3.	Ion-exchange decoration of natural halloysite with Prussian blue	54
3.4.	Measurement of equilibrium vanadium(v) concentration 25 – 90 °C	54
3.4.1.	Design of experiment	54
3.4.2.	Extraction of samples for concentration analysis	55
3.5.	Characterisation of solid products	56
3.5.1.	Transmission electron-microscopy	56
3.5.2.	Scanning electron-microscopy and length distributions	56
3.5.3.	Nitrogen adsorption	57
3.5.4.	FTIR and Raman spectroscopy	58
3.5.5.	X-ray diffraction	58
3.5.6.	ICP atomic emission spectroscopy	58
3.6.	Colorimetric Methods	58

3.6.1.	Measurement of dissolved Al (III) and Si(IV) during halloysite dissolution	58
3.6.2.	Measurement of dissolved vanadium (V) equilibrium concentration	59
3.7.	Hydrogen Adsorption Isotherms	59
3.7.1.	Instrumentation and gas supply	59
3.7.2.	Sample preparation and degassing	60
3.7.3.	Volume calibration	62
3.7.4.	Thermal stability	63
3.7.5.	Measurement of PCT isotherms	63
3.7.6.	Analysis of raw data and temperature correction	64

#### **Chapter 4: Synthesis of $\text{Al}_2\text{Si}_2\text{O}_5(\text{OH})_4$ (Halloysite) Nanotubes in the Presence of $\text{GeO}_2$**

**67**

4.1.	Introduction	67
4.2.	Structural analysis using transmission electron microscopy	67
4.3.	Bulk compositional analysis using electron microscopy and ICP	75
4.4.	Bulk characterisation of pore structure by nitrogen adsorption	78
4.5.	Fourier-transform infrared spectroscopy	80
4.6.	Discussion of the synthesis mechanism	82
4.7.	Conclusions	87

#### **Chapter 5: The Stability of Halloysite Nanotubes in Acid and Alkaline Aqueous Suspensions**

**89**

5.1.	Introduction	89
5.2.	Morphological changes after acid/alkaline treatment	90
5.2.1.	Electron microscopy	90
5.2.2.	Nitrogen adsorption	94
5.3.	Structural changes of halloysite after acid/alkaline treatment	98
5.3.1.	Fourier-transform infrared and Raman spectroscopy	98
5.3.2.	X-ray diffraction	99
5.4.	Solubility of halloysite in acid/alkaline suspensions	100
5.5.	Conclusions	107

<b>Chapter 6: Morphological Control of Synthetic Nickel Silicate <math>\text{Ni}_3\text{Si}_2\text{O}_5(\text{OH})_4</math> Nanotubes in an Alkaline Hydrothermal Environment</b>	<b>109</b>
6.1. Introduction	109
6.2. Optimisation of Ni/ Si ratio in nickel silicate nanotube synthesis	110
6.3. Effect of NaOH concentration on nickel silicate nanotube synthesis	117
6.4. Discussion of formation mechanism	124
6.5. Conclusions	128
<b>Chapter 7: Low Temperature Synthesis of Nanostructured Vanadium Oxide</b>	<b>131</b>
7.1. Introduction	131
7.2. Influence of temperature on vanadium oxide nanostructure	132
7.2.1. Changes in morphology	132
7.2.2. Changes in crystal structure	134
7.3. Influence of temperature on vanadium concentration	137
7.4. Addition of ethylenediamine ligand to synthesis	139
7.5. Conclusions	147
<b>Chapter 8: Hydrogen Adsorption Properties of Metal Oxide Nanotubes</b>	<b>149</b>
8.1. Introduction	149
8.2. Surface area and pore-size distributions of nanotubes	150
8.3. Blank testing and temperature correction of data	155
8.4. Comparison of hydrogen adsorption data	156
8.5. Langmuir-Freundlich fitting of isotherms	158
8.6. Reversibility of hydrogen adsorption	166
8.7. Conclusions	167
<b>Chapter 9: Conclusions and Suggestions for Further Work</b>	<b>169</b>
9.1. Conclusions	169
9.2. Suggestions for Further Work	173

9.2.1.	Hydrothermal synthesis of $\text{Al}_2\text{Si}_2\text{O}_5(\text{OH})_4$ (halloysite) nanotubes	173
9.2.2.	Long-term solution stability of halloysite nanotubes	174
9.2.3.	Hydrothermal synthesis of $\text{Ni}_3\text{Si}_2\text{O}_5(\text{OH})_4$ nanotubes	174
9.2.4.	Hydrothermal synthesis of $\text{VO}_x$ (vanadium oxide) nanotubes	175
9.2.5.	Hydrogen storage properties of nanotubes	175
<b>Appendix A: Electron Microscopy EDX and SAED, and XRD Analysis</b>		<b>177</b>
<b>Appendix B: Colorimetric Data</b>		<b>183</b>
<b>Appendix C: Calculations for Solubility Diagrams</b>		<b>187</b>
<b>Appendix D: Hydrogen Adsorption Calculations</b>		<b>195</b>
<b>References</b>		<b>199</b>
<b>Bibliography</b>		<b>219</b>





# List of tables

2.1	Morphology and hydrothermal synthesis of metal hydroxide and oxide nanotubes with layered structure.	10
2.2	Morphology and hydrothermal synthesis of metal silicate nanotubes with layered structure.	11
2.3	Morphology of metal oxide nanotubes	18
2.4	Electrical and mechanical properties of metal oxide nanotubes at 298 K.	32
2.5	Comparison of the gravimetric storage capacities, operating temperatures and disadvantages associated with current hydrogen storage materials.	42
2.6	Maximum excess hydrogen adsorption capabilities of inorganic nanotubes at different temperatures.	45
3.1	Calculated sample masses after degassing in the PCT-Pro apparatus.	61
3.2	Volume calibration of samples using He at 77 K.	62
4.1	Distribution of morphologies of typical nanostructures (estimated from TEM data) observed in the products of hydrothermal reaction at $\text{GeO}_2$ mole fraction, $X$ varied between 0 and 0.5.	77
5.1	Effect of acid and alkaline treatment of the average morphology of halloysite nanotubes, measured from TEM images.	92
5.2	Changes in halloysite BET specific surface area ( $S_{\text{BET}}$ ) and total pore volume ( $V_{\text{pores}}$ ) under slow transformation in acids or base.	96
5.3	The total concentration of Al(III) $C_{\text{Al(III)}}$ and Si(IV) $C_{\text{Si(IV)}}$ in aqueous suspension, the mole fractions of aluminium in liquid ( $x_{\text{L}}^{\text{Al}}$ ) and solid ( $x_{\text{S}}^{\text{Al}}$ ) phases, and the mole fractions of silicon in liquid ( $x_{\text{L}}^{\text{Si}}$ ) and solid ( $x_{\text{S}}^{\text{Si}}$ ) phases, after 84 days transformation in acids or base.	105
6.1	Morphology of phases observed at different Ni/Si ratios and $C_{\text{NaOH}} = 4 \text{ wt } \%$ .	113
6.2	Characterisation of bulk products at different Ni/Si ratios and $C_{\text{NaOH}} = 4 \text{ wt } \%$ .	115
6.3	Morphology of phases observed in products at different $C_{\text{NaOH}}$ and Ni/Si = 1.5.	118
6.4	Characterisation of bulk products at different NaOH concentrations and Ni/Si ratios.	123

7.1	The variation in nanosheet morphology with varying concentration of ethylenediamine ( $C_{en}$ ) after 7 days hydrothermal treatment at 90 °C.	140
8.1	Typical morphology of nanotubes as measured by HRTEM.	151
8.2	Results of nitrogen adsorption at 77 K on nanotubular samples.	152
8.3	Results of nitrogen adsorption at 77 K on nanotube-PB composites, and bulk $Fe_3[Fe(CN)_6]_2$ .	154
8.3	Gravimetric and volumetric capacities of the nanomaterials, together with the calculated number of $H_2$ molecules, $n_{H_2}$ , per unit cell.	163
8.5	Properties of adsorbed hydrogen layer at 77 K calculated from figures 8.7-8.10, compared with properties of material calculated from nitrogen adsorption (tables 8.2 and 8.3).	164
A.1	Indexing of crystal reflections in halloysite-type nanotubes synthesised in products with mole fraction $GeO_2$ ( $X$ ), in the range 0 – 0.5, by comparison with XRD and SAED data in the literature.	178
A.2	Indexing of $Ni_3Si_2O_5(OH)_4$ and $\beta$ - $Ni(OH)_2$ crystal reflection in the XRD patterns of the unmodified nickel silicate products.	179
C.1	Logarithmic solubility constants for aluminium hydroxides.	188
C.2	Logarithmic solubility constants for $\beta$ - $Ni(OH)_2$ .	189
C.3	Logarithmic solubility constants for $Co(OH)_2$ .	190
C.4	Logarithmic solubility constants for $Fe(OH)_3$ .	191
C.5	Logarithmic solubility constants for $Mg(OH)_2$ .	192
C.6	Logarithmic solubility constants for $Cu(OH)_2$ .	193
C.7	Logarithmic solubility constants for $SiO_2$ .	194
D.1	Physical properties of the nanomaterials measured for hydrogen adsorption.	198

# List of figures

1.1	Some common morphologies of nanostructured particles.	1
1.2	The nomenclature used to describe different parts of a nanotube.	3
2.1	The most common nanotube synthesis methods.	8
2.2	Crystal structures with corresponding TEM images showing how crystal growth readily occurs in all directions in a 3-D crystal structure (image a), but is directed along the basal plane in 2-D crystal structures due to weaker interlayer forces (image b).	13
2.3	Crystal structures with corresponding HRTEM images of (a) titanate (b) halloysite (c) nickel silicate, (d) imogolite, (e) vanadium oxide and (f) magnesium silicate nanotubes.	15
2.4	Schematic diagram of the nanotube axes, and four different types of pore.	16
2.5	TEM images showing (a) the growth of titanate nanosheets via recrystallisation on the surface of a TiO <sub>2</sub> (anatase) nanoparticle, and (b) exfoliation of a nanosheet from a thicker growing nanosheet.	20
2.6	Solubility vs. pH curves for the thermodynamically stable crystalline forms of Mg, Al, Co, Fe, Ni and Cu hydroxides, calculated in this work from experimental solubility constants extrapolated to infinite dilution.	21
2.7	Solubility vs. pH curves for the thermodynamically stable crystalline forms of Mg and Al hydroxides, and SiO <sub>2</sub> at 200 °C, extrapolated to infinite dilution (I = 0).	22
2.8	Morphology of Mg(OH) <sub>2</sub> crystallised at 180 °C for 6 hours in (a) ethylenediamine, (b) distilled water, and (c) absolute ethanol solvents.	23
2.9	Overview of the scrolling mechanisms of nanosheets caused by Structural or environmental factors.	25
2.10	The relationship between tube radius and DFT-calculated strain energy for single walled nanotubes of imogolite, titanates, halloysite and chrysotile.	27
2.11	Bar diagram showing the phase stability of nanotubular materials upon heating.	29
2.12	Schematic diagram of the crystallisation of different titanate morphologies: nanosheets, nanotubes and nanofibres, from solutions containing different concentrations of dissolved Ti(IV).	31

2.13	Simplified structural diagram showing the distribution of hydroxyl Groups on halloysite, nickel silicate and imogolite nanotube surfaces.	33
2.14	Simplified diagram of imogolite structure showing how the replacement of Si(IV)O <sub>4</sub> tetrahedra with Ge(IV)O <sub>4</sub> on the inside of the Al <sub>2</sub> SiO <sub>3</sub> (OH) <sub>4</sub> sheet increases the diameter of the nanotubes.	35
2.15	Schematic diagram of absolute and excess gas adsorption in a solid.	38
2.16	Comparison between the excess adsorption and absolute adsorption Isotherms of the hydrogen storage material Cu <sub>3</sub> (BTC) <sub>2</sub> at 77 K.	40
2.17	PCT isotherms of excess hydrogen adsorption at 298 K for TiS <sub>2</sub> , CuSiO <sub>3</sub> .2H <sub>2</sub> O, Mg <sub>3</sub> Si <sub>2</sub> O <sub>5</sub> (OH) <sub>4</sub> , and titanate nanotubes	46
3.1	Apparatus used to filter vanadium suspensions to collect the solution for concentration analysis.	55
3.2	The flow system for the PCT-Pro 2000 apparatus.	60
4.1	TEM images of halloysite nanotubes synthesised by hydrothermal reaction between Al(OH) <sub>3</sub> and SiO <sub>2</sub> at pH2 and temperature 220 °C for 7 days in the presence of GeO <sub>2</sub> .	68
4.2	TEM and SAED images of nanostructures obtained after 7 days Hydrothermal reaction between Al(OH) <sub>3</sub> and SiO <sub>2</sub> in the presence of GeO <sub>2</sub> at pH2 and temperature 220 °C. The molar fraction of added GeO <sub>2</sub> is (a) X = 0, (b) X = 0.05, (c) X = 0.1 and (d) X = 0.5.	70
4.3	TEM and SAED images of kaolinite nanosheets obtained at X = 0, as viewed along crystallographic directions corresponding to (a) [001], (b) [100], and (c) [010].	71
4.4	HRTEM, SAED images and EDX spectrum of Ge-imogolite nanotubes synthesised at the mole fraction of added GeO <sub>2</sub> X = 0.5.	72
4.5	TEM and SAED images together with EDX spectra of typical nanostructured side products obtained in the hydrothermal reaction at X = 0.5, namely AlOOH (boehmite) (a) nanorods, (b) nanoplates and (c) amorphous Ge-enriched aluminosilicate nanoparticles.	74
4.6	SEM images of products obtained at (a) X = 0, (b) X = 0.05, (c) X = 0.1, (d) X = 0.2, (e) X = 0.5.	76
4.7	Distribution of hydrothermal reaction products as a function of molar	

fraction of added GeO <sub>2</sub> , $X$ .	76
4.8 BJH pore size distributions for aluminosilicate samples obtained under addition of GeO <sub>2</sub> .	79
4.9 BET surface area and total pore volume of nanostructured aluminosilicates hydrothermally prepared at different mole fractions of added GeO <sub>2</sub> .	79
4.10 FTIR spectra of aluminosilicate products synthesised at $X$ equal to (a) 0, (b) 0.05 (c) 0.1, (d) 0.2, and (e) 0.5.	81
4.11 Schematic drawing of the crystal structures of (a) halloysite, and (b) kaolinite as a combination of AlO <sub>6</sub> octahedra with SiO <sub>4</sub> tetrahedra, together with accompanying HRTEM images.	82
4.12 Schematic plan view diagram of rotation of SiO <sub>4</sub> tetrahedra in Al <sub>2</sub> Si <sub>2</sub> O <sub>5</sub> (OH) <sub>4</sub> to reduce the $a$ and $b$ lattice parameters.	83
4.13 Schematic diagram showing extra length required in silicate sheet to form the inner layer of a tube almost 10 nm in diameter.	84
4.14 Schematic diagram showing how inclusion of a GeO <sub>4</sub> tetrahedron (shown in black) may cause stronger bending along the $a$ axis rather than along the $b$ axis for a growing Al <sub>2</sub> Si <sub>2</sub> O <sub>5</sub> (OH) <sub>4</sub> nanosheet elongated in the $b$ dimension.	86
5.1 TEM images with accompanying EDX spectra from highlighted areas of (a) untreated halloysite, halloysite treated for 84 days with (b) 1 mol dm <sup>-3</sup> H <sub>2</sub> SO <sub>4</sub> , or (c) 1 mol dm <sup>-3</sup> NaOH.	91
5.2 HRTEM images showing the tube wall destruction and appearance of particles in halloysite treated with (a) 1 mol dm <sup>-3</sup> H <sub>2</sub> SO <sub>4</sub> and (b) 1 mol dm <sup>-3</sup> NaOH for 84 days.	92
5.3 TEM images of halloysite nanotubes after 84 days treatment with (a) 1 mol dm <sup>-3</sup> acetic acid, and (b) distilled water.	93
5.4 SEM images and histograms of length distribution of nanotubes in (a) halloysite, and halloysite treated with for 28 days with (b) 1 mol dm <sup>-3</sup> H <sub>2</sub> SO <sub>4</sub> and (c) 1 mol dm <sup>-3</sup> NaOH.	94
5.5 The N <sub>2</sub> adsorption and desorption isotherms at -195 °C of halloysite, and halloysite treated with 1 mol dm <sup>-3</sup> NaOH, 84 days, and 1 mol dm <sup>-3</sup> H <sub>2</sub> SO <sub>4</sub> , 84 days.	95
5.6 BJH pore size distributions for halloysite nanotubes treated with	

(a) 1 mol dm <sup>-3</sup> H <sub>2</sub> SO <sub>4</sub> , (b) 1 mol dm <sup>-3</sup> HCl and (c) 1 mol dm <sup>-3</sup> NaOH, for 28 days (solid line), and 84 days (dotted line).	97
5.7 FTIR spectra of (a) untreated halloysite, (b) halloysite treated with 1 mol dm <sup>-3</sup> H <sub>2</sub> SO <sub>4</sub> for 84 days, (c) amorphous SiO <sub>2</sub> (Fisher, 35-70 µm chromatography grade).	98
5.8 Raman Spectra of the lattice region of halloysite treated for 84 days with 1 mol dm <sup>-3</sup> solutions of (a) H <sub>2</sub> SO <sub>4</sub> , (b) NaOH, and (c) untreated halloysite.	99
5.9 XRD patterns (without background correction) of (a) untreated halloysite, and halloysite treated for 84 days with (b) 1 mol dm <sup>-3</sup> NaOH, and (c) 1 mol dm <sup>-3</sup> H <sub>2</sub> SO <sub>4</sub> .	100
5.10 The concentration of total dissolved aluminium C <sub>Al(III)</sub> (a) and silicon C <sub>Si(IV)</sub> (b) as a function of time in the aqueous suspension of halloysite containing 1 mol dm <sup>-3</sup> NaOH, 1 mol dm <sup>-3</sup> H <sub>2</sub> SO <sub>4</sub> , 1 mol dm <sup>-3</sup> HCl, 1 mol dm <sup>-3</sup> acetic acid and pure H <sub>2</sub> O.	101
5.11 The concentration of total Al (III) (a) and Si (IV) (b) as a function of time in the aqueous suspension of halloysite containing 1 mol dm <sup>-3</sup> NaOH, 0.1 mol dm <sup>-3</sup> NaOH, 0.01 mol dm <sup>-3</sup> NaOH.	103
5.12 The concentration of total Al (III) (a) and Si (IV) (b) as a function of time in the aqueous suspension of halloysite containing 1 mol dm <sup>-3</sup> H <sub>2</sub> SO <sub>4</sub> , 0.1 mol dm <sup>-3</sup> H <sub>2</sub> SO <sub>4</sub> , 0.01 mol dm <sup>-3</sup> H <sub>2</sub> SO <sub>4</sub> .	104
5.13 Equilibrium concentration of Al(III) and Si(IV) species in aqueous solution as a function of pH at 298 K for amorphous SiO <sub>2</sub> and Al(OH) <sub>3</sub> (gibbsite).	106
5.14 Scheme of transformation of halloysite (Al <sub>2</sub> Si <sub>2</sub> O <sub>5</sub> (OH) <sub>4</sub> ) nanotubes in strong acid and alkaline solutions leading to formation of amorphous nanoparticles of SiO <sub>2</sub> and amorphous nanosheets of Al(OH) <sub>3</sub> , respectively.	107
6.1 Analysis of nickel silicate nanotube structure(a) HRTEM image of a nickel silicate nanotube formed in 4 wt % NaOH solution at a Ni/Si ratio of 1.5, with insets (bottom left corner) showing a magnified image of the layer structure of the wall and (top right corner) the SAED pattern taken from an agglomeration of nanotubes, (b) a cross-sectional HRTEM image of the nanotubes, and (c) EDX data taken from image (b).	111
6.2 TEM and EDX images of nickel silicate products from 4 wt% NaOH	

	solutions with Ni/Si ratio (a) 1, (b) 1.5, (c) 2 and (d) 3.	112
6.3	TEM image of $\beta$ -Ni(OH) <sub>2</sub> particles formed at Ni/Si = 3, together with HRTEM and EDX images.	113
6.4	SEM images of products at (a) 1, (b) 1.5, (c) 2 and (d) 3 Ni/Si ratios with corresponding percentage length distributions of nanotubes.	114
6.5	XRD patterns of nickel silicates synthesised at Ni/Si ratios (a) 1, (b) 1.5, (c) 2 and (d) 3.	116
6.6	FTIR spectra of nickel silicates synthesised at controlled Ni/Si ratios (a) 1, (b) 1.5, (c) 2 and (d) 3.	116
6.7	BJH pore-size distributions for nickel silicates synthesised at controlled Ni/Si ratios 1, 1.5, 2 and 3 at $C_{\text{NaOH}} = 4$ wt %.	117
6.8	TEM images of nickel silicates formed at (a) 0, (b) 7, (c) 10 and (d) 15 wt % initial NaOH concentration, with corresponding EDX spectra from the centre of the images.	118
6.9	XRD patterns of nickel silicates synthesised at NaOH concentration (a) 0, (b) 4, (c) 7, (d) 10 and (e) 15 wt %.	119
6.10	BJH pore-size distributions obtained from N <sub>2</sub> adsorption at -196 °C, for nickel silicate nanotubes synthesised at 0, 2, 4, 7, 10 and 15 wt % $C_{\text{NaOH}}$ .	120
6.11	SEM images of nanotubes produced at (a) 2, (b) 4, (c) 7 and (d) 10 wt% NaOH with corresponding percentage length distributions.	121
6.12	Solubility diagrams of $\beta$ -Ni(OH) <sub>2</sub> and amorphous SiO <sub>2</sub> at 195 °C in solution with ionicity $I = 0$ .	123
6.13	Proposed reaction mechanism in which an amorphous material $\text{Ni}_{3-x}\text{Si}_{1+y}\text{O}_z(\text{OH})_n$ recrystallises as $\text{Ni}_3\text{Si}_2\text{O}_5(\text{OH})_4$ under hydrothermal treatment at 195 °C.	125
6.14	Schematic phase diagram indicating the typical nanostructures of nickel (II) silicates and $\beta$ -Ni(OH) <sub>2</sub> formed at different NaOH concentration ( $C_{\text{NaOH}}$ ) and molar Ni/Si ratio.	128
7.1	SEM images showing the structure of dodecylamine-intercalated VO <sub>x</sub> after 7 days hydrothermal treatment at (a) 90, (b) 140, (c) 180 and (d) 220 °C.	132
7.2	TEM images showing (a) scrolling of VO <sub>x</sub> nanosheets synthesised at 140 °C around the long axis, (b) fully-formed VO <sub>x</sub> nanotubes synthesised at 180 °C, with an inset showing the cross-section of a nanotube, and (c) VO <sub>x</sub>	



nanosheets synthesised at 220 °C.	133
7.3 Low-angle <i>x</i> -ray diffraction patterns for (a) original dodecylamine-intercalated precursor material, and after 7 days hydrothermal treatment at (b) 140, (c) 180 and (d) 220 °C.	134
7.4 Schematic diagram showing a possible mechanism for VO <sub>x</sub> layer bending to form nanotubes.	135
7.5 XRD patterns of (a) original precursor and after hydrothermal treatment at (b) 140, (c) 180 and (d) 220 °C.	136
7.6 Graph showing the relationship between the logarithm of vanadium concentration (mol dm <sup>-3</sup> ) and the reciprocal of temperature, in degrees Kelvin.	138
7.7 SEM images showing VO <sub>x</sub> after 7 days hydrothermal treatment at 90 °C in solutions containing (a) 0, (b) 0.001, (c) 0.01 and (d) 0.1 mol dm <sup>-3</sup> ethylenediamine.	140
7.8 Evolution in morphology of VO <sub>x</sub> nanosheets after extended treatment in 90 °C ethylenediamine solution.	141
7.9 Low-angle XRD patterns of VO <sub>x</sub> after 7 days reflux at 90 °C in (a) 0.1, (b) 0.01, (c) 0.001, and (d) 0 mol dm <sup>-3</sup> ethylenediamine, compared with (e) the XRD pattern of VO <sub>x</sub> nanotubes synthesised at 180 °C after 7 days hydrothermal treatment.	142
7.10 Progressive scrolling of VO <sub>x</sub> nanosheets around the long axis under the TEM electron beam.	143
7.11 TEM images of VO <sub>x</sub> after 7 days hydrothermal treatment at 130 °C in solution containing (a) 0.00 and (b) 0.01 mol dm <sup>-3</sup> concentrations of ethylenediamine.	144
7.12 Low-angle XRD patterns of VO <sub>x</sub> after 7 days reflux at 130 °C in (a) 0.001 and (b) 0.01 mol dm <sup>-3</sup> ethylenediamine, compared with VO <sub>x</sub> nanotubes synthesised at 180 °C (c).	145
7.13 XRD patterns of VO <sub>x</sub> nanomaterials after 7 days reflux at (a, b) 130 °C in (a) 0.001 and (b) 0.01 mol dm <sup>-3</sup> ethylenediamine, (c,d) 90 °C in (c) 0.01 and (d) 0.1 mol dm <sup>-3</sup> ethylenediamine, compared with VO <sub>x</sub> nanotubes synthesised at 180 °C (e).	146

8.1	HRTEM images of (a) single-walled Ge-imogolite, (b) double-walled Ge-imogolite (c) titanate, (d) nickel silicate, (e) halloysite and (f) vanadium oxide nanotubes.	150
8.2	Pore volume distributions, from nitrogen desorption at 77 K, for single-walled Ge-imogolite double-walled Ge-imogolite, titanate, nickel silicate, halloysite, and VO <sub>x</sub> nanotubes.	152
8.4	TEM images showing (a) titanate nanotubes decorated with 10 wt % Cd <sub>3</sub> [Fe(CN) <sub>6</sub> ] <sub>2</sub> through ion-exchange, <sup>[346]</sup> and (b) halloysite nanotubes decorated with 4.7 wt% Fe <sub>3</sub> [Fe(CN) <sub>6</sub> ] <sub>2</sub> through ion exchange.	154
8.4	Hydrogen adsorption isotherm for non-adsorbing quartz wool sample at 77 K, before and after temperature correction.	155
8.5	Temperature-corrected hydrogen excess adsorption isotherms in the range 0-5 bar for Cd <sub>3</sub> [Fe(CN) <sub>6</sub> ] <sub>2</sub> , Cd <sub>3</sub> [Fe(CN) <sub>6</sub> ] <sub>2</sub> -titanate composite, and titanate, single-walled Ge-imogolite, double-walled Ge-imogolite, nickel silicate nanotubes and Fe <sub>3</sub> [Fe(CN) <sub>6</sub> ] <sub>2</sub> -halloysite composite.	156
8.6	Hydrogen adsorption isotherms at 77 K for (○) natural halloysite and VO <sub>x</sub> nanotubes compared with the blank quartz wool sample following temperature correction.	157
8.7	Langmuir-Freundlich fitting of excess adsorption data for bulk Cd <sub>3</sub> [Fe(CN) <sub>6</sub> ] <sub>2</sub> particles at 77 K (solid line), with the calculated absolute adsorption isotherm (dotted line).	160
8.8	Langmuir-Freundlich fitting of excess adsorption data for (a) titanate nanotubes, and (b) Cd <sub>3</sub> [Fe(CN) <sub>6</sub> ] <sub>2</sub> -titanate nanotube composite at 77 K (solid lines), with the calculated absolute adsorption isotherms (dotted lines).	161
8.9	Langmuir-Freundlich fitting of excess adsorption data for (a) Ge-imogolite single-walled nanotubes, and (b) Ge-imogolite double-walled nanotubes (solid lines), shown with the calculated absolute adsorption isotherms (dotted lines).	162
8.10	Langmuir-Freundlich fitting of excess adsorption data for (□) nickel silicate nanotubes (solid lines), with the calculated absolute adsorption isotherm (dotted lines).	162
8.11	Temperature-corrected isotherms at 77 K showing hydrogen adsorption, hydrogen desorption in single-walled Ge-imogolite, and hydrogen adsorption, hydrogen desorption in double-walled Ge-imogolite.	166

9.1	Scrolling mechanisms of different metal oxide nanotubes proposed in this thesis, (a) halloysite $\text{Al}_2\text{Si}_2\text{O}_5(\text{OH})_4$ , (b) nickel silicate $\text{Ni}_3\text{Si}_2\text{O}_5(\text{OH})_4$ , and (c) vanadium oxide $\text{VO}_{2.43}(\text{RNH}_2)_{0.27}$ .	172
A.1	TEM images and EDX spectra of halloysite nanotubes doped with Ge(IV) at the level of (a) 0.05 wt % and (b) 0.1 wt %.	177
B.1	Sample UV-visible spectra of pyrocatechol violet in the presence of (a) 20 and (b) $10 \mu\text{mol dm}^{-3}$ $\text{AlCl}_3$ solution, and (c) unreacted pyrocatechol violet.	183
B.2	Sample UV-visible spectra of Si(IV) molybdenum blue complex at (a) 0.5, (b) 0.4, (c) 0.3, (d) 0.2 and (e) $0.1 \mu\text{mol dm}^{-3}$ concentrations of dissolved $\text{SiO}_2$ .	184
B.3	Sample UV-visible spectra of V(V)-BPHA complex at (a) 40, (b) 30, (c) 20 and (d) $10 \mu\text{mol dm}^{-3}$ concentrations of dissolved $\text{V}_2\text{O}_5$ .	184
B.4	Calibration curve for $\text{Al(III)}_{(\text{aq})}$ concentration / $\mu\text{mol dm}^{-3}$ vs. absorbance at 580 nm.	185
B.5	Calibration curve for $\text{Si(IV)}_{(\text{aq})}$ concentration/ $\text{mmol dm}^{-3}$ vs. absorbance at 650 nm.	186
B.6	Calibration curve for $\text{V(V)}_{(\text{aq})}$ concentration/ $\mu\text{mol dm}^{-3}$ vs. absorbance at 535 nm.	186

## DECLARATION OF AUTHORSHIP

I, Rachel White, declare that the thesis entitled

### **Metal Oxide and Silicate Nanotubes: Synthesis and Hydrogen Storage Properties**

and the work presented in the thesis are both my own, and have been generated by me as the result of my own original research. I confirm that:

- this work was done wholly or mainly while in candidature for a research degree at this University;
- where any part of this thesis has previously been submitted for a degree or any other qualification at this University or any other institution, this has been clearly stated;
- where I have consulted the published work of others, this is always clearly attributed;
- where I have quoted from the work of others, the source is always given. With the exception of such quotations, this thesis is entirely my own work;
- I have acknowledged all main sources of help;
- where the thesis is based on work done by myself jointly with others, I have made clear exactly what was done by others and what I have contributed myself;
- parts of this work have been published as:

*(Papers Published in Peer-Reviewed Journals)*

1. R.D. White, D.V. Bavykin and F.C. Walsh, The stability of halloysite nanotubes in acid and alkaline aqueous suspensions, *Nanotechnology*, 2012, 23, 6, 065705.
2. R.D. White, D.V. Bavykin and F.C. Walsh, Spontaneous scrolling of kaolinite nanosheets into halloysite nanotubes in an aqueous suspension in the presence of  $\text{GeO}_2$ , *J. Phys. Chem. C*, 2012, 116, 15, 8824-8833.
3. R.D. White, D.V. Bavykin and F.C. Walsh, Morphological control of synthetic  $\text{Ni}_3\text{Si}_2\text{O}_5(\text{OH})_4$  nanotubes in an alkaline hydrothermal environment, *J. Mater Chem. A*, 2013, available as advance web article, DOI: 10.1039/C2TA00257D.

*(Papers to be Submitted to Peer Reviewed Journals)*

4. R.D. White, D.V. Bavykin and F.C. Walsh, Hydrothermal synthesis of metal oxide nanotubes and their applications, *Adv. Mater.*, in preparation.
5. D.V. Bavykin, R.D. White and F.C. Walsh, Nanostructured metal oxides: nanotubes, nanofibres and nanosheets, in: *Nanotechnology for Energy Systems*, vol. 3 in *Nanotechnology Book Series*, A. Eftekhari (ed.), John Wiley & Sons, in preparation.
6. R.D. White, D.V. Bavykin and F.C. Walsh, Low temperature synthesis of vanadium oxide nanowhiskers at 90 °C in the presence of ethylenediamine, *J. Mater. Chem.*, in preparation.

*(Papers Presented at Conferences)*

7. R.D. White, D.V. Bavykin and F.C. Walsh, Spontaneous scrolling of  $\text{Al}_2\text{Si}_2\text{O}_5(\text{OH})_4$  nanosheets into halloysite nanotubes stimulated by structural doping with  $\text{GeO}_2$ , *IEEE Nano 2012*, Birmingham, August 2012.
8. R.D. White, D.V. Bavykin and F.C. Walsh, Stability of  $\text{Al}_2\text{Si}_2\text{O}_5(\text{OH})_4$  (halloysite) nanotubes in acid and alkaline aqueous suspensions, *Dalton Trans. Younger Researchers Symposium*, Warwick, September 2011.
9. D.V. Bavykin, R.D. White, A.N. Kulak, and F.C. Walsh, Control over the structure of titanate nanotube agglomerates, *ACIN 2011*, Namur, Belgium, September 2011.

Signed: .....

Date:.....

## Acknowledgements

First and foremost, I would like to thank my supervisor Dr. Dmitry Bavykin for giving me the opportunity to carry out this research project, and for the invaluable expertise he has shared with me during my time spent working on this PhD project. I am deeply grateful for the support he has given me, without which this project would not have been possible, and it has been a pleasure to work with him. I would also like to thank my advisor, Professor Frank Walsh, for the advice and encouragement he has given me on writing my thesis.

I would also like to thank some of my colleagues and co-workers for the help they have given me in the laboratory. Especial thanks go to Dr. Alex Kulak and Dr. Shuncai Wang for training me to use the electron microscopes. I would also like to acknowledge the help of Professor Pillar Herrasti for the ICP analysis of germanium-doped aluminosilicates, Dr. Mark Light for training me to use the X-ray diffractometer, and Alistair Clarke for his help with the nitrogen adsorption apparatus. The help of Abdul and Blanca with the PCT-Pro apparatus was also very useful in getting me started with the hydrogen adsorption experiments in this project.

I wish to thank Dr. Carlos Ponce-de-Leon Albarran and Dr. Richard Wills for their proof-reading and useful comments during my Nine-month and Transfer Report assessments. I am also grateful to my colleagues in my office and laboratory, especially Mihaela, Irene, Natalya, Andrea, Maria, Recep, Vanessa and Ruben for their friendship and support.

Last but by no means least I wish to express my gratitude to my parents and to my fiancé Mark, who have always been there for me, happy to listen sympathetically to my PhD joys and woes! Their love and support have meant a lot to me these past three years.



## List of Abbreviations

AFM	Atomic force microscopy
BET	Brunauer- Emmett- Teller
BJH	Barrett-Joyner-Halenda
BPHA	n-benzoyl-n-phenylhydroxylamine
CNT	carbon nanotube
CVD	chemical vapour deposition
DFT	density-functional theory
DOE	United States Department of Energy
DWNT	double-walled nanotube
EDX	energy dispersive x-ray spectroscopy
FWHM	full width at half maximum
HRTEM	high-resolution transmission electron microscopy
L-F	Langmuir-Freundlich
MOF	metal-organic framework
MWNT	multiwalled nanotube
NT	nanotube
NS	nanosheet
PB	Prussian blue
PCT	pressure-composition-temperature
SAED	selected-area electron diffraction
SEM	scanning electron microscopy
SWNT	single-walled nanotube
T <sub>d</sub>	tetrahedral
TEM	transmission electron microscopy
TiNT	titanate nanotubes
TPD	temperature-programmed desorption
UV-vis.	Ultraviolet-visible
XRD	x-ray diffraction

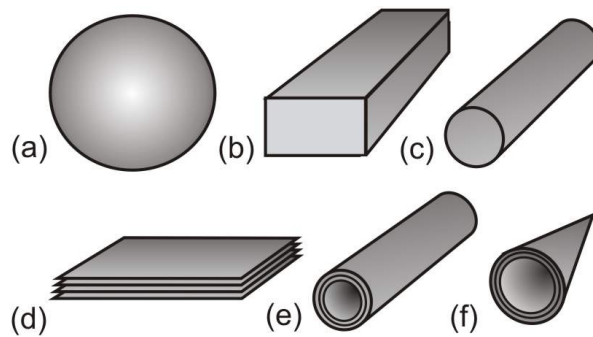




## Chapter 1: Introduction

### 1.1. Background and Motivation

Engineering of materials on the nanoscale is becoming an increasingly important area of research, due to the potential of nanomaterials to drive the miniaturisation of technology and impart unique electrical, physical or optical properties to materials. <sup>[1]</sup> Nanostructured materials have “an internal or surface structure on the nanoscale”, which is between 1 – 100 nm. <sup>[2]</sup> A wide variety of shapes (morphologies) can be found in both synthetic and natural nanostructured materials, including solid or hollow polyhedra, cylinders, spheres, and irregular shapes. These are named according to their geometry or appearance, to which the prefix *nano-* is added (Figure 1.1). This thesis focuses on the synthesis, properties and applications of cylindrical tube-shaped particles, known as nanotubes (Figure 1.1e). The wall of the nanotube can be a single- or multi-layered single-crystal, or can be made of several crystals joined together (polycrystalline).



**Figure 1.1.** Some common morphologies of nanostructured particles: (a) nanosphere, (b) nanofibre, (c) nanorod, (d) nanosheet, (e) nanotube and (f) nano-cone (horn).

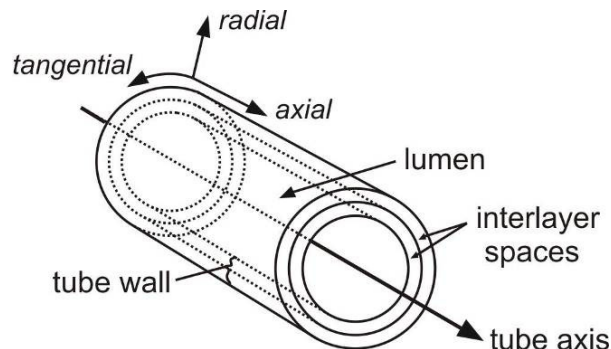
Some nanotubular structures occur naturally in minerals and have been used for centuries in applications such as ceramics, insulation and metallurgy. <sup>[3, 4]</sup> These include the metal silicate minerals  $\text{Al}_2\text{Si}_2\text{O}_5(\text{OH})_4$  (halloysite),  $\text{Mg}_3\text{Si}_2\text{O}_5(\text{OH})_4$  (chrysotile) and  $\text{Al}_2\text{SiO}_3(\text{OH})_4$  (imogolite). The earliest research into synthetic nanotubes focused on carbon nanotubes, which were first discovered in 1952, <sup>[5]</sup> with key steps towards their mass-scale use in research developed by Ijima in 1991. <sup>[6]</sup> The first synthetic non-carbon

nanotubes made from  $\text{WS}_2$  were grown in 1992,<sup>[7]</sup> followed in the same decade by others such as titanate ( $\text{H}_2\text{Ti}_n\text{O}_{2n+1}$ )<sup>[8]</sup> and vanadium oxide ( $\text{VO}_x$ ) nanotubes.<sup>[9]</sup> There are now many known examples of metallic, metal oxide, and metal chalcogenide nanotubes, of which the properties, formation mechanisms, and potential applications are not yet fully understood.

Synthesis of nanotubular structures under carefully controlled conditions together with observation and characterisation of the starting materials and products enables us to enhance our understanding of how and why nanotubular structures form, and to develop new methods of controlling nanotube morphology. Single-crystal nanotubes sourced from natural minerals contain randomly distributed impurities, either in the form of small particles of other minerals mixed amongst the nanotubes, or structural defects such as small amounts of metal ions substituted into the crystal lattice of the nanotube. Synthesis of nanotubes under geologically-inspired controlled hydrothermal conditions allows nanotubes to be made which entirely lack these impurities, or contain them in precise quantities which can be controlled by adding doping species to the reaction mixture. This allows synthetic nanotubes to be adapted for use in different applications, by including or removing different functional groups and defects from the nanotube structures.

The main reason for the recent large-scale research interest and investment in nanotubes is the fact that they are essentially very small, strong containers, which can form colloidal dispersions in solvents, or can be spun into fibrous bundles. Filling of the central cavity or pore inside nanotubes, also known as the ‘lumen’ (see Figure 1.2), could lead to several new technological applications. One such application is the filling of the lumen of a metal oxide nanotube with an electrically conductive material to create nano-sized electronic wires,<sup>[10]</sup> or surface coatings for electrodes.<sup>[11, 12]</sup> Other potential applications for nanotubes utilise the functional groups on the surfaces of metal oxide nanotubes to bind small molecules, trapping them inside the tube. In solution environments the tube ends may be covered with slowly-dissolving chemical stoppers, creating an ideal ‘timed-release’ capsule for *in-vitro* drug delivery.<sup>[13 -15]</sup> Nanotubes which have a very good biocompatibility, such as  $\text{Al}_2\text{Si}_2\text{O}_5(\text{OH})_4$ , could be particularly suitable for this application.<sup>[16]</sup> For applications in which nanotubes may be exposed to

corrosive solution environments, knowledge of their long-term stability in solutions is important.



**Figure 1.2.** The nomenclature used to describe different parts of a nanotube. The italic labels describe the directions along the nanotube which are linked to specific crystallographic axes.

The highly porous nature of nanotubes has also led to investigation into their use as gas adsorbents. Hydrogen gas is currently used in many industrial processes, and if hydrogen is to replace fossil fuels in mobile applications such as powering car engines, a suitable method of storing and transporting hydrogen must be developed. Current methods of hydrogen storage as compressed gas or liquid are not ideal because of the safety issues surrounding the use of high pressures and low temperatures, and the likelihood of leaks.<sup>[17]</sup>

Storage of hydrogen through chemical absorption or physical adsorption of  $H_2$  molecules by solid materials has been investigated for more than two decades, and although many intriguing new materials have been created to meet this need there is still no single material which meets the US Department of Energy (DOE) 2015 targets of (i) more than 9 wt % adsorption of hydrogen under modest pressures ( $< 200$  bar), (ii) a volumetric storage of 81 g hydrogen per litre, and (iii) favourable kinetics of hydrogen adsorption and release (desorption), occurring within a few minutes.<sup>[18]</sup> The hydrogen adsorption properties of many newly discovered nanotubular materials have not yet been investigated. The latter part of this thesis discusses the results of volumetric hydrogen adsorption experiments designed to quantify and compare the hydrogen adsorption properties of several different metal oxide nanotubes.

## 1.2. Aims and Objectives

The aims of this thesis are to increase understanding of the synthesis mechanisms leading to the formation of metal oxide nanotubes under hydrothermal conditions, and to investigate whether these nanotubes are viable materials for hydrogen storage. The research therefore pursued the following objectives:

- development of a synthesis method for halloysite ( $\text{Al}_2\text{Si}_2\text{O}_5(\text{OH})_4$ ) multiwalled nanotubes, which occur naturally but have not yet been synthesised in quantities more than a few milligrams;
- manipulation of the conditions (i.e. temperature, solvent composition) in existing hydrothermal synthesis procedures of nickel silicate ( $\text{Ni}_3\text{Si}_3\text{O}_5(\text{OH})_5$ ) and vanadium oxide ( $\text{VO}_x$ ) nanotubes, in order to identify the optimal synthesis conditions and understand the reaction mechanisms;
- comparison of these synthesis procedures and previously studied details of titanate ( $\text{H}_2\text{Ti}_x\text{O}_{2x+1}$ ) nanotubes synthesis with an aim to highlighting the structural and morphological factors in these crystalline materials which cause their spontaneous conversion into nanotubes under hydrothermal conditions;
- assessment of the long-term solution stability of halloysite ( $\text{Al}_2\text{Si}_2\text{O}_5(\text{OH})_4$ ) nanotubes in dilute and concentrated acidic and alkaline solutions;
- use of volumetric (Sieverts) apparatus to quantify the adsorption of hydrogen onto metal oxide nanotubes including halloysite, nickel silicates, vanadium oxide multiwalled nanotubes and germanium-imogolite single-walled nanotubes, with an aim to understanding the structural and morphological factors that improve or inhibit adsorption of hydrogen in nanotubular materials. Formation of composite materials of metal oxide nanotubes with nanoporous Prussian blue analogue materials ( $\text{M}_x[\text{Fe}(\text{CN})_6]_2$ ,  $\text{M} = \text{Cd}, \text{Fe}$ ) to investigate whether this improves the hydrogen adsorption properties.

### 1.3. Thesis Outline

This thesis is divided into review, methodology, and results and analysis chapters, followed by a conclusions chapter in which the results are summarised and suggestions for further work are made. In Chapter 2 a thorough literature review of the hydrothermal synthesis, physical/chemical properties and hydrogen storage properties of metal oxide nanotubes is presented. The hydrogen storage properties of inorganic nanotubes are compared with the data for other leading hydrogen storage materials and the potential advantages of using metal oxide nanotubes in hydrogen storage applications are discussed.

Chapter 3 describes the experiments designed to address the thesis aims in the previous section. The results of these experiments along with discussion of their significance are presented in Chapters 4-8. In Chapter 4, results of the hydrothermal synthesis of halloysite nanotubes ( $\text{Al}_2\text{Si}_2\text{O}_5(\text{OH})_4$ ) from  $\text{Al}(\text{OH})_3$  and  $\text{SiO}_2$  in the presence of  $\text{GeO}_2$  are presented. Chapter 5 presents results of the solution stability and dissolution mechanism of naturally-occurring halloysite nanotubes in acidic and alkaline solutions. In Chapter 6, the effect of varying the ratio of Ni to Si and sodium hydroxide concentration in the hydrothermal synthesis of nickel silicate nanotubes ( $\text{Ni}_3\text{Si}_2\text{O}_5(\text{OH})_4$ ) is studied. Chapter 7 presents the results of attempts to produce vanadium oxide nanotubes at lower temperature by increasing vanadium solubility through complexation with ethylenediamine.

In Chapter 8 the measured hydrogen storage properties of nanotubular metal oxides and their composites with nanoparticulate Prussian blue analogues,  $\text{M}_x[\text{Fe}(\text{CN})_6]_2$ , are presented for analysis and discussion. Finally, the results are drawn together into a set of conclusions in Chapter 9, and suggestions for further work are provided.



## Chapter 2: Literature Review

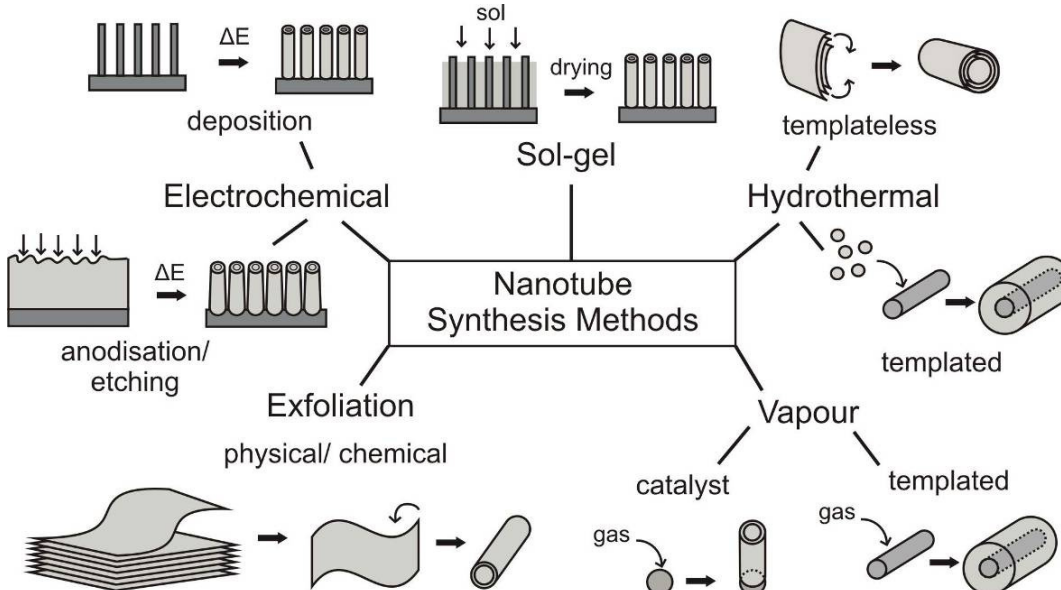
### 2.1. Synthesis of metal oxide nanotubes

#### 2.1.1. Comparison of different synthetic strategies

Nanotubes composed of inorganic materials can be synthesised by many different methods, depending on the structure and bonding nature of the nanotube. For example, crystalline nanotubes made from insoluble materials containing strong covalent bonds (such as carbon or boron nitride) can be assembled via deposition of vapourised atoms onto a catalyst particle, using laser arc-ablation or chemical vapour deposition (CVD) techniques.<sup>[19, 20]</sup> Electrolyte-soluble materials can be used to produce nanotube arrays with an amorphous or polycrystalline structure via electrochemical methods, such as anodisation of a metal or electrodeposition onto a nanoporous template.<sup>[21, 22]</sup> Soluble materials which recrystallise in solution can form nanotubes using hydrothermal or sol-gel methods<sup>[23, 24]</sup> in which the precipitated crystals spontaneously form as nanotubes or are directed into a nanotubular shape by the use of a template. A similar spontaneous scrolling of crystallites into nanotubes can be achieved at room temperature through the exfoliation of 2-D layered crystals (Figure 2.1).<sup>[25, 26]</sup>

Compared with most other methods, hydrothermal synthesis has the advantages of requiring uncomplicated equipment (autoclaves), and being readily scaled up to gram quantities. Additionally, many of the alternative synthesis methods require the use of a nano-/micro-structured catalyst material or template, which has the complication that the template requires prior synthesis and subsequent removal from the nanotubes. On the other hand, a template is not necessary in many hydrothermal methods, as spontaneous scrolling of single crystals to form nanotubes under hydrothermal conditions is known to occur for many different materials that possess a 2-D layered crystal structure.<sup>[27]</sup> For these reasons, templateless hydrothermal synthesis of nanotubes is the chosen method of synthesis in this thesis.





**Figure 2.1.** The most common nanotube synthesis methods.

Many inorganic species with 2-D layered crystal structures have been hydrothermally synthesised as nanotubes, for example metallic bismuth, metal chalcogenides (e.g.  $\text{WS}_2$ ,  $\text{TiS}_2$ ), metal oxides or hydroxides (e.g.  $\delta\text{-MnO}_2$ ,  $\text{Mg}(\text{OH})_2$ ) and metal silicates (e.g.  $\text{Ni}_3\text{Si}_2\text{O}_5(\text{OH})_4$ ).<sup>[28, 29]</sup> The metal oxides are particularly interesting as they can be synthesised from lighter, more readily available materials (containing elements from rows 3 and 4 of the standard periodic table), and are in some cases already found in natural rocks in appreciable quantities.<sup>[30]</sup> This literature review focuses on discussion of the reaction mechanisms of hydrothermal syntheses which form metal oxide nanotubes, and analysis of the thermal, structural and solution properties of both natural and synthetic metal oxide nanotubes with particular reference to their applications as gas adsorbents.

### 2.1.2. Hydrothermal synthesis methods for metal oxide nanotubes

Many metal oxide structures possess a 2-D layered crystal structure, which is considered a necessary requirement for the spontaneous templateless formation of nanotubes under hydrothermal conditions.<sup>[29]</sup> Metal oxides and hydroxides are often composed of symmetric crystal layers, in which the two surfaces of the crystal are identical. On the

other hand, layer asymmetry is common in mixed metal oxides, particularly in metal silicates. The symmetry of the crystal structure affects the nanotube formation mechanism (see section 2.1.3). For this reason, the synthesis methods of oxide/hydroxide and silicate nanotubes are presented separately (Tables 2.1 and 2.2.).

The metal ions which form metal oxide nanotubes are usually from the third and fourth row of the standard periodic table. Layered hydroxides/oxides of heavier metals are less common; the multiwalled nanotubes of the heavier elements tend to include sulphur e.g.  $\text{MoS}_2$ ,  $\text{WS}_2$ , with the exception of some rare-earth hydroxide ( $[\text{Y}, \text{Tb}, \text{Dy}, \text{Ce}](\text{OH})_3$ ) nanotubes with a quasi-layered structure, which are presented elsewhere.<sup>[31-33]</sup>

From the summary of synthesis methods for metal oxide/hydroxide nanotubes presented in Table 2.1, it is clear that the nanotubes have all been synthesised in an alkaline environment, though in many cases the pH before, during and after reaction has not been measured. A significant pH drop is expected during the synthesis of metal hydroxide nanotubes, as the initially present dissolved metal salts react with  $\text{OH}^-_{(\text{aq})}$  to precipitate micro- or nano-sized particles of  $x$ -ray amorphous  $\text{M}(\text{OH})_x \cdot n\text{H}_2\text{O}$  ( $x$  is given by the oxidation state of the metal, e.g.  $\text{Ni}^{(\text{II})}(\text{OH})_2$ ,  $\text{Al}^{(\text{III})}(\text{OH})_3$ ) which are converted to crystalline nanotubes during hydrothermal treatment. This precipitation can only occur under alkaline conditions (see Figure 2.6 page 21). In the case of titanate,  $\delta\text{-MnO}_2$  and  $\text{VO}_x$  metal oxides, solid starting materials are used, and addition of a base may be necessary to facilitate dissolution and recrystallisation of these materials.

The hydrothermal treatment of the precursor suspension under alkaline conditions, usually at or above 200 °C for metal hydroxides and at a lower temperature for metal oxides, results in the formation of nanotubes. Thus far this method, which utilises different bases and solvents depending on the solubility and reactivity of the starting materials, has been successfully applied to several of the lighter metal oxides (table 2.1). However, the synthesis of large quantities of some metal hydroxide nanotubes remains a challenge. For example, following the synthesis protocols of Zhou et al.<sup>[34]</sup> yields only milligram quantities of nanotubes. Templateless hydrothermal synthesis of nanotubes from multilayered hydroxides such as  $\text{Cr}(\text{OH})_3$ ,  $\gamma\text{-FeOOH}$  and  $\text{Zn}(\text{OH})_2$  has yet to be achieved.

**Table 2.1.** Morphology and hydrothermal synthesis of metal hydroxide and oxide nanotubes with layered structure. The abbreviations  $\text{pH}_i$  = initial pH,  $\text{pH}_f$  = final pH after hydrothermal treatment, and \* indicates pH measured in this work. Time abbreviations: min = minutes, h = hours, d= days.

Nanotube	Chemical formula	Outer diameter /nm	Inner diameter /nm	Average length/ nm	Starting materials	$\text{pH}_i$	$\text{pH}_f$	Solvent	T /°C	Duration	Refs.
Magnesium hydroxide	$\text{Mg}(\text{OH})_2$	10 - 20	7 - 12	$\approx 10^3$	$\text{MgCl}_2 + \text{NH}_3 \cdot \text{H}_2\text{O} + \text{NaNO}_3$	-	9*	$\text{H}_2\text{O}/ \text{MeOH}$	250	36 h	[34]
Boehmite	$\gamma\text{-AlOOH}$	5	2	100	$\text{AlCl}_3 + \text{NaNH}_2$	-	-	$\text{H}_2\text{O}$	200	12 h	[35]
Titanate	$\text{H}_2\text{Ti}_n\text{O}_{2n+1}$	10	4	100	$\text{TiO}_2$ (P25)	> 14	-	$\text{NaOH/KOH}$ 40 wt%	90 - 110	4 d	[36]
Vanadium oxide	$\text{VO}_x$	50 - 150	5 - 50	$10^3 - 150^3$	$\text{V}_2\text{O}_5 + \text{C}_n\text{H}_{2n+1}\text{NH}_2$ where $4 < n < 22$	$\approx 10^*$	8.4*	$\text{H}_2\text{O}/ \text{EtOH}$	180	7 d	[37]
Chromium hydroxide	$\text{Cr}(\text{OH})_3$	-	-	-	not yet synthesised	-	-	-	-	-	-
Manganese oxide	$\delta\text{-MnO}_2$	10 - 20	2 - 10	$10^3 - 100^3$	$\alpha\text{-NaMnO}_2$	7	11.7*	$\text{H}_2\text{O}$	120 - 140	4 d	[38]
Lepidocrocite	$\gamma\text{-FeOOH}$	-	-	-	no templateless synthesis	-	-	-	-	-	-
Cobalt oxide	$\text{Co}_3\text{O}_4$	10 - 20	$\approx 10$	$\approx 10^3$	$\text{Co}(\text{NO}_3)_2 + \text{NH}_3 \cdot \text{H}_2\text{O} + \text{NaNO}_3$	-	-	$\text{H}_2\text{O}/ \text{MeOH}$	250	24 h	[34]
Nickel hydroxide	$\text{Ni}(\text{OH})_2$	10 - 20	$\approx 12$	$\approx 10^3$	$\text{Ni}(\text{NO}_3)_2 + \text{NH}_3 \cdot \text{H}_2\text{O} + \text{NaNO}_3$	-	-	$\text{H}_2\text{O}/ \text{MeOH}$	250	24 h	[34]
Copper hydroxide	$\text{Cu}(\text{OH})_2$	10	$\approx 5$	230 - 280	$\text{CuSO}_4 + \text{NaOH}$	>14	-	$\text{NaOH}$ , 4 wt %	25	5.5 min	[39]
Zinc hydroxide	$\text{Zn}(\text{OH})_2$	-	-	-	not yet synthesised	-	-	-	-	-	-

**Table 2.2.** Morphology and hydrothermal synthesis of metal silicate nanotubes with layered structure. The abbreviations  $\text{pH}_i$  = initial pH,  $\text{pH}_f$  = final pH after hydrothermal treatment, and \* indicates pH measured in this work. Time abbreviations: min = minutes, h = hours, d= days.

Nanotube	Chemical formula	Outer diameter /nm	Inner diameter /nm	Average length/ nm	Starting materials	Solvent	$\text{pH}_i$	$\text{pH}_f$	T /°C	Duration	Refs.
Magnesium silicate	$\text{Mg}_3\text{Si}_2\text{O}_5(\text{OH})_4$	25	5	$100 - 10^3$	$\text{SiO}_2 + \text{Mg}(\text{OH})_2$	NaOH, 2 wt%	> 14	-	250	24 - 48 h	[40]
Imogolite	$\text{Al}_2\text{SiO}_3(\text{OH})_4$	2.2 – 2.5	1	20 - 150	$\text{Si}(\text{OEt})_4 + \text{MgCl}_2 \cdot 6\text{H}_2\text{O}$	$\text{H}_2\text{O} + \text{HCl}$	4.3	< 3.5	98	5 -7 d	[41, 42]
Halloysite	$\text{Al}_2\text{Si}_2\text{O}_5(\text{OH})_4$	50 - 100	5 - 15	$2 \times 10^3$	Dilute $\text{AlCl}_3/ \text{Al}(\text{OAc})_3 + \text{Na}_2\text{SiO}_3$	$\text{H}_2\text{O}$	4	5.74 - 6.55	20 - 60	2 -3 m	[43, 44]
Manganese silicate	$\text{Mn}_3\text{Si}_2\text{O}_5(\text{OH})_4$	-	-	-	$\text{Mn}(\text{NO}_3)_2 \cdot 2\text{H}_2\text{O} + \text{Na}_2\text{SiO}_3 + \text{OH}^-$	$\text{EtOH} + \text{H}_2\text{O}$	-	-	180 - 200	48 h	[45]
Magnesium iron silicate	$\text{Mg}_{2.31}\text{Fe}_{0.62}\text{Si}_2\text{O}_5(\text{OH})_4$	30 - 50	5 - 6	300 - 500	$(\text{Mg}, \text{Fe})\text{SiO}_3 + (\text{Mg}, \text{Fe})\text{O}$	NaOH, 1.5 - 2 wt%	> 14	-	250 - 450	15 -24 h	[46]
Cobalt silicate	$\text{Co}_3\text{Si}_2\text{O}_5(\text{OH})_4$	5 - 10	1 - 2	100 - 200	$\text{CoSiO}_3 \cdot 9\text{H}_2\text{O} + \text{Co}(\text{OH})_2$	NaOH, 1.5 - 2 wt%	> 14	-	250 - 350	48 - 72 h	[46]
Nickel phyllosilicate	$\text{Ni}_3\text{Si}_2\text{O}_5(\text{OH})_4$	20	8 - 15	> 100	$\text{NiCl}_2 \cdot 6\text{H}_2\text{O} + \text{Na}_2\text{SiO}_3$	NaOH, 18 wt%	> 14	11.4*	190 - 210	24 h	[47]
		10 -15	2 - 3	$10^3$	$\text{NiSiO}_3 + \text{Ni}(\text{OH})_2$	NaOH, 1.5 - 2 wt%	> 14	-	250 - 450	24 h	[46]
Copper silicate	$\text{CuSiO}_3 \cdot 2\text{H}_2\text{O}$	8 - 10	$\approx 2$	$\approx 500$	$\text{Cu}(\text{NO}_3)_2 \cdot 2\text{H}_2\text{O} + \text{NH}_3 + \text{Na}_2\text{SiO}_3$	2:1 EtOH:H <sub>2</sub> O	9*	10*	180 - 200	48 h	[45]
Zinc silicate	$\text{Zn}_3\text{Si}_2\text{O}_5(\text{OH})_4$	-	-	-	not yet synthesised	-	-	-	-	-	-

Development of synthesis methods for silicate nanotubes (Table 2.2) was initially inspired by naturally occurring nanotubular crystals such as  $\text{Al}_3\text{Si}_2\text{O}_5(\text{OH})_4$  (halloysite),  $\text{Al}_2\text{SiO}_3(\text{OH})_4$  (imogolite) and  $\text{Mg}_3\text{Si}_2\text{O}_5(\text{OH})_4$ . High temperatures ( $\geq 200^\circ\text{C}$ ) are required to precipitate the crystalline layered metal silicates rather than the amorphous species which persist for several months/years in saturated solutions at low temperatures.<sup>[48]</sup> The synthesis of imogolite is an exception, since high-dilution conditions are required to avoid the formation of amorphous silica<sup>[49]</sup> and to directly precipitate imogolite via silicon (IV) and aluminium (III) co-polymerisation at a lower temperature ( $90 - 100^\circ\text{C}$ ).<sup>[50]</sup>

An alkaline environment is required for the synthesis of silicate nanotubes (with the exception of aluminosilicates which require an acidic environment). The solvent may consist of an ethanol/ water mixture or distilled water alone, and typical yields can be up to several grams on a laboratory scale. Difficulties have been encountered in attempts to synthesise pure iron silicates ( $\text{Fe}_3\text{Si}_2\text{O}_5(\text{OH})_4$ ), with flat lamellar particles being precipitated instead.<sup>[51]</sup> There is as yet no report of an attempt to synthesise zinc silicate nanotubes. Calcium, iron, and manganese silicates were reported in 2004 but sufficient details regarding solvent composition to reproduce this synthesis were not given.<sup>[45]</sup>

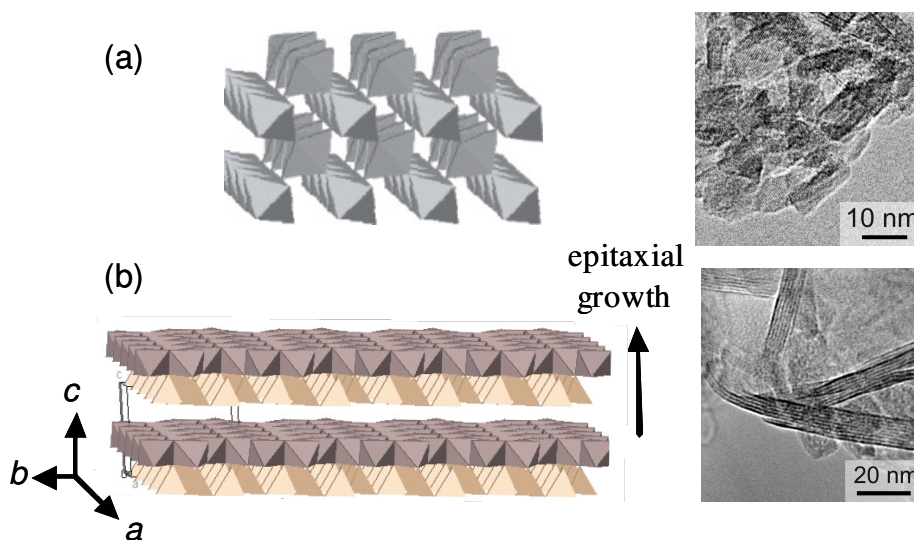
Of all the nanotubes presented in Tables 2.1 and 2.2, only the titanates,  $\text{VO}_x$ , and Mg (chrysotile), Al (imogolite), Ni, and Co silicates have been reliably and reproducibly synthesised in larger quantities (more than a few milligrams) and at high percentage yields. Although halloysite has not yet been synthesised in large quantities (for reasons discussed in Section 2.3), there are large natural reserves available.<sup>[52]</sup> Consequently, research involving these particular nanotubes is at a more advanced stage, and their applications are already being explored in research areas such as dye-sensitised solar cells,<sup>[53]</sup> high surface-area catalysts,<sup>[54]</sup> ion-exchange materials for electrocatalysis,<sup>[47, 55-57]</sup> storage of hydrogen molecules<sup>[57, 58]</sup> and encapsulation of pharmaceuticals.<sup>[59, 60]</sup> Most of the other nanotubes in Tables 2.1 and 2.2 were only reported in a single publication and require reproduction, verification and improvement of synthesis yields before potential applications can be investigated.

## 2.2. Structure of metal oxide nanotubes

### 2.2.1. Crystal structures of metal oxide nanotubes

Nanotubes synthesised via a templateless hydrothermal technique are usually single-crystalline in nature, and based on a curved form of a thin, flat single-crystal polymorph (nanosheet). The structure of these single-crystals is crucial in determining nanotube morphology, as it affects both the strain energy caused by nanosheet curvature and the energetics of nanotube growth through addition of atoms to the nanotube ends.

Since inorganic nanotubes are a recently-discovered class of materials, the precise crystal structures of many nanotubes along with their mechanism of curvature is not yet fully known, because the small crystallite sizes cause broadening of diffraction peaks and lead to some uncertainty in crystal structure. However, it appears that a two-dimensional layered crystal structure is essential, as it promotes the crystallisation of flexible nanosheet structures only a few nm thick (Figure 2.2) which are capable of spontaneous scrolling to form nanotubes.<sup>[29]</sup>



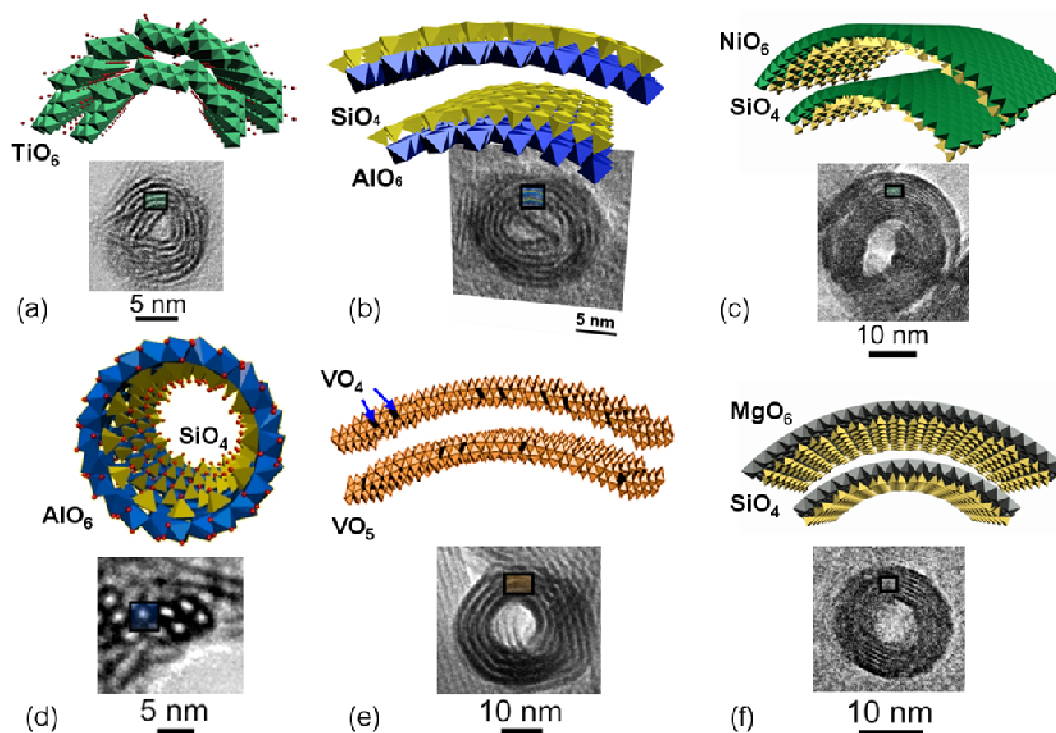
**Figure 2.2.** Crystal structures with corresponding TEM images showing how crystal growth readily occurs in all directions in a 3 D crystal structure (image a), but is directed along the basal plane in 2 D crystal structures due to weaker interlayer forces (image b). The crystals in (a) are TiO<sub>2</sub> (rutile/anatase), and in (b) are Al<sub>2</sub>Si<sub>2</sub>O<sub>5</sub>(OH)<sub>4</sub> (kaolinite).

Such flat nanosheet structures can easily occur in 2-D crystal structures due to the slower rate of crystal growth in the epitaxial direction compared to growth along the crystal planes. This is caused by the weaker interlayer bonding interactions compared to the covalent intra-layer bonds (c.f. graphite<sup>[61]</sup>).

Early reports indicate that nanotubes based on  $M(OH)_x$  or  $MO_x$  where M is a group 2-13 metal in the extended periodic table are composed of the crystal polymorph which is related to the two-dimensional layered  $CdI_2$  structure (e.g.  $\beta$ - $Ni(OH)_2$  and  $\delta$ - $MnO_2$ <sup>[34, 38]</sup>). Other metal oxide nanotubes have a more complex layered crystal structure, with a mixture of oxide/hydroxide groups and structural vacancies, for example titanate nanotubes. The actual composition of the ion-exchanged titanate nanotubes is still open to debate, with  $H_2Ti_nO_{2n+1}$  (titanates),  $H_{4x}Ti_{2-x}\square_xO_4 \cdot 2H_2O$  (lepidocrocite,  $\square$  is a cationic vacancy),  $TiO_2$ -(B), and  $TiO_2$  (tetragonal anatase) having been suggested by various sources.<sup>[62]</sup>

The crystal structure of metal silicate nanotubes described by  $M_xSi_2O_5(OH)_4$  or  $M_2SiO_3(OH)_4$  is even more complex, having an asymmetric layer structure in which  $SiO_4$  tetrahedra are bonded to one surface of a metal hydroxide sheet (Figure 2.3).<sup>[63]</sup> The crystal structure of this metal hydroxide sheet depends on the oxidation state of the metal: trioctahedral sheets are formed for metals in the 2+ oxidation state, and dioctahedral sheets which have 1/3 of cation sites vacant are formed for metals in the 3+ oxidation state.<sup>[63]</sup> Consequently both metal oxidation state and metal cation size affect the overall layer geometry, and the extent of nanotube scrolling (see Section 2.3).

In the  $M_xSi_2O_5(OH)_4$  (chrysotile and halloysite-type) structures the  $SiO_4$  tetrahedra are polymerised and form a continuous distorted hexagonal sheet on the metal hydroxide surface, whereas in the  $M_2SiO_3(OH)_4$  (imogolite) structure the  $SiO_4$  are tri-alumina bound and do not form a continuous polyhedral network (Figure 2.3d). The 0.7 – 0.8 nm interlayer spacing (basal spacing), common to all metal hydroxide-based species such as titanates and metal silicates, results from the weak (hydrogen-bonded) forces between adjacent surface hydroxyl groups.<sup>[64, 65]</sup>



**Figure 2.3.** Crystal structures with the corresponding cross-sectional HRTEM images of (a) titanate nanotubes (b) halloysite (c) nickel silicate, (d) imogolite, (e) vanadium oxide, and (e) magnesium silicate nanotubes. The red spheres in image (a) represent  $\text{Na}^+$  or  $\text{H}^+$  ions; in image (d) they represent hydroxyl groups. The shaded box in each image shows the area represented in the crystal structure diagram. Note that crystal structures (c) and (f) have identical symmetry, and are shown from different angles. The crystal structures in images (d) and (e) are modified from references <sup>[172, 133]</sup> respectively.

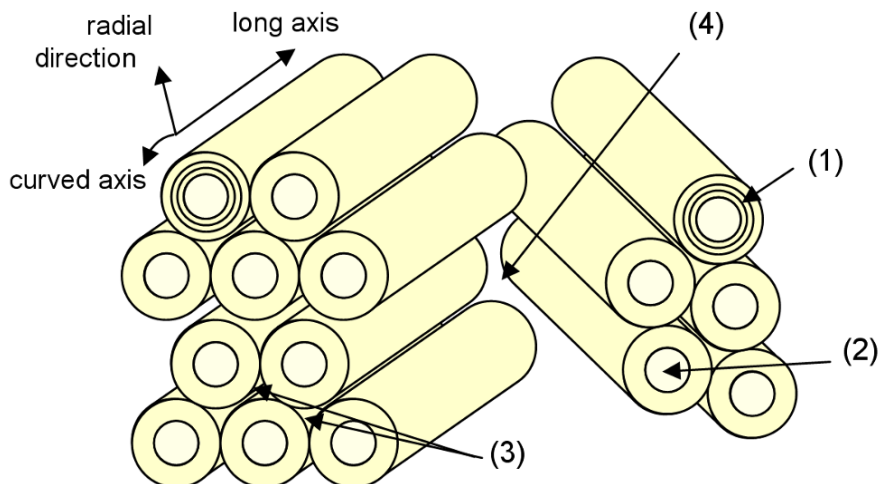
Vanadium oxide nanotubes have been described as mixed vanadium(IV/V) oxides, in which some of the  $\text{V}_2\text{O}_5$  species have been reduced to  $\text{VO}_2$  by redox reactions under the hydrothermal conditions to give an indeterminate  $\text{VO}_x$  structure at 180 °C. <sup>[37]</sup> The interlayer spacing of pure  $\text{V}_2\text{O}_5$  is only 0.437 nm because of interlayer  $\text{V}^{\delta+}\text{-O}^{\delta-}$  polar interactions, <sup>[66]</sup> and must be increased by intercalation in order for the structure to have sufficient flexibility to bend and curve into a nanotubular shape. Amines, with their polar  $\text{NH}_3^+$  head group and adjustable tail group, have proved convenient intercalating agents which form a bilayer between the  $\text{V}_2\text{O}_5$  layers in the starting materials. <sup>[37, 67]</sup> The interlayer spacing of the resulting intercalate depends on the length of the amine tail group, and can be increased to 2 – 4 nm. <sup>[37]</sup> The amine molecule is also responsible for



the hydrothermal redox processes which convert  $V_2O_5$  into a partially reduced structure analogous to  $V_7O_{16}$ , which is believed by some to be the primary driving force for nanotube formation.<sup>[68]</sup> The molecular formula of vanadium oxide nanotubes can be approximated by  $VO_{2.43 \pm 0.03} (RNH_2)_{0.27 \pm 0.01}$ ,<sup>[37]</sup> and the distribution of the V(IV) tetrahedra (approximately 10 % of the total vanadium) in the layers is believed to be anisotropic (see Figure 2.3).

### 2.2.2. Morphology and Porosity

In nanotubes formed from 2-D crystal lattices, the epitaxial crystal direction lies along the tube radius, and the other two crystallographic axes form the circumference and long axis of the tube (Figure 2.4). The closed tubular structure means that the nanotubes grow along their long axis during hydrothermal treatment. After several days hydrothermal treatment (Tables 2.1 and 2.2) the aspect ratio (diameter divided by length) of nanotubes can become very large, up to 500 – 5000. This means that diffusion of ions and small molecules through the interlayer spaces is much slower than in the bulk liquid and gas phases,<sup>[69]</sup> though diffusion rates through the tube centre (lumen) may be comparable.<sup>[70]</sup>



**Figure 2.4.** Schematic diagram of the nanotube axes, and four different types of pore: (1) interlayer, (2) intratubular (lumen), (3) intertubular, and (4) pores between aggregates.

Nanotubular materials have four different types of pores in the micro-/mesoporous range. At the smallest end of the scale are the pores between crystal layers of multiwalled nanotubes (1), which are usually in the ultramicroporous range ( $< 1$  nm). The tube lumen (2) is usually mesoporous ( $\approx 10$  nm), except for the smallest single-walled nanotubes which are microporous. The pores between close-packed nanotubes (3) are normally similar in diameter to the lumen, though they have a different geometry (Figure 2.4). Larger mesopores ( $> 10$  nm) exist between close-packed bundles of tubes (4), and a presence of a large number of these pores distributed across a wide range of diameters indicates poor close-packing in nanotubular solids.

Transmission electron microscopy provides detailed information regarding the structure and shape of individual nanotubes (Figure 2.5), and the standard technique for bulk analysis of pores is nitrogen adsorption and desorption at  $-196$  °C. The specific surface area is calculated from the adsorption isotherm using the BET method,<sup>[71]</sup> and the distribution of pore sizes can be calculated from either the adsorption or desorption isotherm using the BJH method.<sup>[72]</sup> Since the kinetic diameter of the  $N_2$  molecule is  $0.364$  nm,<sup>[73]</sup> nitrogen adsorption is not usually suitable for accessing interlayer pores. The interlayer pores are usually much smaller than the basal spacing (distance from the bottom of a crystal layer to the bottom of the adjacent crystal layer), which is  $0.7$  nm in most multiwalled nanotubes. The limited access of nitrogen to the microporous interlayer spaces usually results in a low ( $< 50$  cm<sup>3</sup>g<sup>-1</sup>) adsorption of nitrogen in the microporous region of the adsorption isotherm ( $P/P_0 < 0.1$ ) for multiwalled nanotubes.

The available specific surface area and porosity data for metal oxide nanotubes is summarised in Table 2.3. The nanotubular structures with the smallest diameters generally have the largest surface area, since nitrogen cannot access the interlayer pores of larger nanotubes with thicker walls. It appears from the literature data that titanate, imogolite and nickel silicate nanotubes have the highest surface areas and are therefore probably the most suitable inorganic nanotubes for use in gas adsorption applications (see Section 2.5). The interlayer spaces in most cases are  $< 0.7$  nm, and access of  $N_2$  molecules is probably blocked by surface functional groups (e.g.  $-OH$ ), or by amine molecules in the case of vanadium oxide nanotubes.

**Table 2.3.** Morphology of metal oxide nanotubes. Abbreviations stand for  $S_{\text{BET}}$  = BET specific surface area,  $V_{\text{pores}}$  = specific adsorption total pore volume,  $n$  = average number of layers,  $d_s$  = basal interlayer spacing,  $d_o$  = approximate outer diameter,  $d_i$  = approximate inner diameter,  $l$  = approximate average length.

Nanotube	Chemical formula	$n$	$d_s$ /nm	$d_o$ /nm	$d_i$ /nm	$l$ /nm	$S_{\text{BET}} / \text{cm}^2 \text{g}^{-1}$	$V_{\text{pores}} / \text{cm}^3 \text{g}^{-1}$	Refs.
Titanate	$(\text{Na/H})_2\text{Ti}_n\text{O}_{2n+1}$	4	0.73	10	4	100	200 - 300	0.22	[74]
Vanadium Oxide	$\text{VO}_{2.43}(\text{RNH}_2)_{0.27}$	20	2 - 4	100	20	$5 \times 10^3$	13 - 80	0.19	[37, 75, 76]
Halloysite	$\text{Al}_2\text{Si}_2\text{O}_5(\text{OH})_4$	28	0.73	50	10	$2 \times 10^3$	16 - 80	0.08 - 0.25	[65]
Imogolite	$\text{Al}_2\text{SiO}_3(\text{OH})_4$	1	-	2.2	1	100	240 - 400	0.12 - 0.15	[77, 78]
Chrysotile	$\text{Mg}_3\text{Si}_2\text{O}_5(\text{OH})_4$	14	0.73	25	5	1000	15 - 90	0.01 - 0.25	[79, 80]
Nickel silicate	$\text{Ni}_3\text{Si}_2\text{O}_5(\text{OH})_4$	7	0.73	20	10	1000	110	0.45	[47, 81]

The total pore volume is similar for all nanotubular structures because, as nanotube diameter increases, the decrease in the specific volume of pores of type (3) is compensated by an increase in the volume of pore of type (2) and (4) (see Figure 2.4). If the nanotube length distribution is wide, the total pore volume may be increased by the creation of a large number of irregular pores of type (4) since close-packing is disrupted. The wide variation in surface area and pore volume observed for halloysite, imogolite and chrysotile nanotubes can be explained by the fact that they are naturally occurring materials, and therefore contain varying amounts of impurities, and have a wide distribution of lengths and diameters.<sup>[65]</sup>

### 2.3. Mechanisms of nanotube formation

The spontaneous synthesis of nanotubes in a hydrothermal environment is widely believed to proceed via the formation of crystalline nanosheets.<sup>[29]</sup> Nanosheets which are flexible and thin ( $< 100$  nm) in the direction of epitaxial crystal growth, and have weak interlayer forces (Van der Waals or hydrogen bonds) may scroll around a particular crystallographic axis to form nanotubes. By way of evidence for this

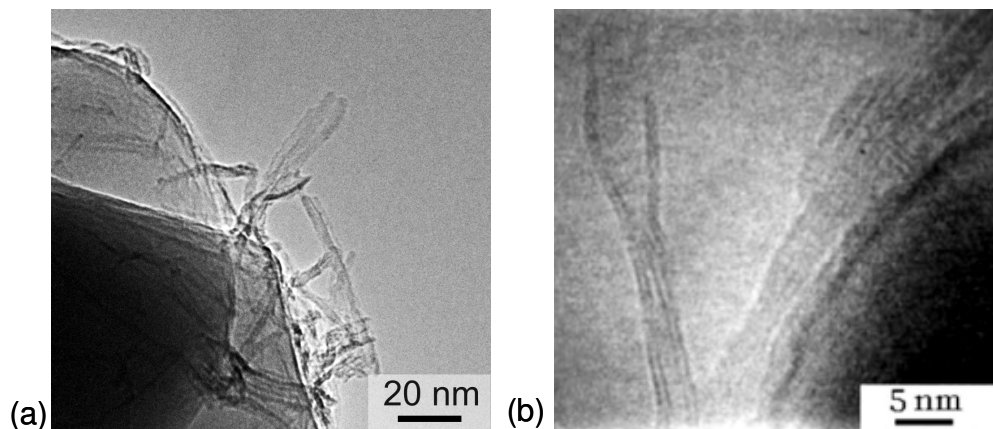
hypothesis, nanosheets have been noted to appear prior to the formation of nanotubes in studies of the syntheses of  $\text{Co}_3\text{O}_4$ ,  $\text{CoO}$ ,  $\text{Ni}(\text{OH})_2$  and  $\text{Mg}(\text{OH})_2$ ,<sup>[34]</sup>  $\gamma\text{-AlOOH}$ ,<sup>[35]</sup>  $\delta\text{-MnO}_2$ ,<sup>[82]</sup> titanate,<sup>[36, 83]</sup>  $\text{VO}_x$ <sup>[84]</sup> and  $\text{Mg}_3\text{Si}_2\text{O}_5(\text{OH})_4$ <sup>[40]</sup> nanotubes. Based on the experimental evidence, it is probable that most metal hydroxide and oxide nanotubes are formed directly from scrolling of nanosheets with crystal structures identical to those of the resulting nanotube.<sup>[26, 84, 85-87]</sup> The nanosheets appear to grow via precipitation from solution over time, eventually scrolling to form nanotubes when they reach a certain critical size.<sup>[36, 88-90]</sup>

Thus the two main stages involved in templateless hydrothermal synthesis of nanotubes are (i) conversion of the starting materials into crystalline nanosheets, followed by (ii) scrolling of the nanosheets to form nanotubes. There are several mechanistic pathways which have been proposed to explain how these stages are achieved, and these are discussed in detail the following two sections.

### 2.3.1. Growth of metal oxide nanosheets

Metal oxide nanosheets with a 2-D crystal structure can be produced by calcination of a powdered precursor material, or by atomic deposition onto a flat surface.<sup>[91, 92]</sup> However, the nanosheets that undergo scrolling into nanotubes under hydrothermal conditions are more often produced *in situ* through exfoliation of one/several crystal layers from bulk particles or through the dissolution and recrystallisation of nanoparticles<sup>[25, 26, 61, 85, 93 - 96]</sup> (see Figure 2.5). These two processes are not mutually exclusive, and may even occur simultaneously.<sup>[61]</sup> Nanosheets produced by exfoliation could grow through a dissolution-recrystallisation mechanism, or precipitated nanosheets could undergo exfoliation into thinner particles.

Exfoliation and recrystallisation have both been suggested to play a role in the synthesis of titanate nanosheets prior to nanotube formation,<sup>[85, 93 - 95]</sup> and there is sufficiently convincing TEM evidence from different stages of the reaction<sup>[93, 94]</sup> (Figure 2.5) to conclude that both mechanisms are involved in the production of thin, flexible titanate nanosheets. Similar effects have been suggested in the formation of  $\text{VO}_x$  nanosheet precursors to nanotubes,<sup>[96]</sup> but the formation mechanism is not well-studied in this case.



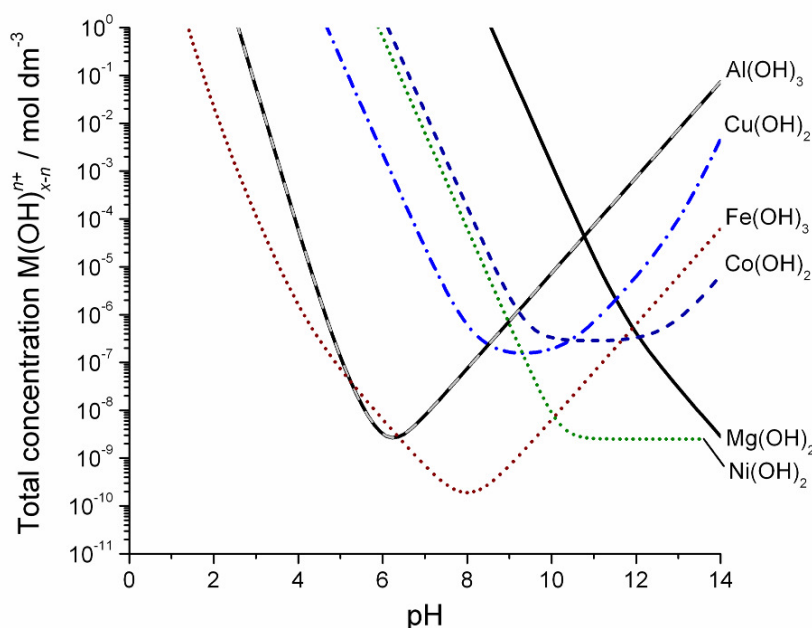
**Figure 2.5.** TEM images showing (a) the growth of titanate nanosheets via recrystallisation on the surface of a  $\text{TiO}_2$  (anatase) nanoparticle, and (b) exfoliation of a nanosheet from a thicker growing nanosheet. Image (a) is unpublished from the work in reference <sup>[97]</sup> and image (b) is reproduced from reference <sup>[93]</sup> Figure 2b with kind permission from Springer Science and Business Media.

In some cases nanosheets are formed purely by exfoliation, and may directly scroll to form nanotubes even at room temperature. This has been demonstrated using some layered Ruddlesden-Popper <sup>[25]</sup> phases and also with  $\text{Al}_2\text{Si}_2\text{O}_5(\text{OH})_4$  (kaolinite), <sup>[98 - 101]</sup>  $\text{TiO}_2$ ,  $\text{MnO}_2$  and  $\text{Ca}_2\text{Nb}_3\text{O}_7$ . <sup>[102]</sup> Recrystallisation rather than exfoliation is proposed as the driving force for the hydrothermal formation of metal silicate nanosheets, <sup>[103]</sup> although there is no conclusive evidence that large nanosheets do not exfoliate prior to nanotube formation. As regards the other metal oxide nanotubes in Tables 2.1 and 2.2, very little is known about the formation mechanisms of their nanosheet precursors, although some early speculations have been made. <sup>[34, 39]</sup>

All solution-based nanosheet-forming processes can be facilitated by the application of heat, stirring, and chemical additives in the solution. Increasing the synthesis temperature increases the rates of dissolution and recrystallisation according to an Arrhenius-type relationship, and stirring facilitates the mass-transfer of solvated species. <sup>[62]</sup> Heating and stirring may also increase the rate of chemical exfoliation by increasing the rate of the intercalation/deintercalation steps. <sup>[104]</sup>

Adding intercalating agents to the reaction solvent increases exfoliation rates by weakening interlayer forces. <sup>[101]</sup> The growth rate of nanosheets through recrystallisation

is also affected by the solvent composition. The addition of acids, bases, and chelating agents, for example, affects both the dissolution rate of the starting materials and the supersaturation of solvated species relative to the crystalline nanosheet structure (Figure 2.6). Conditions close to the minimum solubility pH of the metal hydroxide <sup>[105 - 111]</sup> are necessary to precipitate a large quantity of layered crystalline metal hydroxide nanosheets. For example, extensive precipitation of crystalline Cu(OH)<sub>2</sub> requires much milder conditions (pH ≈ 8) than those for Mg(OH)<sub>2</sub> (pH ≈ 12) at room temperature. As the temperature is increased above room temperature the minimum solubility pH shifts downwards for all metal hydroxides (Figure 2.7), because the hydrolysis of species  $[M(OH)_{x-(n+1)}]^{(n+1)+} + OH^- = [M(OH)_{x-n}]^{n+} + H_2O$  is usually endothermic. <sup>[105 - 111]</sup>

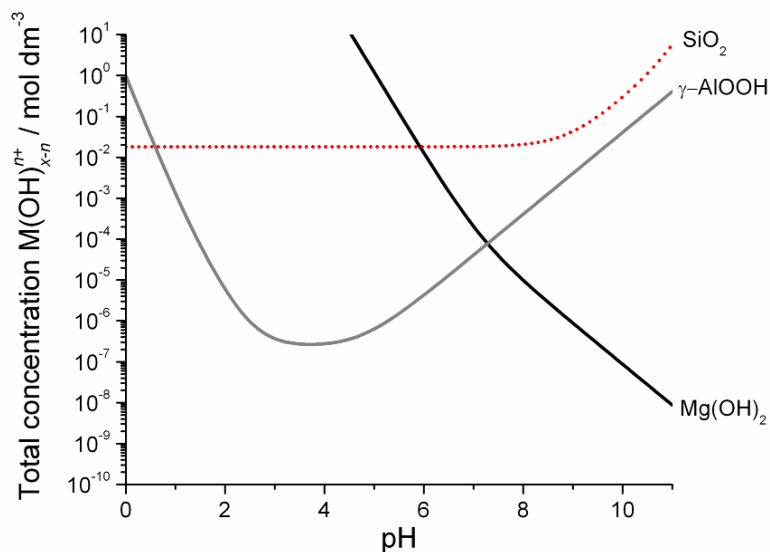


**Figure 2.6.** Solubility versus pH curves for the thermodynamically stable crystalline forms of Mg, Al, Co, Fe, Ni, and Cu hydroxides, calculated in this work from experimental solubility constants extrapolated to infinite dilution (ionic strength of solution,  $I = 0$ ) measured in the literature. <sup>[105 - 111]</sup> Note the logarithmic scale on the y-axis. (See appendix C for derivation of solubility constants).

The precipitation of metal silicate nanosheets is more complicated. For example, synthetic studies have shown that nanotubular chrysotile,  $Mg_3Si_2O_5(OH)_4$ , forms from amorphous starting materials via flat lamellar crystals such as  $Mg(OH)_2$ ,  $Mg_3Si_4O_{10}(OH)_2$ , and  $Mg_3Si_2O_5(OH)_4$ , <sup>[40]</sup> which all contain an octahedral  $Mg(II)O_6$

sheet based on the brucite ( $\text{Mg}(\text{OH})_2$ ) structure. It is believed that during the reaction, these crystals grow from solution and act as nucleation ‘seeds’ for the formation of  $\text{Mg}_3\text{Si}_2\text{O}_5(\text{OH})_4$  nanosheet structures, in which the  $\text{SiO}_4$  tetrahedra are arranged onto one side of the growing  $\text{Mg}(\text{II})\text{O}_6$  sheet.<sup>[40]</sup> In this case, nanosheet formation relies on having (i) a low solubility of  $\text{Mg}(\text{OH})_2$ , and (ii) a reasonably high solubility of  $\text{SiO}_2$  during hydrothermal treatment. These conditions are only met at high solution pH (Figure 2.7) or at higher temperatures  $\gg 200^\circ\text{C}$ .<sup>[107, 108, 112]</sup> The synthesis pH of related silicate nanotubes such as  $(\text{Co},\text{Ni})_3\text{Si}_2\text{O}_5(\text{OH})_4$  may be similarly restricted by the solubility of their hydroxide sheet (e.g.  $\beta\text{-Ni}(\text{OH})_2$ ), but this has not yet been studied.

There is recent evidence to suggest that halloysite nanotubes ( $\text{Al}_2\text{Si}_2\text{O}_5(\text{OH})_4$ ) form by a similar mechanism; the  $\text{Al}_2\text{Si}_2\text{O}_5(\text{OH})_4$  nanosheet structure can form via dissolution-recrystallisation of  $\text{SiO}_4$  with  $\gamma\text{-AlOOH}$  nanosheets (boehmite) during hydrothermal treatment at  $\approx 250^\circ\text{C}$ , pH 2.<sup>[113]</sup> Acidic conditions are necessary, because in alkaline environments tetrahedrally-coordinated  $[\text{Al}(\text{OH})_4]^-_{(\text{aq})}$  reacts with dissolved  $\text{SiO}_2$  species to produce zeolites ( $\text{Na}_2\text{O} \cdot \text{Al}_2\text{O}_3 \cdot x\text{SiO}_2 \cdot y\text{H}_2\text{O}$ ).<sup>[114]</sup>

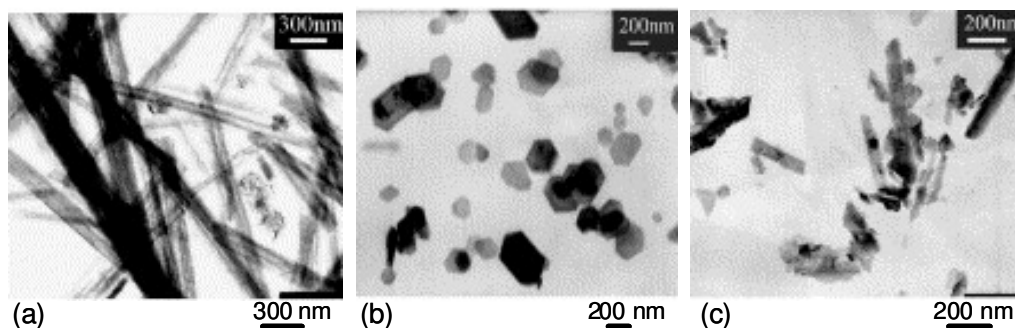


**Figure 2.7.** Solubility versus pH curves for the thermodynamically stable crystalline forms of Mg and Al hydroxides, and  $\text{SiO}_2$  at  $200^\circ\text{C}$ , extrapolated to infinite dilution ( $I = 0$ ).<sup>[106, 107, 111, 112]</sup>

The temperature, pH, and chemical composition of the hydrothermal solution also affect the morphology (shape) of the precipitated nanosheets in addition to their crystal structure. For example, Kahn et al.<sup>[115]</sup> noted that in aqueous ammonia solutions at

200 °C, wide, plate-like sheets of  $\beta$ -Ni(OH)<sub>2</sub> were precipitated at pH 11, whereas elongated flexible  $\alpha$ -Ni(OH)<sub>2</sub> nanosheets were formed at pH 8.5 - 9.5. They suggest that at higher concentrations of base OH<sup>-</sup> directs structure along the [100] and [010] crystallographic directions, but at lower pH, the structure directing affect of SO<sub>4</sub><sup>2-</sup> along the [100] direction dominates. In the synthesis of titanate nanotubes, changing the solvent composition from pure aqueous NaOH by adding KOH changes nanosheet morphology from wider flexible sheets to narrower, elongated sheets, eventually forming more rigid elongated particles known as nanofibres.<sup>[97]</sup> The greater solubility of TiO<sub>2</sub> in KOH is thought to drive faster recrystallisation along the thermodynamically favoured [001] direction, which explains the morphological differences.

Non-aqueous solvents may also direct nanosheet morphology, as shown by the work of Fan et al.,<sup>[116]</sup> who discovered that the shape of Mg(OH)<sub>2</sub> nanosheets recrystallised after 6 hours at 180°C depended on the chemical structure of the solvent (Figure 2.8). The sheets had a hexagonal plate-like shape after treatment in H<sub>2</sub>O, but formed elongated sheets in ethanol, and in ethylenediamine the elongated sheets scrolled to form nanotubes. It appears from these studies that the effects of interaction with solvent molecules on nanosheet formation are complex, and more experiments on nanosheet growth in a variety of solvents are needed before they can be fully understood.



**Figure 2.8.** Morphology of Mg(OH)<sub>2</sub> crystallised at 180 °C for 6 hours in (a) ethylenediamine, (b) distilled water, and (c) absolute ethanol solvents.\*

As they grow, nanosheets need to attain specific dimensions before they are flexible and long or wide enough to “loop round” to form the circumference of a complete nanotube.

\* Reprinted from Fan et al.<sup>[116]</sup> with permission from Elsevier Ltd.



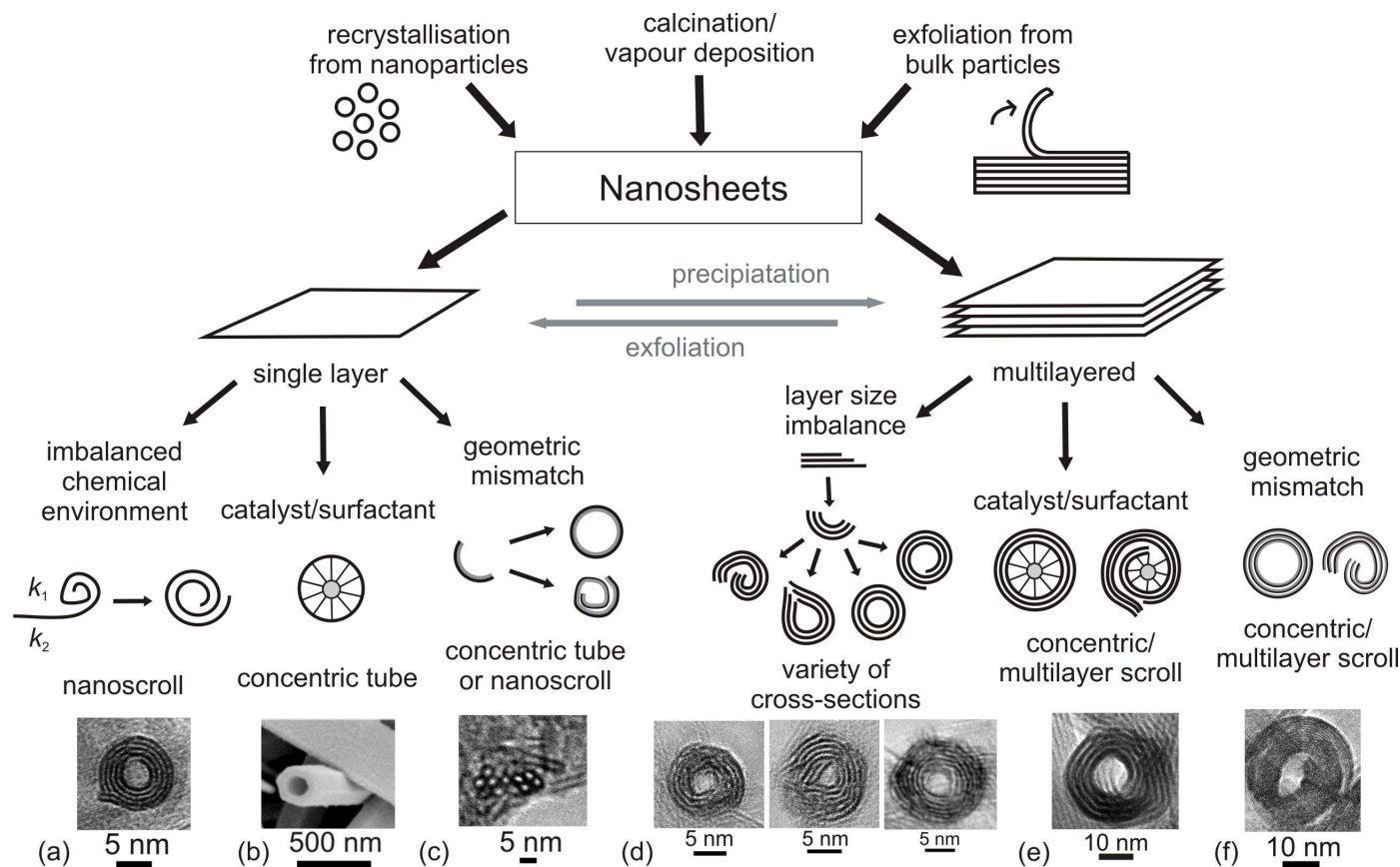
The ideal nanotube radius and cross-sectional shape is different for each crystal structure, and is dictated by energy constraints. These constraints are the focus of the next section on nanosheet scrolling mechanisms.

### 2.3.2. Scrolling of nanosheets into nanotubes

The formation of nanotubes proceeds through the scrolling of nanosheets around a specific crystal growth axis. A variety of different mechanisms have been proposed to explain the scrolling of nanosheets under specific conditions (Figure 2.9). Broadly, the causes of single- or multilayered nanosheet scrolling are described as: (i) an imbalanced chemical environment, (ii) binding to catalyst or surfactant molecules, (iii) a size imbalance between layers caused by anisotropic crystallisation, or (iv) an inherent geometric strain in the crystal layers.

Spontaneous scrolling usually occurs only with single-crystal nanosheets. An exception to this is that catalysts, surfactant micelles and other soft templates can be used to bind nanosheets of an amorphous or polycrystalline nature into a nanotubular shape.<sup>[117]</sup> Otherwise, polycrystalline materials probably could not undergo uniform scrolling, due to their non-uniform structure. Catalysts and templates have also controlled the tubular morphology of some significant crystalline materials, such as graphene nanosheets forming carbon nanotubes (for a recent review see <sup>[118]</sup>).

There are, however, many examples of nanosheets scrolling without the need for a template or catalyst material. In some nanosheets, scrolling is thought to occur spontaneously because their crystal structures possess an internal geometric strain. The geometry of the top surface of their crystal layers is not equivalent to the bottom surface, and this stimulates scrolling of the structure by contracting one surface and expanding the other.<sup>[119]</sup> During the bending of the single or multilayered sheet, the ends of the sheet may meet and polymerise along their edge, forming a concentric tube (e.g.  $\text{Al}_2\text{SiO}_3(\text{OH})_4$  (imogolite) Figure 2.9c), or they may overlap and form a tube with a spiral cross-section (Figure 2.9f), as is sometimes observed with the multilayered silicate nanotubes  $\text{Al}_2\text{Si}_2\text{O}_5(\text{OH})_4$  (halloysite), and  $\text{Mg}_3\text{Si}_2\text{O}_5(\text{OH})_4$  (chrysotile) and  $\text{Ni}_3\text{Si}_2\text{O}_5(\text{OH})_4$  (nickel silicate).



**Figure 2.9.** Overview of the scrolling mechanisms of nanosheets caused by structural or environmental factors. The cross-sectional TEM image of a titanate nanotube (a) and SEM image of Te nanotube (b) were taken from references <sup>[120, 121]</sup> respectively. The cross-sectional TEM images of (c)  $\text{Al}_2\text{GeO}_3(\text{OH})_4$  (germanium-imogolite), (d) titanate, (e) vanadium oxide and (f) nickel silicate nanotubes were recorded in this work using nanotubes synthesised following reaction protocols from references <sup>[37, 47, 122, 97]</sup> respectively.

In some nanotubes such as titanates, the crystal structure contains symmetrical layers in which the internal strain acting on the top and bottom face of the nanosheet is equivalent. According to recent DFT calculations (Figure 2.10), only asymmetric structures can have a radius of curvature at which the overall strain energy in the structure is negative. The strain energy of a symmetric sheet bending into a tubular structure can be described according to the equation <sup>[123, 124]</sup>

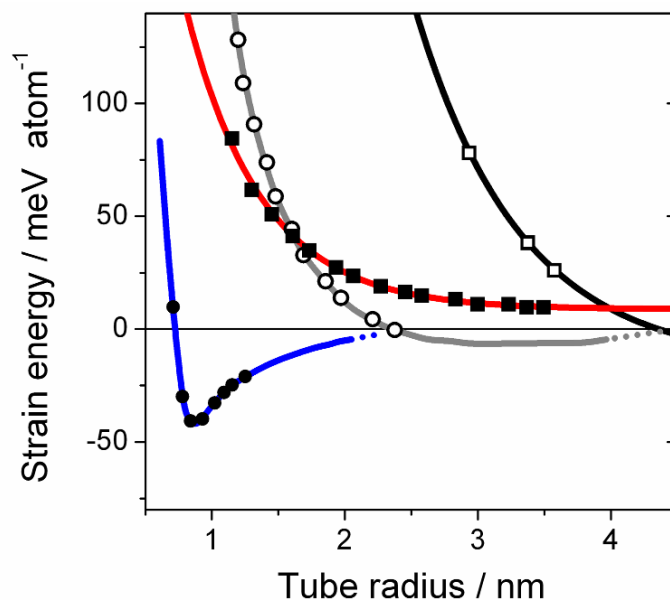
$$E_{str} = \frac{a}{r^2} \quad (2.1)$$

where  $E_{str}$  is the lattice strain energy (the energy difference between the flat and the single-walled tubular structures),  $a$  is a proportionality constant for the bending elasticity which is specific to the crystal structure of the nanosheet, and  $r$  is the radius of the nanotube. This equation gives a positive  $E_{str}$  over all values of  $r$  (see curve for titanate nanotubes in Figure 2.10).

Asymmetric crystal structures, on the other hand, have an additional contribution to strain energy, which can be expressed as <sup>[125]</sup>

$$E_{str} = \frac{a}{r^2} - \frac{b}{r} \quad (2.2)$$

where  $a$  and  $b$  are proportionality constants for the nanosheet elasticity and layer asymmetry, respectively. This causes a negative  $E_{str}$  over a range of tube radii, with a specific energy minimum radius,  $r_0$ . For imogolite ( $\text{Al}_2\text{SiO}_3(\text{OH})_4$ ),  $r_0$  is well-defined and occurs at a very small radius of 0.9 nm (figure 2.10).<sup>[126]</sup> The internal strain in the imogolite structure is extreme, because the  $\text{SiO}_4$  tetrahedra are  $\text{Q}_3\text{Al}$ -bound (tri-alumina substituted), and the tetrahedral Si-O distance is much smaller than the distance between neighbouring octahedral Al-O units (see Figure 2.3). The narrow energy minimum makes the inclusion of several other layers at larger radii to form a multiwalled nanotube highly unlikely.



**Figure 2.10.** The relationship between tube radius and DFT-calculated strain energy (defined as the energy difference between flat and single-walled tubular structures) for single-walled nanotubes of (●) imogolite <sup>[126]</sup>, (■) titanates, <sup>[127]</sup>, (○) halloysite <sup>[125]</sup> and (□) chrysotile <sup>[128]</sup>.

In halloysite ( $\text{Al}_2\text{Si}_2\text{O}_5(\text{OH})_4$ ) and chrysotile ( $\text{Mg}_3\text{Si}_2\text{O}_5(\text{OH})_4$ ), the  $\text{SiO}_4$  tetrahedra are arranged in a hexagonal sheet, and are free to rotate, being only singly bound to the metal hydroxide sheet (see Figure 2.3). Therefore, any geometric mismatch between the  $\text{SiO}_4$  and  $\text{AlO}_6$  or  $\text{MgO}_6$  sheets can be corrected by rotation of the  $\text{SiO}_4$  tetrahedra. <sup>[128, 129]</sup> This means that the overall strain energy in a single-layered sheet is much smaller than in imogolite. The strain energy therefore has a less pronounced minimum, and only becomes negative at much larger radii (2.3 – 4.5 nm for halloysite and > 4.3 nm for chrysotile). <sup>[128, 129]</sup> The larger radius of curvature and wider energy minimum makes the formation of multilayered nanotubes much more likely than for imogolite.

When multilayered nanotubes of halloysite and chrysotile are considered, the energetics become considerably more complicated and have not yet been modelled by DFT. It is believed that in  $\text{Al}_2\text{Si}_2\text{O}_5(\text{OH})_4$  the additional forces of hydrogen bonding between layers tends to promote the formation of the flat mineral kaolinite over the nanotubular mineral halloysite, because the proximity of the hydrogen-bonded groups is greater in the flat form than in the curved form. <sup>[130]</sup> This leads to a lower thermodynamic stability of halloysite nanotubes ( $\Delta G_{f, 298 \text{ K}}^0 = -3780.7 \text{ kJ mol}^{-1}$ ) compared with kaolinite

( $\Delta G_{f, 298\text{ K}}^0 = -3799.4\text{ kJ mol}^{-1}$ ).<sup>[131]</sup> For this reason it has proved difficult to form halloysite under hydrothermal conditions (see Section 2.1.2), because kaolinite is precipitated instead. Alternative routes for halloysite synthesis have relied on disrupting the interlayer hydrogen bonding in kaolinite sheets by forced interlayer hydration or exfoliation, but these are lengthy procedures which require several intercalation steps to prepare the kaolinite for delamination or hydration.<sup>[98 - 101]</sup>

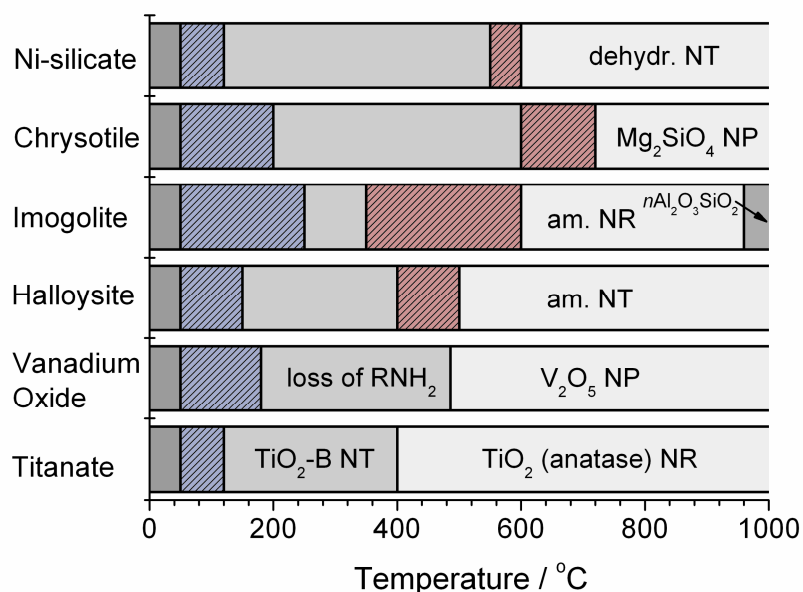
For symmetric crystal structures such as titanates, alternative scrolling mechanisms have been proposed to explain how the multilayered structure can bend in the absence of internal strain. These mechanisms argue that the external environment of the nanosheets can invoke scrolling. The most obvious example of this is the use of catalyst or surfactant molecules (Figure 2.9b and e) which can act as a template, binding the surrounding nanosheet into a tubular conformation, but the synthesis environment may also participate in a more subtle way. It has been suggested that titanate nanosheets may experience an asymmetrical chemical environment (concentration of ions) on the two opposing sides of the nanosheet. This effectively creates two different spring-constants,  $k_1$  and  $k_2$  on the two sides of the sheet, causing single exfoliated titanate layers to scroll, resulting in the observed multiwalled nanotubes with spiral cross-sections (Figure 2.10a).<sup>[120, 132]</sup> However, in light of the fact that several different nanotube cross-sections are often observed (Figure 2.10d), an alternative mechanism was suggested in which rapid crystal growth occurring preferentially along the  $c$ -axis causes an imbalance in the length of the crystal layers along this axis.<sup>[36]</sup> The excess surface energy of the imbalanced layers can be minimised by bending the structure.

In some cases it is possible that more than one mechanism may be involved in scrolling. For example, it is necessary to intercalate amine template molecules to allow bending of form vanadium oxide ( $\text{VO}_x$ ) nanosheets into nanotubes, and in this respect the synthesis resembles a surfactant-driven mechanism. However, it has also been suggested that reduction of  $\text{V}^{(\text{V})}\text{O}_5$  pentahedral units to  $\text{V}^{(\text{IV})}\text{O}_4$  tetrahedral units under heating may occur anisotropically in the structure, and aid scrolling through a geometric mismatch similar in nature to halloysite.<sup>[133, 134]</sup> Although types of scrolling mechanism can be generalised, the scrolling in each nanotubular structure is unique and should be examined on an individual basis.

## 2.4. Properties of metal oxide nanotubes

### 2.4.1. Thermal stability of nanotubes

The thermal stability of nanotubes is of great importance in applications which require nanotubes to withstand high-temperatures, for example their use in fire- and heat-resistant materials.<sup>[135]</sup> The thermal stabilities of the most widely used nanotubes described in Section 2.1.2 are summarised in Figure 2.11. Metal silicate nanotubes undergo structural dehydroxylation in the range 400 – 700 °C, and are stable up to this temperature range, losing only surface and interlayer water. Studies on  $\text{Al}_2\text{Si}_2\text{O}_5(\text{OH})_4$  (halloysite) and  $\text{Ni}_3\text{Si}_2\text{O}_5(\text{OH})_4$  nanotubes have noted that these materials retain their tubular morphology at temperatures well above the dehydroxylation temperature<sup>[47, 136]</sup> despite the change in crystal structure. Halloysite is converted into nanotubes with amorphous crystallinity above 500 °C, and nickel silicate nanotubes apparently retain their dehydroxylated crystal structure at 600 °C. On the other hand,  $\text{Mg}_3\text{Si}_2\text{O}_5(\text{OH})_3$  chrysotile and  $\text{Al}_2\text{SiO}_3(\text{OH})_4$  (imogolite) nanotubes undergo collapse of their structures during dehydroxylation to form nanoparticles or nanorods.<sup>[137, 138]</sup>



**Figure 2.11.** Bar diagram showing the phase stability of nanotubular materials upon heating. The first shaded area (blue) represents loss of surface + interlayer water, and the second shaded area (red) represents structural dehydroxylation. The abbreviations are: NT = nanotubes, NR = nanorods and NP = nanoparticles, am. = amorphous and dehydr. = dehydroxylated.

The titanate structure, related to  $\text{H}_2\text{Ti}_3\text{O}_7$  (tritanic acid) undergoes dehydroxylation more readily, forming a  $\text{TiO}_2$ -(B) nanotubular phase above 150 °C. The nanotubular structure is lost as the structure is converted to anatase nanorods above 400 °C. <sup>[139]</sup> Vanadium oxide nanotubes are highly susceptible to thermal degradation because their nanotubular shape is created by the presence of interlayer amine molecules,  $\text{RNH}_2$ , which allow the  $\text{VO}_x$  layers enough flexibility to bend. The  $\text{RNH}_2$  molecules are not chemically bonded to the  $\text{VO}_x$  layers, and are therefore easily removed upon heating above 180 °C. <sup>[140]</sup> The  $\text{VO}_x$ , with an average oxidation state of 2.45, then undergoes slow oxidation to form nanoparticles of  $\text{V}_2\text{O}_5$  upon further calcination. Therefore, vanadium oxide nanotubes are unlikely to be of any use in high-temperature applications unless it is desirable to use heat to break their structure and release materials stored inside the tubes.

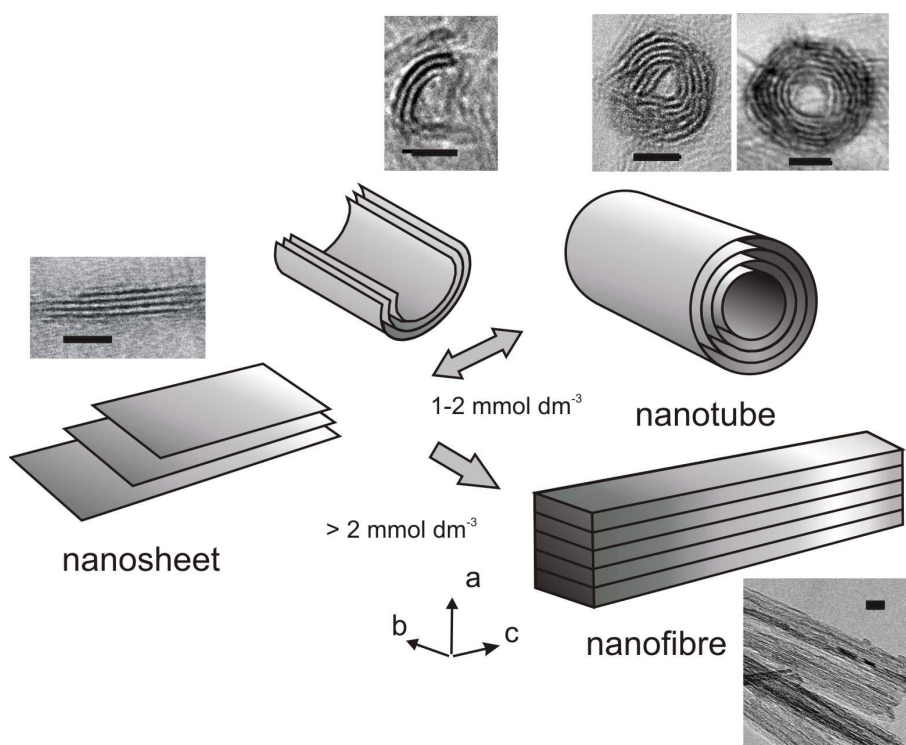
#### 2.4.2. Solution stability of nanotubes and hydrothermal transformation

Many of the proposed applications of nanotubes (e.g. anti-corrosive coatings, drug delivery, electrochemical) require nanotubes to come into contact with solutions. Therefore, knowledge of the stability of nanotubes over a wide range of operational conditions at different proton concentrations and temperatures is highly important.

Regarding the solution stability of nanotubes at room temperature, recent work has demonstrated that titanate nanotubes are acid-soluble, transforming gradually in 0.1 mol  $\text{dm}^{-3}$   $\text{H}_2\text{SO}_4$  solution into  $\text{TiO}_2$  (rutile) nanoparticles, but in pure water and alkaline solutions they possess long-term stability. <sup>[141]</sup> The solution stability of most other metal oxide nanotubes in acid or alkaline solution has not yet been studied in detail, but one study of vanadium oxide nanotubes concluded that they are only soluble in acidic solutions. <sup>[142]</sup> The aluminosilicate nanotubes imogolite and halloysite are expected to be soluble in both acid and alkaline solutions due to their amphoteric Al-OH surface groups, but so far only imogolite solubility in concentrated acid solutions has been demonstrated. <sup>[143]</sup>

Above room temperature, nanotubes may undergo a variety of transformations in a solution-based environment. For example, titanate nanotubes undergo conversion to

nanofibres if the reaction process in which they are formed is intensified (by crystal seeding, stirring, increasing the reaction temperature or increasing KOH/ NaOH ratio of the solvent to increase the dissolved Ti(IV) concentration) or if the duration of the reaction is extended.<sup>[97]</sup> This is believed to occur because the scrolling of titanates can be reversed, and the resulting nanosheets can continue growth along the crystallographic *c* axis, which is the most energetically favourable growth direction (Figure 2.12). The driving force for this process is a reduction in the total surface area, which is ca. 200 – 300 m<sup>2</sup>g<sup>-1</sup> for nanotubes and ca. 20 – 50 m<sup>2</sup>g<sup>-1</sup> for nanofibres,<sup>[97]</sup> which leads to a reduction in the total surface energy.



**Figure 2.12.** Schematic diagram of the crystallisation of different titanate morphologies: nanosheets, nanotubes, and nanofibres, from solutions containing different concentrations of dissolved Ti(IV).<sup>[97]</sup> The scale bar in the TEM images represents 10 nm.

The growth pattern and changes in morphology of other nanotubular structures under intensified hydrothermal conditions have not yet been studied, although it is assumed that they would eventually undergo transformation into a more thermodynamically stable morphology than nanotubes, which are inherently unstable and more reactive compared to bulk materials due to their higher surface area.<sup>[144]</sup>



### 2.4.3. Electrical and mechanical properties

Most metal oxide nanotubes are electrical semiconductors, apart from the metal silicates which are good electrical insulators (see Table 2.4). The mechanical properties of individual nanotubes are commonly measured using the deflection of an AFM tip by the nanotube, or by forced bending in a TEM electron beam.<sup>[145, 146]</sup> On the whole, metal oxide nanotubes have a Young's modulus similar to many metals, but lower than carbon nanotubes, which have a Young's modulus of approximately 300 GPa for multiwalled nanotubes<sup>[145]</sup> and 1.3 TPa for single-walled nanotubes.<sup>[147]</sup>

**Table 2.4.** Electrical and mechanical properties of metal oxide nanotubes at 298 K.

Nanotube	Bulk density / g cm <sup>-3</sup>	Young's Modulus / GPa	Band gap / eV	Conductivity / S m <sup>-1</sup>
Titanate	3.16 <sup>[148]</sup>	-	3.2 <sup>[149]</sup>	$5.5 \times 10^{-3}$ <sup>[149]</sup>
Vanadium Oxide	2.87 <sup>[150]</sup>	20 - 80 <sup>[151]</sup>	0.2 <sup>[151]</sup>	5.0 <sup>[151]</sup>
Halloysite	2.53 <sup>[13]</sup>	300 <sup>[125]</sup>	9.5 <sup>[125]</sup>	-
Chrysotile	2.63 <sup>[152]</sup>	14 - 336 <sup>[153]</sup>	10 <sup>[154]</sup>	$1 \times 10^{-9}$ <sup>[155]</sup>
Imogolite	2.70 <sup>[156]</sup>	182 <sup>[157]</sup>	7.2 <sup>[158]</sup>	$5.9 \times 10^{-6}$ <sup>[159]</sup>

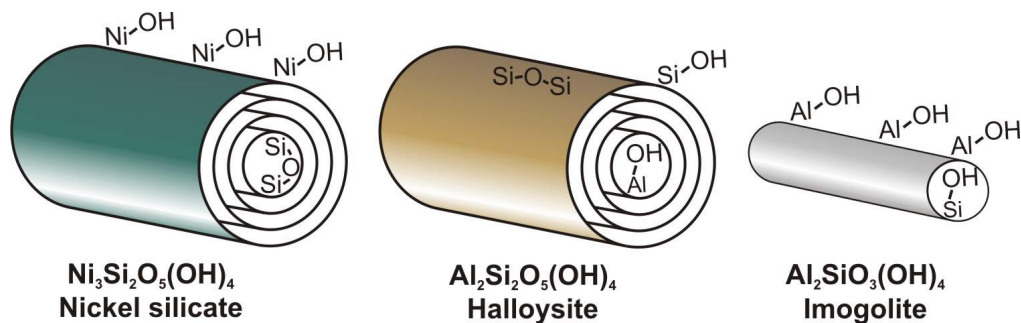
The low thermal and electrical conductivity, high Young's (elastic) modulus and high tensile strength of metal oxide nanotubes have led to extensive research into the formation of metal oxide nanotube-polymer nanocomposites. The presence of halloysite, imogolite and titanate nanotubes has been shown to increase the Young's modulus and tensile strength of a wide variety of polymer materials,<sup>[135, 160-163]</sup> as well as improving their heat-resistant properties.<sup>[135]</sup>

### 2.4.4. Chemical properties and surface functionalisation

The suitability of nanotubes for applications such as catalysts and catalyst supports, nanocomposite materials and pharmaceutical encapsulating agents strongly depends on their chemical properties. The chemical properties of nanotubes are dictated by their surface groups that are accessible to molecules in a solvated or gas phase. Metal oxide

or hydroxide nanotubes composed of symmetric layered structures such as titanate or vanadium oxide nanotubes have metal hydroxyl groups (M-OH) on both the outer and inner surfaces of the curved nanotube layers, although the surfaces are partially blocked by intercalating amine molecules in the case of vanadium oxide nanotubes.

The asymmetrically structured imogolite nanotubes also contain hydroxyl groups on both surfaces, with a single Si-OH group per Si(IV) atom directed inwards towards the centre of the tube, and Al-OH functional groups present on the outside of the tubes. These properties make the formation of titanate and imogolite nanotube aqueous suspensions facile. On the other hand, silicate nanotubes with the  $M_xSi_2O_5(OH)_4$  structure, such as halloysite and nickel silicate, contain M-OH groups in the  $MO_6$  side of each layer, but the  $SiO_4$  tetrahedra are polymerised (see Figure 2.3) and Si-OH groups only exist at the tube ends or at defect sites <sup>[164]</sup> (Figure 2.13). In halloysite the  $SiO_4$  layer is located on the outside on the tubes, but on nickel silicates and chrysotile nanotubes it is located on the inside, meaning that functionalisation of M-OH groups would occur on the opposite surface of the tube compared to halloysite.



**Figure 2.13.** Simplified structural diagram showing the distribution of hydroxyl groups on halloysite, nickel silicate and imogolite nanotube surfaces.

The simplest method of functionalising metal oxide nanotubes is to ion-exchange the surface hydroxyl groups with metal ions. Titanate nanotubes are easily ion-exchanged with alkali-metal <sup>[69]</sup> and transition-metal <sup>[165, 215]</sup> ions by suspension in concentrated solutions of the metal salts. The metal ions can enter the interlayer spaces and form a titanate-metal intercalation compound.<sup>[69]</sup> Halloysite nanotubes,  $Al_2Si_2O_5(OH)_4$ , can also be ion-exchanged, though intercalation compounds only form with larger

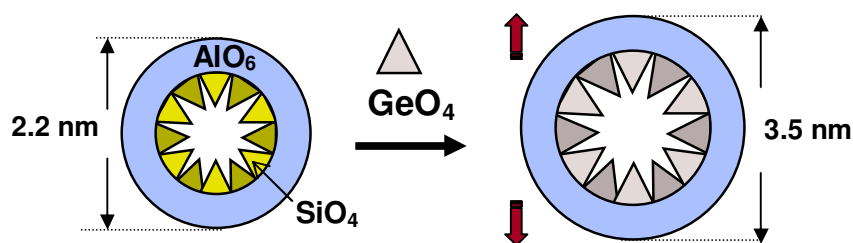
monovalent metal ions such as  $K^+$ ,  $Cs^+$  and  $NH_3^+$ . Smaller ions may become trapped inside the hexagonal-shaped cavity in the silicate surface of the layers (Figure 2.3).<sup>[65]</sup>

The surfaces of nanotubes may also be functionalised through chemical reactions with small molecules. The surface  $-OH$  groups of titanate nanotubes, for example, will readily react with species such as  $H_2O_2$ , amines ( $RNH_2$ ), and silyl ethers ( $R_3Si-OR$ ).<sup>[62]</sup> In halloysite nanotubes,  $-OH$  groups are mostly located on the inner ( $AlO_6$ ) surface of the tubes and at the tube ends. These surfaces have been successfully functionalised with silyl ethers,<sup>[166]</sup> and other small molecules such as dimethyl sulphoxide and formamide.<sup>[65]</sup>

The above functionalisation methods involve adapting nanotubes which have already been synthesised. A more radical method of altering the properties of nanotubes is to add doping species to the original synthesis mixture such that new elements become structurally incorporated within the walls of nanotubes. This occurs in naturally synthesised nanotubes to some extent: natural halloysite typically contains 0.11 - 6 wt % Fe(III) and occasionally 1.96 - 12 wt % Cr(III) impurities substituted for Al(III).<sup>[65]</sup> In a laboratory synthesis the substitution of different atoms into the chemical structure can be performed under carefully controlled conditions.

Synthetic chrysotile ( $Mg_3Si_2O_5(OH)_4$ ) nanotubes have been doped with other metals by substitution of Mg(II) with Ni(II), Fe(II) and Ti(IV) oxides<sup>[167, 168]</sup> in the starting materials. This doping not only affects the surface chemical properties of the nanotubes, but also affects their physical properties and morphology. For example, the substitution of Ni(II) into the chrysotile structure was shown to decrease the diameter and length of the resulting nanotubes, and improve their thermal stability.<sup>[167]</sup> A more dramatic example of using atomic substitution to control nanotube morphology can be found in the work of Levard et al. in which Si(IV) was substituted with Ge(IV) in the imogolite structure.<sup>[122, 169]</sup> The larger atomic radius of Ge(IV) compared to Si(IV) (0.39 and 0.26 Å respectively)<sup>[170]</sup> expands the inner surface of the imogolite tube structure (see Figure 2.3), resulting in an increase in the diameter of imogolite nanotubes, such that the typical 2.2 nm diameter of  $Al_2SiO_3(OH)_4$  nanotubes increases to 3.5 nm in

$\text{Al}_2\text{GeO}_3(\text{OH})_4$  nanotubes. <sup>[171]</sup> The lesser radius of curvature allows the Ge-imogolite nanotubes to exist as both single- and double-walled tubes. <sup>[171, 172]</sup>



**Figure 2.14.** Simplified diagram of imogolite structure showing how the replacement of  $\text{Si(IV)O}_4$  tetrahedra with  $\text{Ge(IV)O}_4$  on the inside of the  $\text{Al}_2\text{SiO}_3(\text{OH})_4$  sheet increases the diameter of the nanotubes.

Structural doping and surface functionalisation of nanotubes is widely used to modify the chemical and physical properties of nanotubes to render them more suitable for specific applications. The following sections of this review examine the suitability of inorganic nanotubes in hydrogen storage applications, and how structural modifications and doping could be introduced to improve their adsorptive properties.

## 2.5. Inorganic nanotubes as hydrogen storage materials

### 2.5.1. Outline of current hydrogen storage methods, aims and challenges

Hydrogen is in many ways an attractive alternative fuel because of its high energy density per unit mass, <sup>[173]</sup> and its potential as a green fuel, if generated from sustainable sources. However, the low energy density of hydrogen per unit volume compared to hydrocarbons, and the large mass of current storage methods makes it challenging to store hydrogen for on-board use as an alternative fuel. <sup>[17]</sup>

The revised 2015 DOE targets for solid storage are 9 wt % mass of hydrogen stored compared to the total mass of the system including the mass of the container, and a volumetric mass density of no less than  $81 \text{ g L}^{-1}$ . <sup>[174]</sup> Thus the main challenge is to reduce the total *weight* of a hydrogen storage system, whilst increasing the density of

the stored hydrogen. This is extremely challenging, as current commercially available technologies have demonstrated. The main current method of storing hydrogen is compressed hydrogen cylinders, which are very bulky (50 kg to hold  $0.1 \text{ m}^3 \text{ H}_2$ ) in order to withstand the high pressures (700 bar, 70 MPa) required to meet the DOE 2010 target of 6 wt %.<sup>[175]</sup> Liquid storage of hydrogen improves the wt % storage, as the hydrogen is denser in the liquid state, but too much energy is required to liquefy compressed hydrogen at cryogenic temperature, and maintaining the low temperature requires a large amount of bulky insulation.<sup>[17]</sup>

The drawbacks associated with these methods have stimulated a great deal of research into making solid materials capable of storing hydrogen, as solid storage at moderate pressures (< 200 bar) has far fewer safety issues than compressed gas or liquid storage, and does not require such heavy containers.<sup>[17]</sup> Highly porous solids with low molecular weight and low density are necessary to meet the DOE gravimetric and volumetric targets. Another important requirement is that the solid materials should both store and release hydrogen at an operating temperature close to room temperature, in order to avoid bulky cryogenic tanks or excessive use of heat. There are currently three main categories of solid storage materials which are being investigated: metal hydrogen-containing compounds which absorb hydrogen via chemical reactions, and hydrogen clathrates and nanoporous solids (foams, metal organic frameworks and nanotubes) which adsorb hydrogen via physisorption. These materials are compared in the following sections of this chapter.

### 2.5.2. Techniques for measuring hydrogen storage

The main three techniques commonly used for measuring hydrogen adsorption and desorption are the volumetric (Sieverts), gravimetric and temperature-programmed desorption (TPD).<sup>[176]</sup> In all methods the sample mass must be measured accurately in order that the gravimetric storage (wt %) of hydrogen may be determined, and must have all surface-adsorbed water removed beforehand by degassing under vacuum. The volumetric and gravimetric techniques are usually performed under isothermal conditions, whereas TPD monitors the flow of hydrogen desorbed from a material

following the application of a thermal ramp.<sup>[176]</sup> The TPD method is less commonly used than the gravimetric and volumetric methods.

In the gravimetric method, hydrogen uptake is calculated from the change in mass of a sample (measured using a highly accurate microbalance), following a step change in the hydrogen pressure surrounding the sample. This technique requires very sensitive equipment, and the hydrogen used should be extremely pure (> 99.99 %), because small impurities such as H<sub>2</sub>O which is nine times heavier than H<sub>2</sub> molecules will cause significant error in the results.<sup>[177]</sup>

In the volumetric method, the sample is placed inside a fixed, known volume, and a known mass of hydrogen gas is expanded into this volume. The hydrogen uptake is calculated from the subsequent drop in pressure which is caused by the adsorption of hydrogen into the sample. Volumetry has practical advantages over gravimetry in the simplicity with which isotherm points can be measured, but unlike gravimetric isotherms the volumetric isotherm points are affected by cumulative errors if one point of the isotherm is determined inaccurately.<sup>[176]</sup>

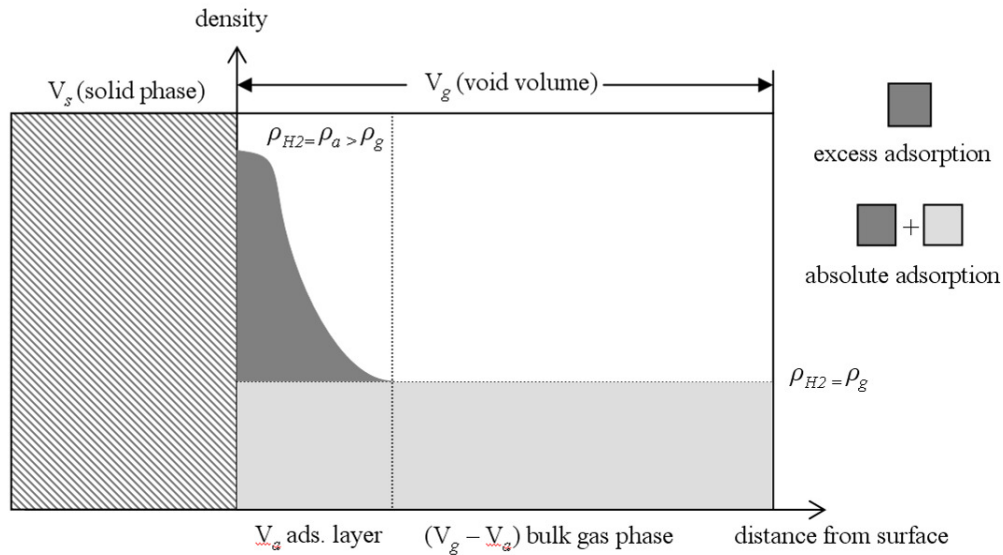
### 2.5.3. PCT isotherms for hydrogen adsorption

The hydrogen adsorption properties of materials are studied through the measurement of pressure-composition-temperature (PCT) isotherms, in which the temperature of the sample is normally held constant for the duration of the experiment, and pressure and composition (mass of hydrogen adsorbed) are varied. To form the isotherm, the mass of hydrogen adsorbed per gram of material (in gg<sup>-1</sup> or wt % units) is plotted against the equilibrium pressure of hydrogen inside the apparatus. Hydrogen adsorption isotherms above the supercritical temperature of 44 K are usually described by a type 1 isotherm,<sup>[178]</sup> in which the mass of hydrogen molecules adsorbed increases steeply at low pressure and approaches a saturation limit as the pressure increases.

To evaluate the hydrogen adsorption properties of a material, it is very useful to know the *absolute* adsorption of hydrogen, i.e. the total mass of hydrogen stored inside the

solid, both as an adsorbed layer on the material surfaces and as a bulk gas contained inside the pores of the material. In many cases the absolute mass of hydrogen stored inside a porous material is difficult to determine experimentally; the *excess* mass of adsorption is usually measured instead.

The difference between the absolute and excess adsorption is explained in Figure 2.15. A layer of adsorbed hydrogen molecules on the surface of a solid occupies a certain volume,  $V_a$ , which grows in volume with increasing  $H_2$  pressure until it reaches saturation at a maximum volume  $V_m$ , beyond which the density and volume of adsorption layer can increase no further. At a given equilibrium hydrogen pressure  $P$ , the adsorbed gas molecules are at a density  $\rho_a$  which is at a maximum at the solid surface and decays towards  $\rho_g$ , the density of the bulk gas, at the edge of the adsorbed layer. The *absolute* mass of hydrogen stored in this material is given by the sum of the mass of the surface adsorbed gas in the volume  $V_a$  and the mass of the bulk gas contained in the total pore volume  $V_g$ . The *excess* mass of adsorption is given by the difference between the mass of gas in the adsorption layer volume  $V_a$  and the mass that would reside in this volume if the gas had the bulk density value  $\rho_g$ .<sup>[179]</sup>



**Figure 2.15.** Schematic diagram of absolute and excess adsorption in a solid with a volume  $V_s$  and a void (pore) volume  $V_g$ . The adsorbed gas is located in the volume  $V_a$  at a density  $\rho_a$  which decays to zero at the solid surface and approaches  $\rho_g$ , the density of the bulk gas contained in the remaining pore volume  $V_g - V_a$ .

By this definition, the excess adsorption mass ( $M_e$ ) is given by the equation

$$M_e = \int_{V_a} \rho_a dV - \rho_g V_a \quad (2.3)$$

The excess adsorption is usually expressed as the gravimetric excess adsorption,  $m_e$ , where the total mass adsorbed  $M_e$  is divided by the mass of the solid sample to give the mass of hydrogen adsorbed per unit mass of sample, in  $\text{g g}^{-1}$  units.

$$m_e = \frac{M_e}{m_s} \quad (2.4)$$

where  $m_s$  is the mass of the solid. Multiplication by a factor of 100 converts  $m_e$  to the gravimetric weight percent (wt %) adsorption.

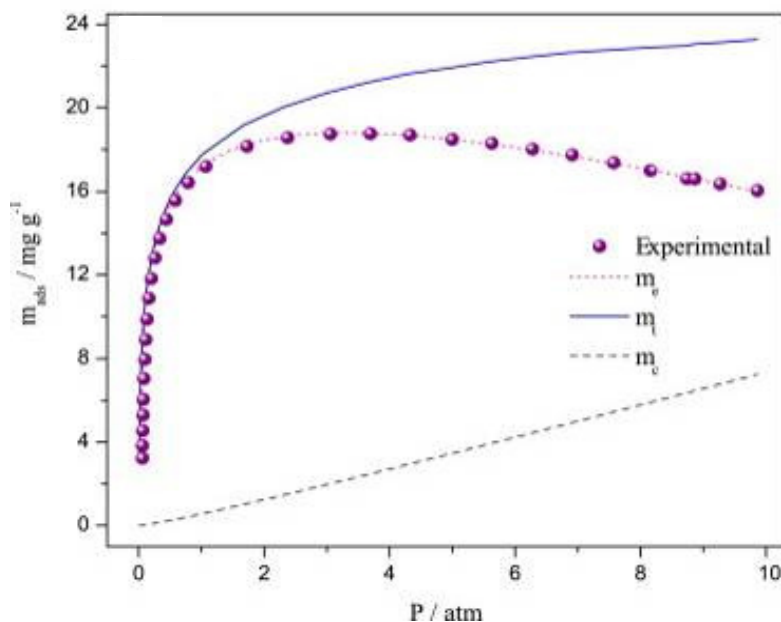
The absolute gravimetric adsorption is obtained from the excess gravimetric adsorption  $m_e$  by adding the mass of gas at density  $\rho_g$  in the total pore volume  $V_{pores}$  in the following equation:

$$m = m_e + \rho_g V_{pores} = m_e + V_{pores} \frac{m_{H_2} P}{RT} \quad (2.5)$$

where  $V_{pores}$  is in  $\text{m}^3 \text{g}^{-1}$  units, and can be estimated from separate nitrogen adsorption experiments.<sup>[180]</sup>

The quantitative difference between the absolute and excess adsorption isotherms is demonstrated in Figure 2.16. As the equilibrium hydrogen pressure increases, the excess adsorption isotherm reaches a maximum value as the density of the surface adsorbed layer reaches saturation ( $V_a = V_m$ ). Beyond this point the excess adsorption decreases with further increase in pressure, because the density of gas  $\rho_g$  in the bulk phase that would fill the adsorption layer volume continues to increase (see Equation (2.3)). The absolute adsorption isotherm, on the other hand, continues to increase above the saturation point, because the density of the bulk gas in the total pore volume given by the term  $V_{pores} \frac{m_{H_2} P}{RT}$  (equivalent to  $m_c$  in Figure 2.16) which increases linearly with increasing pressure is added to the excess adsorption.





**Figure 2.16.** Comparison between the excess adsorption  $m_e$  (dotted line) and absolute adsorption  $m_t$  (solid line) isotherms of the hydrogen storage material  $\text{Cu}_3(\text{BTC})_2$  at 77 K. The numerical difference between the two isotherms is given by  $m_c$  (dotted line). The figure is reproduced from reference <sup>[180]</sup> with permission from the International Journal of Hydrogen Energy.

#### 2.5.4. Current progress in hydrogen storage materials

The stipulation that storage temperatures which are not too extreme, i.e. within the range  $-120 < T < 200$  °C are necessary for energy considerations had ruled out many potential hydrogen storage materials. For hydrogen storage by chemical absorption, the strength of an average chemical bond with hydrogen ( $X\text{-H} = 200 - 500 \text{ kJ mol}^{-1}$ ) is too great for hydrogen to be released at low temperatures. <sup>[181]</sup> For hydrogen storage by physisorption, the opposite end of the temperature scale is problematic: to adsorb hydrogen onto a surface at room temperature the interaction energy must be at least  $\approx 14 \text{ kJ mol}^{-1}$  (0.15 eV), which is far above the usual range of physisorption interaction energies. <sup>[182]</sup>

A number of innovative strategies have been adopted to circumvent these problems, by creating materials which form unusually weak chemical bonds with hydrogen or

unusually strong adsorption interactions. Amino boranes based on  $\text{NH}_3\text{BH}_3$  and alane,  $\text{AlH}_3$  are good example of the former: they can theoretically store up to almost 20 wt % hydrogen and have  $\text{H}_2$  release temperatures below 100 °C. However, there are significant disadvantages to such compounds, including slow release kinetics, and high rehydrogenation pressures.<sup>[183]</sup>

As regards physisorption, great progress has been made in producing low molecular weight materials which have impressively high surface areas exceeding  $3000 \text{ m}^2\text{g}^{-1}$ .<sup>[182]</sup> Metal-organic frameworks (MOFs) currently lead the field, with 7.5 wt % storage achieved with MOF-177 at 77 K. The challenge of room temperature storage has not yet been met by MOFs, zeolites, nanotubes and nanoporous foams (table 2.5), because their interaction energies with  $\text{H}_2$  are typically below  $7 \text{ kJ mol}^{-1}$ ,<sup>[183]</sup> which is far too low for significant adsorption to occur at 298 K.

Early promise for room-temperature adsorption has been shown by a new class of exotic structures known as hydrogen clathrates, cage-like structures in which  $\text{H}_2$  is encapsulated in cavities formed by a special arrangement of molecules which occurs only at precise temperatures and pressures. The simplest clathrate, hydrogen clathrate hydrate,  $x\text{H}_2\cdot\text{H}_2\text{O}$ , where  $x < 2$ , requires pressures around 2 kbar at 300 K to form.<sup>[184]</sup> The addition of small amounts of ligands such as THF (tetrahydrofuran) or TBAB (t-butyl ammonium bromide) can lower the pressure below 100 bar, but this decreases the maximum hydrogen storage to below 5 wt %. The formation kinetics of clathrates are currently too slow for automotive applications, although they may find other uses.

In terms of manufacturing cost, nanoporous polymer foams are the easiest to produce cheaply and in large quantities, as they use existing industrial processes.<sup>[183]</sup> Inorganic nanotubes could also potentially be produced by high-pressure hydrothermal methods on a large scale from low-cost starting materials such as  $\text{SiO}_2$ ,  $\text{Al}(\text{OH})_3$ ,  $\text{TiO}_2$ . Materials such as MOFs, chemical hydrides and carbon materials may be more expensive and complicated to produce as their synthesis can require the use of heavy metals, high temperatures, and complex polymer linkages.

**Table 2.5.** A comparison of the gravimetric storage capacities, operating temperatures, and disadvantages associated with current hydrogen storage materials. The abbreviation rehydr. = rehydrogenation.

Material	Formula (e.g.)	Capacity/ wt %	T/ K	Disadvantages	Refs.
Compressed H <sub>2</sub> (700 bar)	H <sub>2</sub>	4.8, with tank	298	Heavy tank, explosion risk	[185]
Liquid H <sub>2</sub>	H <sub>2</sub>	5.1, with tank	20	Very low T	[186]
<b>Chemical hydrides:</b>					
Alanates	NaAlH <sub>4</sub>	5.6 – 9.3	373 - 473	High rehydr. P	[187]
Borohydrides	(Na,Li)BH <sub>4</sub>	≤ 13.4	> 453	Slow H <sub>2</sub> release	[187]
Amides/ Imides	Mg(NH <sub>2</sub> ) <sub>2</sub>	≤ 7.4	≈ 573	High rehydr. T	[187]
Amino boranes	NH <sub>3</sub> BH <sub>3</sub>	19.6	> 383	Slow H <sub>2</sub> release	[187]
Alane	AlH <sub>3</sub>	10	< 373	High rehydr. P	[187]
<b>Interstitial hydrides:</b>					
Transition metal alloys	TiFe, LaNi <sub>5</sub>	≤ 1.95	≈ 298	Low capacity	[188]
<b>Hydrogen Clathrates:</b>					
ligand-stabilised clathrates	(H <sub>2</sub> ) <sub>x</sub> .THF.17H <sub>2</sub> O	≤ 4	270 - 300	High P, slow formation	[189]
<b>Porous Materials:</b>					
MOFs	[ZnO <sub>4</sub> ] <sup>6+</sup> (R) <sub>n</sub>	≤ 7.5	77	Air sensitive, low T	[190]
Zeolites	Na <sub>2</sub> Al <sub>2</sub> Si <sub>3</sub> O <sub>10</sub> .2H <sub>2</sub> O	≤ 2.5	77	Low capacity, low T	[191]
Carbon materials	C ( + metal doped)	≤ 6.9	77 - 298	Expensive, may need low T	[192]
Polymeric foams	Polymer (R) <sub>n</sub>	≈ 1.5	77	Low capacity, low T	[193]
Inorganic nanotubes	BN, H <sub>2</sub> Ti <sub>3</sub> O <sub>7</sub> , M <sub>x</sub> Si <sub>2</sub> O <sub>5</sub> (OH) <sub>4</sub>	≤ 4	77 - 298	Fairly low capacity, may need low T	[207-217]
Prussian blue analogues	Cu <sub>3</sub> [Co(CN) <sub>6</sub> ] <sub>2</sub>	≤ 1.8	77	Low capacity, low T	[194]

Although it is not always measured, the volumetric storage of hydrogen, measured in grams  $\text{H}_2$  per litre volume ( $\text{g L}^{-1}$ ), is important in addition to the gravimetric storage, because the storage tank should ideally occupy as little volume as possible. From the limited data available it appears that chemical hydrides are usually superior to high surface-area physisorption materials, having volumetric capacities around  $100 \text{ g L}^{-1}$ , compared to approximately  $30 \text{ g L}^{-1}$  for physisorption materials<sup>[195]</sup> which is similar to the capacity of compressed  $\text{H}_2$ .<sup>[185]</sup> By comparison, the 2015 DOE target for volumetric storage of hydrogen is  $81 \text{ g L}^{-1}$ .<sup>[18]</sup>

### 2.5.5. Feasibility of meeting the DOE targets

It is clear that, although superior in several ways, the currently known materials which chemically absorb hydrogen are not ideal, as they suffer from slow reactivity and release of  $\text{H}_2$ , and require high rehydrogenation temperatures and pressures. They also exhibit a tendency to degrade in performance over time and have high air sensitivity, in some cases being explosive upon contact with air.<sup>[195]</sup> Although some compounds such as alanates and amino boranes apparently exceed the DOE targets,<sup>[185]</sup> their use is not practical because of their air-sensitivity, explosive nature, and slow  $\text{H}_2$  release kinetics.

As regards materials designed to adsorb hydrogen, it is expedient to question the feasibility of these materials achieving the 2015 DOE gravimetric and volumetric targets of 9 wt % and  $81 \text{ g L}^{-1}$  adsorption.<sup>[18]</sup> To simultaneously achieve these targets would require the adsorbent material to have a density no larger than  $0.9 \text{ g cm}^{-3}$ , in other words less dense than water. This suggests that only highly porous materials composed of light elements are suitable. Since hydrogen is not known to physisorb beyond a thin layer ( $< 1 \text{ nm}$ ) on any surface, the surface area of the material must be extremely high, greater than  $1000 \text{ m}^2 \text{ g}^{-1}$ , if sufficient hydrogen is to be adsorbed per unit volume. Only 3-D molecular frameworks, single layer graphene, or nanotubes with walls one atom thick will meet this requirement.<sup>[182]</sup>

However, several strategies could be adopted to overcome this limitation of thin-layer adsorption which necessitates the use of very high surface areas only found in a narrow range of materials. One example is the doping of materials with metals to create effects such as charge transfer and the Kubas interaction. According to several theoretical

studies, this may increase the binding energy of hydrogen to the material surface above the normal range of  $2 - 4 \text{ kJ mol}^{-1}$  for weak Van der Waals interactions.<sup>[196 - 200]</sup> This could increase the volumetric hydrogen storage of a material enough that the material density could be  $> 0.9 \text{ g cm}^{-3}$  and the gravimetric storage target would still be met.

Another proposed strategy of increasing hydrogen storage is to use materials with specifically shaped pores, with the idea that ‘clathrates’, specific arrangements of functional groups in space capable of binding several hydrogen molecules, could be formed inside these pores. This possibility has been suggested specifically for inorganic nanotubes, which are discussed in the following section.

#### **2.5.6. Hydrogen storage in inorganic nanotubes**

This thesis focuses on the use of inorganic nanotubes in the storage of hydrogen. The main body of research has centred on carbon nanotubes, because they possess a high surface area and walls one atom thick, and thus meet the requirements discussed in Section 2.3.5. However, the interaction energy of  $\text{H}_2$  with  $\text{sp}^2$  carbon is very weak, approximately  $4 \text{ kJ mol}^{-1}$ ,<sup>[201]</sup> so the raw nanotubes show only modest (1-2 wt %) adsorption at 77 K. Their performance has been improved by doping with metal atoms or ions,<sup>[202, 203]</sup> but still falls short of the DOE targets. This has prompted investigation into other inorganic nanotubes, in order to investigate whether the binding energy of hydrogen with these nanotubes is higher.

Comparison of reported literature values for different nanotubes is difficult due to the different techniques (volumetric, gravimetric, or thermal desorption spectroscopy) used, the different sample masses and volumes, and the varying temperature and pressure ranges studied. There was a great controversy centred around early reports of hydrogen storage in carbon nanotubes, as the values reported were impossibly high,<sup>[176, 182]</sup> bringing the techniques used and the purity of the samples into question. As there is no standard technique for measuring hydrogen adsorption and desorption, the techniques used in each report must be subjected to careful scrutiny before conclusions are reached.

The current published gravimetric data for hydrogen storage in inorganic nanotubes at both cryogenic and ambient temperature is summarised below in table 2.6. Most reports of hydrogen adsorption on microporous and mesoporous materials at 77 K indicate that

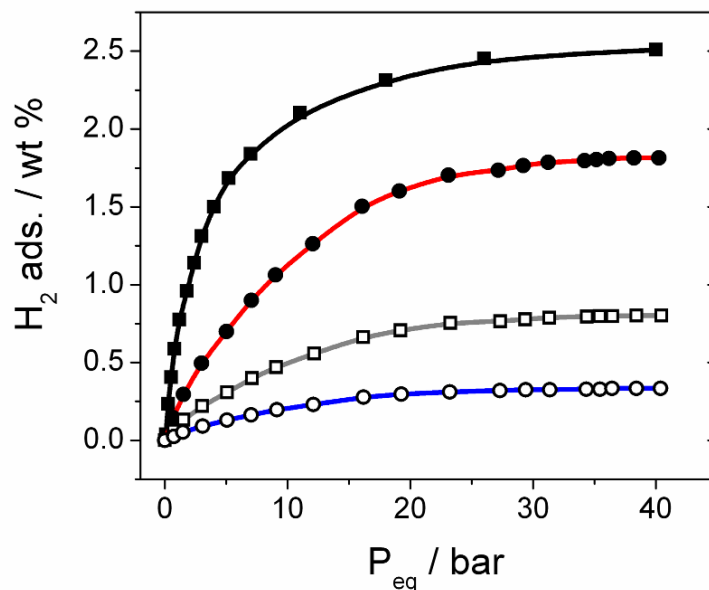
the surface becomes saturated at fairly modest pressures, usually between 1 – 30 bar. Saturation of the adsorption layer at  $\gg 30$  bar usually indicates that additional forces are present which allow  $H_2$  molecules to partially dissociate (as on a Pt or BN surface for example) <sup>[204 - 206]</sup> and pack more closely onto the surface.

**Table 2.6.** Maximum excess hydrogen adsorption capabilities of inorganic nanotubes, at different temperatures. TiNT = titanate nanotubes, and P is the equilibrium saturation pressure at which maximum hydrogen adsorption, in wt %, was achieved.

Nanotube	H <sub>2</sub> ads. / wt %	P / bar	T / K	Technique	Ref.
SWCNT	0.63	< 45	298	TPD	[207]
MWCNT	0.05 1.9	< 45 20	298 77	TPD volumetric	[207] [208]
BN	2.5	100	298	gravimetric	[209]
TiS <sub>2</sub>	2.5	40	298	volumetric	[210]
MgS	2.2	33.6	298	volumetric	[211]
TiNT	0.33 4.0	20 2	298 77	volumetric gravimetric	[212] [213]
Ni <sup>2+</sup> -doped TiNT	1.03	20	298	volumetric	[214]
Pd-doped TiNT	1.03	20	298	volumetric	[212]
Co <sup>2+</sup> -doped TiNT	0.8	20	298	volumetric	[212]
Cu <sup>2+</sup> -doped TiNT	0.34	20	298	volumetric	[212]
TiNT doped with Cd-Prussian blue	12.5	100	77	volumetric	[215]
CuSiO <sub>3</sub> .2H <sub>2</sub> O	1.6	30	298	volumetric	[45]
Mg <sub>3</sub> Si <sub>2</sub> O <sub>5</sub> (OH) <sub>4</sub>	0.72	24	298	volumetric	[45]
SiO <sub>2</sub>	0.07	5	77	gravimetric	[216]
Li-doped SiO <sub>2</sub>	0.18	10	77	gravimetric	[216]
Pd-doped SiO <sub>2</sub>	1.9	35	298	volumetric	[217]

A comparison of the data for the raw, undoped inorganic nanotubes in Table 2.6 reveals that, at room temperature, BN, TiS<sub>2</sub>, and MgS nanotubes achieve the highest gravimetric adsorption. Adsorption on titanate, copper and magnesium silicate nanotubes at room temperature is modest compared to the above materials (see Figure 2.16), but these nanotubes have the advantages of being cheaper to synthesise as they

require less extreme synthesis temperatures and pressures compared to BN and metal sulphide nanotubes.<sup>[209 - 211]</sup> Silica ( $\text{SiO}_2$ ) nanotubes synthesised through templating methods show very poor hydrogen adsorption, adsorbing less than 0.1 wt % even at 77 K.



**Figure 2.17.** PCT isotherms of excess hydrogen adsorption at 298 K for (■)  $\text{TiS}_2$ , (●)  $\text{CuSiO}_3 \cdot 2\text{H}_2\text{O}$ , (□)  $\text{Mg}_3\text{Si}_2\text{O}_5(\text{OH})_4$ , and (○) titanate nanotubes.<sup>[45, 210, 212]</sup> The plots have been rescaled to a linear  $x$ -axis scale for the equilibrium pressure ( $P_{eq}$ ).

The precise mechanism by which hydrogen may adsorb onto the surface of undoped inorganic nanotubes such as metal silicates, titanates or silica has not yet been explored by any research, although several suggestions have been made as to why these single- or multi-layered nanotubes adsorb hydrogen, including the suggestion that “clathrate-type” structures may form in the interlayer spaces of multiwalled titanate nanotubes, explaining the promising 4 wt % adsorption of these nanotubes measured at 77 K.<sup>[213]</sup> It is possible that similar and possibly stronger effects occur in other metal oxide nanotubes which have not yet been studied. This is the reason behind the investigations carried out in this thesis.

It is clear from Table 2.6 that doping inorganic nanotubes with appropriate materials can further enhance their hydrogen adsorption properties. This has been most extensively studied with titanate nanotubes.<sup>[212, 214]</sup> The raw titanate nanotubes studied by Chang et

al.<sup>[212]</sup> adsorbed 0.33 wt % hydrogen at 298 K, which could be increased to slightly above 1 wt % by either doping the titanate nanotubes with Pd nanoparticles through reduction of  $\text{H}_2\text{PdCl}_4$  onto the nanotube surface, or by ion-exchanging the nanotubes with approximately 10 wt %  $\text{Ni}^{2+}$  or  $\text{Co}^{2+}$  ions.<sup>[212, 214]</sup> By way of comparison, the hydrogen adsorption of  $\text{SiO}_2$  nanotubes appears to greatly improved by doping with Pd metal or  $\text{Li}^+$  ions, though it should be noted that the Pd-doped  $\text{SiO}_2$  nanotubes were made via a different method than the other raw and Li-doped  $\text{SiO}_2$  nanotubes, and had a larger surface area.<sup>[216, 217]</sup>

The decoration (via ion-exchange) of titanate nanotube surfaces with microporous  $\text{Cd}_3[\text{Fe}(\text{CN}_6)]_2$  Prussian blue analogues appears to give a large increase in the cryogenic adsorption of hydrogen at 77 K, up to 12.5 % which would exceed the DOE target, but it is worth noting that (i) this effect does not appear to operate at room temperature,<sup>[215]</sup> which limits its application, (ii) cadmium compounds are highly toxic, and thus large scale use would not be advisable and (iii) the isotherms in this report have a rather unusual appearance compared with previous data for nanotubes (Figure 2.17), which could be caused by idiosyncrasies of the equipment at low temperature (see Chapter 8 for explanation on how raw data should be temperature-corrected).

It has been suggested that doping nanotubes with metals or metal ions increases hydrogen adsorption by inducing an uneven distribution of charge between the nanotube surface and the doping material, which could distort the electron distribution of surface-adsorbed hydrogen molecules and thus provide an extra contribution to bonding.<sup>[218, 219]</sup> The form of doping which has achieved the most successful results is based around a phenomenon known as ‘hydrogen spillover’, in which catalyst particles of a material on which hydrogen has a low energy barrier to dissociation at room temperature, such as Pt, are decorated onto the surface of a porous material. Hydrogen molecules dissociate on the surface of the catalyst particles, and the dissociated molecules may then diffuse onto the surface on which the catalyst particles are adsorbed. This method has already achieved promising results in MOFs,<sup>[220]</sup> and could also be applied in some metal-doped nanotubes.<sup>[221]</sup> Fully describing the mechanism of hydrogen adsorption on doped nanotubes would require a comparative study of results from computational methods such as grand canonical Monte Carlo simulations<sup>[222]</sup> with experimental data.





## Chapter 3: Experimental Methodology

In this thesis, nanostructured metal oxides were synthesised using hydrothermal methods and were analysed for their hydrogen adsorption properties using a volumetric method. This Chapter describes in detail the experimental procedures which were followed. Section 3.1 describes the reagents and range of conditions which were used to synthesise nanosheets and nanotubes consisting of (1) Ge-doped aluminosilicates, (2) germanium-imogolite  $\text{Al}_2\text{GeO}_3(\text{OH})_4$ , (3) nickel silicates, and (4, 5) vanadium oxide. Section 3.2 describes experiments designed to measure the long term stability of naturally occurring (non-synthetic) halloysite nanotubes in concentrated and dilute acid and alkaline suspensions, and Section 3.3 outlines the decoration of natural halloysite with Prussian blue  $\text{Fe}_3[\text{Fe}(\text{CN})_6]_2$  nanoparticles. Section 3.4 explains how apparatus was designed to measure the relationship between the equilibrium vanadium concentration and temperature in the vanadium oxide nanotube synthesis precursor suspension (described in Section 3.1.4). Section 3.5 outlines the techniques (electron microscopy, nitrogen adsorption, Fourier-transform infrared spectroscopy, Raman spectroscopy and  $x$ -ray diffraction) used to characterise the solid products of the hydrothermal reactions from section 3.1 and the acid and alkaline treated halloysite nanotubes from Section 3.2. The use of colorimetric analysis to determine solution concentrations of metal species is described in Section 3.6. Finally, the volumetric analysis of hydrogen adsorption properties of the nanostructured materials is described in Section 3.7.

### 3.1. Hydrothermal synthesis procedures

#### 3.1.1. Germanium-doped aluminosilicates

A synthesis procedure was adapted from methods of preparation of kaolinite,  $\text{Al}_2\text{Si}_2\text{O}_5(\text{OH})_4$ , reported in references <sup>[113, 223]</sup>. 2.5 mmol of  $\text{Al}(\text{OH})_3$  was mixed with  $(2.5-x)$  mmol of  $\text{SiO}_2$  and  $x$  mmol of  $\text{GeO}_2$  ( $x = 0, 0.125, 0.25, 0.5$  and  $1.25$ ), following the addition of  $20 \text{ cm}^3$  distilled water ( $< 20 \mu\text{S m}^{-1}$ ). The molar fraction of added  $\text{GeO}_2$  ( $X$ ), calculated as the amount of  $\text{GeO}_2$  divided by the sum of  $\text{SiO}_2 + \text{GeO}_2$  ( $X = x/2.5$ ),

was equal to 0, 0.05, 0.1, 0.2, and 0.5, respectively. The resulting suspensions were stirred vigorously for 15 minutes in a polypropylene beaker and sonicated for 5 minutes to break up aggregates of starting material. The sonicated mixtures were acidified to pH 2 by adding  $1 \text{ mol dm}^{-3}$  HCl drop-wise, then transferred to a Teflon-lined autoclave and heated at  $220^\circ\text{C}$  for 7 days. After the reaction, the white powdery solid samples were separated from the fluid and thoroughly washed with water until the conductivity of the solution was  $< 20 \mu\text{S m}^{-1}$ . The samples were dried for 24 hours under vacuum at  $25^\circ\text{C}$ .

### 3.1.2. Single- and double-walled germanium-imogolite nanotubes

Pure germanium imogolite, in which Ge atoms occupy all the sites usually filled with Si in the imogolite structure, was synthesized using a procedure based on that of Levard et al.<sup>[122]</sup> For the synthesis of double-walled germanium imogolite, 1.207 g of  $\text{AlCl}_3 \cdot 6\text{H}_2\text{O}$  was dissolved in  $10 \text{ cm}^3$  distilled water ( $< 10 \mu\text{S m}^{-1}$ ) to make a  $0.5 \text{ mol dm}^{-3}$  solution. Meanwhile, 0.261 g of  $\text{GeO}_2$  was dissolved in  $10 \text{ cm}^3$  of a  $0.5 \text{ mol dm}^{-3}$  NaOH (Fisher Scientific,  $> 97\%$ ) solution. This solution containing dissolved Ge(IV) was added drop wise to the  $\text{AlCl}_3 \cdot 6\text{H}_2\text{O}$  solution, at a rate of  $1.5 \text{ cm}^3$  per minute under vigorous stirring, resulting in a solution with a final  $\text{AlCl}_3 \cdot 6\text{H}_2\text{O}$  concentration of  $0.25 \text{ mol dm}^{-3}$ . The hydrolyzed solution was left to stir ( $\approx 200 \text{ rpm}$ ) overnight for at least 12 hours until the solution was transparent, and was then transferred to a  $40 \text{ cm}^3$  Teflon-lined steel autoclave and heated at  $95^\circ\text{C}$  for 5 days. Afterwards the solution was cooled and salts were removed via dialysis against distilled water in a dialysis cassette containing a 10,000 Da membrane. The distilled water was changed every 12 hours until the conductivity was  $\leq 10 \mu\text{S m}^{-1}$ . Solid Ge-imogolite fibres consisting of bundles of close-packed nanotubes were then obtained from the purified suspension remaining in the dialysis cassette by evaporating the water from the suspension on the surface of a glass crystallizer at  $50 - 60^\circ\text{C}$ .

The synthesis of single-walled Ge-imogolite was performed in an identical fashion, apart from the doubling of all quantities of  $\text{AlCl}_3 \cdot 6\text{H}_2\text{O}$ ,  $\text{GeO}_2$  and NaOH solids dissolved into the starting materials to make a doubly-concentrated solution with a  $0.5 \text{ mol dm}^{-3}$  concentration of  $\text{AlCl}_3 \cdot 6\text{H}_2\text{O}$ , in line with the experimental methods of Maillet et al.<sup>[171]</sup>

### 3.1.3. Nickel silicates

A procedure adapted and modified from the work of Yang et al. <sup>[47]</sup> was followed. Nickel chloride,  $\text{NiCl}_2 \cdot 6\text{H}_2\text{O}$  (Scientific & Chemical supplies Ltd., cat. number NI030) was added to  $30 \text{ cm}^3$  distilled water in a polypropylene beaker and stirred until all the salt had dissolved.  $4 \text{ cm}^3$  of  $0.5 \text{ mol dm}^{-3}$  of  $\text{Na}_2\text{SiO}_3$  (Alfa Aesar, cat. number 17568) solution was rapidly added resulting in a light green precipitate; the mixture was then stirred for 10 minutes. The mass of  $\text{NiCl}_2 \cdot 6\text{H}_2\text{O}$  used was 0.47, 0.71, 0.95 and 1.4 g corresponding to a molar Ni/Si ratio of 1, 1.5 2, and 3 respectively. After stirring, a controlled mass of NaOH (Fisher Scientific, > 97 %) was added to the suspension to make a solution containing 0, 2, 4, 7, 10 or 15 wt% NaOH (6 g NaOH added = 15 wt %). The suspension was stirred for a further 10 minutes, and then transferred to an autoclave and heated at  $195^\circ\text{C}$  for 2 days without any stirring. The solid products were separated from solution, and washed by centrifugation until the conductivity of the washing solution was  $\approx 10 \mu\text{S m}^{-1}$ . The solids were then dried for 24 hours under vacuum at  $25^\circ\text{C}$ .

### 3.1.4. Vanadium oxide nanotubes

To synthesize vanadium oxide ( $\text{VO}_x$ ) nanotubes, the method of Niederberger et al. <sup>[37]</sup> was followed. A mixture of 15 mmol (2.73 g)  $\text{V}_2\text{O}_5$  (Acros Organics, > 98 %) and 15 mmol (2.18 g) dodecylamine (Acros Organics, > 98 %) was dispersed in  $5 \text{ cm}^3$  ethanol then stirred vigorously for 2 hours.  $15 \text{ cm}^3$  of distilled water ( $< 10 \mu\text{S m}^{-1}$ ) was immediately added and the suspension was stirred ( $\approx 200 \text{ rpm}$ ) for 48 hours. This formed a dodecylamine-intercalated- $\text{V}_2\text{O}_5$  precursor suspension, which was transferred to an autoclave and heated for 7 days at  $180^\circ\text{C}$ . The resulting black solid was washed 3 times with approximately  $100 \text{ cm}^3$  ethanol, followed by 3 washes with approximately  $50 \text{ cm}^3$  hexane to remove any excess amine then dried for 24 hours under vacuum at  $25^\circ\text{C}$ .

### 3.1.5. Low temperature synthesis of vanadium oxides

In order to investigate the effect of temperature and solvent type on the synthesis of vanadium oxide nanostructures, the method given in Section 3.1.4 was used without alteration except that a synthesis temperature of 140 °C was used for 7 days. A synthesis temperature of 220 °C was also used in a separate 7 day hydrothermal treatment to investigate the effects of excessive heating.

Experiments were also carried out at a much lower temperature under atmospheric conditions without the use of an autoclave. The dodecylamine-intercalated- $V_2O_5$  precursor suspension was prepared exactly the same way as in Section 3.1.4. The resulting 20 cm<sup>3</sup> suspension was transferred into a round-bottomed glass flask connected to a glass condenser filled with flowing water and heated to 90 °C in an oil bath for up to 21 days. The solution reached reflux conditions at 90 °C within a few hours after the evaporation of most of the 5 cm<sup>3</sup> ethanol added to the precursor. After reaching 90 °C the suspension was not stirred. Small samples of solid (< 200 mg) were removed periodically and washed with ethanol and hexane before drying under vacuum at 25 °C.

The above procedure was repeated with the addition of liquid ethylenediamine (Aldrich, 99 %) to the dodecylamine-intercalated- $V_2O_5$  precursor suspension before heating at 90 °C, to make a 0.001, 0.01, 0.1 or 1 mol dm<sup>-3</sup> ethylenediamine solution. The ethylenediamine was added as a chelating agent to increase the solubility of V(V) species at 90 °C.

## 3.2. Stability experiments for natural halloysite

The long term stability of halloysite nanotubes,  $Al_2Si_2O_5(OH)_4$ , in solution was measured by aging natural samples of halloysite in acid and alkaline solutions of varying strength and concentration and determining the concentration of dissolved Al(III) species Si(IV) and characterising the remaining solids over a period of time from 0 – 84 days (3 months).

### 3.2.1. Reagents

Sodium hydroxide (NaOH, > 97 %), sulphuric acid (H<sub>2</sub>SO<sub>4</sub>, > 95 %), hydrochloric acid (HCl, 35-38 % solution), acetic acid (CH<sub>3</sub>COOH, > 99 %) and ammonium molybdate ((NH<sub>4</sub>)<sub>2</sub>MoO<sub>4</sub>, > 98 %), were purchased from Fisher Scientific UK. Samples of natural halloysite (cat. number 685445), pyrocatechol violet (cat. number 32672), hexamethylenetetramine (≥ 99.5 %), L-(+)-tartaric acid (≥ 99.5 %) and L-(+)-ascorbic acid (≥ 99.0 %) were purchased from Sigma Aldrich. All chemicals were used without further purification.

### 3.2.2. Long term stability studies of halloysite

For each sample, 100 mg of halloysite was weighed to an accuracy of ± 0.5 mg inside 30 cm<sup>3</sup> polypropylene vials and 10 cm<sup>3</sup> of 0.001 – 1 mol dm<sup>-3</sup> NaOH, H<sub>2</sub>SO<sub>4</sub>, HCl, and CH<sub>3</sub>COOH aqueous solutions were added under stirring using an Eppendorf pipette, to an accuracy of ± 0.08 cm<sup>3</sup>. A blank sample of halloysite suspended in distilled water was also prepared. All vials were closed and kept at room temperature (22 ± 2 °C) without any further stirring.

### 3.2.3. Preparation of solids for sample characterisation

After a period of 28 or 84 days, the solids were extracted from the solution by vacuum filtration, and thoroughly washed with distilled water until the conductivity of the washing solution was < 10 μS m<sup>-1</sup>. The products were then dried overnight under vacuum at 25 °C.

### 3.2.4. Preparation of solution for colorimetric analysis

At specific points in time during the acid/base treatment of halloysite, the total concentrations of dissolved Al(III) and Si(IV) were measured using colorimetric methods with pyrocatechol violet <sup>[224]</sup> and molybdate <sup>[225]</sup> respectively (Section 3.5.1). To prepare samples for analysis, an aliquot of 0.02 – 0.2 cm<sup>3</sup> was taken from each sample suspension at half the solution depth, and diluted until the estimated total Al (III)

concentration was in the range  $5 - 20 \mu\text{mol dm}^{-3}$  and estimated total Si(IV) concentration was in the range  $0.05 - 0.5 \text{ mmol dm}^{-3}$ .

### 3.3. Ion-exchange decoration of natural halloysite with Prussian blue

To produce halloysite decorated with Prussian blue ( $\text{Fe}_3[\text{Fe}(\text{CN})_6]_2$ ) for hydrogen adsorption studies (Section 3.7), 1 g of halloysite was ion-exchanged with  $\text{Fe}^{2+}$  by suspension in  $50 \text{ cm}^3$  of a saturated  $0.75 \text{ mol dm}^{-3}$   $\text{FeSO}_4$  solution, followed by vigorous stirring for 36 hours. The solution was then removed under vacuum filtration and the solids were washed by centrifugation in distilled water until the sample conductivity was  $< 10 \mu\text{S m}^{-1}$ . The sample was dried overnight under vacuum, then suspended in  $50 \text{ cm}^3$  of a  $0.25 \text{ mol dm}^{-3}$  solution of  $\text{K}_3[\text{Fe}(\text{CN})_6]$  and stirred vigorously for 24 hours, to produce small particles of  $\text{Fe}_3[\text{Fe}(\text{CN})_6]_2$  on the nanotube surface. The nanotubes were washed by centrifugation in distilled water until the conductivity was  $< 10 \mu\text{S m}^{-1}$ . The solids were then dried under vacuum overnight at  $25^\circ\text{C}$ .

### 3.4. Measurement of equilibrium vanadium(V) concentration 25 - $90^\circ\text{C}$

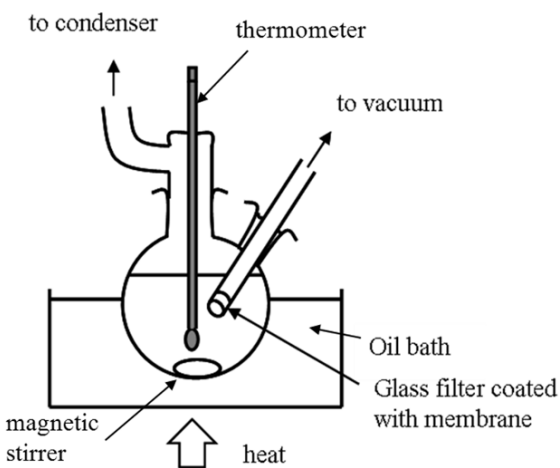
#### 3.4.1. Design of experiment

The purpose of this experiment was to establish a numerical relationship between the equilibrium concentration of dissolved vanadium (V) and the synthesis temperature during the synthesis of  $\text{VO}_x$  nanostructures from a suspension of dodecylamine-intercalated  $\text{V}_2\text{O}_5$  (section 3.1.4). It is impractical to measure V(V) concentration at higher temperatures close to and above the boiling point of the solution (which is between  $90\text{-}100^\circ\text{C}$ ), since the extracted samples will become concentrated through rapid evaporation of solvent during extraction and give erroneous results. Therefore, the equilibrium concentration of dissolved V(V) was measured within the range  $25 - 90^\circ\text{C}$ , and the concentration-temperature relationship was extrapolated up to  $180^\circ\text{C}$  to estimate the equilibrium concentration of the dissolved V(V) during the synthesis of  $\text{VO}_x$  nanotubes.

To determine the equilibrium concentration of vanadium (v) at various temperatures, a dodecylamine-intercalated  $V_2O_5$  precursor suspension was prepared (see Section 3.1.4) in a Pyrex glass round-bottom flask. The suspension was transferred to an oil bath on a stirrer hotplate, and  $150\text{ cm}^3$  distilled water was added. The diluted suspension was then heated to  $90\text{ }^\circ\text{C}$  and stirred vigorously for 24 hours, which from measurements of vanadium (V) concentration using the BPHA method <sup>[226]</sup> (see Section 3.5.2) over 3 days was found to be sufficient time to establish equilibrium. Three small solution samples of  $2\text{ cm}^3$  volume were collected using a special apparatus (Section 3.4.2), and set aside for concentration analysis. The temperature of the apparatus was subsequently reduced to 78, 65, 50, 38 and  $26\text{ }^\circ\text{C}$ , in sequence; three  $2\text{ cm}^3$  solution samples were collected at each temperature. The time allowed for equilibrium to be reached was scaled up accordingly at the lower temperatures; two days were required at 65 and  $78\text{ }^\circ\text{C}$ , 4 days at  $50\text{ }^\circ\text{C}$ , and 7 days at 38 and  $26\text{ }^\circ\text{C}$  in order to establish an equilibrium concentration of vanadium (V), which was approached from supersaturation.

### 3.4.2. Extraction of samples for concentration analysis

The special design of the heating apparatus (Figure 3.1) enables solution to be rapidly filtered through a track-etch membrane (pore size 200 nm) and a grade 4 ground glass filter (pore size  $10 - 16\text{ }\mu\text{m}$ ) under vacuum. This allows safe filtration which is rapid enough to collect solution before it undergoes too much cooling.



**Figure 3.1.** Apparatus used to filter vanadium suspensions to collect the solution for concentration analysis.



The track-etch membrane was connected to the glass filter by attaching dry, clean Teflon tape around the membrane edges. The suspension was stirred at a rate of approximately 200-300 rpm, and the oil bath was also stirred at this rate to ensure an even heating distribution.

### **3.5. Characterisation of solid products**

#### **3.5.1. Transmission electron-microscopy**

All solid samples from Sections 3.1 and 3.2 were examined using electron microscopy. Transmission electron microscopy (TEM) micrographs were prepared on S147-3 copper grids coated with perforated carbon film (Agar Scientific), by moving the grid through a finely powdered sample several times. TEM images were recorded using a JEOL 3010 transmission electron microscope operating at an accelerating voltage of 300 kV. This instrument was also used to perform selected area electron diffraction (SAED) and energy dispersive *x*-ray spectroscopy (EDX). The EDX spot size was in the range 20 – 50 nm. To ensure that the micrographs represented the sample composition as accurately as possible, at least 20 different areas of the TEM grid were analysed for each sample. It should be noted that electron microscopy only characterises a microgram-sized portion of the sample, and bulk characterisation techniques such as nitrogen adsorption, ICP atomic emission spectroscopy and X-ray diffraction should be used to support the TEM observations where possible.

#### **3.5.2. Scanning electron-microscopy and length distributions**

Samples for scanning electron micrographs were prepared by depositing a few milligrams of powder onto double-sided graphite conductive tape. SEM images were recorded using a JSM 6500F thermal emission scanning electron microscope, operating at an accelerating voltage of 15 kV.

To measure length distributions of nanotubular samples from Sections 3.1.3 and 3.2.3, a few milligrams of the sample was suspended in 5 cm<sup>3</sup> of ethanol during 1 hour of

vigorous stirring. The suspensions were deposited as  $1 \mu\text{m}^3$  drops onto ultrasonically-cleaned pieces of silicon wafer, and were left in air until the ethanol had evaporated. SEM images of these suspensions deposited onto the silicon wafers were analysed using digital imaging software (Corel graphics suite) to produce a percentage length distribution of nanotubes. The length of at least 100 nanotubes was measured in each sample, and the images were carefully studied at higher magnification ( $\times 10$ -20 k) to rule out artefacts (such as nanotubes overlaying each other) as far as possible. However, it should be noted that some artefacts could not be eliminated, such as the bright haloes caused by excess secondary electrons which may appear around non-conductive particles. These haloes make the particle appear up to  $\approx 10 \text{ nm}$  larger around the edges.

### 3.5.3. Nitrogen adsorption

Nitrogen adsorption isotherms at  $-196^\circ\text{C}$  were used for bulk analysis of the specific surface area, pore volume, and pore size distribution of all samples. The instrumentation used was a Micromeritics Gemini 2375 Surface Area Analyser.

All samples were subjected to calcination pre-treatment under vacuum to remove surface adsorbed water from pores. For all the samples, it was found that 1 hour at  $120^\circ\text{C}$  was sufficient to remove  $> 95\%$  of the adsorbed water, except in the case of Ge-imogolite nanotubes which are highly microporous. The Ge-imogolite samples were calcined at  $200^\circ\text{C}$  for 12 hours. The mass of the samples was measured after calcination using a balance accurate to  $\pm 0.05 \text{ mg}$ .

The total free space in the tube containing the sample was calibrated against a reference volume using helium gas. The ambient pressure,  $P_0$  was measured and data points were collected for adsorption and desorption at various pressure,  $P$ , between  $0 < P/P_0 < 1$  using nitrogen gas (BOC, 99.99 %). The isotherm points plotted were expressed as volume adsorbed per unit mass of sample, in  $\text{cm}^3\text{g}^{-1}$  units. This quantity was calculated by the Analyser at each  $P/P_0$  using a nitrogen equation of state at  $77 \text{ K}$ .

BJH pore-size distributions were calculated from the desorption isotherm by applying the Barrett-Joyner-Halenda scheme for mesopore size distribution.<sup>[72]</sup> The desorption isotherm is used in preference to the adsorption isotherm because of the spherical shape

of the gas-liquid interface in desorption. The BET specific surface area of the sample was calculated using BET theory,<sup>[71]</sup> and the specific total pore volume was defined as the cm<sup>3</sup> volume of nitrogen adsorbed per gram of material at pressure  $P/P_0 = 0.97$ .

#### **3.5.4. FTIR and Raman spectroscopy**

Fourier transform infrared (FTIR) spectroscopy was performed on the samples from Sections 3.1.1, 3.1.3, and 3.2.3 (germanium aluminosilicates, nickel silicates, and acid/alkali treated halloysite respectively). The instrumentation used was a Nicolet iS10 spectrometer (Thermo Fisher Scientific) with a “golden gate” attachment for solid samples.

Raman spectra of the products of section 3.2.3 were performed using a Renishaw 2000 spectrometer with HeNe laser ( $\lambda = 632.8$  nm) excitation.

#### **3.5.5. X-ray diffraction**

X-ray diffraction was performed on nickel silicate, vanadium oxide and acid- and alkaline-treated halloysite samples using a D5000 diffractometer (Siemens), with CuK $\alpha$  radiation ( $\lambda = 0.154$  nm). The diffractometer was optimised for finely powdered samples.

#### **3.5.6. ICP atomic emission spectroscopy**

Analysis of the Al, Si, and Ge content in the Ge-doped aluminosilicates produced in section 3.1.1 was performed using ICP (inductively coupled plasma) spectroscopy by a Perkin-Elmer Optima 2100 DV system.

### **3.6. Colorimetric Methods**

#### **3.6.1. Measurement of dissolved Al (III) and Si(IV) during halloysite dissolution**

For analysis of Al(III), the diluted solution from Section 3.2.3 was acidified with sulphuric acid, then mixed with 0.1 cm<sup>3</sup> of 1.3 mmol dm<sup>-3</sup> pyrocatechol violet in 9 cm<sup>3</sup> pH 5.9 hexamine buffer, made up to 10 cm<sup>3</sup> with distilled water and allowed to develop

colour for 15 minutes at room temperature. The concentration of the complex was determined using a UV-vis spectrometer (Scinco Neosys 2000) by measuring the characteristic absorbance band at 580 nm.

For analysis of Si(IV), the diluted solution was mixed with 0.08 cm<sup>3</sup> of 0.1 mol dm<sup>-3</sup> ammonium molybdate, forming a complex which was then reduced to deep-blue molybdenum blue, H<sub>8</sub>SiMo<sub>12</sub>O<sub>40</sub>·12H<sub>2</sub>O by the addition of 0.08 cm<sup>3</sup> of 0.1 mol dm<sup>-3</sup> of ascorbic acid. After 1 hour colour development, the characteristic absorbance of the molybdenum blue was measured at 650 nm (see Appendix B, page 183, for characteristic spectra of Al(III)-pyrocatechol violet and Si(IV)-molybdenum blue complexes, and page 185 for calibration curves).

### **3.6.2. Measurement of dissolved vanadium (V) equilibrium concentration**

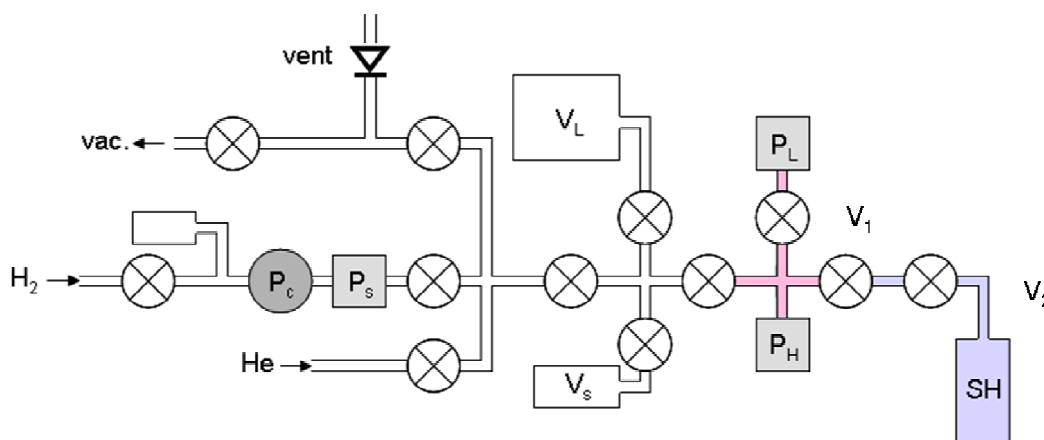
Each 2 cm<sup>3</sup> sample extracted at 25 – 90 °C was re-heated to the temperature at which it was extracted inside a closed vial in a hot water bath. The samples were then mixed with 2 cm<sup>3</sup> of 0.012 mol dm<sup>-3</sup> BPHA (N-benzoyl phenyl hydroxylamine) solution in chloroform, and thoroughly shaken for 30 seconds. The organic layer was extracted, and the aqueous layer was washed with 2 cm<sup>3</sup> of chloroform. This chloroform was added to the previous organic layer, and the resulting purple solution was made up to 10 cm<sup>3</sup> with additional chloroform. The concentration of the complex was determined by measuring the characteristic absorbance band at 535 nm (see Appendix B, page 183-186, for characteristic spectra of the V(V)-BPHA complex, and for calibration curves).

## **3.7. Hydrogen Adsorption Isotherms**

### **3.7.1. Instrumentation and gas supply**

Hydrogen adsorption and desorption was measured using a PCT-Pro 2000 (Hy-Energy) volumetric apparatus (Figure 3.2). To control the temperature of the sample holder below room temperature, a Cryo-Pro cryostat with an internal heater and temperature controller was connected to a supply of liquid nitrogen, to cool the sample with liquid or evaporated nitrogen. The PCT-Pro was connected to a supply of zero grade hydrogen

gas (BOC) with 99.995 – 99.999 % purity. For adsorption studies, the calibrated volume of 4.64 cm<sup>3</sup> was used to contain the hydrogen gas aliquot prior to expansion into the sample holder (Figure 3.2). The aliquot pressure was set using an ER3000 electronic pressure controller. The external temperature around the sample holder was controlled using a thermostat heater coil wrapped around the sample holder, and the temperature in the centre of the sample was measured using a Pt sensor with an accuracy of  $\pm 2.8 \times 10^{-3}$  K at 77 K. The pressure was measured by two MKS type 870B/ 87B pressure transducers: one reading pressures between 0 - 5 bar with a percentage accuracy 1 %, and one reading at above 5 bar with a percentage accuracy 1 %. At 150 bar (15 MPa) this corresponds to  $\pm 1.5$  bar uncertainty.



**Figure 3.2.** The flow system for the PCT-Pro 2000 apparatus. The  $\otimes$  symbol is a valve operated by an external nitrogen pressure. SH is the sample holder, V<sub>L</sub> is a large reservoir volume, V<sub>s</sub> a small reservoir volume, and P<sub>s</sub>, P<sub>L</sub> and P<sub>H</sub> refer to the supply, low and high pressure transducers respectively. P<sub>c</sub> is the electronic pressure controller. The shaded areas, labelled V<sub>1</sub> (pink) and V<sub>2</sub> (blue), refer to the 4.64 cm<sup>3</sup> calibrated reservoir volume and the sample holder volume respectively.

### 3.7.2. Sample preparation and degassing

The weight of the powdered samples was measured on a mass balance accurate to  $\pm 0.05$  mg. The samples were then carefully transferred into the steel sample holder together with steel spacers which reduced the free volume inside the sample holder. Non-adsorbing quartz wool was placed above the sample to prevent upward suction of

powered material during sample evacuation. The sample holder was then connected to the PCT-Pro apparatus using a copper gasket to prevent leaks, and the sample was evacuated for 12 hours.

Each sample was calcined during the 12 hour evacuation period at a specific temperature appropriate to their structure, in order to remove most of the surface adsorbed water (see Section 3.5.3). For the natural halloysite nanotubes (3.2.1), halloysite- $\text{Fe}_3[\text{Fe}(\text{CN})_6]_2$  composite (3.3), synthetic nickel silicate (3.1.3) and vanadium oxide (3.1.4) nanotubes, a calcination temperature of 120 °C was sufficient. Experiments in a separate degassing apparatus in which the sample mass was measured before and after calcination showed that after calcination there was a 4 % mass loss for halloysite, and the halloysite- $\text{Fe}_3[\text{Fe}(\text{CN})_6]_2$  composite (which was shown by EDX to contain  $\approx 4.7$  wt %  $\text{Fe}_3[\text{Fe}(\text{CN})_6]_2$ ). The nickel silicate nanotubes used were synthesised using a 1.5 Ni/Si ratio in a 4 wt % NaOH solution. These nanotubes showed a 7 % mass loss after calcination. For vanadium oxide nanotubes, there was 5 % loss in mass upon heating. It was important that the temperature did not exceed 120 °C, otherwise interlayer amine molecules may be removed (see Section 2.4.1.) The mass loss percentages have been used to calculate the final sample mass after degassing from the initial mass in Table 3.1.

**Table 3.1.** Calculated sample masses after degassing in the PCT-Pro apparatus.  $T_c$  is the calcination temperature,  $m_i$  is the initial mass and  $m_f$  is the sample mass after calcination.

Sample	$m_i$ /g	$T_c$ / °C	$m_f$ /g	wt % $\text{H}_2\text{O}$ removed
Quartz wool (blank)	0.2671	120	0.2671	< 1
Halloysite MWNTs	0.2669	120	0.2562	4
Halloysite + 4.7 wt% $\text{Fe}_3[\text{Fe}(\text{CN})_6]_2$ composite	0.2671	120	0.2564	4
Nickel silicate MWNTs	0.2685	120	0.2497	7
Ge-imogolite SWNTs	0.2673	150	0.2245	16
Ge-imogolite DWNTs	0.2061	150	0.1731	16
Vanadium oxide MWNTs	0.2557	120	0.2419	5

Although a calcination temperature 200 - 250 °C is necessary for the microporous Ge-imogolite single- and double-walled nanotubes (3.1.2) to remove all adsorbed water,<sup>[227]</sup> such high temperatures would damage the cryostat system. Therefore an external calcination temperature of 200 °C, the temperature limit of the cryostat, was used to remove adsorbed water during evacuation. This corresponded to a temperature of 150 - 155 °C inside the sample. Based on the specific pore volume data from reference<sup>[78]</sup> it can be assumed that  $\approx 85\%$  of the surface adsorbed water was removed by this treatment. A drop in mass of 16 % for both samples was measured on the degassing apparatus at this temperature.

### 3.7.3. Volume calibration

After sample degassing, the sample holder volume was cooled to the required temperature in the range 77 - 298 K using the cryostat and the sample holder free volume was calibrated using helium gas (BOC, 99.996 %). Five cycles of adsorption followed by desorption of helium in the pressure range 0 – 3 bars were performed over a period of 90 minutes. The change in equilibrium pressure after opening the valves between  $V_1$  and  $V_2$  (Figure 3.2) was used by the apparatus to calculate the total free volume of the sample holder ( $V_2$ ), based on the assumption that helium is not adsorbed by the sample or sample holder (as a very light element, He exhibits low Van-der Waals binding potential, and above its critical temperature of 5.19 K it cannot condense on a surface). The calibrated volumes of each sample are given in Table 3.2 together with the standard deviation of the ten volume measurements (5  $\times$  adsorption and 5  $\times$  desorption).

**Table 3.2.** Volume calibration of samples using He at 77 K. The free volume given is the volume that the same mass of helium gas would occupy at room temperature (298 K).

Sample	Mass/ g	Free volume / cm <sup>3</sup>	Free volume Standard deviation / cm <sup>3</sup>
Quartz wool (blank)	0.2671	24.8418	0.2557
Halloysite	0.2562	24.424	0.2343
Halloysite + 4.7 wt% Fe <sub>3</sub> [Fe(CN) <sub>6</sub> ] <sub>2</sub> composite	0.2564	24.2704	0.2289
Nickel silicate	0.2497	22.5041	0.2041

Ge-imogolite SWNTs	0.2245	22.5879	0.2048
Ge-imogolite DWNTs	0.1731	23.4660	0.2432
Vanadium Oxide	0.2419	22.1193	0.2125

It is desirable to have all measurements of free volume as similar as possible (within one standard deviation) to the blank non-adsorbing sample, so that temperature corrections made to the blank sample (see Section 3.7.6.) can be extended to all samples. This was attempted in all cases by using steel spacers to minimize the sample volumes, but it is difficult to achieve an exact volume consistently.

#### 3.7.4. Thermal stability

The thermal stability of the sample depended on the temperature used. At temperatures close to 298 K which were not regulated by the cryostat, the thermal stability of the sample was  $\pm 0.1$  °C due to heating and cooling of the sample during gas adsorption/desorption. At 77 K, when the sample was immersed in liquid nitrogen, which was continually replenished by a steady flow of liquid nitrogen from the cryostat, the thermal stability was  $\pm 0.02$  °C. At intermediate temperatures of 77 – 298 K controlled by the cryostat, the thermal stability was  $\pm 0.5$  °C as the temperature was controlled by a flow of evaporating liquid nitrogen, the rate of which is more difficult to control.

#### 3.7.5. Measurement of PCT isotherms

Pressure-composition-temperature (PCT) isotherms were recorded in the pressure range 0 – 150 bar (15 MPa) for adsorption and 150 – 0 bar for desorption. At least 25 data points were recorded over this pressure range, with a higher density of points ( $> 10$ ) recorded in the range 0 – 10 bar.

Points were recorded by setting an aliquot pressure inside the calibrated  $4.64 \text{ cm}^3$  reference volume and opening the valves between  $V_1$  and  $V_2$  (Figure 3.2) to expand the gas into the entire volume. The pressure was measured every 5 seconds until the rate of



change in gas adsorbed by the sample was  $< 1 \times 10^{-4}$  wt %  $\text{min}^{-1}$ , so that the pressure readings were taken very close to equilibrium pressure.

### 3.7.6. Analysis of raw data and temperature correction

The data output from the PCT-Pro was analysed using an inbuilt Hy analysis macro in the software Igor 5.3. The macro contains information about the precise volume of the apparatus, which allows calculation of the pressure drop that is due to adsorption on materials as opposed to gas expansion into  $V_2$ . This pressure drop can be converted into a mass percentage of hydrogen adsorbed per gram of substance, i.e. wt % adsorption (see Section 2.5.2).

The Igor software contains functions which correct the data to allow for real gas compressibility (compressibility factor  $Z$ ) in the equation

$$pV = nRT \cdot Z(p, T) \quad (3.1)$$

where  $Z$  is a function of pressure and temperature determined by the equation of state (EOS) of hydrogen. The Igor software also applies a linear temperature correction factor to the data,<sup>[228]</sup> which takes into account the fact that the sample holder volume ( $V_2$ ) is not at the same temperature as the reservoir volume ( $V_1$ ) in which each aliquot is held prior to expansion. It is assumed that a linear temperature gradient exists between the two volumes, such that an averaged temperature  $T_f$  would be given by<sup>[228]</sup>

$$T_f = \frac{(T_1 \times V_1) + (T_2 \times V_2)}{V_1 + V_2} \quad (3.2)$$

where  $T_1$  is the temperature of the reservoir and  $T_2$  is the temperature of the sample holder. Because the exact volume that is held at temperature  $T_2$  is unknown (it does not exactly correspond to  $V_2$  as it depends upon the level of liquid  $\text{N}_2$  and heat transfer coefficients within the system), the Igor software applies a value of  $T_f$  to determine an effective sample holder volume,  $V_{\text{eff}}$ , in place of  $V_2$ , the measured sample holder volume, resulting in a temperature-corrected PCT isotherm. The effective sample holder

volume for the temperature correction is given by substituting  $V_{\text{eff}}$  for  $V_2$  in equation (3.2) and rearranging to give

$$V_{\text{eff}} = \frac{V_1(T_1 - T_f)}{(T_f - T_2)} \quad (3.3)$$

Since the pressure drop corresponding to adsorption is proportional to  $1/V_{\text{eff}}$ , the temperature correction ratio applied to the data by the Igor software is equal to

$$T_{\text{ratio}} = \frac{(T_f - T_2)}{(T_1 - T_f)} \quad (3.4)$$

Consequently, measurement of a blank sample that does not adsorb hydrogen is important: a temperature correction factor must be found that results in a PCT curve that is as close as possible to zero over the entire pressure range for a non-adsorbing sample. <sup>[228]</sup> This factor can then be used to correct data for all the adsorbing samples which have the same free volume and are at the same temperature as the blank sample.



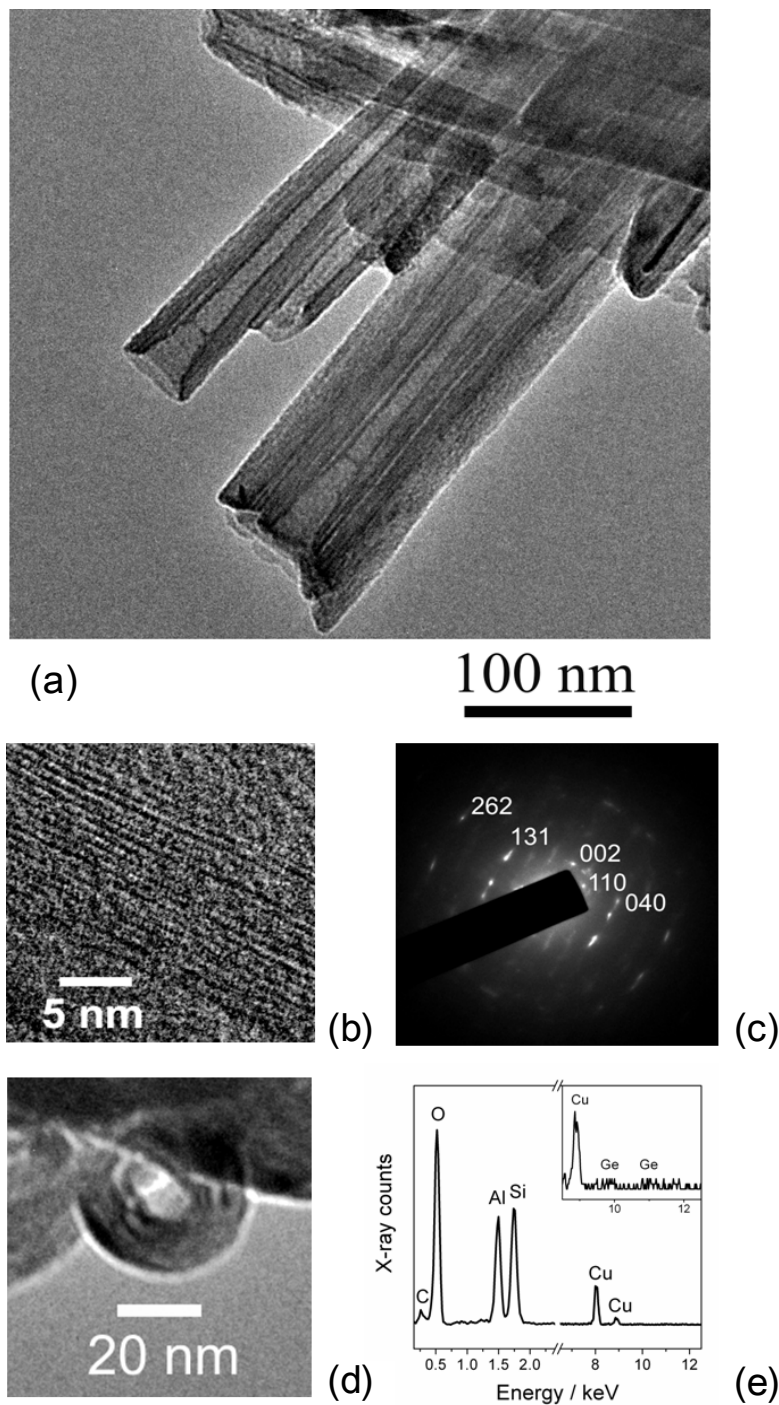
## Chapter 4: Synthesis of Al<sub>2</sub>Si<sub>2</sub>O<sub>5</sub>(OH)<sub>4</sub> (Halloysite) Nanotubes in the Presence of GeO<sub>2</sub>

### 4.1. Introduction

The conclusion from previous studies that Al<sub>2</sub>Si<sub>2</sub>O<sub>5</sub>(OH)<sub>4</sub> exhibits a strong tendency to crystallise as flat plate-like crystals of kaolinite rather than nanotubular halloysite because of the superior thermodynamic stability of kaolinite <sup>[131]</sup> has previously presented a barrier to synthesis of halloysite nanotubes in large quantities.<sup>[65]</sup> The work in this chapter was inspired by the use of substitution of Si(IV) atoms with Ge(IV) atoms to alter the curvature of nanotubes composed of a different aluminosilicate material, imogolite, Al<sub>2</sub>SiO<sub>3</sub>(OH)<sub>4</sub> (see Section 2.3.3). In this Chapter, the results of systematic substitution of a varying mole fraction (*X*) of Si(IV) with Ge(IV) in a typical kaolinite synthesis (Section 3.1.1) of 7 days duration at pH 2, 220 °C are presented for discussion. Five separate reactions with Al(OH)<sub>3</sub>, SiO<sub>2</sub> and GeO<sub>2</sub> as starting materials were performed with the mole fraction (*X*) of GeO<sub>2</sub>/[SiO<sub>2</sub> + GeO<sub>2</sub>] equal to 0, 0.05, 0.1, 0.2 and 0.5, and the solid products were collected for detailed structural and bulk analysis.

### 4.2. Structural analysis using transmission electron microscopy

Using TEM techniques, a progressive increase in curvature of the Al<sub>2</sub>Si<sub>2</sub>O<sub>5</sub>(OH)<sub>4</sub> structure was observed in the range  $0 < X < 0.2$ , such that the flat kaolinite particles observed in the absence of GeO<sub>2</sub> ( $X = 0$ ) underwent a transformation into fully-formed multiwalled nanotubes (MWNTs) by  $X = 0.2$ . These MWNTs are exemplified by the TEM image in Figure 4.1a, which shows nanotubes obtained after 7 days of hydrothermal reaction. The nanotubes are straight and fully-formed with a typical outer diameter between 40 and 60 nm, and an inner diameter of 5-15 nm with walls consisting of 25 - 40 layers. The length of the tubes can exceed 500 nm. Some tubes are larger, with an outer diameter of more than 100 nm, and display a tube-in-tube morphology with distinct outer and inner layers of growth.



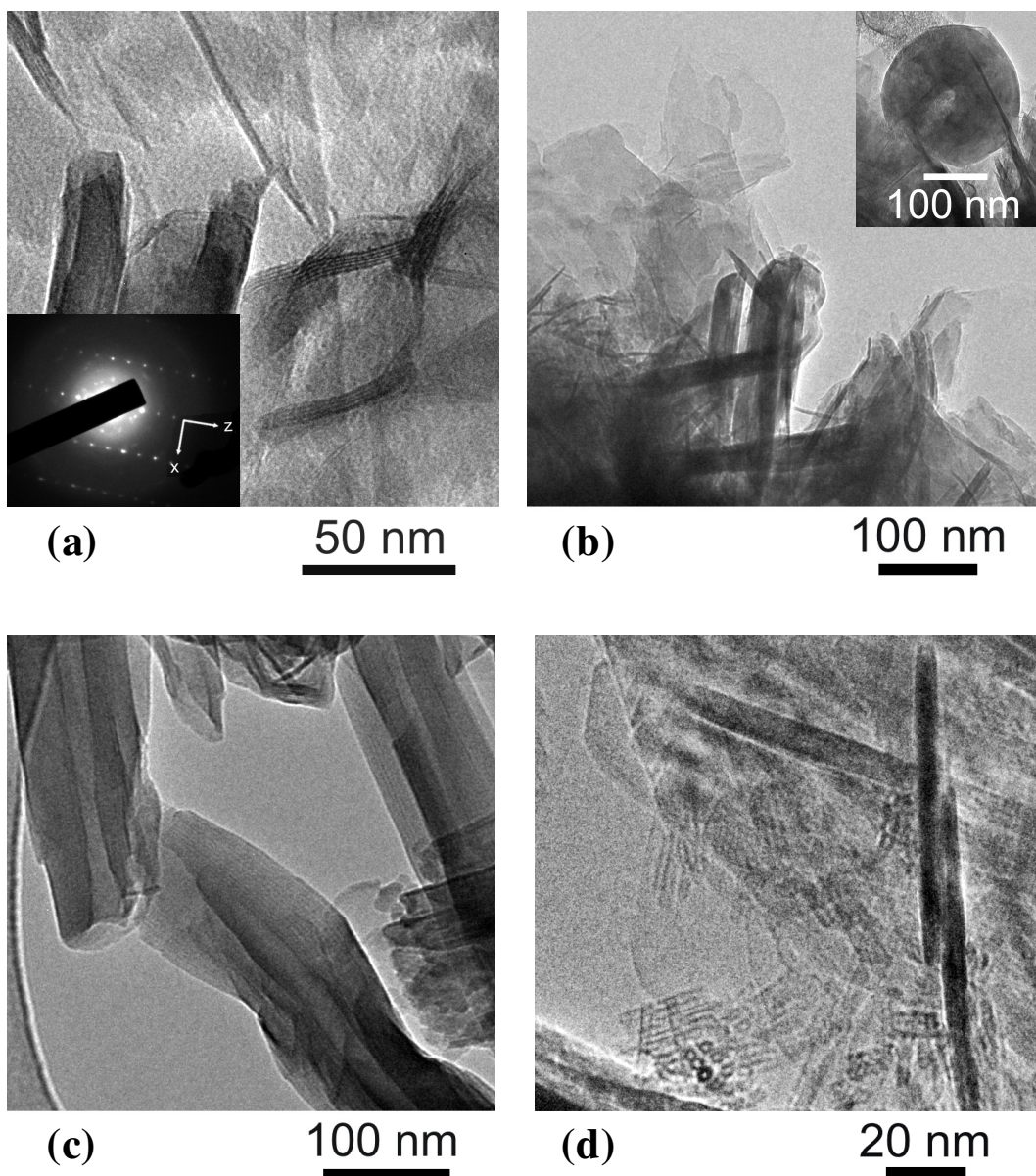
**Figure 4.1.** TEM images of (a) halloysite nanotubes synthesised by hydrothermal reaction between  $\text{Al}(\text{OH})_3$  and  $\text{SiO}_2$  at pH 2 and temperature 220 °C for 7 days in the presence of  $\text{GeO}_2$  ( $X = 0.2$ ), (b) and (c) are HRTEM and SAED images of nanotube wall, (d) is a cross-section of a nanotube and (e) is an EDX spectrum taken from the nanotube, with an enlarged inset showing 9 – 12 keV range. The minor C and Cu peaks are background signals from the TEM grid.

The HRTEM image of the wall of the nanotubes (Figure 4.1b) shows two types of characteristic lattice fringes 0.7 nm (in the radial direction of the tube) and 0.45 nm (in the axial direction of the tube). The SAED image of this area (Figure 4.1c) also shows narrow diffraction spots corresponding to the reflections from the (001) and (020) crystallographic planes of halloysite, suggesting that the nanotubes are single crystals and that the gap between the layers in the wall of the nanotubes is associated with the *c*-axis whereas the long axis of the tubes corresponds to the crystallographic *b*-axis of the halloysite unit cell.<sup>[65]</sup>

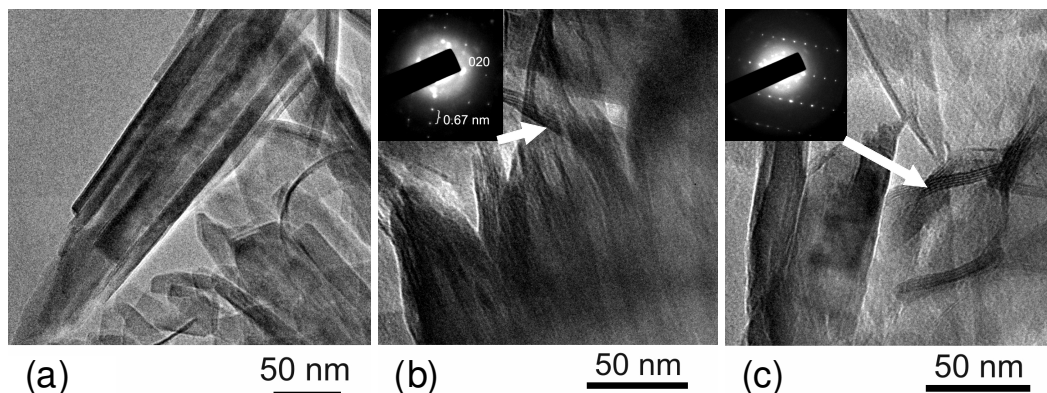
Compositional analysis using EDX spectra from a selected area containing only the MWNTs indicates that they do not contain enough Ge atoms for any peaks to be properly distinguished from the base line (see Figure 4.1e). EDX Analysis of 7 different MWNTs indicates that the nanotubes probably do not contain any more than 0.2 % Ge atoms substituted for Si. This was confirmed by separate experiments which found the EDX detection limits of Ge adsorbed on Al<sub>2</sub>Si<sub>2</sub>O<sub>5</sub>(OH)<sub>4</sub> nanotubes to be approximately 0.12 % Ge of the total moles Si + Ge (see Appendix A for determination of EDX detection limits for Ge in the Al<sub>2</sub>Si<sub>2</sub>O<sub>5</sub>(OH)<sub>4</sub> structure). The molar ratio between aluminium and silicon in the MWNTs is in the range 0.92 - 1.02. It is therefore clear that the structure of these nanotubes can be described as germanium-doped halloysite nanotubes Al<sub>2</sub>Si<sub>2-x</sub>Ge<sub>x</sub>O<sub>5</sub>(OH)<sub>4</sub>, where  $x \leq 0.004$ .

In order to understand the mechanism of halloysite nanotube formation in the presence of GeO<sub>2</sub>, the products of reaction at different Ge(IV) mole fractions, *X*, from 0 to 0.5 were systematically studied using electron microscopy. Figure 4.2 shows the typical nanostructures of aluminosilicates obtained at *X* equal to 0, 0.05, 0.1 and 0.5. At *X* = 0 (Figure 4.2a), the main product is flexible sheet-like structures of kaolinite, which typically contain 6 - 18 layers, and are up to 13 - 15 nm thick. The interlayer lattice fringes observed on TEM are approximately 0.7 nm corresponding to the *c*-spacing of crystalline kaolinite. The SAED pattern also showed reflections from the (*h*0*l*) planes of kaolinite (see inset in Figure 4.2a). It is interesting to note that the rate of crystallization of kaolinite is different for all 3 crystallographic directions. The size of a typical individual nanosheet is up to 50 nm along [100] and more than 200 nm along the [010] direction (see Figure 4.3). Thus, the synthetic kaolinite is elongated along the

crystallographic  $b$ -axis, suggesting that the rate of crystallization along each crystallographic axis decreases in the order  $r_{010} > r_{100} \gg r_{001}$ .



**Figure 4.2.** TEM and SAED images nanostructures obtained after 7 days hydrothermal reaction between Al(OH)<sub>3</sub> and SiO<sub>2</sub> in the presence of GeO<sub>2</sub> at pH 2 and temperature 220 °C. The molar fraction of added GeO<sub>2</sub> is (a)  $X = 0$ , (b)  $X = 0.05$ , (c)  $X = 0.1$  and (d)  $X = 0.5$ . The inset in (b) shows a spheroidal kaolinite particle, which comprises approximately 10 – 20 % of the total mass of kaolinite in the sample.



**Figure 4.3.** TEM and SAED images of kaolinite nanosheets obtained at  $X = 0$ , as viewed along crystallographic directions corresponding to (a) [001], (b) [100], and (c) [010]. The part of the image from which the SAED was taken is indicated by an arrow.

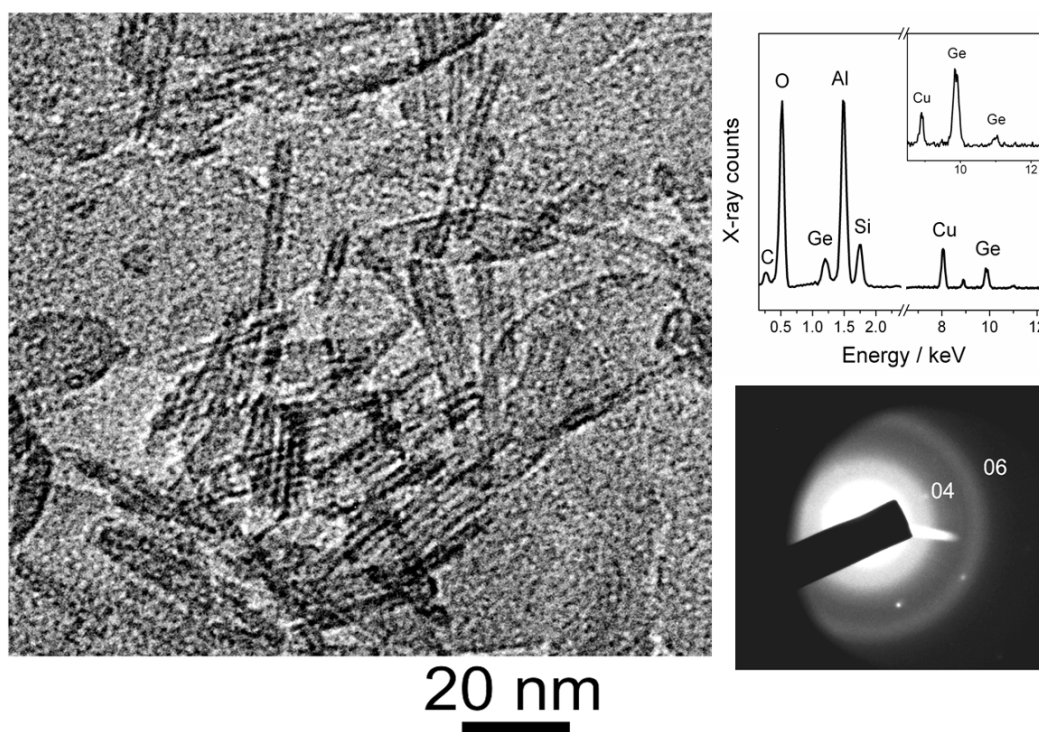
The addition of  $\text{GeO}_2$  up to  $X = 0.05$  does not significantly change the morphology of the products, except for the occasional formation of spheroidal kaolinite particles (Figure 4.2b), with a presumed layered ‘onion-like’ structure. Such particles were also observed as impurities in natural halloysite.<sup>[229]</sup> A previous study of spherical kaolinite formation concluded that spherical morphologies tend to crystallise from solutions with an over-saturated concentration of  $\text{Si(IV)}_{(\text{aq})}$  and  $\text{Al(III)}_{(\text{aq})}$  species,<sup>[230]</sup> whereas reaction at lower concentrations results in crystallisation of flat kaolinite nanostructures. Spheroidal kaolinite is also believed to be an intermediate in halloysite formation.<sup>[231]</sup>

An increase of  $X$  to the value of 0.1 results in formation of a small amount of the multiwalled nanotubes (MWNTs) with 50 – 100 nm outer diameter also corresponding to single-crystal halloysite nanotubes. Geometrically, the tubes are crooked, only partially wrapped and not well formed (Figure 4.2c). Only few isolated aggregates of nanotubes are observed by TEM, alongside kaolinite sheets which had not wrapped to become tubes.

A further increase in the amount of added  $\text{GeO}_2$  to the value  $X = 0.5$  leads to the complete disappearance of the halloysite-like MWNTs accompanied by formation of a mixture of various nanostructured aluminosilicates including small short nanotubes (Figure 4.2d). An HRTEM image of these nanotubes (Figure 4.4) indicates that their



morphology closely resembles that of the aluminogermanate imogolite-type Al<sub>2</sub>GeO<sub>3</sub>(OH)<sub>4</sub> nanotubes synthesised in the work of Levard et al.<sup>[122]</sup> The tubes are characterised by an average outer diameter of 3 nm and typical length in the range of 20 - 30 nm, similar to nanotubes previously synthesised at 95 °C.<sup>[169, 232]</sup> The walls of the nanotubes are not characterised by an apparent multilayer structure. The observed 3 nm diameter suggests that the single-walled nanotubes contain both silicon and germanium atoms, as recent combined cryogenic TEM and Small Angle X-ray Scattering (SAXS) experiments show that pure single-walled Al<sub>2</sub>GeO<sub>3</sub>(OH)<sub>4</sub> nanotubes have a larger average diameter close to 3.5 nm.<sup>[171, 232]</sup> The SAED image of the obtained nanotubes (Figure 4.4) shows concentric rings related to diffraction from (04) and (06) crystallographic planes of two-dimensional aluminogermanate (Al<sub>2</sub>GeO<sub>3</sub>(OH)<sub>4</sub>) nanotubes<sup>[233]</sup> (a weak (71) reflection was also observed, see Table A1 in Appendix A for indexing of diffraction reflections).

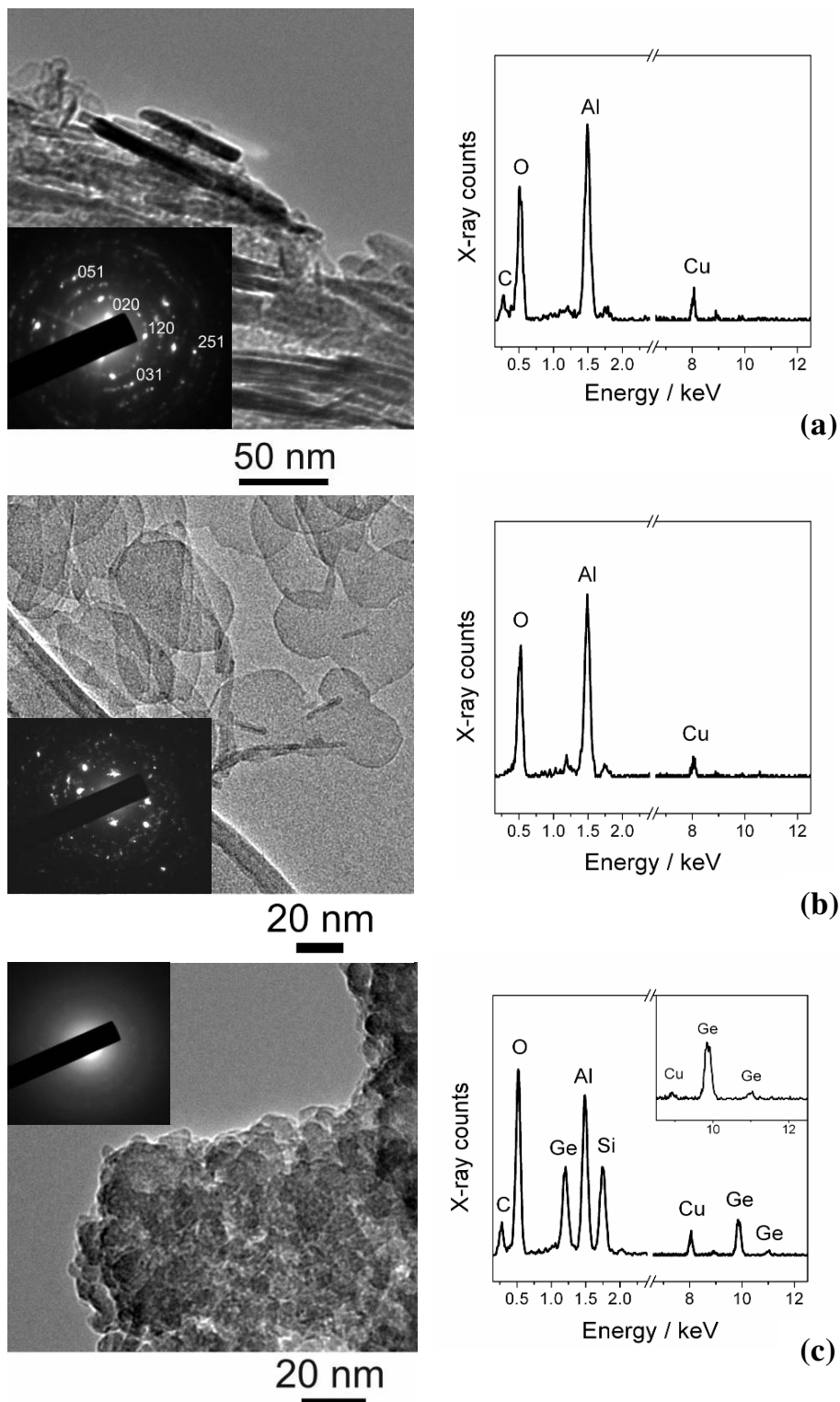


**Figure 4.4.** HRTEM, SAED images and EDX spectrum of Ge-imogolite nanotubes synthesised at the mole fraction of added GeO<sub>2</sub>  $X = 0.5$ . The EDX spectrum is influenced by the background presence of  $\gamma$ -AlOOH nanoplates (boehmite) showing an excess of aluminium and oxygen.

Although the exact chemical composition of the synthesized single-walled nanotubes is difficult to determine using an EDX spectrum (Figure 4.4) due to strong interference from nearby  $\gamma$ -AlOOH particles, the crystal structure is believed to correspond to germanium doped  $\text{Al}_2\text{Si}_{1-x}\text{Ge}_x\text{O}_3(\text{OH})_4$  nanotubes, where  $x$  is approximately equal to 0.35. It is interesting to observe that these nanotubes can form at 220 °C, compared to the original synthesis of imogolite-like  $\text{Al}_2\text{GeO}_3(\text{OH})_4$  nanotubes obtained from diluted solutions at 95 °C,<sup>[122]</sup> especially as the non-doped imogolite  $\text{Al}_2\text{SiO}_3(\text{OH})_4$  is metastable with respect to both halloysite and kaolinite.<sup>[234]</sup>

The formation of both multilayered halloysite nanotube and single-walled imogolite-type aluminogermanate nanotubes is also accompanied by the formation of additional nanostructured reaction products, which are shown in Figure 4.5. Thin plate-like (nanosheets) and rod-like (nanorods) structures (Figure 4.5a and b) appear for all 0 - 0.5 mole fractions of GeO<sub>2</sub>,  $X$ . According to the SAED images, the reflection of both nanosheets and nanorods can be indexed to  $\gamma$ -AlOOH, boehmite (see Table A1 in Appendix A).<sup>[235]</sup> The EDX data also confirm that both nanorods and nanosheets contain exclusively Al and O, in a 1:1.8 molar ratio. The  $\gamma$ -AlOOH nanosheets consist of 100 - 300 nm sized plates with a pseudohexagonal shape. The rod-like particles are characterised by 5 nm diameter and 100 - 300 nm length. It is probable that the larger flaky particles are  $\gamma$ -AlOOH rod-like precipitates that have grown into larger crystals in the hydrothermal HCl environment at low pH.<sup>[236]</sup> The total number of these particles, and the number of platy particles vs. rods, increases with  $X$ . It has been shown that the rapid precipitation of  $\gamma$ -AlOOH from Al(III) solutions at low pH and above 200 °C is the first step in the formation of kaolinite, and aqueous Si(IV) species react with the  $\gamma$ -AlOOH surface.<sup>[113]</sup> Therefore, the presence of  $\gamma$ -AlOOH in the reaction products is probably associated with hydrolysis of unreacted Al(III) from the starting materials.

Another relatively common side product of hydrothermal reaction, observed for all values of  $X$ , are spheroidal nanoparticles with an average diameter 5 - 10 nm (Figure 4.5c). Compositional analysis using the EDX spectrum of spheroidal particles synthesised at  $X = 0.5$  indicates that they contain germanium, silicon and aluminium atoms. The SAED image also shows no specific diffractions from crystallographic planes, confirming an amorphous nature of these germanium enriched aluminosilicates.



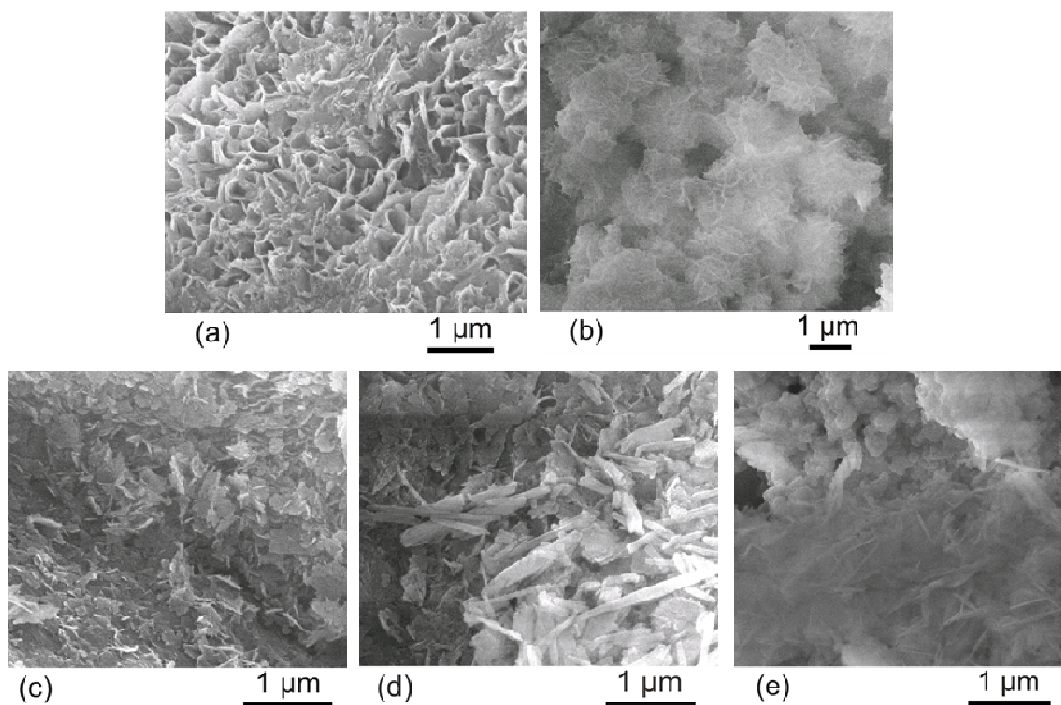
**Figure 4.5.** TEM and SAED images together with EDX spectra of typical nanostructured side products obtained in the hydrothermal reaction at  $X = 0.5$ , namely  $\text{AlOOH}$  (boehmite) (a) nanorods, (b) nanoplates and (c) amorphous Ge-enriched aluminosilicate nanoparticles.

Since the number of OH groups present is unknown, these nanoparticles can be represented by  $a\text{SiO}_2 \cdot b\text{GeO}_2 \cdot c\text{Al}_2\text{O}_3$  and the area under the EDX peaks suggests that  $a = c = 1$ , and  $b = 0.1$  when  $X = 0.5$ . The value of  $b$  is dependent on  $X$ ;  $b = 0.03$  when  $X = 0.2$ , but  $a$  and  $c$  are approximately equal for all values of  $X$ . Although the exact structure of these nanoparticles is unknown, they are formed alongside imogolite-type nanotubes and may bear some structural similarities to the amorphous aluminogermanates synthesized by Levard et al. from solutions with lower hydrolysis (OH/Al) ratios.<sup>[169, 237]</sup> Their NMR and EXAFS (Extended X-ray Fine Structure Spectroscopy) results suggest a small (< 7%) fraction of tetrahedrally coordinated Al, together with a lower number of Al atoms in the second coordination shell of Ge than in Ge-imogolite. They propose a linkage between tetrahedrally coordinated Al and polymerized Ge-O-Ge chains. Further analysis of the  $X = 0.5$  sample using NMR and EXAFS techniques would be useful in quantifying the Al and Ge coordination environments, and the similarity of the amorphous nanoparticles to the Ge-imogolite structure.

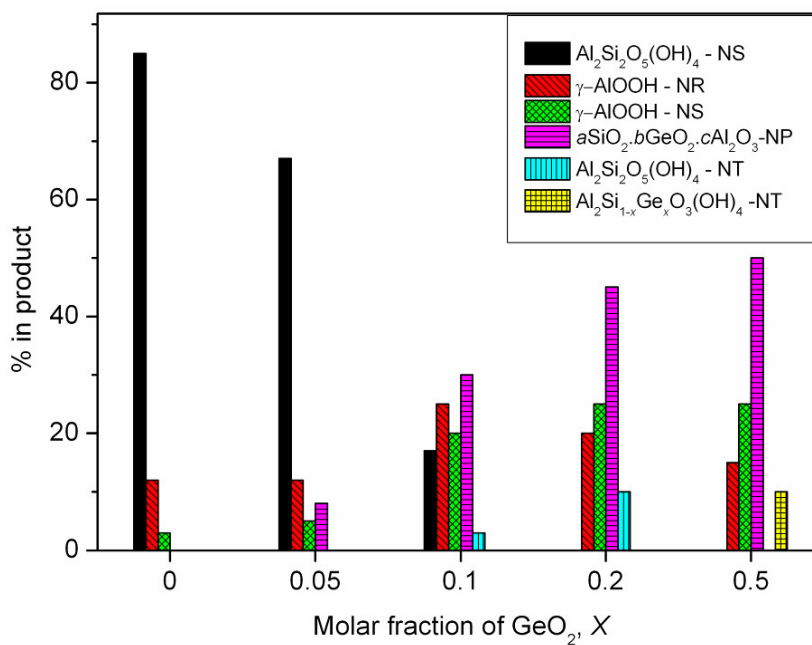
### 4.3. Bulk compositional analysis using electron microscopy and ICP

It is clear from the electron micrographs in the previous section that the products of synthesis at all values of  $X$ , the mole fraction GeO<sub>2</sub>, are not pure phases but are, in fact, a mixture of different crystalline and non-crystalline materials. Using the large collection of more than 20 TEM and SEM images taken of each sample and the ICP (Inductively-Coupled Plasma atomic emission spectroscopy) technique which measures relative amounts of each type of atom in the bulk sample, it is possible to estimate the bulk composition of each product at different  $X$ . As this is a complex, multi-phase mixture, x-ray diffraction techniques are not very useful in this instance.

Comprehensive analysis of all the TEM and SEM images (see Figure 4.6 for representative SEM images) of the samples obtained at different  $X$  allows estimation of the relative amount of each characteristic nanostructure, which is shown in Table 4.1 alongside the ICP results, and BET surface area and pore volumes derived from N<sub>2</sub> adsorption isotherms (see Section 4.4). The estimated percentages of each nanostructure from Table 4.1 are shown graphically in Figure 4.7 as a function of  $X$ .

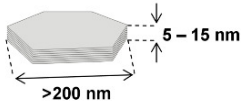
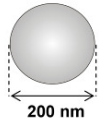
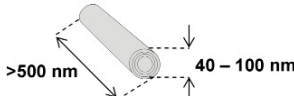
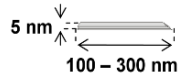
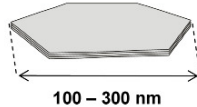

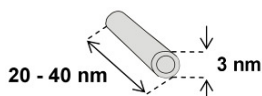


**Figure 4.6.** SEM images of products obtained at (a)  $X = 0$ , (b)  $X = 0.05$ , (c)  $X = 0.1$ , (d)  $X = 0.2$ , (e)  $X = 0.5$ . Some  $\text{Al}_2\text{Si}_2\text{O}_5(\text{OH})_4$  nanotubes are visible at the surface in image (d).



**Figure 4.7.** Distribution of hydrothermal reaction products as a function of molar fraction of added  $\text{GeO}_2$ , X. Abbreviations NS = nanosheets, NR = nanorods, NP nanoparticles, NT = nanotubes.

**Table 4.1.** Distribution of morphologies of typical nanostructures (estimated from TEM data) observed in the products of hydrothermal reaction at GeO<sub>2</sub> mole fraction,  $X$  varied between 0 and 0.5. The schematic images show the typical geometry and dimensions of nanostructures.

Formula + Morphology	Shape + Dimensions	Distribution in wt % at				
		$X = 0$	0.05	0.1	0.2	0.5
Al <sub>2</sub> Si <sub>2</sub> O <sub>5</sub> (OH) <sub>4</sub> NS*		85	67	17	-	-
Al <sub>2</sub> Si <sub>2</sub> O <sub>5</sub> (OH) <sub>4</sub> NSp		-	8	-	-	-
Al <sub>2</sub> Si <sub>2</sub> O <sub>5</sub> (OH) <sub>4</sub> MWNT		-	-	3	10	-
γ-AlOOH NR		12	12	25	20	15
γ-AlOOH NS		3	5	20	25	25
$a$ SiO <sub>2</sub> · $b$ GeO <sub>2</sub> · $c$ Al <sub>2</sub> O <sub>3</sub> NP		-	8	30	45	50
Al <sub>2</sub> Si <sub>1-x</sub> Ge <sub>x</sub> O <sub>3</sub> (OH) <sub>4</sub> SWNT		-	-	-	-	10
BET Specific surface area (m <sup>2</sup> g <sup>-1</sup> )		90	204	285	301	328
Total Specific pore volume (cm <sup>3</sup> g <sup>-1</sup> )		0.38	0.85	1.20	0.66	0.35
Molar ratio (Al:Si:Ge) in the solid products	Al	0.34:	0.38:	0.47:	0.45:	0.36:
	Si	0.66:	0.61:	0.52:	0.53:	0.59:
	Ge	0.0	0.007	0.009	0.02	0.05

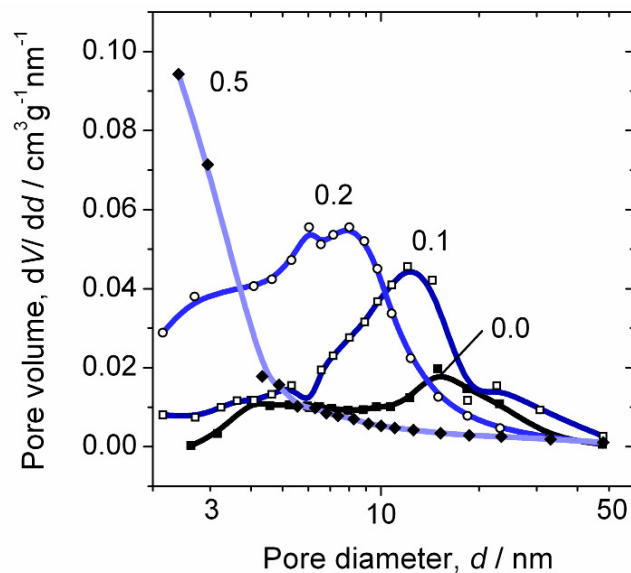
Apparently, as the mole fraction of added GeO<sub>2</sub> increases, the precipitation of all Al<sub>2</sub>Si<sub>2</sub>O<sub>5</sub>(OH)<sub>4</sub> morphologies decreases in favour of amorphous  $a$ SiO<sub>2</sub>· $b$ GeO<sub>2</sub>· $c$ Al<sub>2</sub>O<sub>3</sub> nanoparticles. At the same time, however, the remaining Al<sub>2</sub>Si<sub>2</sub>O<sub>5</sub>(OH)<sub>4</sub> shows an

increased tendency to precipitate as nanotubes (halloysite) rather than nanosheets of kaolinite. When  $X$  is approaching 0.5 the formation of imogolite-type aluminogermanate SWNTs occurs instead. Nanostructured  $\gamma$ -AlOOH (both nanosheets and nanorods) are observed at all values of  $X$ .

The ICP results in Table 4.1, which show the average molar ratio between the elements Al, Si and Ge in the bulk solid products, give a more complete picture of the chemical composition of the bulk samples, and how this differs from the starting materials. An increase in  $X$  from 0 to 0.5 results in an almost linear increase in germanium content in the solid products. However, the values of Ge/(Ge + Si) ratio in the bulk solid products are much lower than  $X$  suggesting that most of the original GeO<sub>2</sub> remains dissolved in solution after 7 days rather than contributing to the structure of the solid products. It was also found that at all  $X$ , the Al/(Si+Ge) ratio in solid products is lower than the “initial” Al/(Si+Ge) ratio in reactants, which was selected to be equal to one. This reflects the fact that under the reaction conditions (pH 2 and 220 °C) the solubility of Al (III) is higher than Si (IV) (see Chapter 2.3.1) The excess of Si in the precipitates was not accounted for by the structures observed with SEM and TEM (Table 4.1 and Figure 4.7) suggesting that the samples also contain an unaccounted amorphous SiO<sub>2</sub> phase which was difficult to separately observe and identify by TEM and EDX. The values of the Al/(Si+Ge) ratio are in the range 0.5 – 0.6 at  $X = 0, 0.05$  and  $0.5$ , but are very close to 1 at  $X = 0.1$  and  $0.2$ , in which halloysite nanotubes are formed, suggesting that these samples contain less amorphous SiO<sub>2</sub>.

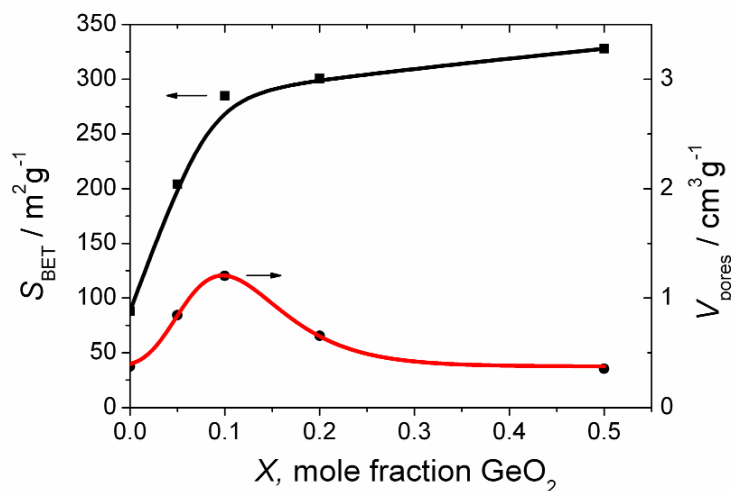
#### 4.4. Bulk characterisation of pore structure by nitrogen adsorption

To investigate the pore structure of the samples, bulk analysis was performed using nitrogen adsorption in conjunction with BET and BJH analysis. Figure 4.8 shows the BJH pore-size distributions of samples obtained at different  $X$ . According to these data, the mean pore size of the product decreases as the mole fraction of added GeO<sub>2</sub> increases. An increase in  $X$  is also accompanied by a decrease in the volume of pores with diameter greater than 12 nm, associated with the reduction of number of loosely-packed aggregates of kaolinite nanosheets, which form large mesopores.



**Figure 4.8.** BJH pore size distributions for aluminosilicate samples obtained under addition of  $\text{GeO}_2$ . The numerical labels correspond to  $X$ , the mole fraction of added  $\text{GeO}_2$ .

The substantial increase in the volume of pores with diameter less than 5 nm at  $X > 0.2$  is probably caused by pores between an increasing number of  $a\text{SiO}_2 \cdot b\text{GeO}_2 \cdot c\text{Al}_2\text{O}_3$  nanoparticles as well as by pores inside and between imogolite-type aluminogermanate nanotube aggregates. The large volume of pores sized between 6 and 9 nm at  $X = 0.2$  can be explained by the presence of halloysite intra- and intertubular pores (BJH has a tendency to underestimate small mesopore sizes).<sup>[36]</sup>



**Figure 4.9.** BET surface area,  $S_{\text{BET}}$  (■) and total pore volume,  $V_{\text{pores}}$  (●) of nanostructured aluminosilicates hydrothermally prepared at different mole fractions of added  $\text{GeO}_2$  ( $X$ ).

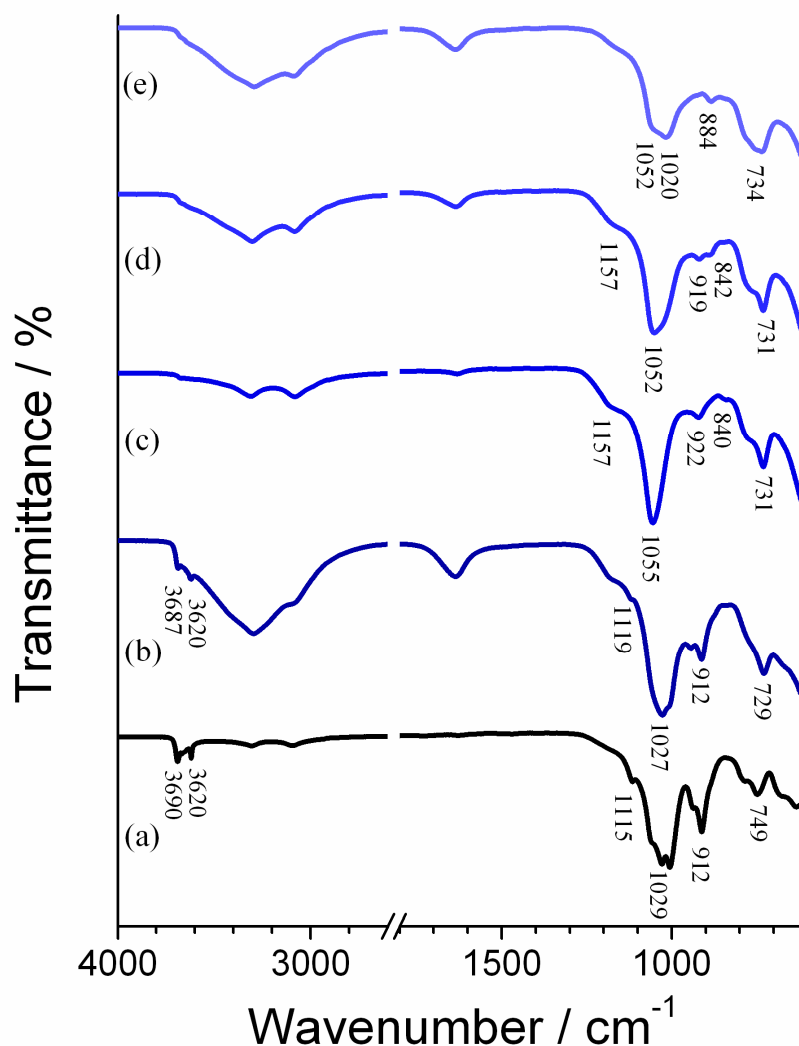


The addition of GeO<sub>2</sub> to the starting materials results in a non-linear increase in the BET specific surface area of the bulk sample from 89.7 m<sup>2</sup>g<sup>-1</sup> for pure kaolinite to 327.8 m<sup>2</sup>g<sup>-1</sup> for the product mixture obtained at  $X = 0.5$  (Figure 4.9). The sharp rise in the surface area at low  $X$  (between 0 and 0.1) can be attributed to the replacement of most of the Al<sub>2</sub>Si<sub>2</sub>O<sub>5</sub>(OH)<sub>4</sub> nanosheets with 5 - 10 nm diameter amorphous  $a\text{SiO}_2 \cdot b\text{GeO}_2 \cdot c\text{Al}_2\text{O}_3$  nanoparticles (Table 4.1), or amorphous SiO<sub>2</sub> particles, which have a much larger surface area. The amount of GeO<sub>2</sub> added does not have such a strong influence on the adsorption total pore volume, but the rise and subsequent decrease in pore volume around  $X = 0.1$  may result from a greater diversity of particle sizes than in, for example the  $X = 0$  sample (which mainly contains larger kaolinite particles), or the  $X = 0.5$  sample (which mainly contains smaller particles). A wider pore-size distribution may disrupt close-packing of particles and create larger pores between them.

#### 4.5. Fourier-transform infrared spectroscopy

FTIR spectroscopy of the products for all values of  $X$  (Figure 4.10) showed that as  $X$  increases, many of the peaks present when  $X = 0$  (synthetic kaolinite) in both the lattice ( $< 1200 \text{ cm}^{-1}$ ) and hydroxyl-stretching ( $3000 - 4000 \text{ cm}^{-1}$ ) regions are replaced with peaks at different frequencies. When  $X \geq 0.1$  the 912 and 936 cm<sup>-1</sup> Al-OH bending modes characteristic of kaolinite<sup>[113]</sup> disappear and are replaced by a new band at  $\approx 920 \text{ cm}^{-1}$ , which can be assigned to Al-O-Ge deformations.<sup>[238]</sup> Additionally, the Si-O stretching modes at 1029 and 1115 cm<sup>-1</sup> characteristic of the  $X = 0$  product<sup>[239]</sup> merge and develop a shoulder peak at  $\approx 1020 - 1030 \text{ cm}^{-1}$  characteristic of an increasing number of tetrahedral asymmetric Si-O-Ge stretching modes<sup>[240, 241]</sup> occurring in the amorphous  $a\text{SiO}_2 \cdot b\text{GeO}_2 \cdot c\text{Al}_2\text{O}_3$  nanoparticles, which are relatively numerous when  $X \geq 0.1$ . The additional band at 884 cm<sup>-1</sup> under  $X = 0.5$  can be assigned to Ge-O-Ge vibrations,<sup>[242]</sup> which presumably occur in the amorphous nanoparticles, since the imogolite-like Al<sub>2</sub>Ge<sub>1-x</sub>Si<sub>x</sub>O<sub>3</sub>(OH)<sub>4</sub> nanotubes consist of a dioctahedral gibbsite sheet in which the inner surface is bonded with isolated Q<sub>3</sub>Al (tri-alumina substituted silicate or germanate) units, and therefore do not contain polymerized Si or Ge.<sup>[243, 244]</sup> None of the vibrations characteristic of germanium-substituted imogolite observed by Wada et

al.<sup>[233]</sup> were seen under  $X = 0.5$  (Figure 4.10e), but this may be due to the small percentage by weight of these  $\text{Al}_2\text{Ge}_{1-x}\text{Si}_x\text{O}_3(\text{OH})_4$  nanotubes in the products (Table 4.1).



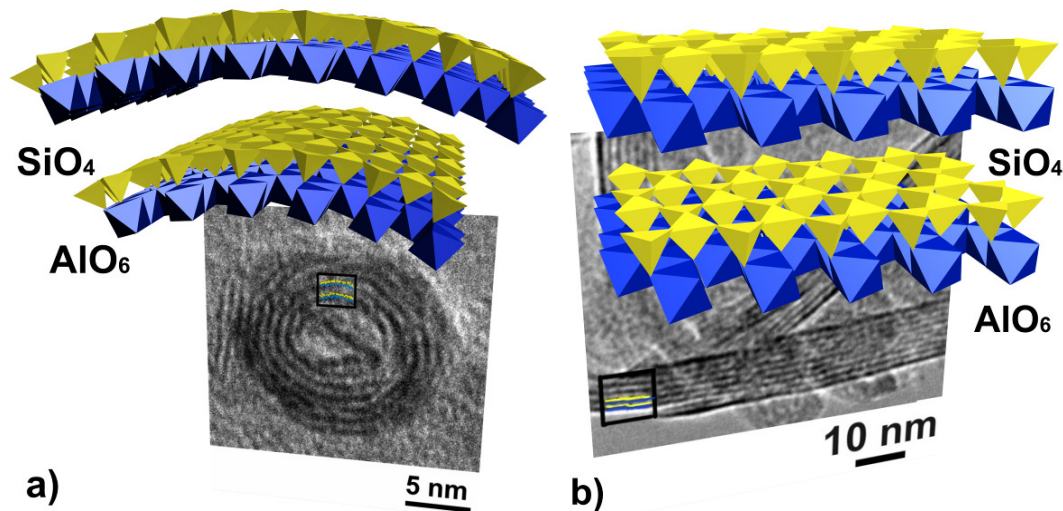
**Figure 4.10.** FTIR spectra of aluminosilicate products synthesised at  $X$  equal to (a) 0, (b) 0.05 (c) 0.1, (d) 0.2, and (e) 0.5.

The band at  $\approx 840 \text{ cm}^{-1}$  for the products where  $X = 0.1$  and  $0.2$  may be assigned to a Si-O-Al deformation in halloysite,<sup>[245]</sup> but is extremely weak. The complex stretching band at  $3620 - 3690 \text{ cm}^{-1}$  characteristic of the  $\nu_1$ -  $\nu_4$  modes of kaolinite hydroxyl groups<sup>[246]</sup> disappears for  $X > 0.05$ , suggesting a large decrease in the amount of kaolinite

nanosheets present, which supports the distribution of morphologies observed by TEM (Figure 4.7). The band at  $\approx 730\text{ cm}^{-1}$  corresponding to Al-OH vibrations characteristic of  $\gamma$ -AlOOH<sup>[247]</sup> increases in strength when  $X$  increases from 0.05 to 0.1, corresponding to the large increase in the number of precipitated  $\gamma$ -AlOOH nanosheets and nanorods observed between these two values.

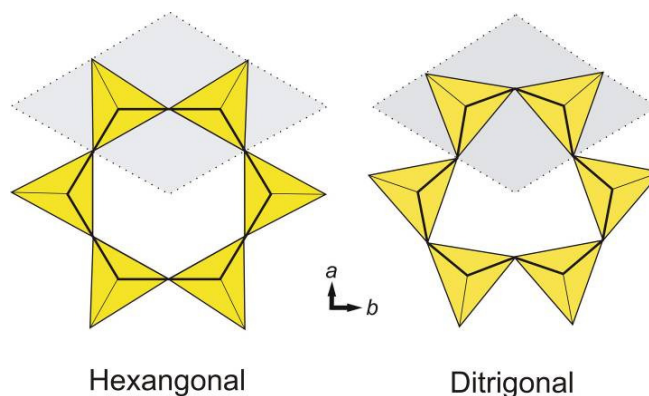
#### 4.6. Discussion of the synthesis mechanism

As discussed in the literature review (section 2.3), there are many different driving forces for the curving of flat nanosheets to form multilayered nanotubes. In the case of the halloysite structure, the internal layer strain caused by the geometric mismatch between the octahedral Al(III)O<sub>6</sub> gibbsite sheet and the tetrahedral SiO<sub>4</sub> sheet, which has larger unit cell dimensions, is believed to be the driving force for the sheet curvature to form multilayered halloysite nanotubes (Figure 4.11).<sup>[65]</sup>



**Figure 4.11.** Schematic drawing of the crystal structures of (a) halloysite, and (b) kaolinite as a combination of AlO<sub>6</sub> octahedra with SiO<sub>4</sub> tetrahedra, together with accompanying HRTEM images. The solid rectangle in the HRTEM image of the halloysite nanotube shows the area corresponding to the drawing. OH groups and crystallographic water between layers in both halloysite and kaolinite are not shown for clarity.

The most stable arrangement of the SiO<sub>4</sub> sheet in terms of Si-O repulsion is hexagonal, but this has lattice parameters of  $a = 5.29 \text{ \AA}$  and  $b = 9.16 \text{ \AA}$ ,<sup>[248]</sup> which do not match the AlO<sub>6</sub> lattice parameters of  $a = 5.07 \text{ \AA}$  and  $b = 8.66 \text{ \AA}$ .<sup>[130]</sup> Therefore, the SiO<sub>4</sub> tetrahedra in the structure rotate slightly towards a ditrigonal arrangement (Figure 4.12) and a compromise is reached between minimising the dimensional misfit and reducing the Si-O repulsion. Thus, the lattice parameters of halloysite and kaolinite are  $a = 5.14 \text{ \AA}$  and  $b = 8.93 \text{ \AA}$ ,<sup>[65]</sup> and the sheet experiences internal strain in both the  $a$  and  $b$  directions.

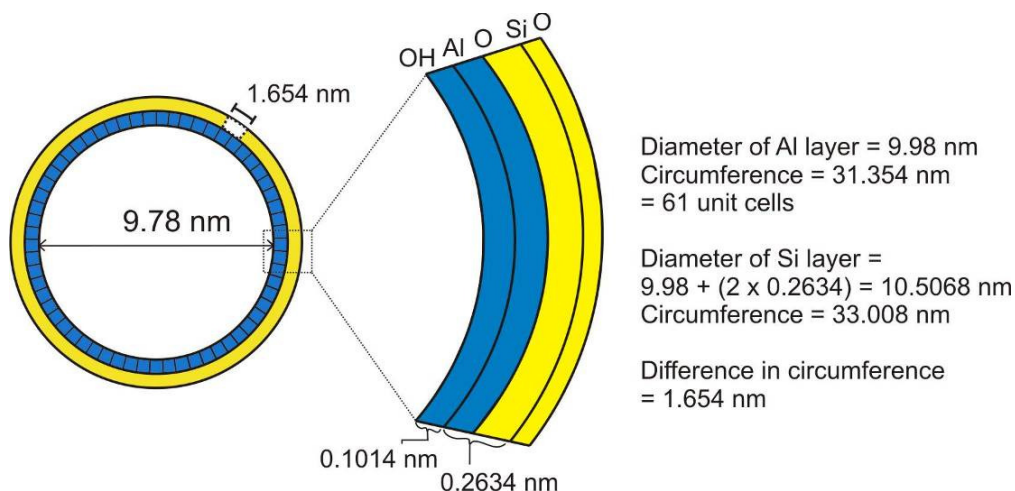


**Figure 4.12.** Schematic plan view diagram of rotation of SiO<sub>4</sub> tetrahedra in Al<sub>2</sub>Si<sub>2</sub>O<sub>5</sub>(OH)<sub>4</sub> to reduce the  $a$  and  $b$  lattice parameters. The shaded grey area represents the unit cell.

The scrolling of multiwalled halloysite observed both in nature and in the  $X = 0.2$  Ge(IV) sample occurs around the  $b$ -axis, rather than the  $a$ -axis.<sup>[101, 248]</sup> Nanotubes of typical inner diameter  $\approx 10 \text{ nm}$  and outer diameter  $\approx 50 \text{ nm}$  are observed to form. By considering the scrolling of a single-layer sheet of Al<sub>2</sub>Si<sub>2</sub>O<sub>5</sub>(OH)<sub>4</sub> on the inner surface of the tube, an explanation can be advanced as to why such scrolling is observed.

When an Al<sub>2</sub>Si<sub>2</sub>O<sub>5</sub>(OH)<sub>4</sub> sheet with the lattice parameters of kaolinite is scrolled around  $b$  to form a tube  $\approx 10 \text{ nm}$  in diameter, typical of the inner wall of a halloysite nanotube, containing 61 unit cells, it can be shown that the SiO<sub>4</sub> layer requires an additional 1.654 nm length along the  $a$  axis (Figure 4.13). This extra required length could be partly added by relaxing the tetrahedral rotation to increase the  $a$  dimension by  $0.15 \text{ \AA}$  per unit cell, however, this would also increase the  $b$  dimension, which would be energetically unfavourable as it would increase the geometric mismatch strain along the axis of the

tube. The fact that the lattice parameters of halloysite (tubes) and kaolinite (sheets) do not differ measurably supports this argument,<sup>[101]</sup> suggesting that the sheet probably does not undergo tetrahedral relaxation (towards a hexagonal SiO<sub>4</sub> arrangement) during scrolling to relieve internal strain as previously suggested.<sup>[130]</sup>



**Figure 4.13.** Schematic diagram showing extra length required in silicate sheet to form the inner layer of a tube almost 10 nm in diameter. The internal dimensions of the sheet are obtained from reference.<sup>[130]</sup>

The extra length could also be added through inclusion of some GeO<sub>4</sub> unit cells in the SiO<sub>4</sub> layer, with lattice parameter  $a \approx 6.1 \text{ \AA}$ , which is approximately  $0.9 \text{ \AA}$  larger than SiO<sub>4</sub>.<sup>†</sup> For this to occur, a 30 % atomic substitution of SiO<sub>4</sub> with GeO<sub>4</sub> would be necessary for the inner layer of the tube to curve to form a tube 10 nm in diameter. However, halloysite consists of many layers, and if the tube contained additional layers until an outer layer with diameter of 50 nm, then only 6 wt% substitution of SiO<sub>4</sub> with GeO<sub>4</sub> would be necessary for this outer layer to curve. So, on average, the nanotube would need to contain 18 % of SiO<sub>4</sub> substituted with GeO<sub>4</sub>. Although EDX (Figure 4.1)

<sup>†</sup> The  $a$  parameter for a hexagonal SiO<sub>4</sub> or GeO<sub>4</sub> lattice can be calculated using the

formula  $a = \frac{4}{3}\sqrt{6}l$ , where  $l$  is the bond length.<sup>[248]</sup> Using an estimated Ge-O bond length

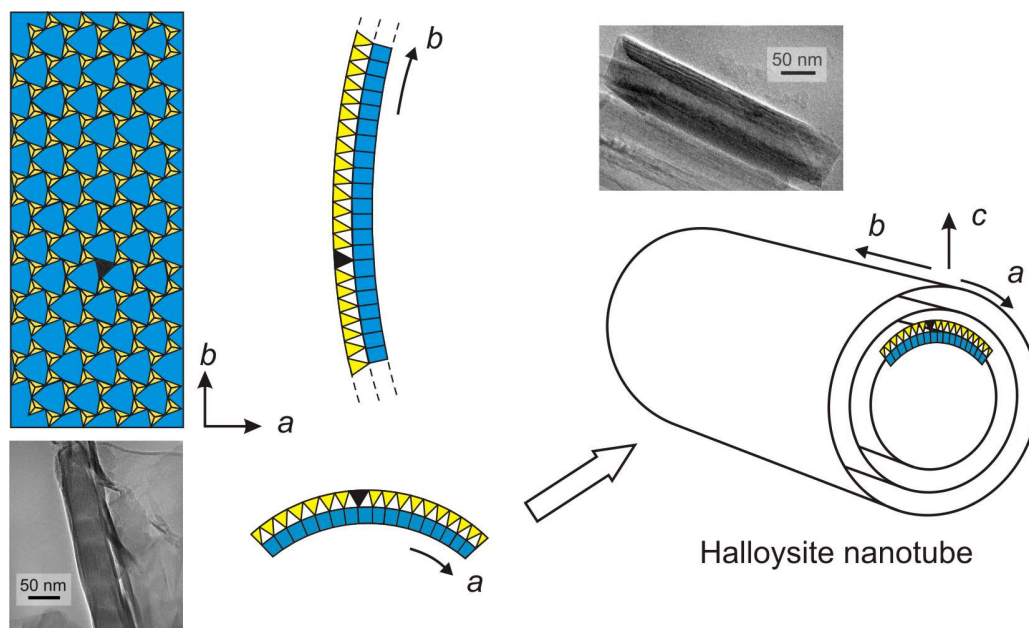
of  $1.89 \text{ \AA}$  gives  $a = 6.173 \text{ \AA}$ . But since the geometry deviates from hexagonal towards trigonal the true  $a$  value will be a little smaller.

of the  $X = 0.2$  nanotubes shows that this is not the case, it is possible to see how even a much smaller substitution of Si(IV) with Ge(IV) could be sufficient to stimulate scrolling of the nanosheets.

As the SiO<sub>4</sub> tetrahedra form an interconnected network in halloysite, the stress effect associated with substitution of Si(IV) with a Ge(IV) atom in the layer would be larger than assumed in the above model (Figure 4.13) since, due to rotation of the interconnected tetrahedra, this stress could easily propagate to the second atomic neighbours, increasing the circumference of the Si(IV) layer by more than  $\approx 0.9$  Å per unit cell. Also, the presence of Si(IV) vacancies in the structure could aid the curving of the halloysite structure, since a Si(IV) vacancy occupies more space than a SiO<sub>4</sub> tetrahedron due to repulsion of neighbouring negatively charged O atoms.<sup>[249]</sup> The number of these Si(IV) vacancies may be increased in the presence of a 0.1 – 0.2 mole fraction GeO<sub>2</sub> ( $X$ ): without the ability to accurately quantify the Si(IV) content of the tubes, and compare them with the kaolinite nanosheets it is not possible to prove this conclusively, but it is interesting to note that in the samples where some tubular halloysite is formed, the Al/(Si+Ge) ratio of the bulk products is higher (Table 4.1), or in other words fewer Si(IV) atoms are precipitated in the solid product.

Apparently, halloysite usually scrolls around the crystallographic  $b$  axis rather than  $a$ ,<sup>[98, 99]</sup> which could be associated with the difference in the relative rates of crystallization of kaolinite nanosheets along these axes. The crystallization rate of kaolinite along  $b$  ([010] direction) is much greater than along  $a$  ([100] direction) (see Figure 4.3), resulting in the elongated shape of the growing nanosheets which have a characteristic size  $\gg 100$  nm along  $b$  and  $< 100$  nm along the  $a$  axis. Since the length of the nanosheet in the [010] direction is larger than in the [100] direction, the inclusion of a GeO<sub>4</sub> tetrahedron or a Si(IV) vacancy and the distribution of stress in both directions would cause a stronger bending of the shorter side compared to the longer side (figure 4.14). As a result, the axial direction of the synthesized nanotubes coincides with the direction of fastest growth of the nanosheet precursor, whereas, for example, in the case of titanate nanotubes, the direction of fastest growth coincides with the direction tangential to the nanotube surface.<sup>[250]</sup> This illustrates possible differences in the driving force for halloysite and titanate nanosheet curvature, i.e. an imbalance in the width of

the nanosheet layers in the case of titanate nanotubes<sup>[97]</sup> (see Section 2.3.2 page 24) and uneven stress distribution on the two opposing (aluminium- and silicon-rich) sides of kaolinite nanosheets in the case of halloysite nanotubes.



**Figure 4.14.** Schematic diagram showing how inclusion of a  $\text{GeO}_4$  tetrahedron (shown in black) may cause stronger bending along the  $a$  axis rather than along the  $b$  axis for a growing  $\text{Al}_2\text{Si}_2\text{O}_5(\text{OH})_4$  nanosheet elongated in the  $b$  dimension. Several layers bent along  $a$  form a halloysite nanotube. The TEM image on the left corresponds to an elongated nanosheet viewed down along the  $c$ -axis as shown in the top diagram, and the TEM image on the right shows a halloysite nanotube.

A higher fraction of Ge(IV) in the starting materials ( $X = 0.5$ ) completely changes the structure of the crystalline aluminosilicate materials formed by the reaction, through the inclusion of up to 35 %  $\text{GeO}_4$  into the structure leading to the formation of a different phase,  $\text{Al}_2\text{Si}_x\text{Ge}_{1-x}\text{O}_3(\text{OH})_4$ , which is related to single-walled imogolite nanotubes. It appears that upon incorporation of larger amounts of Ge(IV) into the aluminosilicates, the single-walled imogolite-type structure is favored over a multiwalled halloysite-type structure, and this raises an interesting point, namely whether an increasing presence of Ge(IV) can induce a “switch over” in structure from the less curved  $\text{Al}_2\text{Si}_{2-x}\text{Ge}_x\text{O}_5(\text{OH})_4$  ( $x < 0.004$ ) multiwalled halloysite-type nanotubes to the smaller, more curved imogolite-type single or double walled nanotubes  $\text{Al}_2\text{Si}_{1-x}\text{Ge}_x\text{O}_3(\text{OH})_4$  ( $x \approx 0.35$ ).

## 4.7. Conclusions

The partial substitution of  $\text{GeO}_2$  for  $\text{SiO}_2$  in a typical hydrothermal synthesis of kaolinite at  $\text{pH}=2$  and a temperature of  $220\text{ }^\circ\text{C}$  leads to an increased tendency of  $\text{Al}_2\text{Si}_2\text{O}_5(\text{OH})_4$  to crystallise as tubular halloysite rather than planar kaolinite. As the molar fraction of added  $\text{GeO}_2$  ( $X$ ) is increased from 0 to 0.2, a progressive change in morphology of the re-crystallized layered  $\text{Al}_2\text{Si}_2\text{O}_5(\text{OH})_4$  is observed in the sequence kaolinite nanosheets, spheroidal kaolinite, halloysite nanotubes. Nanotubular halloysite is formed at  $X$  in the range 0.1 - 0.2 and is characterised by a multilayered wall structure with typical internal diameter 5-15 nm and average length ca. 1000 nm. The nanotubes do not contain germanium in detectable quantities, but up to 0.2 %  $\text{GeO}_4$  substitution for  $\text{SiO}_4$  tetrahedra may occur, suggesting that the scrolling of the nanosheets could be attributed to a slight increase in the crystallographic misfit with  $\text{AlO}_6$  octahedra caused by the inclusion of a small number of  $\text{GeO}_4$  tetrahedra or  $\text{Si(IV)}$  vacancies, which occupy more space than  $\text{SiO}_4$ .

A further increase in  $X$  to 0.5 results in precipitation of single wall silicon doped aluminogermanate imogolite-type nanotubes  $\text{Al}_2\text{Si}_{1-x}\text{Ge}_x\text{O}_3(\text{OH})_4$  ( $x \approx 0.35$ ) with a characteristic internal diameter of 0.9-1.2 nm and average length 20-30 nm. In addition to these crystalline nanostructures, nanosheets and nanorods of  $\gamma\text{-AlOOH}$  (boehmite) as well as amorphous Ge-containing aluminosilicates are formed over a wide range of  $X$ . Additional analysis, such as NMR and EXAFS techniques, would be useful in describing the structure of the Ge-containing phases (single-walled nanotubes and amorphous particles) obtained at  $X = 0.5$ , and in examining their structural evolution during the 7 days reaction.

The precise effect that  $\text{Ge(IV)}$  has on the curvature of aluminosilicate nanosheets to promote nanotubes (halloysite) instead of flat layered structures (kaolinite) is as yet unclear. However, these new findings provide an insight into the conditions suitable for forming a variety of curved and flat aluminosilicate or aluminogermanate structures under hydrothermal conditions as well as offering a convenient route for the synthesis of halloysite nanotubes from concentrated suspension.





## Chapter 5: The Stability of Halloysite Nanotubes in Acid and Alkaline Aqueous Suspensions

### 5.1. Introduction

As nanostructured materials become more widely used, there is a growing need to understand the mechanisms of morphological changes and physical degradation of these nanomaterials under various operational conditions. Knowledge of the conditions under which halloysite retains its tubular shape, and how it is modified by different solution environments, is important in practical applications (see Section 2.4.2, page 30).

The thermal stability of naturally-occurring  $\text{Al}_2\text{Si}_2\text{O}_5(\text{OH})_4$  (halloysite) nanotubes has been well-studied in recent work<sup>[136, 251]</sup> (see Section 2.4.1, page 29). In contrast, the chemical stability of halloysite nanotubes in corrosive environments has not yet been systematically studied. The outer surface of halloysite nanotubes contains  $\text{SiO}_4$  tetrahedra, whereas the inner surface contains octahedral  $\text{Al-OH}$  functionalities (see Figure 4.11, page 82), resulting in a difference in acid-base properties for both surfaces and affecting their interaction with solvents. The  $\text{Al-OH}$  groups are hydrated, and can exchange protons,<sup>[252]</sup> whereas the  $\text{SiO}_4$  tetrahedra are fully interconnected by  $\text{Si-O-Si}$  bonds. Therefore, only  $\text{Si-OH}$  groups at the tube ends and defect sites are hydrated.<sup>[164]</sup> Thus, hydrolysis of the inner and outer nanotube surfaces, comprised of  $\text{Al-O}$  and  $\text{Si-O}$  bonds respectively, should proceed differently in the presence of  $\text{H}^+$  or  $\text{OH}^-$  ions.

In this chapter, the results of a systematic study of the long term stability of halloysite at room temperature in  $0.001 - 1 \text{ mol dm}^{-3}$  solutions of different acids ( $\text{H}_2\text{SO}_4$ ,  $\text{HCl}$ , and acetic acid), a strong base ( $\text{NaOH}$ ), and distilled water are presented. The observed structural and morphological changes of halloysite nanotubes are linked to the steady state concentration of dissolved silicon (IV) and aluminium (III) in the liquid phase, and the dissolution mechanism is discussed.

## 5.2. Morphological changes after acid/alkaline treatment

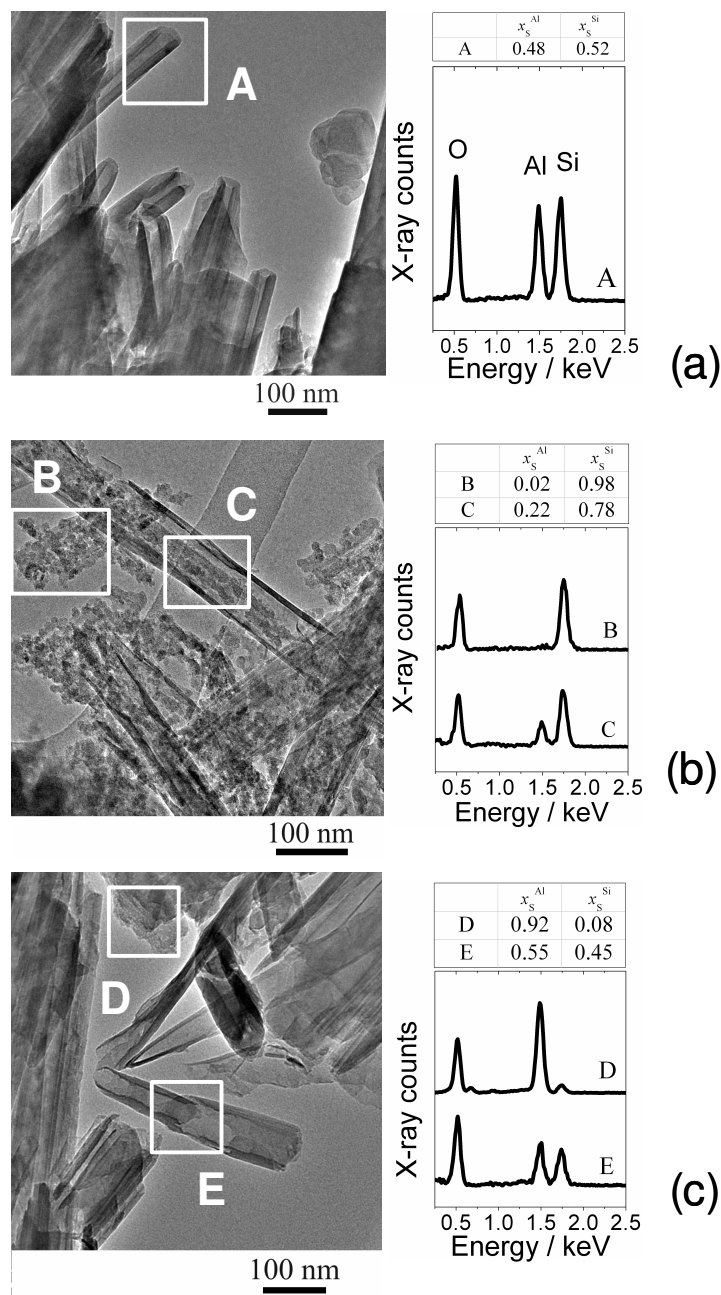
### 5.2.1. Electron microscopy

The halloysite nanotubes used in this work were naturally-occurring samples purchased from Sigma Aldrich (cat. no. 685445). A TEM image of the raw, untreated halloysite is shown in Figure 5.1a. The natural halloysite shows characteristic tubular-shaped objects with an average external diameter of 45 nm, an internal diameter of 15 nm and a wall thickness of 15 nm. The nanotube walls have a characteristic multilayered structure, with a spacing of 0.7 nm between the layers. The natural halloysite also contains a small number of randomly shaped impurities of flat objects (nanosheets).

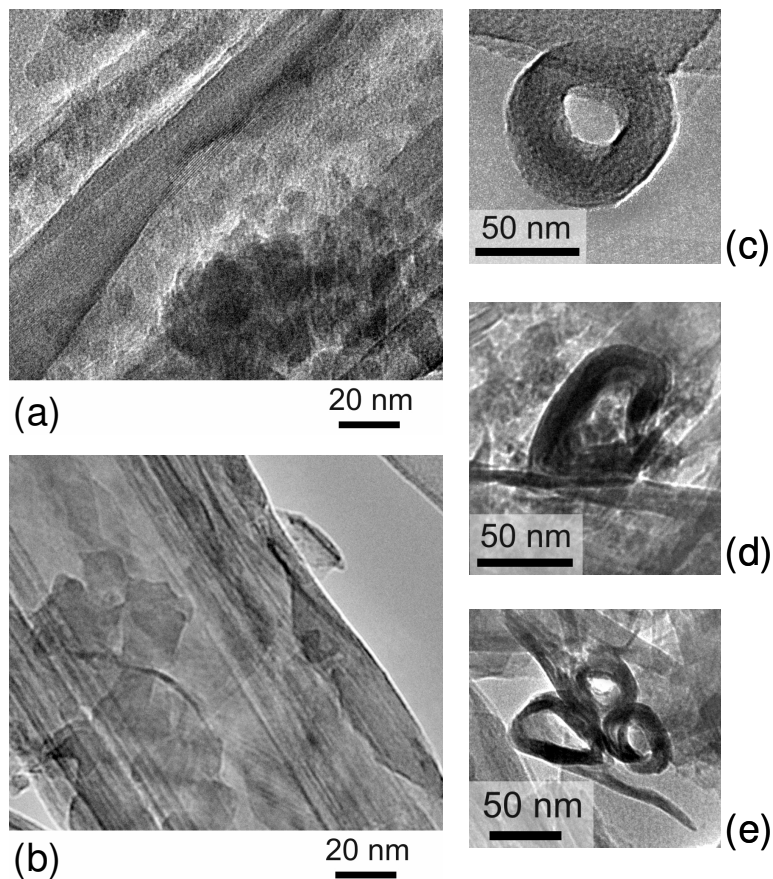
The treatment of halloysite with 1 mol dm<sup>-3</sup> H<sub>2</sub>SO<sub>4</sub> results in significant alteration of the morphology of halloysite nanotubes. The TEM image (Figure 5.1b) reveals that acid treatment results in the filling of most of the nanotubes with small spheroidal nanoparticles approximately 10 nm in diameter. These nanoparticles can be found mostly inside the tubes as well as outside and, where present outside the tubes, they tend to form small aggregates. The energy dispersive x-ray (EDX) mapping of the area suggests that these particles are enriched with silicon, and are therefore most likely particles of amorphous silica. The inner walls of the tubes are also roughened and thinned, and even broken in some places (Figure 5.2). After acid treatment for 84 days, the average external diameter of the tubes is the same, whereas the average internal diameter has increased to 22.9 nm, and the average wall thickness has decreased to 10.3 nm (35 % thinner). These data suggest that dissolution of halloysite in acid may predominantly occur at the inner surface of the tubes, which consists of AlO<sub>6</sub> octahedra. Treatment of halloysite with 1 mol dm<sup>-3</sup> HCl yields similar results (see Table 5.1).

After treatment of natural halloysite with 1 mol dm<sup>-3</sup> NaOH (see Figure 5.1c), the tube walls also show thinning and surface roughening. However, no nanoparticles are observed inside the tubes; there are only nanoparticles and nanosheets which aggregate outside the tubes. The nanosheets could have originated from collapsed nanotubes, in which, due to dissolution, the walls have been extensively thinned resulting in their rupturing and falling apart (Figure 5.2b and e). The nanoparticles are most likely

products of recrystallisation and according to EDX mapping (Figure 5.1c) both the nanoparticles and nanosheets are enriched with aluminium. After alkaline treatment, the average internal diameter had increased to 22.8 nm, the average wall thickness had decreased to 11.4 nm (28 % thinner), and the average external diameter was unchanged.



**Figure 5.1.** TEM images with accompanying EDX spectra from highlighted areas of (a) untreated halloysite, halloysite treated for 84 days with (b) 1 mol dm<sup>-3</sup> H<sub>2</sub>SO<sub>4</sub>, or (c) 1 mol dm<sup>-3</sup> NaOH. The boxes A-E indicate the area measured in the corresponding EDX spectrum.

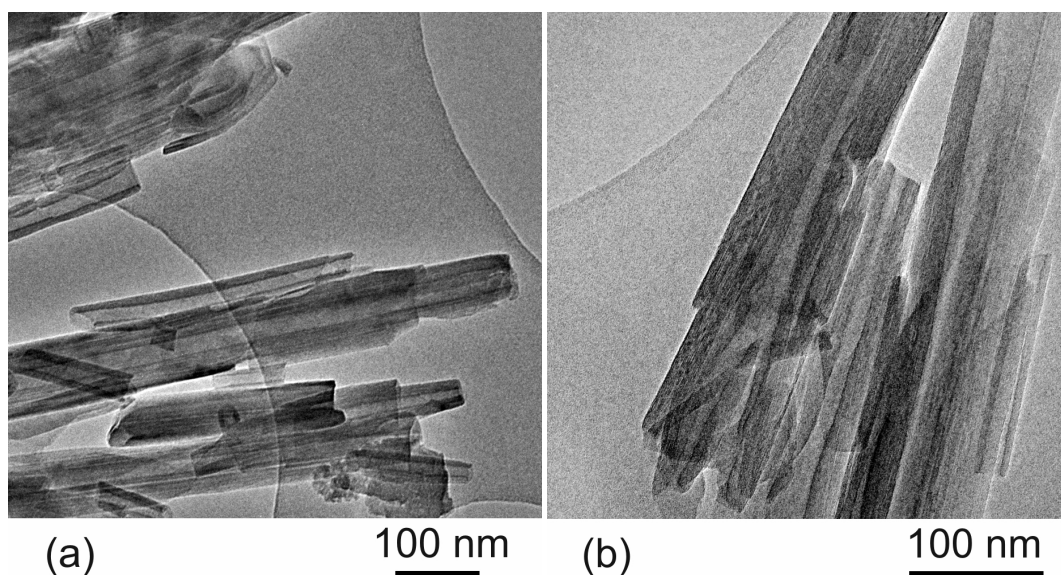


**Figure 5.2.** HRTEM images showing the tube wall destruction and appearance of particles in halloysite treated with (a) 1 mol dm<sup>-3</sup> H<sub>2</sub>SO<sub>4</sub> and (b) 1 mol dm<sup>-3</sup> NaOH for 84 days. The end-on TEM images of tubes on the right show (c) untreated halloysite, and (d),(e) halloysite treated for 84 days with 1 mol dm<sup>-3</sup> H<sub>2</sub>SO<sub>4</sub> and NaOH respectively.

**Table 5.1.** Effect of acid and alkaline treatment of the average morphology of halloysite nanotubes, measured from TEM images.

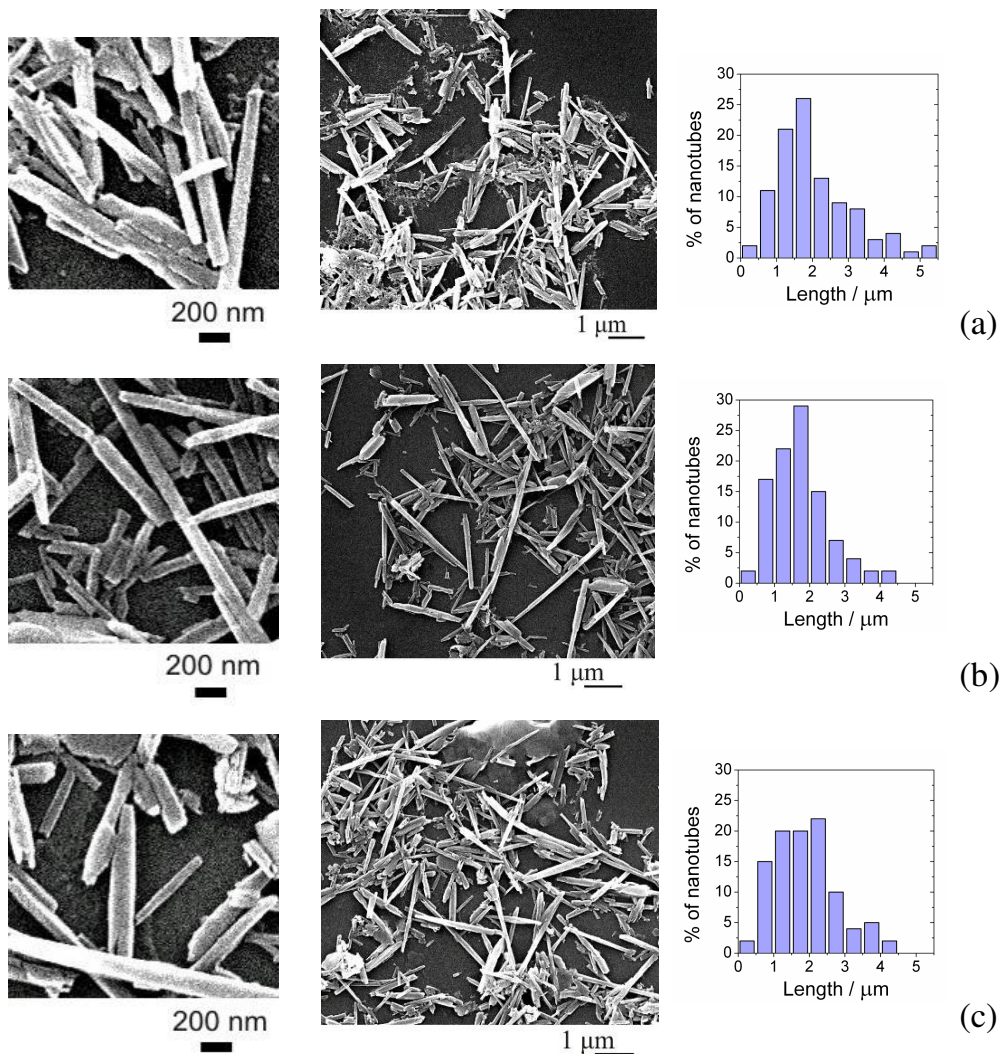
Solution Composition	Time of treatment (days)	Inner diameter (nm)	Wall thickness (nm)	Average length (μm)
Initial halloysite	0	15	15	2.06
1 mol dm <sup>-3</sup> HCl	28	20.2	12.8	1.86
1 mol dm <sup>-3</sup> HCl	84	22.9	10.6	-
1 mol dm <sup>-3</sup> H <sub>2</sub> SO <sub>4</sub>	28	19.2	11.8	1.72
1 mol dm <sup>-3</sup> H <sub>2</sub> SO <sub>4</sub>	84	22.9	10.3	-
1 mol dm <sup>-3</sup> NaOH	28	20.0	11.8	1.91
1 mol dm <sup>-3</sup> NaOH	84	22.8	11.4	-

Treatment of halloysite in  $1 \text{ mol dm}^{-3}$  acetic acid, and  $0.1 \text{ mol dm}^{-3}$  solutions of  $\text{H}_2\text{SO}_4$ ,  $\text{HCl}$ , or  $\text{NaOH}$  results in a much lesser change to the nanotube morphology; the inner surface of the tubes is slightly roughened and there is evidence of some silica nanoparticles (see Figure 5.2a, bottom of image). However, this is an insignificant amount compared to the presence of silica particles after treatment in the  $1 \text{ mol dm}^{-3}$  solutions of strong acids (see Figures 5.1 and 5.2). In less concentrated solutions of  $0.1 \text{ mol dm}^{-3}$  acetic acid or  $\leq 0.01 \text{ mol dm}^{-3}$   $\text{H}_2\text{SO}_4$ ,  $\text{HCl}$ , or  $\text{NaOH}$  there was no observable change to the halloysite morphology by TEM, and the tubes were identical to those treated in solutions of distilled water (Figure 5.3b).



**Figure 5.3.** TEM images of halloysite nanotubes after 84 days treatment with (a)  $1 \text{ mol dm}^{-3}$  acetic acid, and (b) distilled water.

To determine the length distribution of the halloysite nanotubes before and after acid/alkali treatment, SEM was used to image larger areas of the sample. Figure 5.4 shows that after acid and alkaline treatment in strong  $1 \text{ mol dm}^{-3}$  solutions, most of the nanotubes retained their elongated shape. The accompanying length distributions (see the histograms in Figure 5.4) show that after dissolution in acid or alkali over 28 days, the length distribution of the nanotubes only becomes slightly narrower and the tubes do not become much shorter on average (see Table 5.1) suggesting that the dissolution is mainly occurring at the nanotube walls, rather than at the nanotube ends.

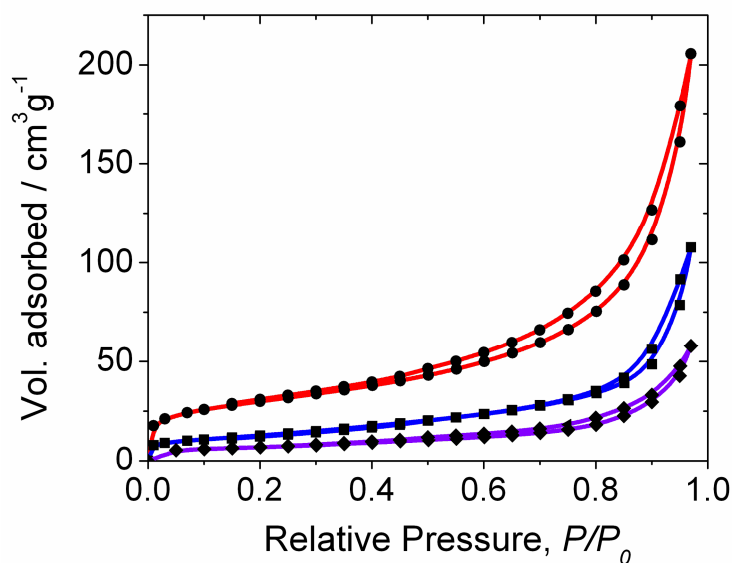


**Figure 5.4.** SEM images and histograms of length distribution of nanotubes in (a) halloysite, and halloysite treated with for 28 days with (b) 1 mol dm<sup>-3</sup> H<sub>2</sub>SO<sub>4</sub> and (c) 1 mol dm<sup>-3</sup> NaOH.

### 5.2.2. Nitrogen adsorption

The acid or base assisted alteration of halloysite morphology observed by TEM is in agreement with the N<sub>2</sub> adsorption data. Figure 5.5 shows isotherms of N<sub>2</sub> adsorption on the surface of halloysite nanotubes treated with acid or base. In the case of 1 mol dm<sup>-3</sup> H<sub>2</sub>SO<sub>4</sub> the isotherm is characterised by a larger amount of microporous adsorption at  $P/P_0 < 0.1$  compared to untreated halloysite, whereas the appearance of the adsorption/desorption hysteresis shows no difference. In contrast, the N<sub>2</sub> adsorption

isotherm for halloysite treated with  $1 \text{ mol dm}^{-3}$  NaOH shows very little increase in microporous adsorption compared with untreated halloysite, but shows narrowing of the adsorption/desorption hysteresis at  $P/P_0 = 0.8$  due to collapse of the nanotubular pores.



**Figure 5.5.** The  $\text{N}_2$  adsorption and desorption isotherms at  $-195^\circ\text{C}$  of ( $\diamond$ ) halloysite, and halloysite treated with: ( $\blacksquare$ )  $1 \text{ mol dm}^{-3}$  NaOH, 84 days, and ( $\bullet$ )  $1 \text{ mol dm}^{-3}$   $\text{H}_2\text{SO}_4$ , 84 days.

The values of BET surface area ( $S_{\text{BET}}$ ) and total pore volume ( $V_{\text{pores}}$ ) for halloysite treated with both acid and alkaline solution are shown in Table 5.2. All treatments result in an increase in both  $S_{\text{BET}}$  and  $V_{\text{pores}}$  compared to the original halloysite. The treatment with both HCl and  $\text{H}_2\text{SO}_4$  results in almost linear growth of  $S_{\text{BET}}$  and  $V_{\text{pores}}$  with time, whereas in the case of NaOH, the initial growth is followed by steady state values after 28 days. The largest increase in  $S_{\text{BET}}$  and  $V_{\text{pores}}$  (almost threefold after 28 days and fourfold after 84 days) occurs in  $1 \text{ mol dm}^{-3}$   $\text{H}_2\text{SO}_4$ . The treatment of halloysite with  $\text{H}_2\text{O}$  also results in an increase of  $S_{\text{BET}}$ , indicating a possible reason for the large variation in its reported specific surface area ( $23 - 80 \text{ m}^2 \text{ g}^{-1}$ ) in the literature,<sup>[65, 166, 253, 254]</sup> due to the differences in the hydration “pre-history” of the halloysite samples. The large variation in reported surface area values also arises from the different crystallisation conditions of natural halloysite obtained from different suppliers; the average inner diameter and length of the tubes can vary widely.<sup>[255]</sup>

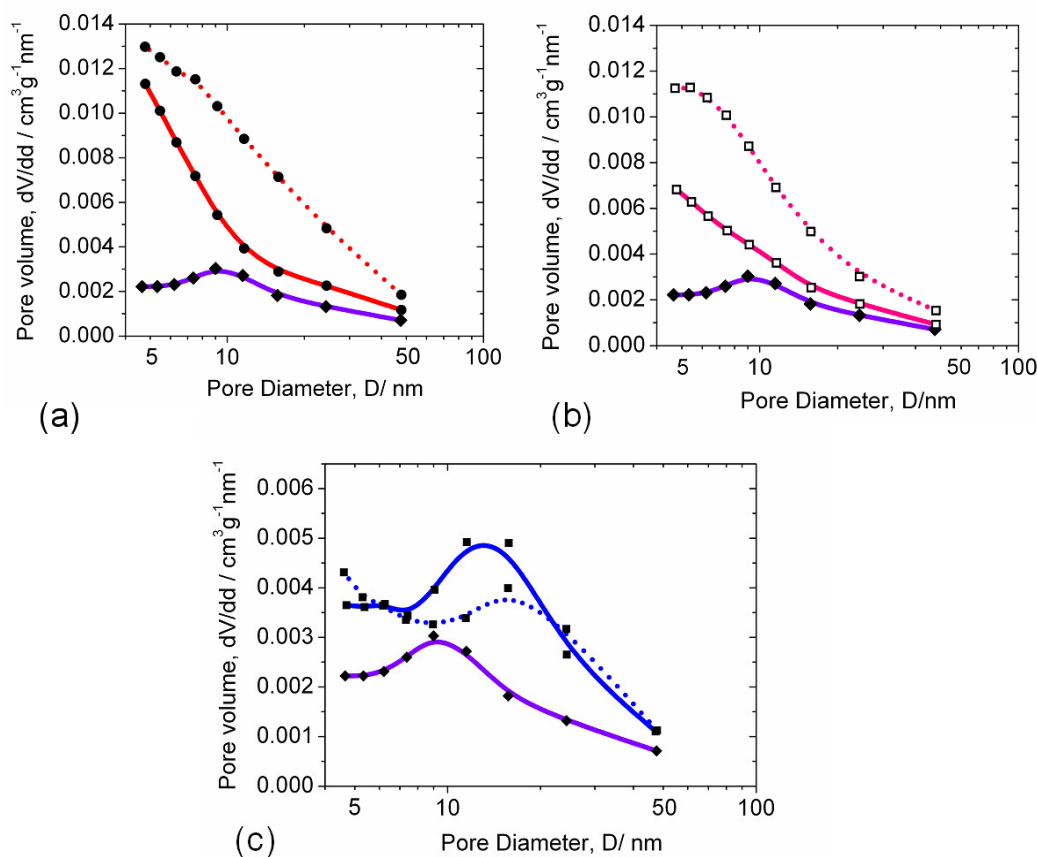


**Table 5.2.** Changes in halloysite BET specific surface area ( $S_{\text{BET}}$ ) and total pore volume ( $V_{\text{pores}}$ ) under slow transformation in acids or base at  $22 \pm 2$  °C.

Solution composition	Time of treatment (days)	$S_{\text{BET}}$ ( $\text{m}^2 \text{g}^{-1}$ )	$V_{\text{pores}}$ ( $\text{cm}^3 \text{g}^{-1}$ )
Initial halloysite	0	24.3	0.090
H <sub>2</sub> O	28	30.5	0.108
H <sub>2</sub> O	84	31.3	0.108
1 mol dm <sup>-3</sup> NaOH	28	45.0	0.165
1 mol dm <sup>-3</sup> NaOH	84	47.0	0.168
1 mol dm <sup>-3</sup> HCl	28	54.2	0.144
1 mol dm <sup>-3</sup> HCl	84	91.2	0.245
1 mol dm <sup>-3</sup> H <sub>2</sub> SO <sub>4</sub>	28	70.7	0.184
1 mol dm <sup>-3</sup> H <sub>2</sub> SO <sub>4</sub>	84	102.2	0.322

Figure 5.6 shows the BJH pore size distributions (determined from the desorption isotherms) of halloysite treated with 1 mol dm<sup>-3</sup> H<sub>2</sub>SO<sub>4</sub>, HCl and NaOH. The untreated halloysite is characterised by a wide pore size distribution between 4.5 and 48 nm, due to the wide distribution in nanotube sizes (see Figure 5.4). The peak at around 9 – 10 nm pore diameter is associated with adsorption inside the nanotubes (intra-tubular), whereas the pores between close packed nanotubes (inter-tubular) are usually characterized by larger pore sizes.<sup>[36]</sup>

The treatment of natural halloysite with 1 mol dm<sup>-3</sup> H<sub>2</sub>SO<sub>4</sub> and HCl results in a significant increase in the pore volume associated with small mesopores indicated by the masking of the original peak at 9 – 10 nm and appearance of a strong shoulder peak at pore sizes less than 5 nm in the BJH pore size distribution curve. These small mesopores are probably associated with the agglomerates of silicon-enriched nanoparticles observed in the TEM images (see Figure 5.1b). Further increase in the duration of treatment from 28 to 84 days results in a shift of BJH pore size distribution towards larger diameters suggesting that the continuation of nanoparticle growth probably occurs via an Ostwald ripening mechanism.



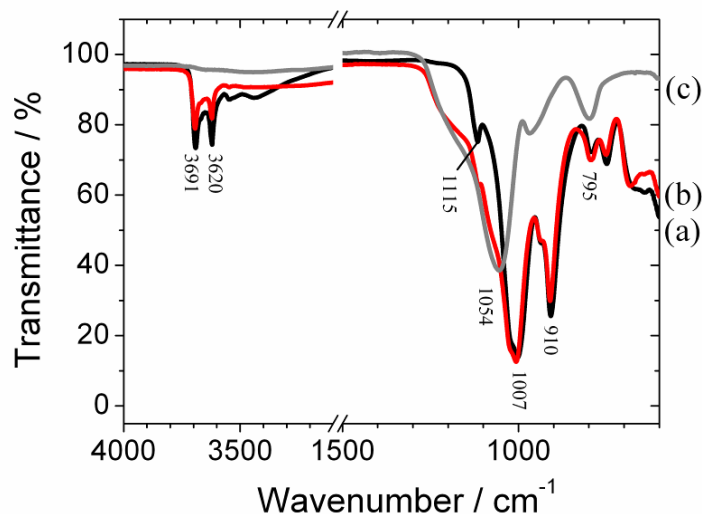
**Figure 5.6.** BJH pore size distributions for halloysite nanotubes treated with (a) 1 mol dm<sup>-3</sup> H<sub>2</sub>SO<sub>4</sub>, (b) 1 mol dm<sup>-3</sup> HCl and (c) 1 mol dm<sup>-3</sup> NaOH, for 28 days (solid line), and 84 days (dotted line). (♦) is untreated halloysite.

In contrast, the treatment of natural halloysite with 1 mol dm<sup>-3</sup> NaOH for 28 days (Figure 5.6c) results in a shift of the peak maximum in the BJH pore size distribution curve from 9 to 15 nm, suggesting an increase in the average diameter of the inner pores of the nanotubes. The growth of the inner diameter of the nanotubes is caused by slow thinning of the tube walls due to progressive dissolution of the aluminosilicate layers as seen in the TEM images (Figure 5.1c). An increase in the duration of treatment to 84 days results in further shifting of the peak position to higher diameters accompanied by a widening distribution without a change in  $V_{\text{pores}}$ . This suggests that the decrease of  $S_{\text{BET}}$  and  $V_{\text{pores}}$  associated with the collapse of some nanotubes is compensated for by an increase of  $S_{\text{BET}}$  and  $V_{\text{pores}}$  due to formation of aluminium-enriched, isolated, sheet-like objects observed in the TEM images of Figure 5.1c.

### 5.3. Structural changes of halloysite after acid/alkaline treatment

#### 5.3.1. Fourier-transform infrared and Raman spectroscopy

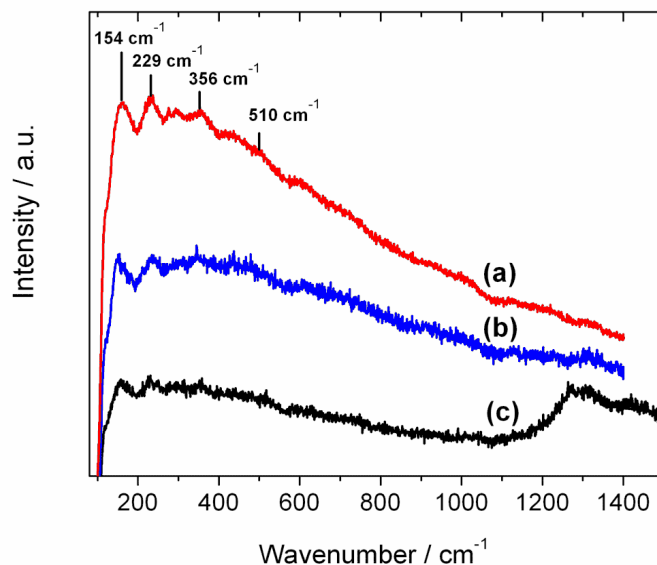
Figure 5.7 shows infrared (FTIR) spectra of natural halloysite (original and treated with  $1 \text{ mol dm}^{-3} \text{ H}_2\text{SO}_4$  in aqueous suspension for 84 days) as well as a sample of amorphous  $\text{SiO}_2$  (a- $\text{SiO}_2$ ) (Fisher, 35-70  $\mu\text{m}$  chromatography grade). Most of the major bands of the acid treated halloysite can be assigned to Al-OH bending ( $910 \text{ cm}^{-1}$ ), Si-O-Si symmetric stretching ( $1007 \text{ cm}^{-1}$ ), and surface hydroxyl translation ( $795 \text{ cm}^{-1}$ ).<sup>[113, 256]</sup> The position of these bands coincides with bands of untreated halloysite except for the additional shoulder, which appears in the region between  $1100$  and  $1200 \text{ cm}^{-1}$ . This shoulder is probably associated with the silicon-rich nanoparticles observed in the TEM images, since the FTIR spectrum of amorphous  $\text{SiO}_2$  shows a characteristic Si-O stretching band in the same area. The treatment of natural halloysite with  $1 \text{ mol dm}^{-3} \text{ NaOH}$  does not significantly affect the position and intensity of bands in the FTIR spectrum.



**Figure 5.7.** FTIR spectra of (a) untreated halloysite, (b) halloysite treated with  $1 \text{ mol dm}^{-3} \text{ H}_2\text{SO}_4$  for 84 days, (c) amorphous  $\text{SiO}_2$  (Fisher, 35-70  $\mu\text{m}$  chromatography grade).

The Raman spectra of all samples in Figure 5.8 are characterised by a large background signal exhibiting three major peaks at  $154$ ,  $229$ , and  $356 \text{ cm}^{-1}$ , which can be assigned to

O-Al-O and O-H-O symmetric stretches, and Al-OH bending modes respectively.<sup>[245]</sup> The broad Si-O stretching band at  $\approx 510\text{ cm}^{-1}$  in the acid-treated sample may be caused by the presence of amorphous silica. Large background caused by fluorescence and a small signal-to-noise ratio in the Raman spectra of samples and the closeness of the peaks to the filter-cut off point prevent the exact identification of spectral changes associated with acid or base assisted dissolution of halloysite.

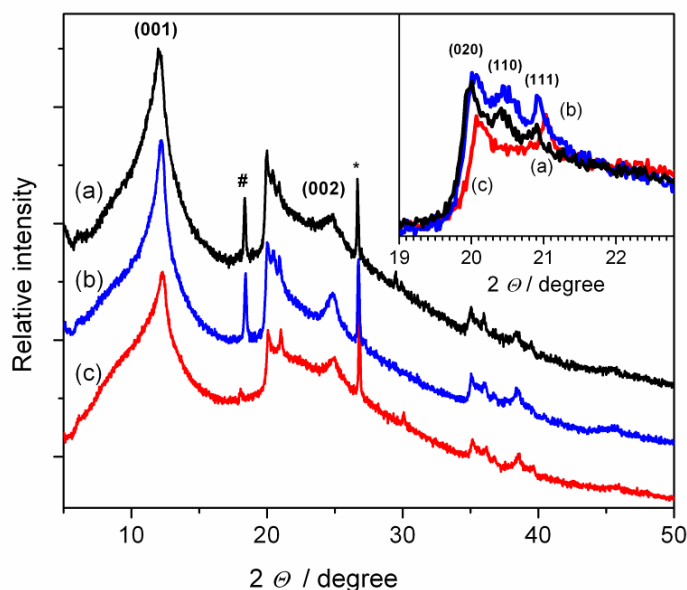


**Figure 5.8.** Raman Spectra of the lattice region of halloysite treated for 84 days with  $1\text{ mol dm}^{-3}$  solutions of (a)  $\text{H}_2\text{SO}_4$ , (b)  $\text{NaOH}$ , and (c) untreated halloysite.

### 5.3.2. X-ray diffraction

Figure 5.9 shows the XRD pattern of natural halloysite treated with acid or base solutions. The reflections from the halloysite crystal structure are characterised by relatively wide lines with a small signal/noise ratio. In addition to the identified reflections from halloysite,<sup>[65]</sup> there are reflections from impurities of quartz ( $\text{SiO}_2$ ) and alunite ( $\text{KAl}_3(\text{SO}_4)_2(\text{OH})_6$ ) nanocrystals.<sup>[65, 136]</sup> Analysis of the XRD patterns of the samples indicates only minor differences in the diffraction pattern of natural halloysite after alkaline treatment with  $1\text{ mol dm}^{-3}$   $\text{NaOH}$ . Treatment for 84 days with  $1\text{ mol dm}^{-3}$   $\text{H}_2\text{SO}_4$ , however, causes a decrease in the intensities of the halloysite reflections relative to the quartz impurities and complete quenching of the (110) reflection, suggesting alteration of the crystal ordering due to the corrosion of nanostructures in an acidic

environment. The reflection from the alunite decreased significantly, which is probably due to its dissolution in concentrated acid.<sup>[257]</sup> The appearance of the shoulder at  $10^\circ$  can be associated with some disorder in the (001) interlayer spacing due to partial hydration, usually resulting in shifting of the reflection to smaller angles.<sup>[258]</sup> The absence of any new reflections in the acid and alkaline-treated samples suggests that in both cases the aluminium enriched nanosheet particles and silicon enriched spheroidal nanoparticles have an amorphous structure.

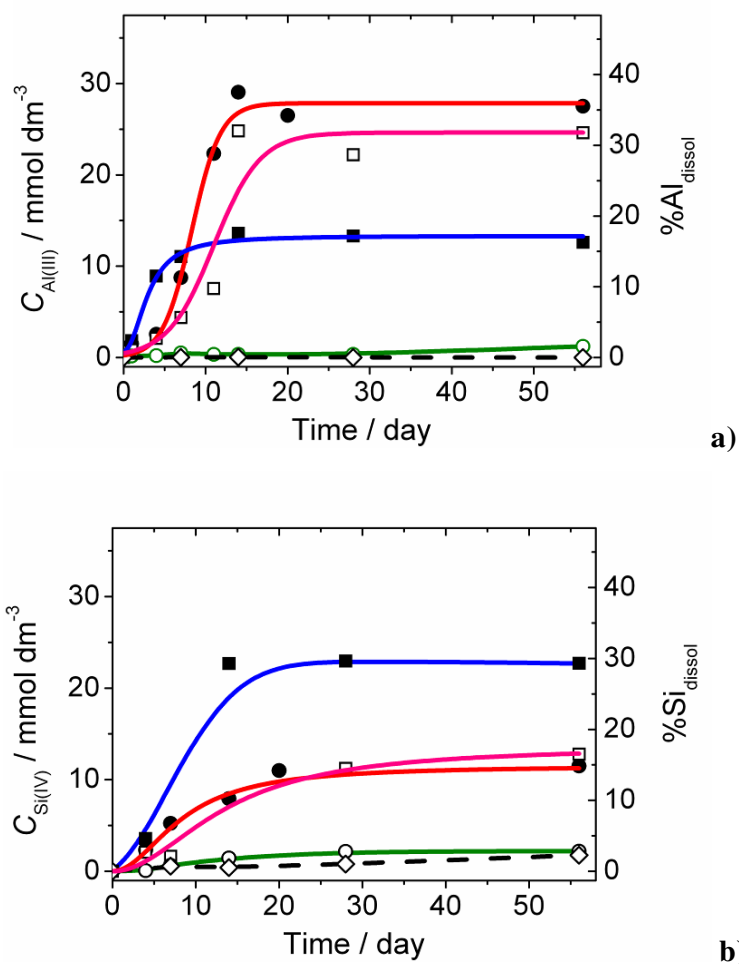


**Figure 5.9.** XRD patterns (without background correction) of (a) untreated halloysite, and halloysite treated for 84 days with (b) 1 mol dm<sup>-3</sup> NaOH, and (c) 1 mol dm<sup>-3</sup> H<sub>2</sub>SO<sub>4</sub>. The reflections marked with \* and # correspond to quartz and alunite impurities, respectively. The inset shows magnified XRD pattern in the range of  $2\theta$  between 19 and 23 degrees.

#### 5.4. Solubility of halloysite in acid/alkaline suspensions

The acid and base assisted transformations of natural halloysite are accompanied by the release of various forms of soluble aluminium (III) and silicon (IV) species into the aqueous solution, the exact distribution of which depends on the pH. The total concentration of aluminium (III) ( $C_{\text{Al(III)}}$ ) and silicon (IV) ( $C_{\text{Si(IV)}}$ ) species can be determined using optical spectroscopy. The results of colorimetric analysis of  $C_{\text{Al(III)}}$  and  $C_{\text{Si(IV)}}$  from dissolved halloysite in 1 mol dm<sup>-3</sup> solutions of acids or base are plotted as a

function of time in Figure 5.10. The graphs show that a steady state values of  $C_{\text{Al(III)}}$  and  $C_{\text{Si(IV)}}$  are obtained after 14 – 21 days. The concentration  $C_{\text{Al(III)}}$  is higher in acid than in alkali solution, whereas the concentration  $C_{\text{Si(IV)}}$  is greater in an alkaline than in acidic environments. Such behaviour is probably related to the greater solubility of silicon dioxide in an alkaline environment compared to an acidic environment (see Figure 5.13 page 106). The kinetic curves of Si (IV) and Al (III) released in acid solutions have a characteristic sigmoidal shape, with an induction period of approximately two days, in which the rate of dissolution is close to 0. The rate of halloysite dissolution, shown in the gradient of Figure 5.10a, reaches a maximum by approximately the 10<sup>th</sup> day of reaction.



**Figure 5.10.** The concentration of total dissolved aluminium  $C_{\text{Al(III)}}$  (a) and silicon  $C_{\text{Si(IV)}}$  (b) as a function of time in the aqueous suspension of halloysite containing (■) 1 mol dm<sup>-3</sup> NaOH, (●) 1 mol dm<sup>-3</sup> H<sub>2</sub>SO<sub>4</sub>, (□) 1 mol dm<sup>-3</sup> HCl, (○) 1 mol dm<sup>-3</sup> acetic acid and (◇) pure H<sub>2</sub>O. The estimated error of concentration determination is  $\pm 10\%$ .

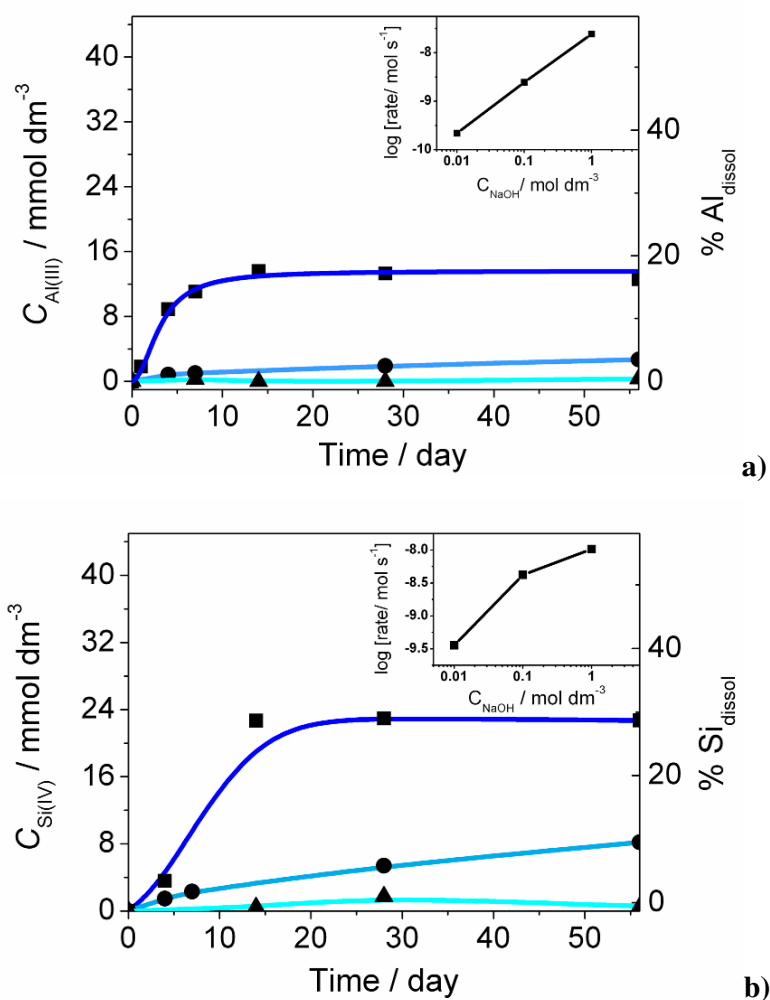
In contrast, the dissolution of halloysite nanotubes in  $1 \text{ mol dm}^{-3}$  NaOH is characterised by the immediate appearance of dissolved aluminium (III) and silicon (IV) in solution, indicating a difference in the mechanism of halloysite corrosion in acid or base media. The maximal rate of dissolution in alkaline solution is similar to that in acid solution. The rate of halloysite degradation in HCl solution is slightly lower than that in  $\text{H}_2\text{SO}_4$ , but the similar steady state concentrations of both of  $C_{\text{Al(III)}}$  and  $C_{\text{Si(IV)}}$  suggests a similar degree of decomposition. The treatment of halloysite with water or acetic acid results in release of a trace amount (less than  $1 \text{ mmol dm}^{-3}$ ) of Al(III) and Si(IV) in solution without significant alteration of the shape of the nanotubes (Figure 5.3).

From the values of  $C_{\text{Al(III)}}$  and  $C_{\text{Si(IV)}}$  the degree of dissolution of halloysite ( $\% \text{ Al}_{\text{dissol}}$ ,  $\% \text{ Si}_{\text{dissol}}$ ) can be determined as a percentage of the maximal concentrations of  $C_{\text{Al(III)}}$  and  $C_{\text{Si(IV)}}$  in the case of complete dissolution of the initial halloysite (right hand side y-axes in Figure 5.10). After 28 days in  $1 \text{ mol dm}^{-3}$  NaOH, approximately 17 % of the Al(III) and 29 % of the Si(IV) in halloysite are dissolved. The degree of dissolution for Al(III) and Si(IV) in  $1 \text{ mol dm}^{-3}$   $\text{H}_2\text{SO}_4$  is 35 % and 15 %, respectively, in good agreement with the observed thinning of the tube walls (Table 5.1).

The rate of halloysite dissolution in an alkaline environment is affected by the concentration of NaOH. Figure 5.11 shows the kinetic curves of  $C_{\text{Al(III)}}$  and  $C_{\text{Si(IV)}}$  growth during dissolution of halloysite after addition of NaOH. A decrease in NaOH concentration results in a decrease in the rate of halloysite dissolution. In the case of diluted NaOH solutions ( $0.1 \text{ mol dm}^{-3}$  and  $0.01 \text{ mol dm}^{-3}$ ), both values  $C_{\text{Al(III)}}$  and  $C_{\text{Si(IV)}}$  do not reach equilibrium even after 2 months at room temperature. The insets in Figure 5.11a and 5.11b show logarithmic plots of the initial rate of aluminium (III) and silicon (IV) solvation, determined from the tangent to the kinetic curve at time equal to zero, as a function of initial NaOH concentration. These data suggest that the release of dissolved Al(III) and Si(IV) can be considered as a pseudo-first-order reaction.

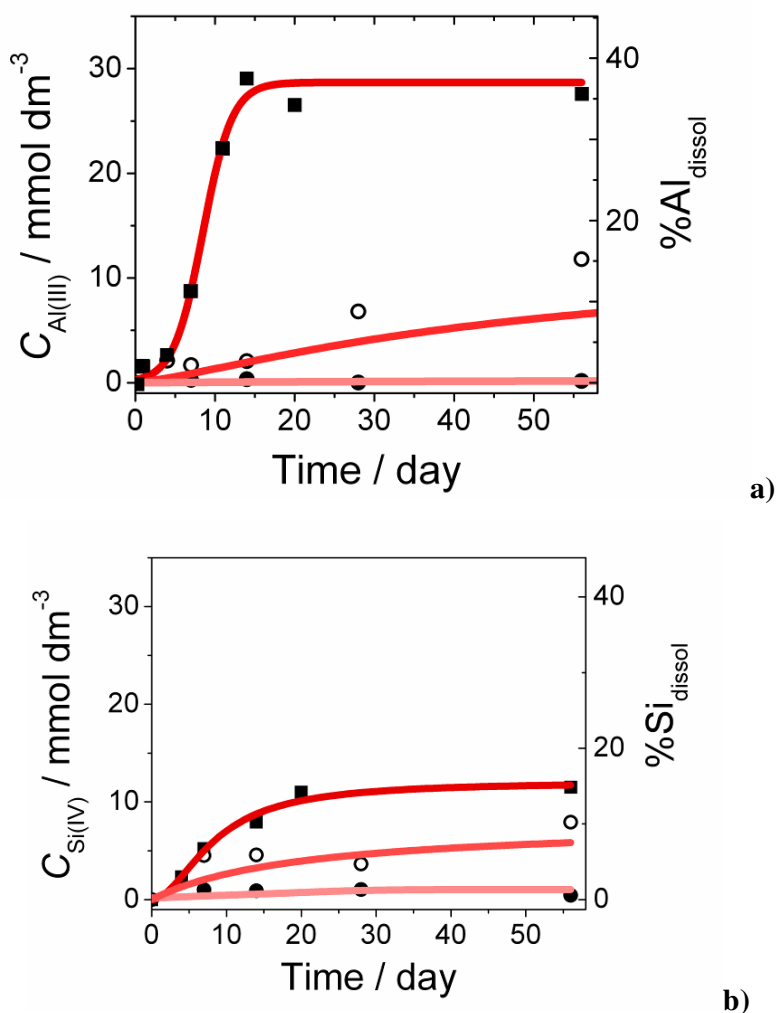
The effect of acid concentration on the initial dissolution rate of Al(III) and Si(IV) from the halloysite structure does not follow such a straightforward relationship (Figure 5.12), which is probably due to the apparent “induction period” which precedes the removal of Al(III) and Si(IV) from the halloysite structure, causing an almost zero

initial dissolution rate at all concentrations of acid. Unlike Al(III) solubility at different acid concentrations, the measured concentration of Si(IV) in  $0.1 \text{ mol dm}^{-3} \text{ H}_2\text{SO}_4$  solution after 7 days is almost as high as that in  $1 \text{ mol dm}^{-3}$  solution, and the Si(IV) present in solution is equivalent to the amount dissolved in  $0.1 \text{ mol dm}^{-3} \text{ NaOH}$ . The fact that in weaker acid solutions ( $< 1 \text{ mol dm}^{-3}$  concentration) the ratio of dissolved Al(III) to Si(IV) is close to one after 50 days suggests that removal of the more acid-soluble Al(III) species from the halloysite structure directly facilitates the removal to  $\text{SiO}_4$  tetrahedra to which they are bonded.



**Figure 5.11.** The concentration of total Al (III) (a) and Si (IV) (b) as a function of time in the aqueous suspension of halloysite containing (■)  $1 \text{ mol dm}^{-3} \text{ NaOH}$ , (●)  $0.1 \text{ mol dm}^{-3} \text{ NaOH}$ , (▲)  $0.01 \text{ mol dm}^{-3} \text{ NaOH}$ . Insets show logarithm of the initial rate of  $C_{\text{Al(III)}}$  and  $C_{\text{Si(IV)}}$  growth as a function of concentration of NaOH.





**Figure 5.12.** The concentration of total Al (III) (a) and Si (IV) (b) as a function of time in the aqueous suspension of halloysite containing ( $\blacksquare$ ) 1  $\text{mol dm}^{-3}$   $\text{H}_2\text{SO}_4$ , ( $\circ$ ) 0.1  $\text{mol dm}^{-3}$   $\text{H}_2\text{SO}_4$ , ( $\bullet$ ) 0.01  $\text{mol dm}^{-3}$   $\text{H}_2\text{SO}_4$ .

According to the stoichiometric composition of halloysite ( $\text{Al}_2\text{Si}_2\text{O}_5(\text{OH})_4$ ) the mole fraction of aluminium ( $x_{\text{S}}^{\text{Al}}$ ) and silicon ( $x_{\text{S}}^{\text{Si}}$ ) in the solid phase, defined as the amount of aluminium or silicon per sum amount of aluminium and silicon, is equal to 0.5 in the pure substance. However, the steady state (equilibrium)  $C_{\text{Al(III)}}$  and  $C_{\text{Si(IV)}}$  concentrations in Figures 5.10a and 5.10b deviates from that stoichiometry. In acid solution, the mole fraction of dissolved aluminium ( $x_{\text{L}}^{\text{Al}}$ ) determined as  $C_{\text{Al(III)}}/(C_{\text{Al(III)}} + C_{\text{Si(IV)}})$  is higher than mole fraction of silicon ( $x_{\text{L}}^{\text{Si}}$ ) (see Table 5.3) suggesting that due to the mass balance the solid sample is enriched with silicon (IV). EDX mapping of different areas

in the TEM images (see Figure 5.1b) allows us to conclude that this excess Si(IV) is mainly accumulated in the form of SiO<sub>2</sub> nanoparticles inside as well as outside nanotubes.

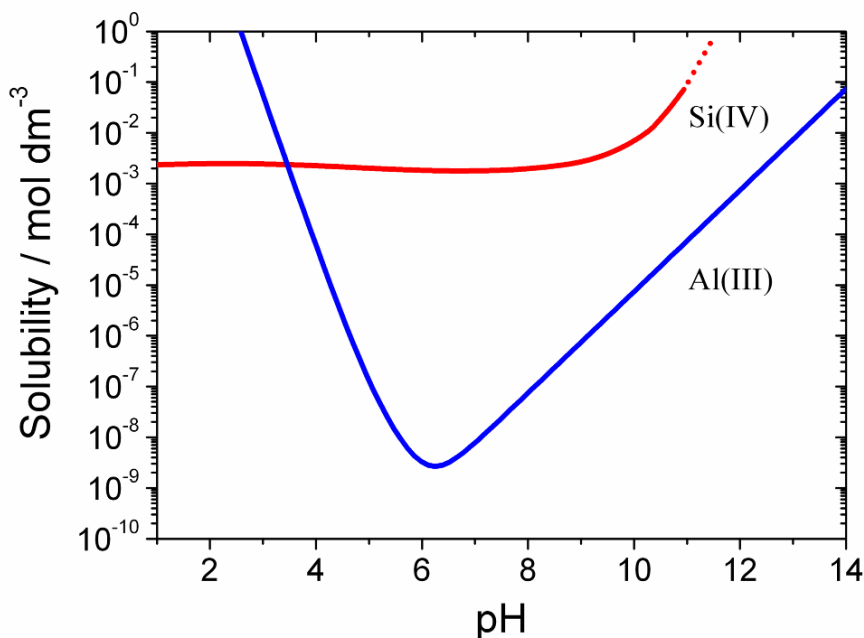
**Table 5.3.** The total concentration of Al(III)  $C_{\text{Al(III)}}$  and Si(IV)  $C_{\text{Si(IV)}}$  in aqueous suspension, the mole fractions of aluminium in liquid ( $x_{\text{L}}^{\text{Al}}$ ) and solid ( $x_{\text{S}}^{\text{Al}}$ ) phases, and the mole fractions of silicon in liquid ( $x_{\text{L}}^{\text{Si}}$ ) and solid ( $x_{\text{S}}^{\text{Si}}$ ) phases, after 84 days transformation in acids or base. The quantities  $x_{\text{S}}^{\text{Al}}$  and  $x_{\text{S}}^{\text{Si}}$  were determined from EDX analysis of large aggregates in the solid products of acid and base treatment.

Solution Composition	Time of treatment (days)	Al(III)			Si(IV)		
		$C_{\text{Al(III)}}$ (mmol dm <sup>-3</sup> )	$x_{\text{L}}^{\text{Al}}$	$x_{\text{S}}^{\text{Al}}$	$C_{\text{Si(IV)}}$ (mmol dm <sup>-3</sup> )	$x_{\text{L}}^{\text{Si}}$	$x_{\text{S}}^{\text{Si}}$
Initial halloysite	0	0	0	0.47	0	0	0.53
H <sub>2</sub> O	84	0.01	0.01	0.47	1.75	0.99	0.53
1 mol dm <sup>-3</sup> NaOH	84	12.6	0.35	0.82	22.71	0.65	0.18
1 mol dm <sup>-3</sup> HCl	84	34.4	0.73	-	12.76	0.27	-
1 mol dm <sup>-3</sup> H <sub>2</sub> SO <sub>4</sub>	84	27.5	0.71	0.31	11.5	0.29	0.69

In alkaline solution, the mole fraction of dissolved silicon ( $x_{\text{L}}^{\text{Si}}$ ) determined as  $C_{\text{Al(III)}}/(C_{\text{Al(III)}} + C_{\text{Si(IV)}})$  is higher than the mole fraction of aluminium ( $x_{\text{L}}^{\text{Al}}$ ), suggesting that the solid sample is enriched with Al(III). EDX mapping of different areas in Figure 5.1c shows that the excess Al(III) is contained inside the nanosheets, which could be formed from collapsed halloysite nanotubes which have lost most of their Si(IV), leading the remaining octahedral Al(III) gibbsite framework behind. The halloysite nanotubes which are still present after 84 days treatment show a slightly reduced ( $x_{\text{S}}^{\text{Si}}$ ) (Figure 5.1c), suggesting that they are undergoing this process of Si(IV) removal, and will eventually also be converted to amorphous Al(OH)<sub>3</sub> nanosheets.

Despite the fact that both  $C_{\text{Al(III)}}$  and  $C_{\text{Si(IV)}}$  are stabilised after 14 - 21 days during treatment of nanotubes with 1 mol dm<sup>-3</sup> acid or base, the transformation of nanotubes to SiO<sub>2</sub> nanoparticles or Al(OH)<sub>3</sub> nanosheets progresses even further during 84 days of

treatment, as seen from the TEM and  $N_2$  adsorption data. Thus, these concentrations can be considered as steady state, rather than equilibrium values.

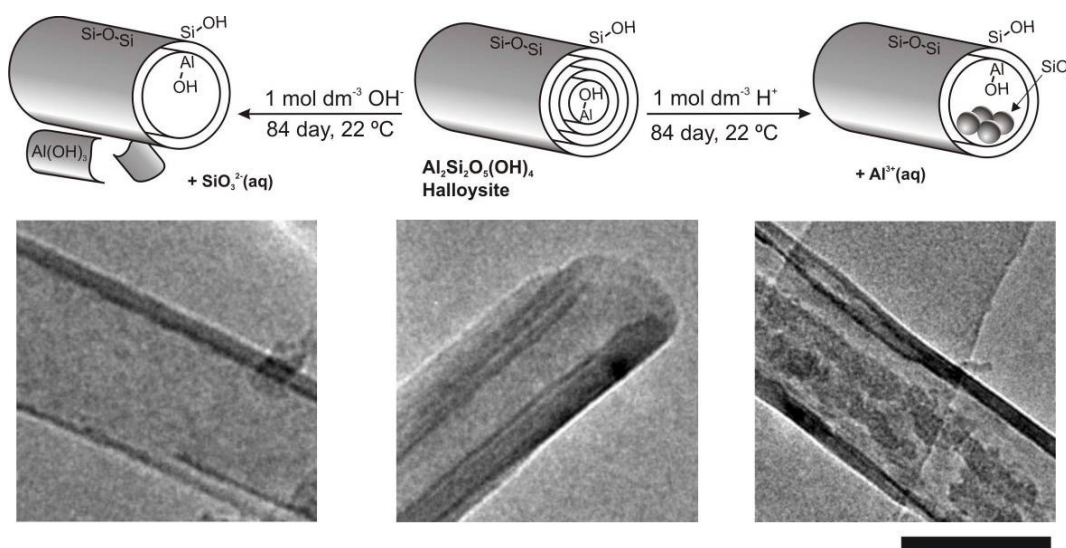


**Figure 5.13.** Equilibrium concentration of Al(III) and Si(IV) species in aqueous solution as a function of pH at 298 K, taken from the solubility data of Alexander et al.<sup>[259]</sup> and Wesolowski and Palmer,<sup>[260]</sup> for amorphous  $SiO_2$  and  $Al(OH)_3$  (gibbsite) respectively. Note the logarithmic scale on the y-axis.

The mechanism of acid assisted corrosion of halloysite nanotubes is schematically shown in Figure 5.14. The inner (concave) surface of halloysite composed by  $AlO_6$  octahedrons is firstly attacked by the acid resulting in the release of Al(III) to the solution after an induction period. Further dissolution predominantly continues on the concave surface leading to the release of silicon (IV), which rapidly reaches a saturated concentration at low pH (see figure 5.13 for solubility of  $SiO_2$  and  $Al(OH)_3$  at different pH) and precipitates in the form of amorphous  $SiO_2$  nanoparticles inside the nanotubes. Over a long period of time, the inner diameter of nanotubes and the diameter of  $SiO_2$  nanoparticles increase.

The decomposition of halloysite in  $1 \text{ mol dm}^{-3}$  NaOH solution is also initiated on the concave surface of nanotubes leading to release of Si(IV) into the solution, where

solubility in alkaline environment is greater than that of Al(III) (Figure 5.13). Unlike corrosion in acid environment, the crystallisation of saturated Al(III) occurs predominantly outside the nanotubes in the shape of flat nanocrystals. It is possible that partially dissolved, layered fragments of the halloysite walls composed of  $\text{AlO}_6$  octahedrons provide seeds for the crystallisation of  $\text{Al}(\text{OH})_3$  nanosheets. Further dissolution of halloysite results in a decrease in the wall thickness and an increase in the inner diameter of the nanotubes (Figure 5.14).



**Figure 5.14.** Scheme of transformation of halloysite ( $\text{Al}_2\text{Si}_2\text{O}_5(\text{OH})_4$ ) nanotubes in strong acid and alkaline solutions leading to formation of amorphous nanoparticles of  $\text{SiO}_2$  and amorphous nanosheets of  $\text{Al}(\text{OH})_3$ , respectively. The scale bar represents 50 nm.

## 5.5. Conclusions

The study of the stability of aqueous suspensions of natural halloysite has shown that halloysite is kinetically stable in water and in  $\leq 0.1 \text{ mol dm}^{-3}$  acetic acid solutions at room temperature. It is also kinetically stable in dilute ( $1 \text{ mmol dm}^{-3}$ ) inorganic acid and alkaline solutions. In concentrated ( $0.01 - 1 \text{ mol dm}^{-3}$ ) solutions of strong acids and bases, however, extensive dissolution is initiated by dissolution of the inner Al-OH surface catalysed by acidic or basic species, leading to progressive thinning of the tubes

from the inside. In strong acid solutions, the greater solubility of Al(III) vs. Si(IV) leads to the formation of small SiO<sub>2</sub> nanoparticles inside the tubes, enhancing the surface area and pore volume of the sample. In NaOH solutions the greater solubility of Si(IV) vs. Al(III) leads to the formation of fragmented flaky particles containing layers of Al(OH)<sub>3</sub>. In NaOH the initial rate of the dissolution follows pseudo first order reaction kinetics. In H<sub>2</sub>SO<sub>4</sub> the kinetic curves of dissolution are characterized by an ‘induction’ period of time.

The revealed long term behaviour of halloysite nanotubes could be useful in applications where interactions of halloysite with acidic and alkaline environments are considered. The methods also provide a convenient tool for increasing the specific surface area and pore volume of nanotubes without significant alteration of their shape, and the incorporation of SiO<sub>2</sub> nanoparticles inside the hollow cavity of halloysite nanotubes using acid treatment. The ability to make the tube walls of halloysite thinner in concentrated NaOH solution without creating SiO<sub>2</sub> nanoparticles inside the tubes may also prove useful in applications where a larger internal diameter is required, such as the encapsulation of large protein molecules or polymers.

## Chapter 6: Morphological Control of Synthetic Nickel Silicate $\text{Ni}_3\text{Si}_2\text{O}_5(\text{OH})_4$ Nanotubes in an Alkaline Hydrothermal Environment

### 6.1. Introduction

Nickel (II) silicates are of particular interest as lithium battery anode materials,<sup>[47]</sup> and also as core-shell encapsulation agents for catalytic nanoparticles.<sup>[261 - 263]</sup> Nanotubular  $\text{Ni}_3\text{Si}_2\text{O}_5(\text{OH})_4$  is particularly promising in these applications because it has a large specific surface area and mesoporous volume in which the pore geometry is highly regular.<sup>[81]</sup> The nanotube walls are multilayered, with each layer composed of an trioctahedral  $\text{Ni}(\text{II})\text{O}_6$  sheet which forms the outside, bonded to an  $\text{SiO}_4$  tetrahedral sheet which forms the inside of the tube.<sup>[264]</sup> This dual functionality is desirable since it pairs the ion-intercalating and adjustable magnetic properties of a nickel compound with the inertness and stabilising influence of a tetrahedral silicate structure.<sup>[47]</sup>

The morphology of  $\text{Ni}_3\text{Si}_2\text{O}_5(\text{OH})_4$  nanotubes is highly important in their applications: the diameter and length of nanotubes affects the rate of diffusion of  $\text{Li}^+$  in a lithium battery,<sup>[265, 266, 267]</sup> and their hierarchical microstructure affects the close-packing of nanotubes onto the anode surface.<sup>[268]</sup> Additionally, if nickel silicate nanotubes can be arranged as a hollow sphere, in a similar fashion to their copper analogues,<sup>[269, 270]</sup> they could be used in core-shell catalyst particles where the shell controls the rate of reaction and protects the catalyst,<sup>[261 - 263]</sup> or used to adsorb and store small molecules/ions in solution.<sup>[271]</sup> The nanotube dimensions should influence the selectivity of the shell for differently-sized particles.

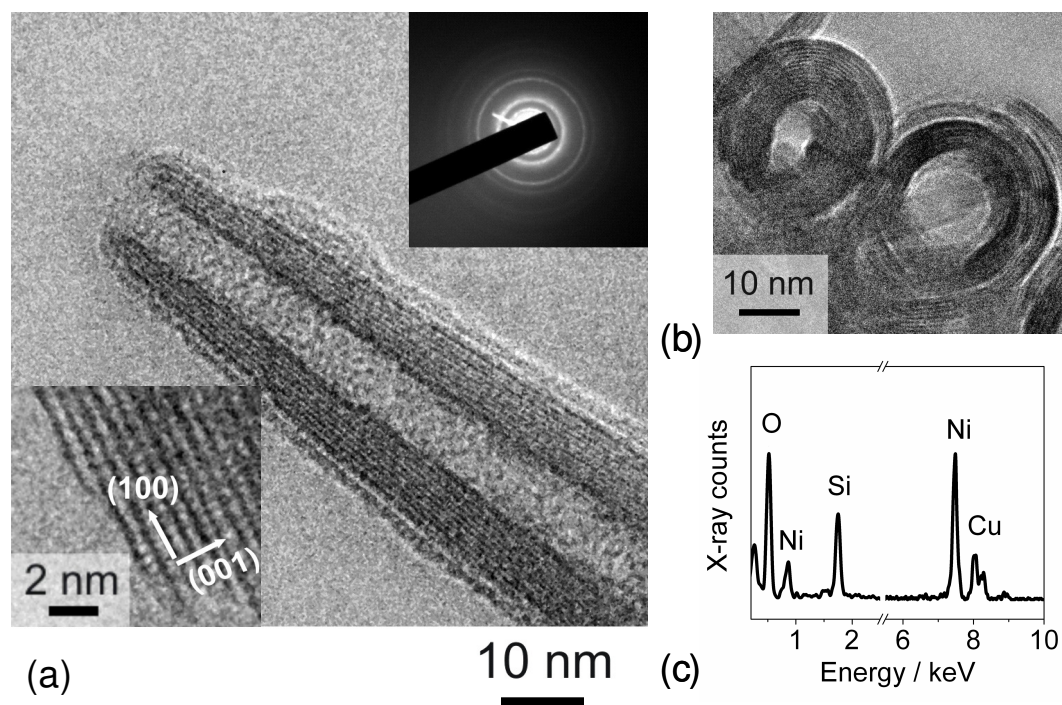
In the hydrothermal preparation of nickel silicate nanotubes, the method of Yang et al.<sup>[47]</sup> has significant advantages over other methods<sup>[81, 167, 264]</sup> in that it requires a much lower temperature of 190 – 210 °C, and does not require any special conditions such as

an inert atmosphere or non-aqueous solvent. In their hydrothermal synthesis a strongly alkaline environment was used, with 6 g NaOH added to 34 ml of solution, corresponding to 15 wt % NaOH in solution. They noted that the initial concentration of alkali in the form of NaOH was crucial in the formation of nanotubes: using 2 g of NaOH in the starting materials produced curled nanosheets instead of tubes according to their report. The effect of changing the NaOH concentration and the Ni/Si ratio in the starting materials was not further investigated.

In this chapter, the influence of changing the NaOH concentration ( $C_{\text{NaOH}}$ ) and the Ni/Si ratio of the starting materials on the morphology and porosity of the as-obtained nanotubes was systematically studied, and the range of conditions under which  $\text{Ni}_3\text{Si}_2\text{O}_5(\text{OH})_4$  nanotubes form were identified.

## 6.2. Optimisation of Ni/ Si ratio in nickel silicate nanotube synthesis

Firstly, experiments were carried out to determine the optimum Ni/Si molar ratio for nanotube synthesis in solution whilst keeping  $C_{\text{NaOH}}$  constant at 4 wt%. When a purely stoichiometric ratio of Ni/Si = 1.5 was used, an almost 100 % yield of nanotubes was obtained. An HRTEM image (Figure 6.1) of a typical nanotube in this sample clearly shows a multiwalled structure with a spacing of approximately 0.7 nm between layers, and an apparent spacing of 0.45 nm parallel to the tube axis. This 0.45 nm spacing can be attributed to the d-spacing between the (200) planes <sup>[264]</sup> suggesting that the nanotubes are scrolled around the [100] direction. The  $\text{Ni}_3\text{Si}_2\text{O}_5(\text{OH})_4$  hexagonal crystal structure of nanotubes<sup>[264]</sup> is confirmed by SAED and XRD (Figures 6.1 and 6.5). The EDX analysis of the nanotube composition shows that they are characterised by a molar Ni/Si ratio of 1.5. Although the yield of tubes is approximately 98 – 100 %, some of them are only partially scrolled (Figure 6.2), or have an irregular, conical morphology. The typical cross-section of the nanotubes is a spiral or concentric shape (Figure 6.1b). The typical inner diameter of the tubes is 10 nm, the typical outer diameter is 20 nm, and the lengths range from 30 to 225 nm.



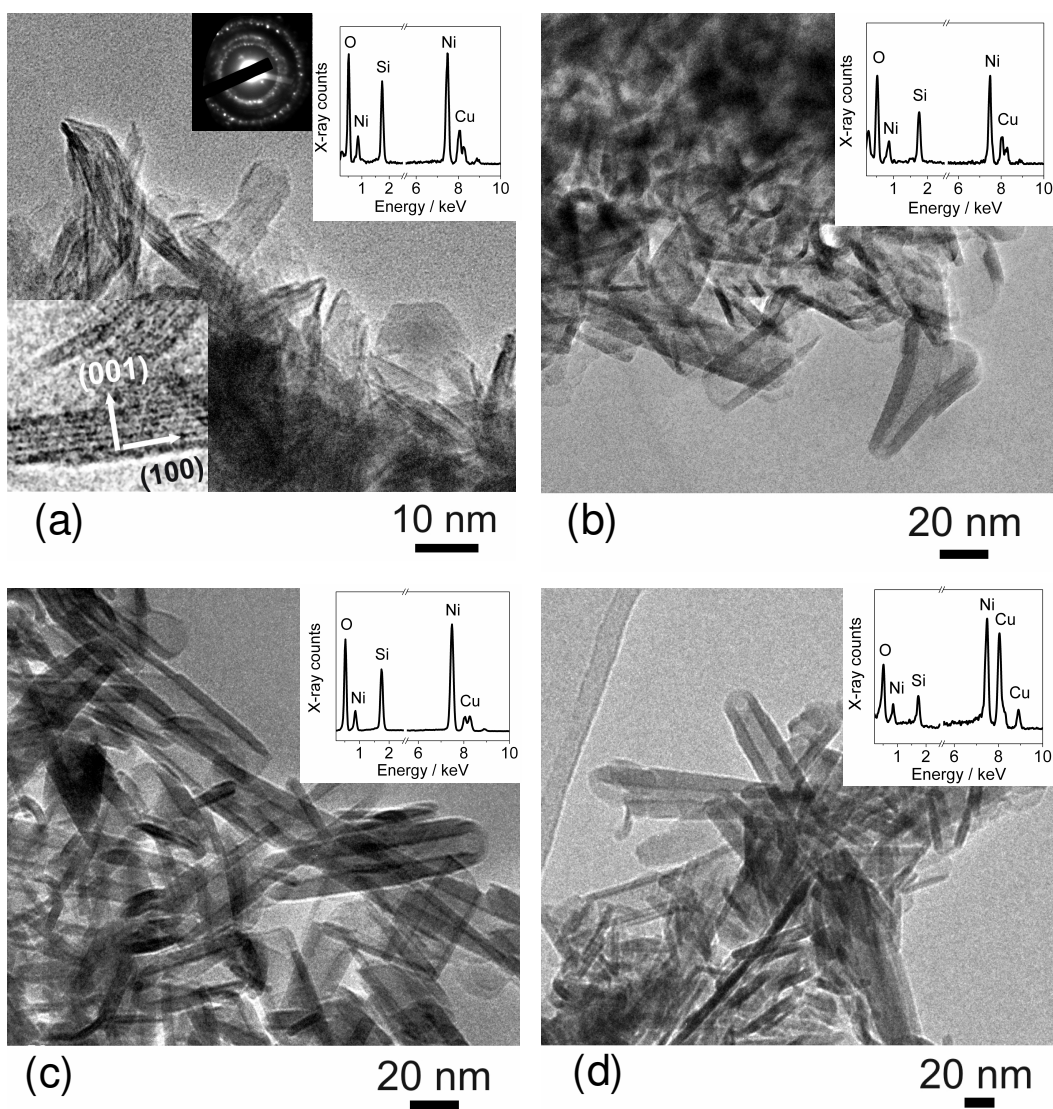
**Figure 6.1.** Analysis of nickel silicate nanotube structure, showing (a) HRTEM image of a nickel silicate nanotube formed in 4 wt % NaOH solution at a Ni/Si ratio of 1.5, with insets (bottom left corner) showing a magnified image of the layer structure of the wall with orientation of the crystal planes and (top right corner) the SAED pattern taken from an agglomeration of nanotubes, (b) a cross-sectional HRTEM image of the nanotubes, and (c) EDX data taken from image (b). The EDX signal for Cu is a background signal from the TEM grid.

Upon increasing the Ni/Si ratio above 1.5, formation of  $\text{Ni}_3\text{Si}_2\text{O}_5(\text{OH})_4$  nanotubes still occurs (Figure 6.2) and is increasingly accompanied by the growth of platy particles (see Figure 6.3) which were identified by XRD and FTIR<sup>[272, 273]</sup> as  $\beta\text{-Ni}(\text{OH})_2$  (Figures 6.4 and 6.5). In the absence of reference intensity ratios for this binary mixture, a precise quantitative analysis of the samples by XRD is difficult, however, the molar Ni/Si ratios in the products (determined by EDX) suggest that for initial molar ratios Ni/Si = 2 and 3, the products contain approximately 6 and 10 wt %  $\beta\text{-Ni}(\text{OH})_2$  respectively.

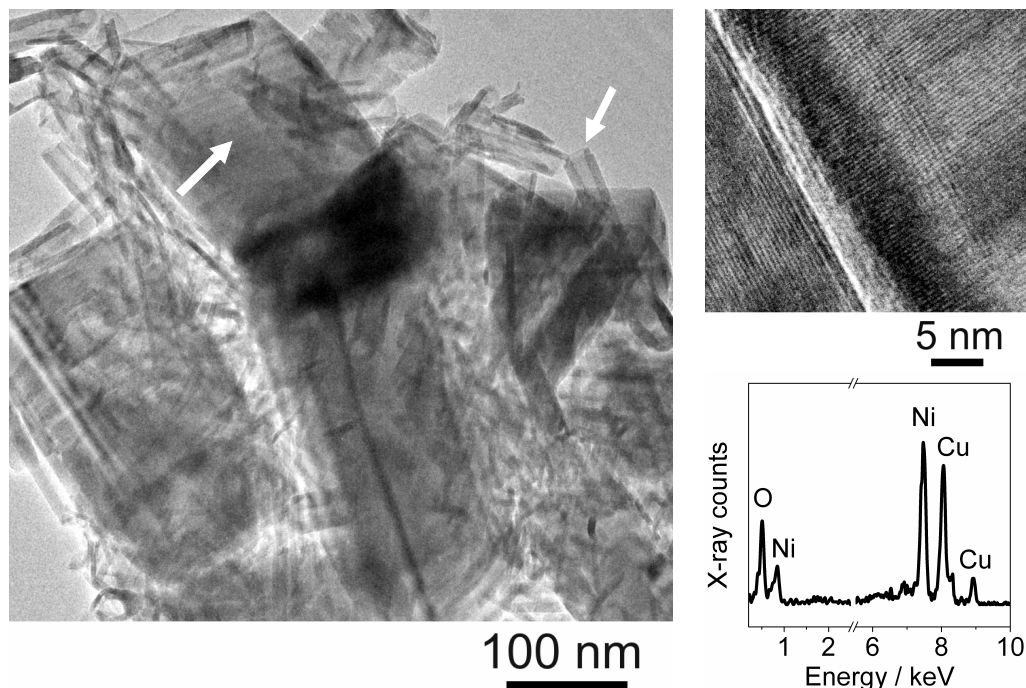
Analysis of the  $\beta\text{-Ni}(\text{OH})_2$  (001) peak at full width at half maximum (FWHM) using the Scherrer formula<sup>[274]</sup> with  $K = 0.94$  for cube-shaped crystals suggested that the  $\beta$ -



$\text{Ni}(\text{OH})_2$  particles increased in thickness (coherent area) as the Ni/Si ratio of the starting materials increased, such that the  $\beta\text{-Ni}(\text{OH})_2$  particles were approximately 90 nm thick in the Ni/Si = 2 sample and 200 nm thick in the Ni/Si = 3 sample (Table 6.1).



**Figure 6.2.** TEM and EDX images of nickel silicate products from 4 wt% NaOH solutions with Ni/Si ratio (a) 1, (b) 1.5, (c) 2 and (d) 3. The HRTEM inset in the bottom left corner of image (a) shows the layered structure of the nanosheets. The EDX spectra were taken from the centre of the images.

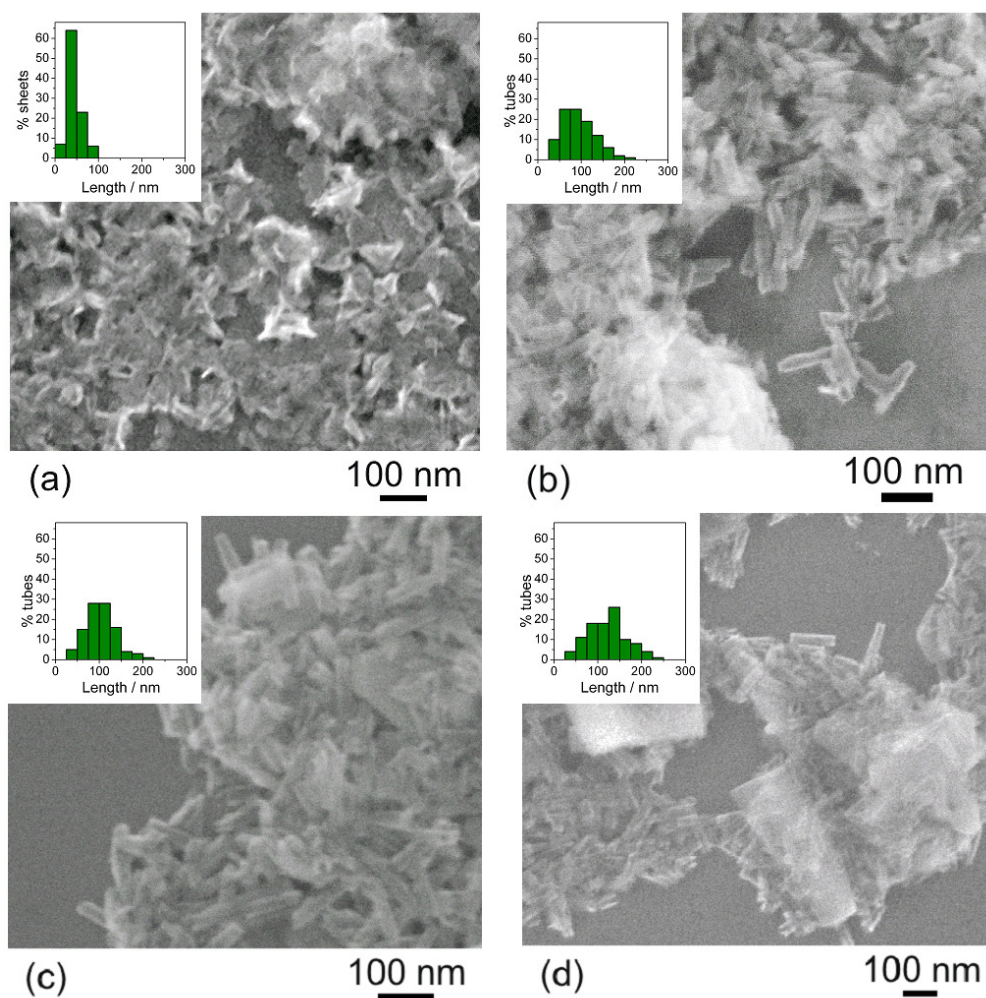


**Figure 6.3.** TEM image of  $\beta$ -Ni(OH)<sub>2</sub> particles formed at Ni/Si = 3, together with HRTEM and EDX images. The arrow on the left indicates a  $\beta$ -Ni(OH)<sub>2</sub> particle and the arrow on the right indicates a Ni<sub>3</sub>Si<sub>2</sub>O<sub>5</sub>(OH)<sub>4</sub> nanotube.

**Table 6.1.** Morphology of phases observed at different Ni/Si ratios and  $C_{\text{NaOH}} = 4$  wt %. Abbreviations:  $l$  = average length (observed by SEM),  $d_i$  = range of internal nanotube diameters,  $d_o$  = range of external diameters (observed by TEM), and  $t$  is the particle thickness along [001] estimated from the XRD pattern using the Scherrer formula. The morphological abbreviations are C = conical, T = tubular, S = sheets. Morphologies are listed in order of their abundance in the sample.

Phase	$C_{\text{NaOH}}$ / wt %	Ni/Si ratio	$l$ /nm	$d_i$ / nm	$d_o$ / nm	$t$ / nm	No. of layers	Morphology
$\text{Ni}_3\text{Si}_2\text{O}_5(\text{OH})_4$	4	1	20	-	-	5	4 - 10	S + C
		1.5	100	7 - 25	20 - 35	10	6 - 15	T + C
		2	100	10 - 25	20 - 35	10	8 - 14	T + C
		3	120	12 - 20	20 - 30	16	8 - 18	T + C
$\beta\text{-Ni}(\text{OH})_2$	4	1.5	50	-	-	60	130	S
		2	200	-	-	90	200	S
		3	500	-	-	200	440	S

Increasing the Ni/Si ratio to 3 also appears to cause a small increase in the average length of the  $\text{Ni}_3\text{Si}_2\text{O}_5(\text{OH})_4$  nanotubes from 100 to 120 nm, whilst slightly narrowing the range of the outer and inner diameters (see Figure 6.4 and Table 6.1). Analysis of the (002) peak FWHM using the Scherrer formula with  $K = 0.9$  to estimate the average particle thickness along the [001] crystallographic direction in the bulk sample suggests that the nanotube walls have a similar average thickness of  $\approx 10$  nm at all Ni/Si ratios, except at Ni/Si = 3 where they become slightly thickened to  $\approx 17$  nm (Table 6.1). It should be noted that these values are estimates only since the peak width is also affected by the amount of curvature in the crystal lattice and the degree of crystallinity of the samples.<sup>[275]</sup>



**Figure 6.4.** SEM images of products at (a) 1, (b) 1.5, (c) 2 and (d) 3 Ni/Si ratios with corresponding percentage length distributions of nanotubes.

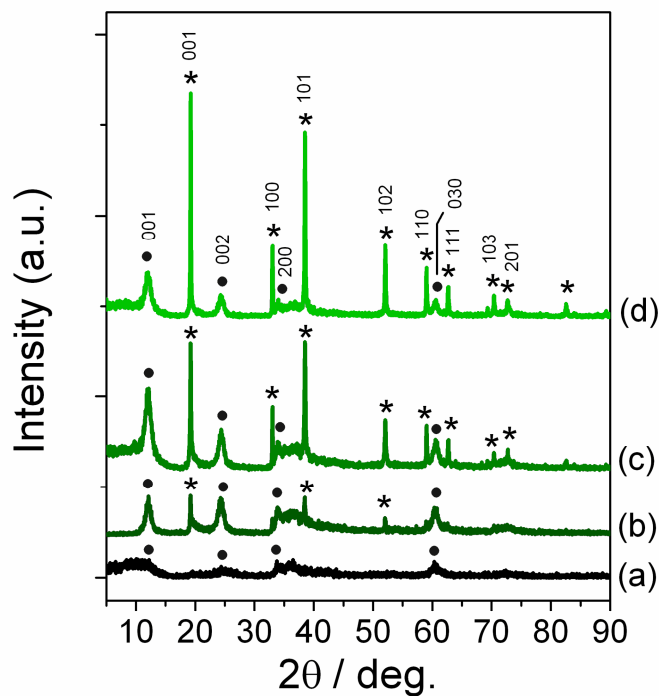
In contrast to the above observations, when the initial Ni/Si ratio is decreased to a value of 1, small nanosheets 10 - 20 nm wide are formed instead of nanotubes (Figure 6.2a). The sheets appear to possess a multilayered structure; SAED shows a diffraction pattern similar to  $\text{Ni}_3\text{Si}_2\text{O}_5(\text{OH})_4$  (Figure 6.2a) <sup>[47]</sup> but EDX confirmed that the stoichiometry of these particles is deficient in Ni(II), with a Ni/Si ratio of 1.3 (Table 6.2). It is probable that the nanosheets have the same crystal structure as the nanotubes but with a higher number of Ni(II) vacancies. Although some of the nanosheets have a flat geometry, many are curved, presumably bending around the [100] direction as in the case of the  $\text{Ni}_3\text{Si}_2\text{O}_5(\text{OH})_4$  nanotubes.

**Table 6.2.** Characterisation of bulk products at different Ni/Si ratios and  $C_{\text{NaOH}} = 4$  wt %.

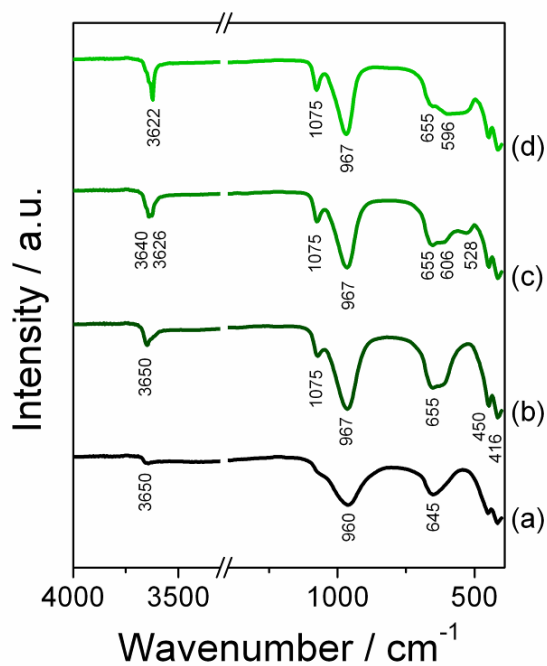
Abbreviations:  $S_{\text{BET}}$  = BET specific surface area, and  $V_{\text{pores}}$  = total pore volume.

$C_{\text{NaOH}} / \text{wt } \%$	Initial Ni/Si ratio	$S_{\text{BET}} / \text{m}^2 \text{g}^{-1}$	$V_{\text{pores}} / \text{cm}^3 \text{g}^{-1}$	Ni/Si ratio (products)
4	1	170	0.222	1.3
4	1.5	134	0.423	1.5
4	2	103	0.294	2
4	3	92	0.283	3.6

The XRD pattern of the Ni/Si = 1 sample (Figure 6.5) shows the characteristic reflections of  $\text{Ni}_3\text{Si}_2\text{O}_5(\text{OH})_4$ , but with approximately half the area under these reflection peaks compared with the Ni/Si = 1.5 sample, suggesting a lower degree of crystal ordering in the nanosheets than in the nanotubes observed at Ni/Si = 1.5. The FTIR results also show vibrational bands characteristic of the  $\text{Ni}_3\text{Si}_2\text{O}_5(\text{OH})_4$  structure, <sup>[167]</sup> but at a weaker intensity (see Figure 6.6). The crystal thickness of the nanosheets formed at Ni/Si = 1 estimated from the FWHM of the (002) peak in the XRD pattern was 5 nm compared with 10 nm in the Ni/Si = 1.5 and 2 samples, which supports the TEM observation that the number of crystal layers in the nanosheets is less than the number of layers in the nanotubular samples (Table 6.1 and Figure 6.2).

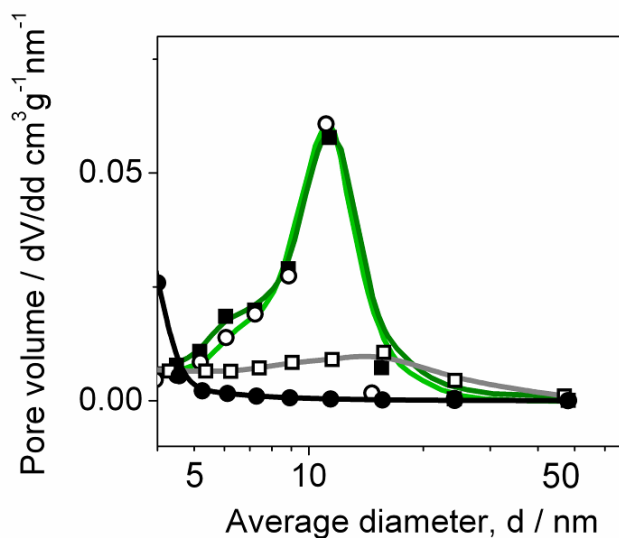


**Figure 6.5.** XRD patterns of nickel silicates synthesised at Ni/Si ratios (a) 1, (b) 1.5, (c) 2 and (d) 3. Peaks for  $\text{Ni}_3\text{Si}_2\text{O}_5(\text{OH})_4$  are labelled with (•), peaks for  $\beta\text{-Ni}(\text{OH})_2$  are labelled with (\*)



**Figure 6.6.** FTIR spectra of nickel silicates synthesised at controlled Ni/Si ratios (a) 1, (b) 1.5, (c) 2 and (d) 3.



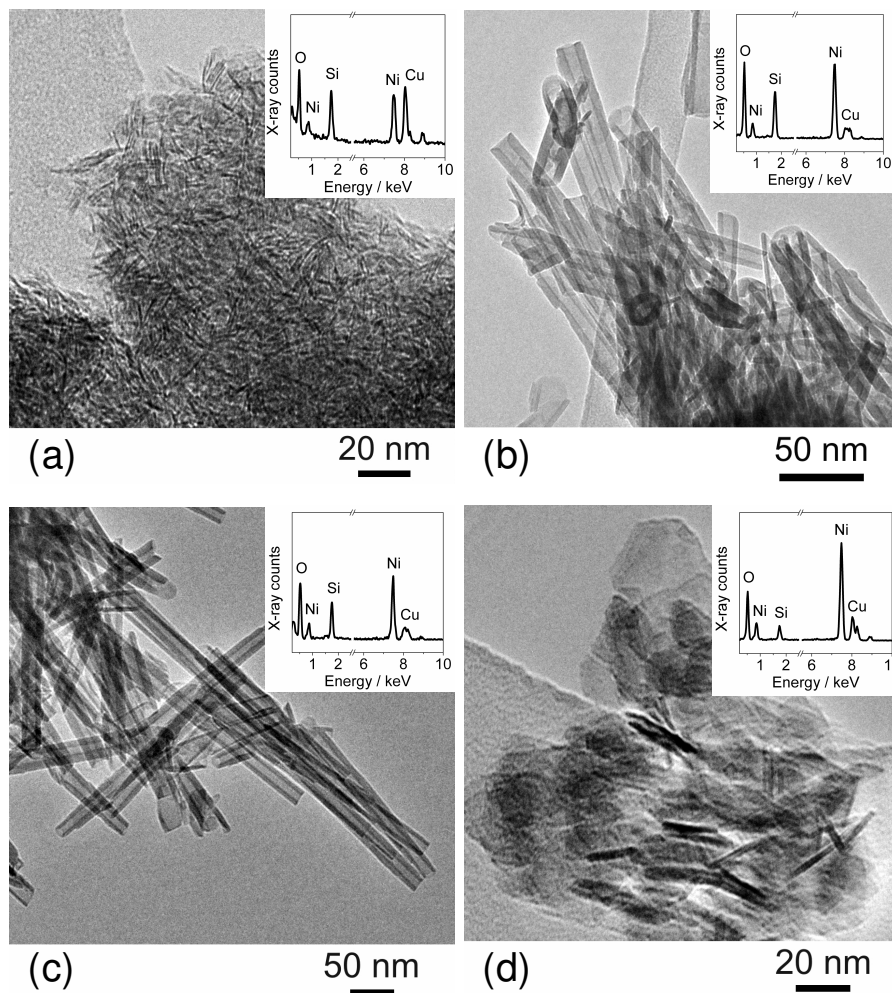


**Figure 6.7.** BJH pore-size distributions for nickel silicates synthesised at controlled Ni/Si ratios (●) 1, (■) 1.5, (○) 2 and (□) 3 at  $C_{\text{NaOH}} = 4$  wt %.

The BJH pore size distribution of the Ni/Si = 1 sample (Figure 6.7) provides the additional information that the pore diameters in the sample are almost exclusively < 5 nm, indicating that the nanosheets have smaller and more uniform pore sizes than the nanotubes formed at Ni/Si = 1.5-3. This is due to their smaller size and narrower length distribution (Figure 6.4a). The presence of large ( $\approx 200$  nm)  $\beta$ -Ni(OH)<sub>2</sub> particles in the Ni/Si = 3 sample causes a decrease in the total pore volume and a widening of the pore-size distribution (Figure 6.7 and Table 6.2), because the large particles disrupt the close-packing of the nanotubes (see Figure 6.3) and reduce the volume of inter-tubular pores.

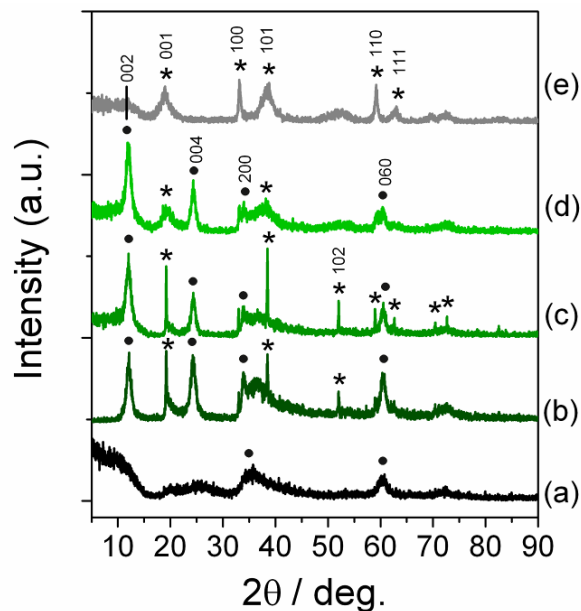
### 6.3. Effect of NaOH concentration on nickel silicate nanotube synthesis

The effect of altering the initial concentration of NaOH added ( $C_{\text{NaOH}}$ ) whilst keeping the Ni/Si ratio constant at 1.5 was also investigated. It was found that nanotubes are only formed in the range of  $C_{\text{NaOH}}$  between 2 and 10 wt. %. Increasing  $C_{\text{NaOH}}$  appears to dramatically increase the length of the tubes (Figure 6.8). For example, the typical length of tubes formed at 2 wt % NaOH is 90 nm whereas at 10 wt % the nanotubes are on average 290 nm long (see Table 6.3 and Figure 6.10). The most marked increase in length occurs in the range  $7 < C_{\text{NaOH}} < 10$  wt %.



**Figure 6.8.** TEM images of nickel silicates formed at (a) 0, (b) 7, (c) 10 and (d) 15 wt % initial NaOH concentration, with corresponding EDX spectra from the centre of the images.

According to the TEM data, as  $C_{\text{NaOH}}$  is increased the average outer diameter of the nanotubes grows slightly (from approximately 25 nm at  $C_{\text{NaOH}} = 2$  wt % to 28 nm at  $C_{\text{NaOH}} = 12$  wt %), whilst the average number of layers in their wall grows from ca. 8 at  $C_{\text{NaOH}} = 2$  wt % to ca. 16 at  $C_{\text{NaOH}} = 10$  wt %. This increase of the wall thickness results in a slight decrease in the average inner diameter of the nanotubes from approximately 19 nm to 16 nm. The average coherence area along [001] derived from the (002) XRD peak (Figure 6.9) using the Scherrer equation (Table 6.3) suggests that the increase in wall thickness with increasing  $C_{\text{NaOH}}$  is not linear, but shows a larger increase in the range  $C_{\text{NaOH}} = 7 - 10$  wt % than in the range  $C_{\text{NaOH}} < 7$  wt %.



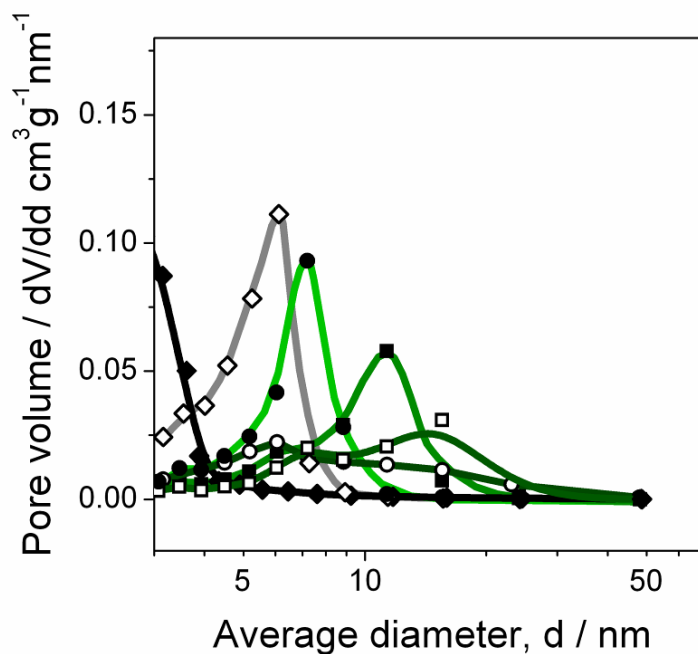
**Figure 6.9.** XRD patterns of nickel silicates synthesised at NaOH concentration (a) 0, (b) 4, (c) 7, (d) 10 and (e) 15 wt %. Peaks for  $\text{Ni}_3\text{Si}_2\text{O}_5(\text{OH})_4$  are labelled with (●), peaks for  $\beta\text{-Ni}(\text{OH})_2$  are labelled with (\*).

**Table 6.3.** Morphology of phases observed in products at different  $C_{\text{NaOH}}$  and  $\text{Ni/Si} = 1.5$ . Abbreviations:  $l$  = average length (observed by SEM),  $d_i$  = range of internal nanotube diameters,  $d_o$  = range of external diameters (observed by TEM), and  $t$  is the particle thickness along [001] estimated from the XRD pattern. The morphological abbreviations are C = conical, T = tubular, S = sheets. Morphologies are listed in order of their abundance in the sample.

Phase	$C_{\text{NaOH}}$ / wt %	Ni/Si ratio	$l$ / nm	$d_i$ / nm	$d_o$ / nm	$t$ / nm	No. of layers	Morphology
$\text{Ni}_3\text{Si}_2\text{O}_5(\text{OH})_4$	0	1.5	10	-	-	4	2-5	S
	2	1.5	90	8 - 25	20 - 30	-	4 - 12	C + T + S
	4	1.5	100	7 - 25	20 - 35	10	6 - 15	T + C
	7	1.5	170	8 - 20	20 - 30	11	7 - 16	T
	10	1.5	290	8 - 25	20 - 35	17	6 - 18	T
$\beta\text{-Ni}(\text{OH})_2$	4	1.5	50	-	-	60	130	S
	7	1.5	300	-	-	400	880	S
	10	1.5	33	-	-	10	22	S
	15	1	27	-	-	8	3 - 6	S
		1.5	40	-	-	-	4 - 15	S



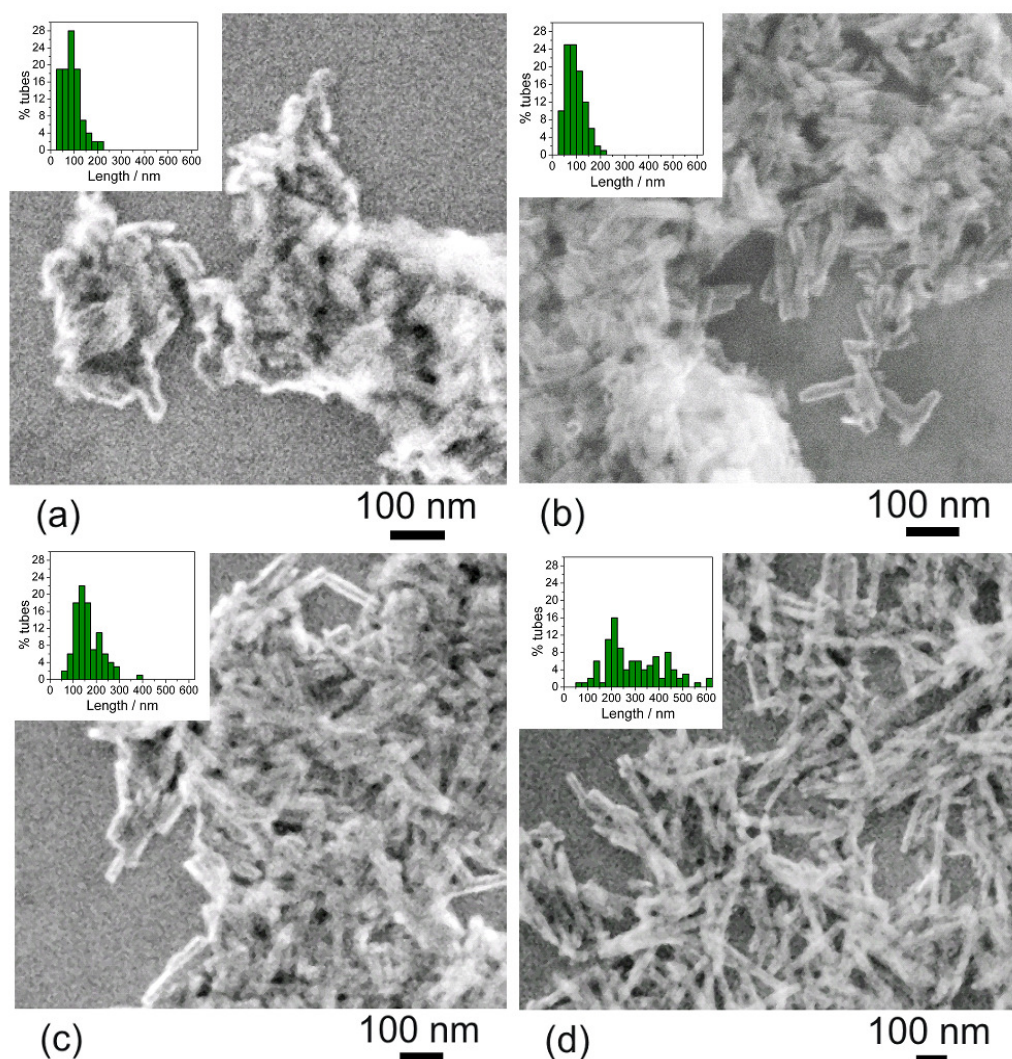
The pore-size distribution of the bulk samples obtained using liquid nitrogen adsorption and the BJH algorithm showed that upon increasing  $C_{\text{NaOH}}$  the pore sizes became more widely distributed and the mean pore size increased (Figure 6.10). The pore-size distribution of the samples at  $2 \leq C_{\text{NaOH}} \leq 10$  wt % features two characteristic peaks, one at 5 – 6 nm and another at a larger pore diameter. The position and magnitude of the peak at small pore diameter does not vary much with  $C_{\text{NaOH}}$ , whereas the position of the other peak ( $> 6$  nm) shifts to larger pore diameters with increasing  $C_{\text{NaOH}}$ . The apparent contradiction between the decreasing inner diameter of the nanotubes and the increasing average pore size with increasing  $C_{\text{NaOH}}$  indicates that the total pore volume in the sample is a combination of the inter-tubular pores formed between agglomerated nanotubes with the intra-tubular pores formed by the lumen of the nanotubes. The size of the inter-tubular pores usually depends on the length of the nanotubes,<sup>[36]</sup> because an increase in the nanotube length increases steric hindrance to their close-packing, resulting in larger inter-tubular pore sizes.



**Figure 6.10.** BJH pore-size distributions obtained from  $\text{N}_2$  adsorption at  $-196^\circ\text{C}$ , for nickel silicate nanotubes synthesised at ( $\blacklozenge$ ) 0, ( $\bullet$ ) 2, ( $\blacksquare$ ) 4, ( $\square$ ) 7, ( $\circ$ ) 10 and ( $\diamond$ ) 15 wt %  $C_{\text{NaOH}}$ .

The TEM and SEM observations (Figures 6.5 and 6.11) clearly show that the length distribution of the nanotubes widens with increasing  $C_{\text{NaOH}}$ . The presence of a few much

longer tubes in amongst shorter tubes disrupts the close-packing, causing widening and flattening of the  $> 6$  nm peak in the pore-size distribution (Figure 6.10). The pores observed below ca. 6 nm are probably caused by the intra-tubular pores and pores between aggregates of close-packed nanotubes (note that BJH may underestimate some pore sizes by more than 1 nm<sup>[276]</sup>). The specific surface area of all samples  $2 \leq C_{\text{NaOH}} \leq 10$  wt % was very similar, close to 130 m<sup>2</sup>g<sup>-1</sup> but the adsorption total pore volume at  $P = P_0$  was much lower in the 2 wt % sample due to the negligible volume of inter-tubular pores larger than 10 nm (Figure 6.10).



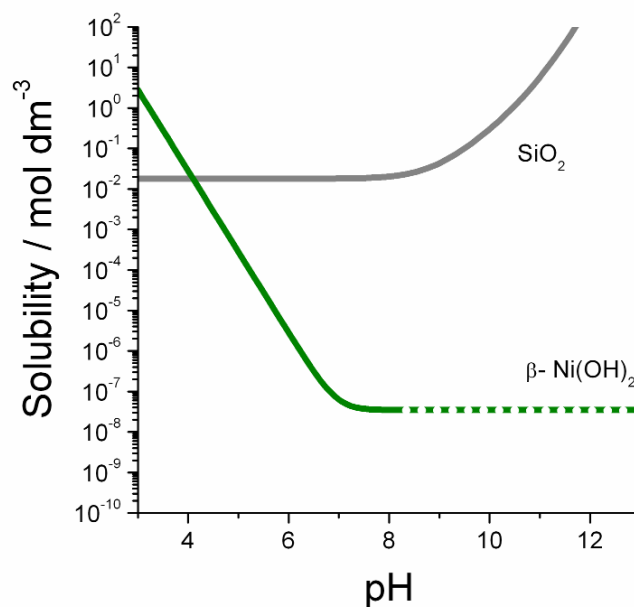
**Figure 6.11.** SEM images of nanotubes produced at (a) 2, (b) 4, (c) 7 and (d) 10 wt% NaOH with corresponding percentage length distributions. The bright haloes around the particle edges are caused by secondary electrons (see Chapter 3 page 57).

If  $C_{\text{NaOH}}$  is further increased to 15 wt% plate-like hexagonal particles (nanoplates) with a characteristic width ranging from 30 – 50 nm and thickness in the range 4 - 10 nm are formed instead of tubes. These nanoplates have a layered structure and contain a similar number of layers (4-15) to the  $\text{Ni}_3\text{Si}_2\text{O}_5(\text{OH})_4$  nanotubes formed at lower  $C_{\text{NaOH}}$ . EDX analysis of the nanoplates shows a large Si deficiency in their structure indicated by a higher Ni/Si molar ratio of 7 in the products (Figure 6.8). The XRD pattern also shows peaks characteristic of  $\beta\text{-Ni}(\text{OH})_2$  with broadening due to the small particle size (Figure 6.9e). Interestingly, similar results are also obtained at  $C_{\text{NaOH}} = 15 \text{ wt } \%$ ,  $\text{Ni/Si} = 1$ , which were the conditions used by Yang et al. in their recent publication.<sup>[47]</sup> This demonstrates a greater reliability of our method to produce nanotubes using a molar stoichiometry  $\text{Ni/Si} = 1.5$  and a lower ( $\leq 10 \text{ wt } \%$ ) NaOH concentration. It appears that if  $C_{\text{NaOH}}$  is raised above 10 wt %, most of the  $\text{SiO}_2$  which forms after hydrolysis of the initial  $\text{Na}_2\text{SiO}_3$  remains in solution after the hydrothermal treatment, since the solubility of Si(IV) in the presence of such high  $\text{OH}^-_{(\text{aq})}$  concentrations at 195 °C is very high (Table 6.2 and Figure 6.12),<sup>[112, 131, 277]</sup>. This causes the precipitation of Ni(II)-rich products.

If no NaOH is added to the starting materials, small ( $< 10 \text{ nm}$  long) aggregated multilayered nanoparticles of  $\text{Ni}_3\text{Si}_2\text{O}_5(\text{OH})_4$  are formed (Figure 6.8a). In the XRD pattern (Figure 6.9a), broad (002), (200) and (060) reflections characteristic of  $\text{Ni}_3\text{Si}_2\text{O}_5(\text{OH})_4$  were observed, and the particle thickness was estimated at 4 nm from the (002) peak using the Scherrer formula, which is in good agreement with the TEM data (Figure 6.8). An aggregation of the particles was found to have a Ni/Si ratio of 1 using EDX (Table 6.4). The excess of Si(IV), present mainly in the form of very small ( $< 5 \text{ nm}$ ) nanoparticle of amorphous silica, may be attributed to the low solubility of Si(IV) at low pH, which may be estimated as  $18 \text{ mmol dm}^{-3}$  at the final reaction pH of 6.5 (see Figure 6.12 and table 6.4). This is more than an order of magnitude smaller than the Si(IV) solubility under the conditions where nanotubes are formed. The specific area of the small  $\text{Ni}_3\text{Si}_2\text{O}_5(\text{OH})_4$  nanoparticles ( $508 \text{ m}^2 \text{ g}^{-1}$ ) is much greater than that of the nanotubes, and BJH analysis indicates a very large number of micropores (Figure 6.10).

**Table 6.4.** Characterisation of bulk products at different NaOH concentrations and Ni/Si ratios. Abbreviations  $S_{\text{BET}}$  = BET specific surface area,  $V_{\text{pores}}$  = total pore volume,  $\text{pH}_i$  = initial pH before hydrothermal treatment, and  $\text{pH}_f$  = final pH. In the final column the solubility of Si(IV) is estimated at the final reaction pH using figure 6.12.

NaOH / wt %	Initial Ni/Si ratio	$S_{\text{BET}} / \text{m}^2 \text{g}^{-1}$	$V_{\text{pores}} / \text{cm}^3 \text{g}^{-1}$	Ni/Si ratio (products)	$\text{pH}_i$	$\text{pH}_f$	Estimated amorph. $\text{SiO}_2$ solubility/ mol $\text{dm}^{-3}$ (fig. 6.12)
0	1.5	508	0.334	1.0	10	6.5	0.018
2	1.5	139	0.301	1.5	13	10.7	2.1
4	1	170	0.222	1.3	14	10.4	0.83
4	1.5	134	0.423	1.5	>14	10.6	1.4
4	2	103	0.294	2	>14	10.5	1.3
4	3	92	0.283	3.6	>14	11.0	5.5
7	1.5	114	0.396	1.5	>14	10.3	0.68
10	1.5	135	0.366	1.5	>14	10.4	0.83
15	1	-	-	9.6	>14	11.4	27
15	1.5	169	0.295	7.1	>14	11.4	27



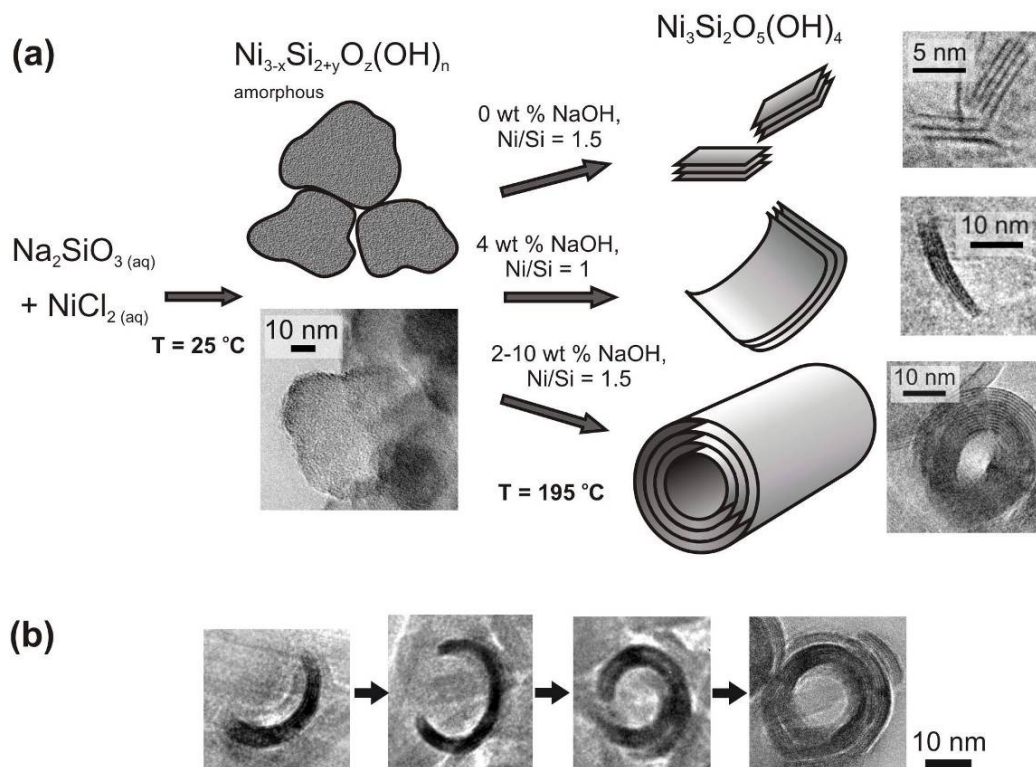
**Figure 6.12.** Solubility diagrams of  $\beta\text{-Ni(OH)}_2$  and amorphous  $\text{SiO}_2$  at 195 °C in solution with ionicity  $I = 0$ , calculated using data from <sup>[105, 112, 131, 277]</sup> (see Appendix C). Note that a logarithmic scale is used on the y-axis, and also that the solubility of  $\beta\text{-Ni(OH)}_2$  is uncertain above pH 8, <sup>[105, 282]</sup> as different studies have yielded different results.

## 6.4. Discussion of formation mechanism

To understand the formation mechanism of the observed  $\text{Ni}_3\text{Si}_2\text{O}_5(\text{OH})_4$  morphologies under different  $C_{\text{NaOH}}$  and molar Ni/Si ratios, the precipitate formed in the Ni/Si = 1.5 precursor suspension prior to the addition of NaOH and hydrothermal treatment was collected through vacuum filtration without washing and characterised using TEM. The results show that the starting material before the hydrothermal treatment is composed of particles 30 – 50 nm in diameter (Figure 6.13), which were shown by SAED to have an amorphous structure. EDX mapping of different areas of the sample shows that the distribution of Ni and Si in the particles is not uniform, and the stoichiometry can be approximated by  $\text{Ni}_{3-x}\text{Si}_{2+y}\text{O}_z(\text{OH})_n$ , where  $0 < x, y < 1$ , and  $z$  and  $n$  are unknown.

There are two major mechanisms by which nanosheets and nanotubes form in hydrothermal solutions: recrystallisation of dissolved species or exfoliation of sheets from bulk particles.<sup>[25, 26, 278-280]</sup> The above information leads us to propose a reaction scheme in which the amorphous nickel silicate starting material is transformed into crystalline  $\text{Ni}_3\text{Si}_2\text{O}_5(\text{OH})_4$  nanosheets via a dissolution-recrystallisation process at high temperature (Figure 6.13) rather than via the exfoliation of sheets from layered  $\text{Ni}(\text{OH})_2$  particles followed by the deposition and crystallization of silicate tetrahedrons from solution on their surface. It is probable that under hydrothermal conditions dissolution of amorphous nickel silicate is accompanied by the nucleation and growth of multilayered nanosheets of  $\text{Ni}_3\text{Si}_2\text{O}_5(\text{OH})_4$  as soon as the concentration of dissolved Ni(II) and Si(IV) increases above the solubility of the nanosheets. Under certain conditions which allow the precipitation of  $\text{Ni}_3\text{Si}_2\text{O}_5(\text{OH})_4$  with a high degree of crystallinity, the growing nanosheet bends around the crystallographic [100] direction and the ends of the scrolling sheet meet to form a nanotube 10 – 20 nm in diameter once it reaches a specific length  $\gg$  30 nm width  $\gg$  30 nm to form the circumference of a complete tube, as observed in the TEM images in Figure 6.13b. From the fact a small number of partially-scrolled intermediate nanosheets (incomplete tubes) observed in the Ni/Si = 1.5 products are always very short ( $\leq$  50 nm) along the [100] direction (see Figure 6.2b and Figure 6.8b and c), it appears likely that the nanotubes continue to grow along the axial [100] direction after scrolling of the nanosheets is complete. There is a

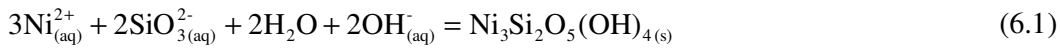
distinctive similarity between the mechanisms of formation of nickel silicate and titanate nanotubes, which follow a similar growth process to the above. [281]



**Figure 6.13.** (a) Proposed reaction mechanism in which amorphous material  $\text{Ni}_{3-x}\text{Si}_{1+y}\text{O}_z(\text{OH})_n$  recrystallises as  $\text{Ni}_3\text{Si}_2\text{O}_5(\text{OH})_4$  under hydrothermal treatment at  $195^\circ\text{C}$ . When no NaOH is added, the crystals do not grow much beyond the nucleation stage, and when the molar Ni/Si ratio is equal to 1 crystal growth does not proceed beyond curved sheets 15-20 nm long. It is only when  $\text{Ni/Si} = 1.5$  and  $C_{\text{NaOH}} = 2 - 10 \text{ wt } \%$  that the extent of recrystallisation allows the formation of complete tubes within 48 hours. The scheme in (b) shows cross-sectional TEM images of nanosheets at different stages of scrolling found in the sample obtained at  $\text{Ni/Si} = 1.5$ ,  $C_{\text{NaOH}} = 4 \text{ wt } \%$ , demonstrating the formation of nanotubes through bending of the nanosheets as they grow.

The formation of  $\text{Ni}_3\text{Si}_2\text{O}_5(\text{OH})_4$  nanotubes occurs within 2 days when the Ni/Si ratio is  $\geq 1.5$  and the concentration of added NaOH is in the range 2 – 10 wt %. In contrast,  $\text{Ni}_3\text{Si}_2\text{O}_5(\text{OH})_4$  nanosheets are observed in reaction mixtures to which no NaOH was added, or which were Ni(II)-deficient ( $\text{Ni/Si} = 1$ ). In the former case, only

$\text{Ni}_3\text{Si}_2\text{O}_5(\text{OH})_4$  small crystals were produced which had a uniform micropore size distribution and large surface area, indicating that crystal seeding occurs rapidly, but crystal growth is a slow process in the absence of added NaOH. This can be explained if we consider the chemical reactions which occur during hydrothermal treatment. The dissolution of the amorphous  $\text{Ni}_{3-x}\text{Si}_{2+y}\text{O}_z(\text{OH})_n$  starting material will release species such as  $\text{Ni}^{2+}_{(\text{aq})}$  and  $\text{SiO}_3^{2-}_{(\text{aq})}$  into solution. This initial dissolution process will be accelerated by the presence of  $\text{OH}^{-}_{(\text{aq})}$  ions, which can hydrolyse Ni-O and Si-O bonds. The released solution species can then react in several ways, for example:



In equation (6.1) above, the formation of  $\text{Ni}_3\text{Si}_2\text{O}_5(\text{OH})_4$  consumes  $\text{OH}^{-}_{(\text{aq})}$  ions from solution, which causes the observed drop in pH during the reaction (see Table 6.4). In the  $C_{\text{NaOH}} = 0$  wt % sample, this seeding process would have depleted the already low initial concentration of  $\text{OH}^{-}_{(\text{aq})}$ , making the pH fall below 7 and thus reducing the rate of subsequent crystal growth by decreasing the solution concentration of Si(IV) species (Figure 6.12) and lowering the rate of  $\text{Ni}_3\text{Si}_2\text{O}_5(\text{OH})_4$  precipitation (Equation (6.1)). The drop in pH results in precipitation of dissolved Si(IV) species in the form of the amorphous  $\text{SiO}_2$  particles observed in the sample (Equation (6.3)). At the other end of the scale, addition of NaOH up to  $C_{\text{NaOH}} = 15$  wt % results in an excess of  $\text{OH}^{-}_{(\text{aq})}$ , which appears to favour precipitation of  $\beta\text{-Ni}(\text{OH})_2$  over  $\text{Ni}_3\text{Si}_2\text{O}_5(\text{OH})_4$ . This may be due to the fact that the precipitation of  $\beta\text{-Ni}(\text{OH})_2$  in equation (6.2) consumes a larger quantity of  $\text{OH}^{-}_{(\text{aq})}$  (and therefore depends more strongly on  $C_{\text{NaOH}}$ ) than precipitation of  $\text{Ni}_3\text{Si}_2\text{O}_5(\text{OH})_4$  in Equation (6.1). Additionally, the solubility of Si(IV) is much greater under the reaction conditions (Table 6.4 and Figure 6.12), causing leaching out of the Si(IV) ions from the nickel silicates and favouring the reverse direction of Equation (6.1).

When the reaction mixture is Ni(II)-deficient (Ni/Si ratio is 1), and  $C_{\text{NaOH}} = 4$  wt %, only multilayered  $\text{Ni}_3\text{Si}_2\text{O}_5(\text{OH})_4$  nanosheets are formed with a larger size than in the



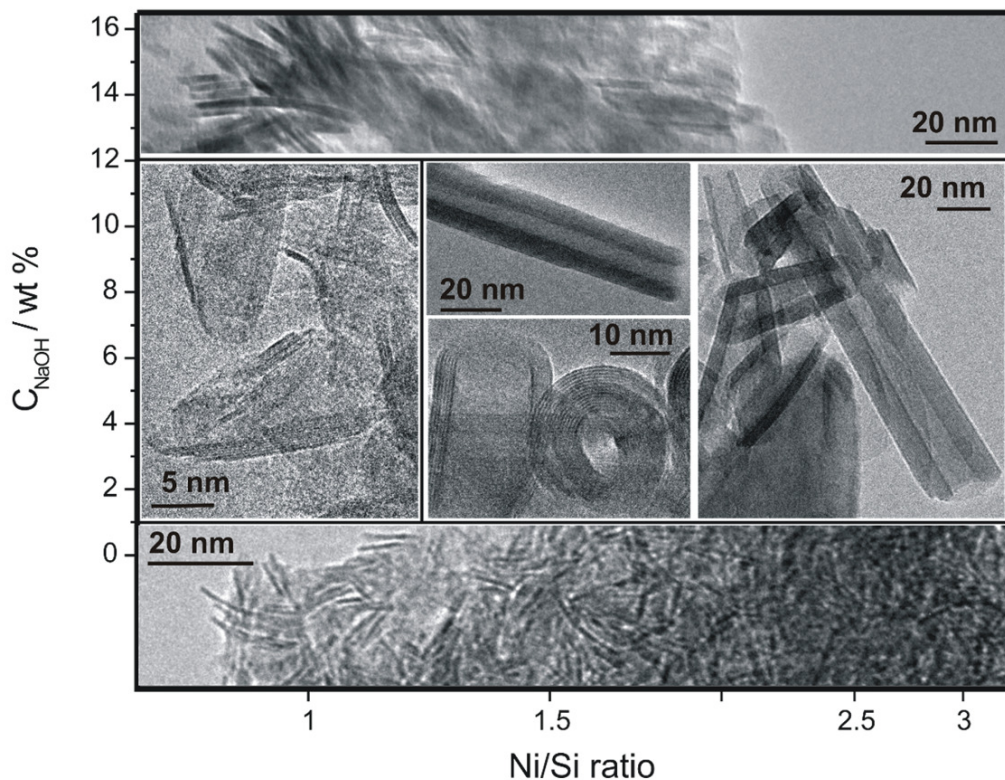
case of Ni/Si ratio 1.5 and  $C_{\text{NaOH}} = 0$  wt %. It is remarkable that deviation from the stoichiometry Ni/Si = 1.5 towards a decrease in nickel content results in a disruption in nanotube formation, whereas the opposite deviation does not interfere with the growth of nanotubes and only results in appearance of additional  $\beta\text{-Ni(OH)}_2$  as a by-product of excess nickel (II), which has very low solubility above pH 6.<sup>[105, 282]</sup> Such asymmetry provides an additional insight into the mechanism of nanotube growth. The dissolution of amorphous  $\text{Ni}_{3-x}\text{Si}_{2+y}\text{O}_z(\text{OH})_n$  under hydrothermal conditions results in the appearance of nickel (II) and silicon (IV) species in solution accompanied by the formation of multilayered nanosheets of  $\text{Ni}_3\text{Si}_2\text{O}_5(\text{OH})_4$ . Dissolved nickel (II) and silicon (IV) cause the growth of these nanosheets via crystallization on their edges. During their growth the nanosheets experience a mechanical tension inherent to their crystal structure which causes their curvature.<sup>[36]</sup> Apparently, a stoichiometric excess of added silicon (Ni/Si = 1) results in the appearance of nickel vacancies in the nanosheets (see Figure 6.2a and Table 6.2), which disrupts the crystal structure (as evidenced by line broadening in the XRD pattern, Figure 6.5) and lessens the scrolling of the nanosheets (figure 6.14a and b), ultimately preventing them from scrolling into nanotubes. In contrast, a stoichiometric excess of added nickel (Ni/Si  $\geq$  1.5) does not cause silicon vacancies in the nanosheets and the excess of nickel (II) is precipitated in the form of  $\beta\text{-Ni(OH)}_2$  (figure 6.3), which form complete nanotubes (see Figure 6.2) with the excess of nickel (II) precipitated in the form of  $\beta\text{-Ni(OH)}_2$ .

The increase in the average length of the  $\text{Ni}_3\text{Si}_2\text{O}_5(\text{OH})_4$  nanotubes with increasing added  $C_{\text{NaOH}}$  between 2 and 10 wt % can be explained by the fact that addition of  $\text{OH}_{(\text{aq})}$  would increase the dissolution rate of the amorphous starting material, and would thus increase the concentration of dissolved Ni(II) and Si(IV) species (equation (6.1)). This potentially increases the growth rate of the nanotubes,<sup>[283]</sup> meaning that as the activity of  $\text{OH}_{(\text{aq})}$  in the solution is increased, the tubes become longer on average. The increase in the average nanotube length caused by intensification of the synthesis process is also in agreement with a similar tendency observed during the formation of titanate nanotubes, reflecting a certain commonality in the mechanisms of these two processes.<sup>[97, 284]</sup>



## 6.5. Conclusions

The effect of both the molar ratio Ni/Si in the starting materials ( $\text{NiCl}_2$  and  $\text{Na}_2\text{SiO}_3$ ) and the concentration of aqueous NaOH in the precursor suspension on the structure, morphology and dimensions of nanostructured nickel silicates formed under hydrothermal conditions at 195 °C have been systematically studied. Figure 6.14 schematically illustrates the distribution of typical products at variable reaction conditions.



**Figure 6.14.** Schematic phase diagram indicating the typical nanostructures of nickel (II) silicates and  $\beta\text{-Ni(OH)}_2$  formed at different NaOH concentration ( $C_{\text{NaOH}}$ ) and molar Ni/Si ratio.

It has been found that multiwalled nanotubes of  $\text{Ni}_3\text{Si}_2\text{O}_5(\text{OH})_4$  with a typical inner diameter of 8 – 25 nm are formed at  $\text{Ni/Si} \geq 1.5$  and  $C_{\text{NaOH}}$  is in range 2 – 10 wt %. Over this range of NaOH concentration, the average length of the nanotubes increases from 90 to 300 nm, and the length distribution widens as  $C_{\text{NaOH}}$  is increased. When

$C_{\text{NaOH}}$  is below 2 wt %,  $\text{Ni}_3\text{Si}_2\text{O}_5(\text{OH})_4$  nanosheets with a characteristic thickness of only 4 nm are obtained. Above 10 wt%, all Si(IV) is leached from the structure to produce small  $\beta\text{-Ni}(\text{OH})_2$  nanoplates as the only product.

An increase in the Ni/Si ratio in the reaction mixture results in formation of nanotubes contaminated with  $\beta\text{-Ni}(\text{OH})_2$  nanoplates, whereas a decrease in the Ni/Si ratio below the stoichiometric proportion of 1.5 disrupts the formation of nanotubes leading to partially curved multilayered Ni(II)-deficient  $\text{Ni}_3\text{Si}_2\text{O}_5(\text{OH})_4$  nanosheets with an arc-shaped cross-section.

The obtained results allow us to not only recommend a simple and effective method for exerting control over nanotube morphology including the length distribution and pore diameters, but also to provide an insight into the mechanism of the reaction, which proceeds through the following stages: precipitation of amorphous  $\text{Ni}_{3-x}\text{Si}_{2+y}\text{O}_z(\text{OH})_n$  followed by its dissolution under alkaline hydrothermal conditions, which results in the crystallisation of multilayered nanotubes or nanosheets of  $\text{Ni}_3\text{Si}_2\text{O}_5(\text{OH})_4$ , which scroll into nanotubes under the reaction conditions. Nanosheets at several different stages of scrolling were detected using HRTEM and reported for the first time.

The range of novel nanostructured nickel silicates (nanotubes and nanosheets) prepared in this chapter could be potentially useful in applications such as coating for lithium battery anode surfaces and catalysis.



## Chapter 7: Low Temperature Synthesis of Nanostructured Vanadium Oxide

### 7.1. Introduction

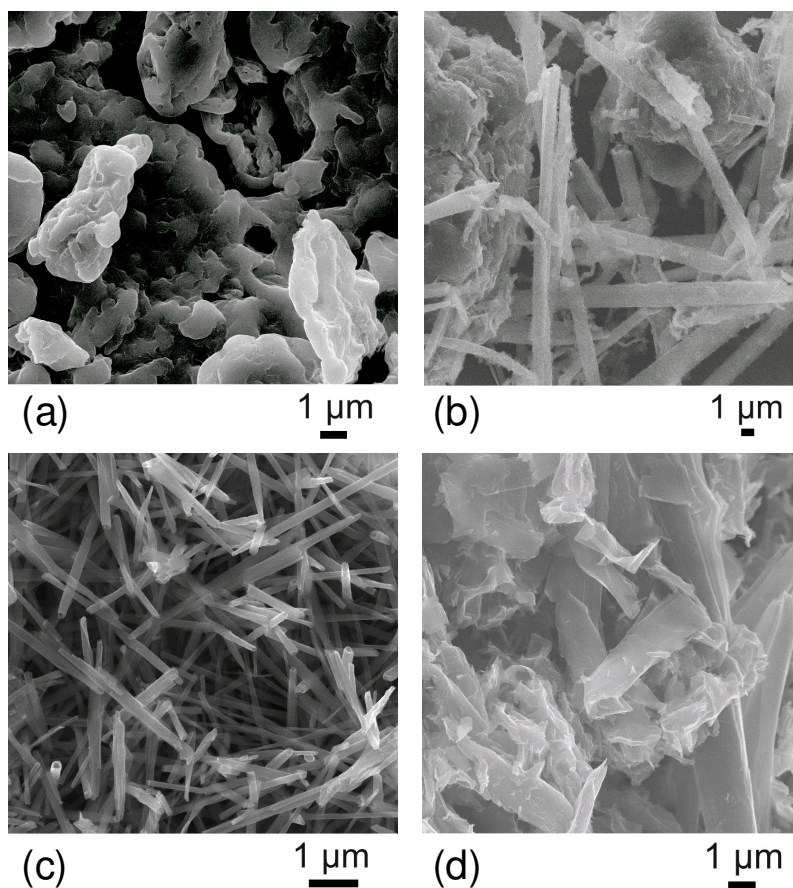
The purpose of the work in this chapter was to synthesise dodecylamine-intercalated vanadium oxide ( $\text{VO}_x$ ) structures at different temperatures outside the temperature range in which nanotubes normally form, in order to deduce the evolution of  $\text{VO}_x$  elongated structures and the scrolling mechanism by which nanotubes are formed. This approach has been successful with titanate nanotubes: analysis of the morphology and crystal structure of the reaction products observed below and above the typical nanotube synthesis temperature (nanosheets and nanofibres respectively) has allowed the proposal of a mechanism based on preferential crystallisation of titanate nanosheets along the [001] crystallographic direction, followed by scrolling of elongated nanosheets around [010] to form nanotubes.<sup>[97]</sup>

The addition of a chemical species which aids the dissolution of metal oxide species was shown to lower the temperature of titanate nanotube synthesis<sup>[97, 285]</sup> by increasing the solubility of Ti(IV) in the precursor materials ( $\text{TiO}_2$  P25 nanoparticles) and thus increasing the rate of crystallisation of nanosheets at a given temperature. This was achieved through mixing  $10 \text{ mol dm}^{-3}$  potassium hydroxide (KOH) solution into the highly concentrated  $10 \text{ mol dm}^{-3}$  NaOH solvent. Vanadium oxide nanotubes, on the other hand, are synthesised in an aqueous, weakly alkaline ( $\text{pH} < 10$ ) solvent containing an excess of primary amines ( $\text{RNH}_2$ ).<sup>[37]</sup> The addition of the bidentate basic ligand ethylenediamine to the reaction suspension was shown by preliminary experiments (Section 7.4) to increase the solubility of the dodecylamine-intercalated  $\text{V}_2\text{O}_5$  precursor materials at room temperature. Therefore, the effect of adding this ligand at 90, 130 °C was studied in this chapter in an attempt to form  $\text{VO}_x$  nanotubes below the normal synthesis temperature of 180 °C.

## 7.2. Influence of temperature on vanadium oxide nanostructure

### 7.2.1. Changes in morphology

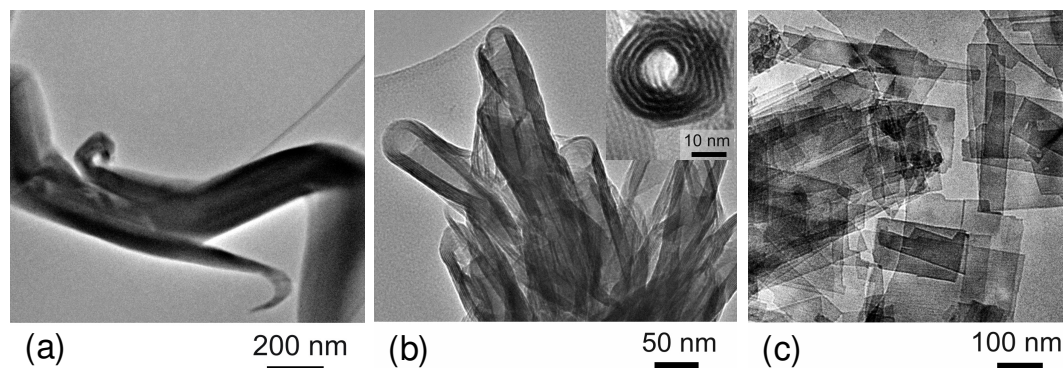
As described in the literature review (section 2.1),  $\text{VO}_x$  nanotubes are formed via the hydrothermal treatment of an aqueous precursor suspension of amine-intercalated  $\text{V}_2\text{O}_5$ . In this work, the amine selected as the intercalating agent was dodecylamine,  $\text{C}_{12}\text{H}_{25}\text{NH}_2$ , and the molar ratio of V: amine in the starting materials was 2:1 (see sections 3.1.4 p. 51). The effect of altering the hydrothermal treatment temperature of the dodecylamine-intercalated  $\text{VO}_x$  precursor suspension was studied at 4 different temperatures: 90, 140, 180 and 220 °C. SEM images of the products after 7 days hydrothermal treatment at each temperature are shown below in Figure 7.1.



**Figure 7.1.** SEM images showing the structure of dodecylamine-intercalated  $\text{VO}_x$  after 7 days hydrothermal treatment at (a) 90, (b) 140, (c) 180 and (d) 220 °C.

At 180 °C elongated  $\text{VO}_x$  nanotubes are formed with a 100 % yield, and are characterised by an external diameter 50 – 150 nm, an internal diameter 10 – 40 nm, and a length of up to 5 microns. At 140 and 220 °C, either side of the optimum nanotube synthesis temperature,  $\text{VO}_x$  nanosheets are formed instead of nanotubes. The morphology of these nanosheets is very different; those formed at 140 °C are elongated, having a length in the range 5 – 45  $\mu\text{m}$  and width in the range 1 – 3  $\mu\text{m}$ . The aspect ratio (length/width) of these nanosheets can be as large as 27, whereas the nanosheets formed at 220 °C have a morphology approaching that of a square, with length 0.2 – 10  $\mu\text{m}$ , width 0.1 – 1.6  $\mu\text{m}$  and an average aspect ratio  $\approx 5$ . After 7 days hydrothermal treatment at 90 °C the nanoparticles observed appear to be almost unchanged from the precursor material (see Figure 7.8a page 141).

The TEM image of the sample in Figure 7.2a shows the flexible nature of the nanosheets formed at 140 °C; the ends of the sheets demonstrate some scrolling behaviour, forming scroll-like shapes with a diameter of 100 – 200 nm at the ends of the nanosheet. By contrast, the nanosheets formed at 220 °C (Figure 7.2c) are rigid and inflexible, due to the loss of amine molecules from the interlayer spaces (see Figure 7.3). They appear to be thinner than the nanosheets formed at 140 °C, which is probably the result of particle exfoliation triggered by the loss of interlayer amine. At 180 °C, nanotubes with an almost perfectly circular cross-section are formed (Figure 7.2b).



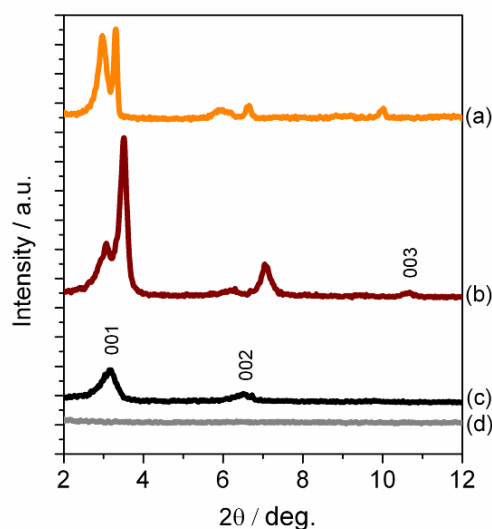
**Figure 7.2.** TEM images showing (a) scrolling of  $\text{VO}_x$  nanosheets synthesised at 140 °C around the long axis, (b) fully-formed  $\text{VO}_x$  nanotubes synthesised at 180 °C, with an inset showing the cross-section of a nanotube, and (c)  $\text{VO}_x$  nanosheets synthesised at 220 °C.



These results show that an increase in hydrothermal synthesis temperature up to 180 °C promotes the morphological changes nanoparticles → elongated nanosheets → nanotubes. If the synthesis temperature is raised above 180 °C, the intercalated structure collapses due to loss of interlayer amine.

### 7.2.2. Changes in crystal structure

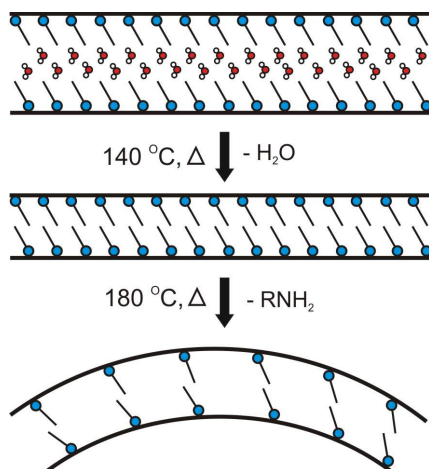
The crystal structures of the bulk samples synthesised at 140, 180 and 220 °C were analysed using X-ray diffraction. The diffraction peaks at low angles ( $2\theta < 12^\circ$ ) show the (001), (002) and (003) reflections from the interlayer spaces, and the diffraction peaks at higher  $2\theta$  show the internal structure of the  $\text{VO}_x$  layers. The low angle diffraction peaks in Figure 7.3 show that the dodecylamine-intercalated precursor material with approximate stoichiometry  $\text{V}_2\text{O}_5(\text{C}_{12}\text{H}_{25}\text{NH}_2)_2 \cdot n\text{H}_2\text{O}$  <sup>[286]</sup> formed prior to hydrothermal treatment contains two different interlayer spacings, which can be measured as 2.67 and 2.97 nm using the intense (001) peaks. Since the length of the dodecylamine molecule is calculated as 1.49 nm, <sup>[287]</sup> and the carbon chain probably lies at an angle close to  $54.75^\circ$  from the  $\text{V}_2\text{O}_5$  surface (assuming tetrahedral bond angles), the interlayer space occupied by the dodecylamine bilayer is approximately 2.43 nm. Therefore, the 2.67 and 2.97 nm spacings probably represent the intercalation of single and double layers of  $\text{H}_2\text{O}$  respectively (the  $\text{H}_2\text{O}$  molecule has a Van der Waals radius  $\approx 0.3$  nm <sup>[288]</sup>).



**Figure 7.3.** Low-angle x-ray diffraction patterns for (a) original dodecylamine-intercalated precursor material, and after 7 days hydrothermal treatment at (b) 140, (c) 180 and (d) 220 °C.

After 7 days of hydrothermal treatment at 140 °C the two (001) peaks of the precursor material have shifted to 2.52 and 2.89 nm, with the larger area under the 2.52 nm peak (figure 7.3). This change suggests that upon heating the precursor undergoes almost complete dehydration of the interlayer space, and possibly also a slight change in the conformation of the amine chains between layers without the removal of amine molecules from the interlayer spaces by heating.

After 7 days treatment at 180 °C only one (001) peak is observed at 2.78 nm which is in good agreement with previous work on dodecylamine-intercalated  $\text{VO}_x$  nanotubes.<sup>[289]</sup> The FWHM broadening in the major peak suggests a smaller average crystallite size than at 140 °C (see Figures 7.2a and b) as well as a lesser crystallographic ordering, which may be consistent with loss of more than two-thirds of the amine molecules from the interlayer space leading to the proposed molecular formula of the nanotubes  $\text{VO}_{2.43 \pm 0.03} (\text{RNH}_2)_{0.27 \pm 0.01}$ .<sup>[37]</sup> The single (001) peak suggests that scrolling of the nanosheets into nanotubes creates a single interlayer environment containing a specific geometric arrangement of the amine alkyl chains. The different interlayer spacing compared to the sample treated at 140 °C could be caused by a geometric rearrangement of the amine molecules as the structure curves, with the alkyl chains at a higher angle to the curved surface. It is possible that loss of most of the amine molecules is a requirement for the structure to achieve enough flexibility to bend (Figure 7.4).

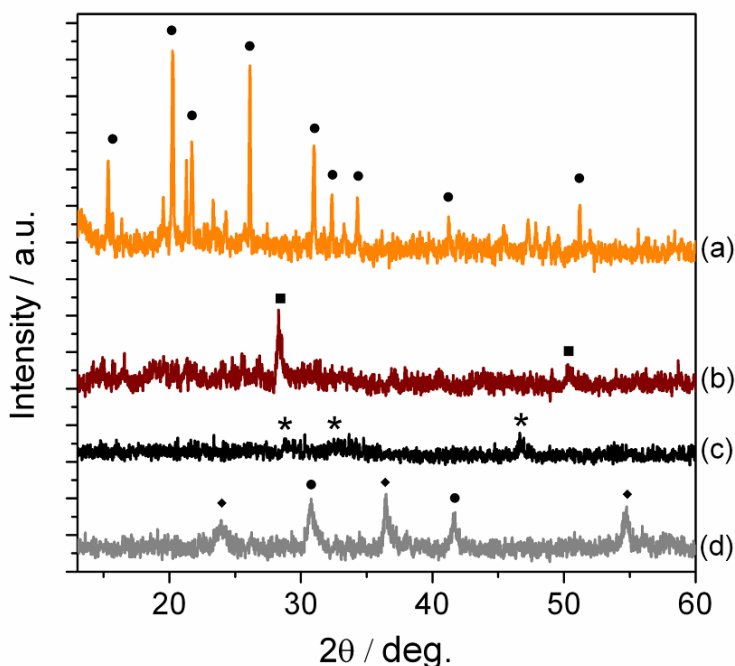


**Figure 7.4.** Schematic diagram showing a possible mechanism for  $\text{VO}_x$  layer bending to form nanotubes. Intercalating water is lost from the structure, and the loss of amine molecules upon further heating makes the interlayer space less rigid, allowing the structure to bend.



After 7 days treatment at 220 °C, all of the intercalated amine has been removed and interlayer diffraction peaks are no longer observed (Figure 7.3d). According to the TEM images the  $\text{VO}_x$  structure has collapsed into thin, fragmented nanosheets with a structure partially oxidised to  $\text{V}_2\text{O}_5$  (see Figure 7.5).

Structural analysis of the  $\text{VO}_x$  layers using XRD at higher values of  $2\theta$  is shown in Figure 7.5. The precursor material can be indexed to a pure crystalline  $\text{V}_2\text{O}_5$  phase. After hydrothermal treatment at 140 °C for 7 days all of these structural peaks disappear, and are replaced by two peaks at  $2\theta = 28.3, 50.3$ , which cannot be indexed to any of the common  $\text{V}_n\text{O}_{2n+1}$  phases.<sup>[290]</sup> The small number of peaks suggests that the vanadium oxide layers are not characterised by a regular short-range order, and probably have a stoichiometry somewhere between  $\text{V}_2\text{O}_5$  and  $\text{VO}_{2.45}$  (or  $\text{V}_{20}\text{O}_{49}$ ), the formula of  $\text{VO}_x$  nanotubes.<sup>[37]</sup>



**Figure 7.5.** XRD patterns of (a) original precursor and after hydrothermal treatment at (b) 140, (c) 180 and (d) 220 °C. The symbols correspond to (●)  $\text{V}_2\text{O}_5$  (\*)  $\text{VO}_{2.45}$  (■) unknown  $\text{V}_2\text{O}_5 - \text{VO}_{2.45}$  phase, and (♦) unknown  $\text{V}_2\text{O}_5 - \text{VO}_2$  phase.

After hydrothermal treatment at 180 °C, some broad diffraction peaks are observed corresponding to the  $\text{VO}_x$  ( $x = 2.43$ ) structure, which is similar to the  $\text{V}_7\text{O}_{16}$  structure.<sup>[68]</sup>

The clearest peak is the third peak corresponding to the [310] reflection.<sup>[68]</sup> After treatment at 220 °C, different diffraction peaks are observed which suggest partial re-oxidation of the structure to V<sub>2</sub>O<sub>5</sub> alongside an unknown phase (which may lie somewhere between the V<sub>3</sub>O<sub>8</sub> and V<sub>2</sub>O<sub>5</sub> structures, but cannot be indexed to any known phase). The broadening of the crystal reflections after hydrothermal treatment at 140 - 220 °C indicates a decrease in average particle size from the precursor material (Figure 7.5).

### 7.3. Influence of temperature on vanadium concentration

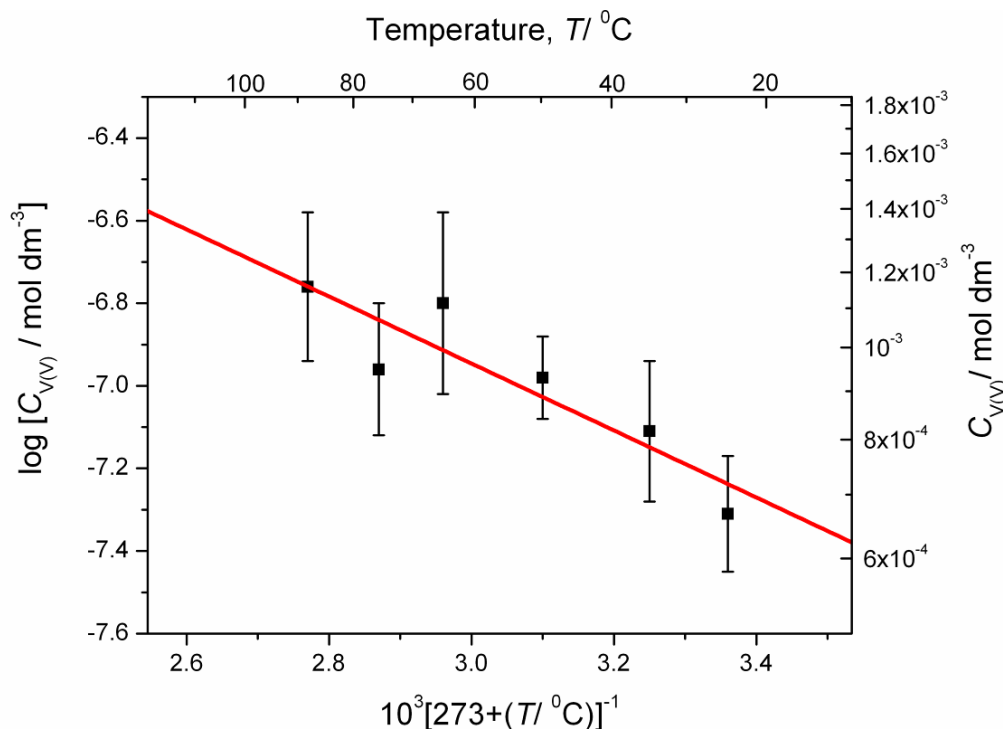
From the SEM images (Figure 7.1), it is clear that after hydrothermal treatment of the V<sub>2</sub>O<sub>5</sub>-dodecylamine precursor at 140-180 °C the resulting vanadium oxide nanosheets or nanotubes are longer and thinner than the original precursor particles (Figure 7.8a). The particles are most likely growing longer through dissolution and recrystallisation of the solvated V(V)<sub>(aq)</sub> species onto the edges of particles. An experiment was designed to estimate the relationship between vanadium solubility and temperature in the range 25 – 90 °C (see Chapter 3.4.). The relationship can be extrapolated to 180 °C in order to estimate the equilibrium concentration of vanadium at the nanotube synthesis temperature.

The graph in Figure 7.6 shows the least squares linear regression fit of the measured data, plotted as the logarithm of vanadium concentration against the reciprocal of temperature. Each point represents the mean of the three measurements taken at each temperature, and the error bars represent the standard deviation of each point. It can be seen from the graph that the standard deviation is greater at higher temperature: this is caused by the difficulty of rapidly transferring the heated solutions into a vial during filtration before any cooling and precipitation of vanadium has occurred.

The equation of the linear fit is given by:

$$\log_e[C_{\text{V(V)}} / \text{mol dm}^{-3}] = \frac{-0.811}{10^3 \cdot T / \text{K}} - 4.511 \quad (7.1)$$

Extrapolation of this line to 180 °C gives a V(V) concentration of 1.83 mmol dm<sup>-3</sup>. This is almost triple the concentration at 25 °C. The slope of the graph represents  $-10^{-3}(\Delta H/R)$ , where  $\Delta H$  is the enthalpy of dissolution and  $R$  is the molar gas constant. Hence the enthalpy of vanadium dissolution from dodecylamine-intercalated V<sub>2</sub>O<sub>5</sub> can be estimated as 6.7 kJ mol<sup>-1</sup>. This is actually very similar to the enthalpy of dissolution of TiO<sub>2</sub> P25 nanoparticles in pure KOH solution. [97]



**Figure 7.6.** Graph showing the relationship between the logarithm of vanadium concentration (mol dm<sup>-3</sup>) and the reciprocal of temperature, in degrees Kelvin. The error bars show the standard deviation for each point. The right-hand y-axis shows the measured solution concentration of vanadium, and the top x-axis shows the temperature in degrees Celsius.

Thus, the solubility of dodecylamine-intercalated V<sub>2</sub>O<sub>5</sub> precursor material in aqueous solution increases with temperature, and can be estimated as being almost 3 times greater at 180 °C than at room temperature. This undoubtedly increases the rate of dissolution and recrystallisation of the precursor material, such that elongated structures are formed within 7 days above 90 °C. Vanadium oxide nanotubes are elongated along the [110] crystallographic direction, [68] which corresponds to the preferred direction of crystal growth of the nanosheets after scrolling.

From the results of this section and the previous section, it appears likely that in order to lower the  $\text{VO}_x$  nanotube synthesis temperature to below 100 °C under ambient pressure, it is necessary to (i) decrease the enthalpy of V(V) dissolution to  $\ll 6.7 \text{ kJmol}^{-1}$  to increase the rate of nanosheet growth from the initial nanoparticles (Figure 7.8a) and (ii) alter the solvent composition so that  $\approx 2/3$  dodecylamine molecules are removed from the interlayer spaces at a temperature below 180 °C. In the next section, the use of the ethylenediamine ligand to achieve these aims was explored.

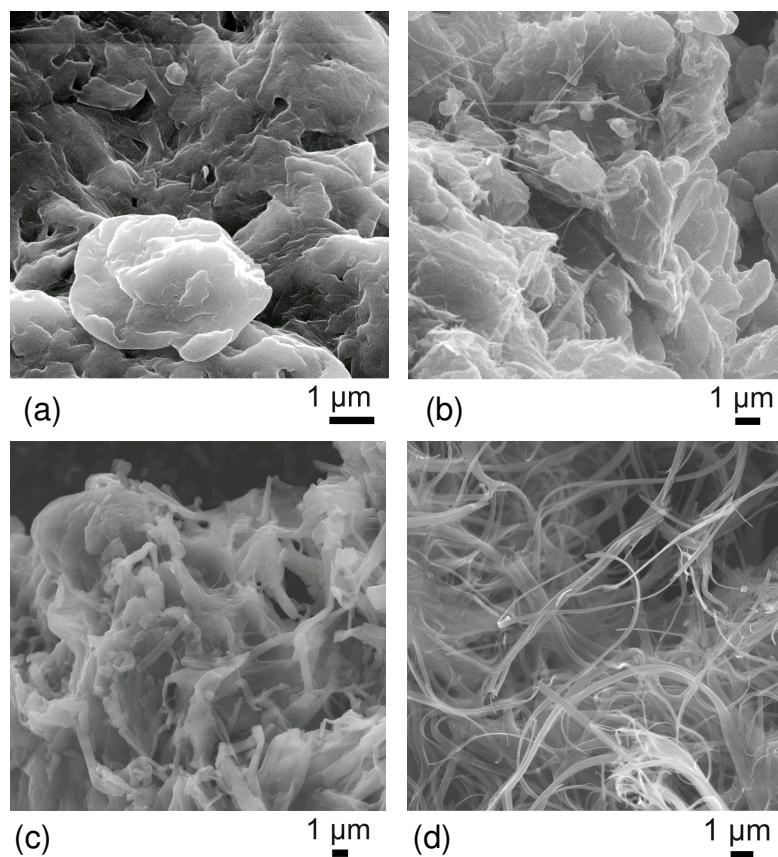
#### 7.4. Addition of ethylenediamine ligand to synthesis

As a bidentate ligand, ethylenediamine (en) should be capable of forming complexes with V(V) such as  $[\text{VO}_2(\text{H}_2\text{O})_2(\text{en})]^-$  or possibly even  $[\text{VO}_2(\text{en})_2]^{3-}$ . The formation constants for these complexes are not known, but based on the knowledge of (en) complexes of other transition metal ions <sup>[291]</sup> it is assumed that formation of these complexes is energetically favourable. Therefore, addition of ethylenediamine to a suspension of  $\text{V}_2\text{O}_5$  is expected to increase the equilibrium concentration of the solvated V(V) species: preliminary experiments showed that 0.02 g solid  $\text{V}_2\text{O}_5$  in a  $10 \text{ cm}^3$  aqueous suspension is rapidly dissolved when ethylenediamine is added to the solution at a concentration of  $0.01 \text{ mol dm}^{-3}$  under stirring.

Although other multidentate ligands such as EDTA, may have more favourable energies of complexation with V(V), ethylenediamine was chosen as the chelating agent in this work because of its simple  $(\text{CH}_2\text{NH}_2)_2$  structure. This avoids the more complicated bonding effects and redox processes that may occur as side reactions if double bonds such as  $\text{C}=\text{O}$  were present.

Ethylenediamine was added to the  $\text{V}_2\text{O}_5$ -dodecylamine precursor suspension prior to 90 °C reflux under ambient pressure, at a concentration of 0.001, 0.01 or  $0.1 \text{ mol dm}^{-3}$  (see Section 3.1.5, page 52). The results of 7 days hydrothermal treatment of these suspensions at 90 °C is shown in Figure 7.7. The precursor material showed a growing tendency to transform into thin elongated nanosheets with increasing ethylenediamine concentration, until at  $0.1 \text{ mol dm}^{-3}$  concentration a 100 % yield of these long, ribbon-like nanosheets was obtained within 7 days. The nanosheets also became longer and

thicker with increasing ethylenediamine concentration, reaching up to 30  $\mu\text{m}$  in length in the 0.1  $\text{mol dm}^{-3}$  suspension (Table 7.1).

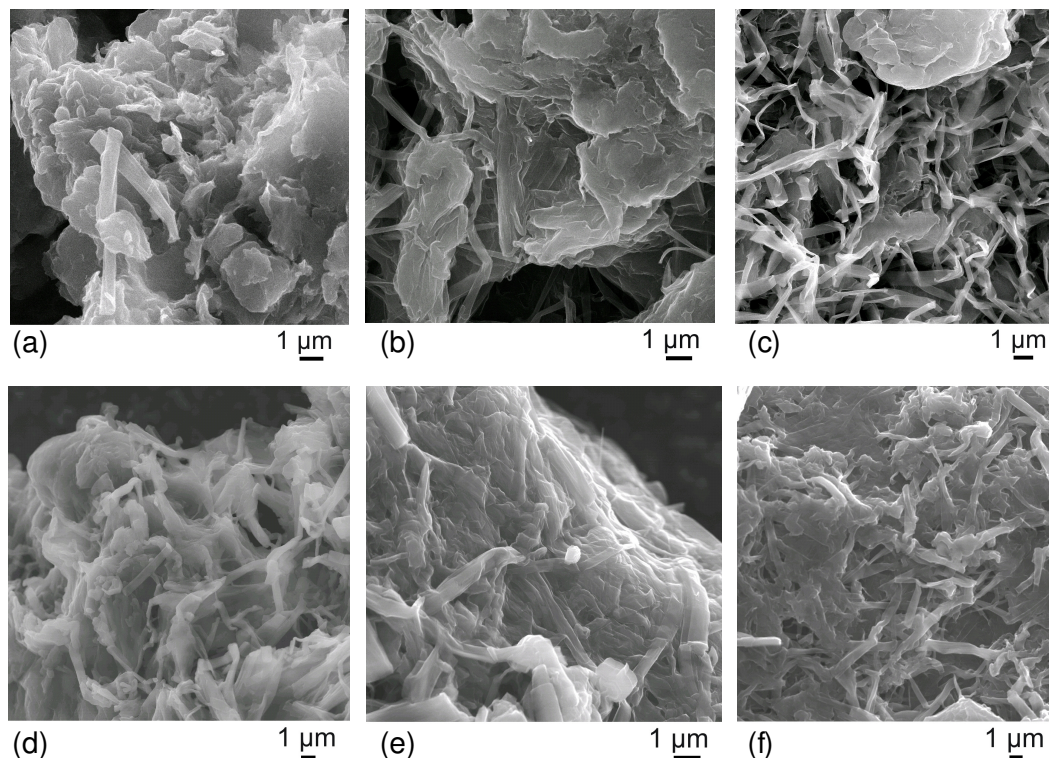


**Figure 7.7.** SEM images showing  $\text{VO}_x$  after 7 days hydrothermal treatment at 90 °C in solutions containing (a) 0, (b) 0.001, (c) 0.01 and (d) 0.1  $\text{mol dm}^{-3}$  ethylenediamine.

**Table 7.1.** The variation in nanosheet morphology with varying concentration of ethylenediamine ( $C_{\text{en}}$ ) after 7 days hydrothermal treatment at 90 °C. The particle thickness was measured using TEM.

$C_{\text{en}} / \text{mol dm}^{-3}$	Length/ $\mu\text{m}$	Width/ $\mu\text{m}$	Thickness/ nm
precursor	0.8 - 10	0.1 - 5	> 10
0	1 - 5	0.3 - 2	$\approx 6$
0.001	1 - 5	0.2 - 1	3 - 12
0.01	1.2 - 10	0.5 - 5	6 - 20
0.1	0.8 - 30	0.05 - 1	6 - 30

Extended hydrothermal treatment of the samples in 0.001 and 0.01 mol dm<sup>-3</sup> solutions of ethylenediamine resulted in an increase in the yield of nanosheets, until after 21 days treatment at 0.001 mol dm<sup>-3</sup> and 14 days at 0.01 mol dm<sup>-3</sup> concentrations the yield approached 100 % (Figure 7.7). After extended hydrothermal treatment of 14 - 21 days in 0.1 mol dm<sup>-3</sup> ethylenediamine solution the nanosheets remained unchanged from those formed after 7 days; the SEM images were identical to Figure 7.7 d.



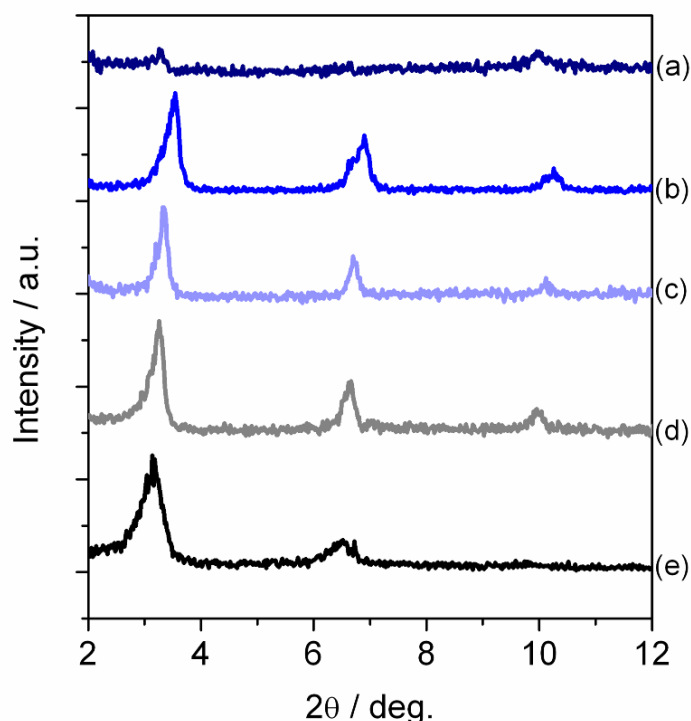
**Figure 7.8.** Evolution in morphology of VO<sub>x</sub> nanosheets after extended treatment in 90 °C ethylenediamine solution. SEM image (a) is the precursor material, and images (b), (c) are after treatment at in 0.001 mol dm<sup>-3</sup> ethylenediamine for 14 and 21 days respectively. Images (d), (e) and (f) are after treatment in 0.01 mol dm<sup>-3</sup> ethylenediamine for 7, 14, and 21 days respectively.

The XRD results after 7 days hydrothermal treatment at 90 °C (Figure 7.9) revealed that the presence of ethylenediamine has no effect on the VO<sub>x</sub> layer structure (see Figure 7.13 c and d), but in the low angle diffraction pattern the (001), (002) and (003) peaks are increasingly shifted to smaller *d*-spacings as the solution concentration of ethylenediamine increased. In the absence of ethylenediamine the interlayer spacing calculated from the (001) peak was 2.71 nm, and the products treated in 0.001 and 0.01



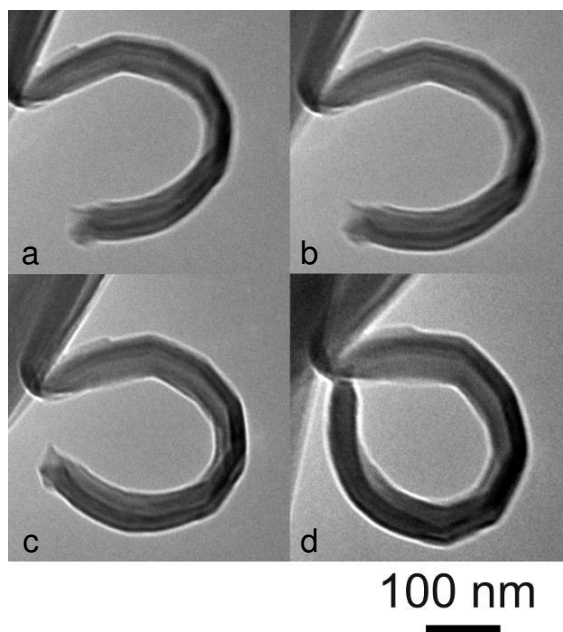
$\text{mol dm}^{-3}$  solution had interlayer spacings of approximately 2.66 and 2.51 nm respectively. As suggested in Section 7.2, the 2.66 nm interlayer spacing probably corresponds to a singly-hydrated intercalate  $\text{VO}_x(\text{RNH}_2)_y \cdot \text{H}_2\text{O}$ . The tenfold increase in the solution concentration of ethylenediamine from 0.001 to 0.01  $\text{mol dm}^{-3}$  may lead to loss of some of the interlayer water, reducing the interlayer space to 2.51 nm.

The shape of the (001) peaks (a)-(d) in Figure 7.9 cannot be directly compared with the peaks for  $\text{VO}_x$  nanotubes (e) as a smaller surface area of powder was used in the XRD sample holder than in (e). At 0, 0.001 and 0.01  $\text{mol dm}^{-3}$  ethylenediamine concentrations it is probable that the intercalate is described by  $\text{VO}_x(\text{RNH}_2)_n \cdot n\text{H}_2\text{O}$ , but in 0.1  $\text{mol dm}^{-3}$  solution the dodecylamine was almost completely (ca. 90 %) removed from the interlayer spaces, as evidenced by the almost total loss of the (001) and (002) diffraction peaks. Therefore, the nanosheets produced in 0.1  $\text{mol dm}^{-3}$  ethylenediamine at 90 °C would not be able to form amine-intercalated nanotubes as almost all the amine has been lost from the interlayer spaces.



**Figure 7.9.** Low-angle XRD patterns of  $\text{VO}_x$  after 7 days reflux at 90 °C in (a) 0.1, (b) 0.01, (c) 0.001, and (d) 0  $\text{mol dm}^{-3}$  ethylenediamine, compared with (e) the XRD pattern of  $\text{VO}_x$  nanotubes synthesised at 180 °C after 7 days hydrothermal treatment.

Although none of the elongated nanosheets formed at any concentration of ethylenediamine had undergone scrolling to form nanotubes, the uneven heating effect of a moving TEM electron beam when viewing the samples was seen to stimulate scrolling around the short axis of one of the nanosheets, forming a loop similar in diameter to a large  $\text{VO}_x$  nanotube within one minute of exposure to the beam (Figure 7.10). The cause of this bending may be uneven removal of the remaining amine molecules from the interlayer spaces (see figure 7.4) by the electron beam. Alternatively, uneven heating of the nanosheet on one surface more than the other may cause expansion of the heated surface or even a redox reaction of  $\text{V}^{(\text{V})}$  with the remaining amine molecules, both of which would stimulate bending of the sheet away from the electron beam. The series of images in Figure 7.10 may provide an insight into how nanotube formation occurs, beginning with a loop at the end of a nanosheet that closes along the edge to form a complete tube.

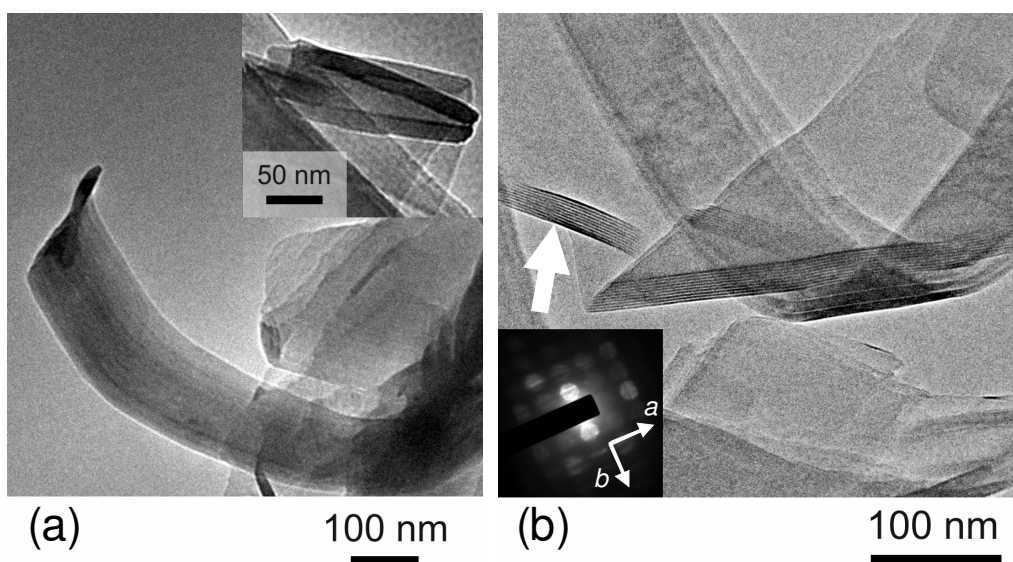


**Figure 7.10.** Progressive scrolling of  $\text{VO}_x$  nanosheets (a-d) around the long axis under the TEM electron beam. The nanosheets were synthesised from the addition of  $0.1 \text{ mol dm}^{-3}$  ethylenediamine ligand to  $\text{V}_2\text{O}_5$ -dodecylamine precursor and hydrothermal treatment at  $90^\circ\text{C}$  for at 7 days.

Since the nanosheets formed in the presence of ethylenediamine at  $90^\circ\text{C}$  exhibited a scrolling tendency under the electron beam, the temperature of synthesis was raised by



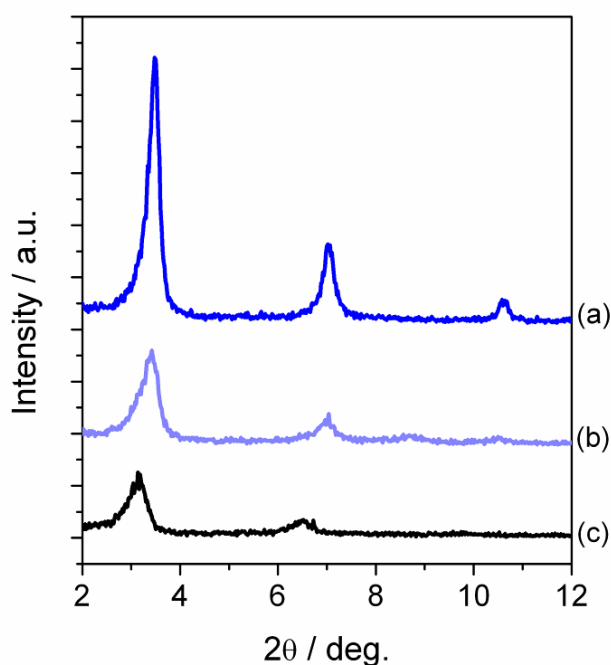
40 °C to investigate whether nanotube scrolling can be stimulated by heating at a higher temperature. Figure 7.11 shows the products after treatment of the precursor material at 130 °C for 7 days in the presence of ethylenediamine ligand. After 7 days hydrothermal treatment at an ethylenediamine concentration of  $0.001 \text{ mol dm}^{-3}$ , a few short tube-like structures which appeared to have formed from scrolling nanosheets were observed in the product in amongst mostly flat  $\approx 0.5 \text{ }\mu\text{m}$  long nanosheets (Figure 7.11a). At a higher ethylenediamine concentration of  $0.01 \text{ mol dm}^{-3}$  the nanosheets also showed a scrolling tendency, around the [110] crystallographic direction (see inset Figure 7.11 b). These nanosheets were larger in all crystallographic directions (Figure 7.11b), having a typical length greater than  $1 \text{ }\mu\text{m}$  and thickness of 20 nm. No tube-like structures were observed, although the number of nanosheets with scrolled ends observed was greater than in the product synthesised at a  $0.001 \text{ mol dm}^{-3}$  ethylenediamine concentration.



**Figure 7.11.** TEM images of  $\text{VO}_x$  after 7 days hydrothermal treatment at 130 °C in solution containing (a)  $0.001$  and (b)  $0.01 \text{ mol dm}^{-3}$  concentrations of ethylenediamine. The arrow in image (b) shows the part of the image from which the SAED is taken. The small arrows *a* and *b* refer to the crystallographic directions [100] and [010] respectively.<sup>[68]</sup>

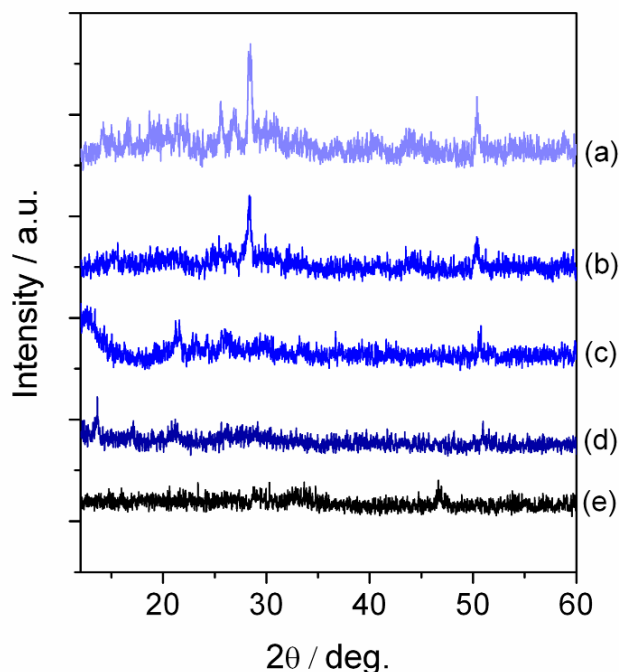
Low-angle XRD analysis of the products (Figure 7.12) showed that the interlayer spacing of the nanosheets synthesised at 130 °C remained constant at 2.54 nm as the ethylenediamine concentration increased from  $0.001$  to  $0.01 \text{ mol dm}^{-3}$ . This interlayer

spacing is very similar to the spacing of the largest peak observed in the sample treated at 140 °C, suggesting that the nanosheets consist of dehydrated dodecylamine-intercalated  $\text{VO}_x$  layers. The smaller interlayer spacing compared to 2.78 nm for  $\text{VO}_x$  nanotubes (Figure 7.12c) suggests that the loss of intercalated amine in both samples is not great enough to stimulate scrolling into nanotubes.



**Figure 7.12.** Low-angle XRD patterns of  $\text{VO}_x$  after 7 days reflux at 130 °C in (a) 0.001 and (b) 0.01 mol dm<sup>-3</sup> ethylenediamine, compared with  $\text{VO}_x$  nanotubes synthesised at 180 °C (c).

Examination of the higher angle XRD patterns of all the nanosheets synthesised in ethylenediamine solutions which showed partial or complete scrolling revealed that the scrolling tendency of the amine-intercalated nanosheets cannot be predicted from the crystal structure of their  $\text{VO}_x$  layers. For example, the nanosheets synthesised in 0.001 and 0.01 mol dm<sup>-3</sup> ethylenediamine at 130 °C, and at 0.01 and 0.1 mol dm<sup>-3</sup> ethylenediamine at 90 °C all showed scrolling tendencies despite having differences in crystal structure of their layers compared with the fully-scrolled  $\text{VO}_x$  nanotubes synthesised at 180 °C (Figure 7.13). This suggests that changes in crystal structure caused by the reduction of the initial  $\text{V}_2\text{O}_5$  layers to the approximate  $\text{VO}_{2.43}$  stoichiometry characteristic of nanotubes synthesised at 180 °C<sup>[37]</sup> is not the main driving force for layer scrolling.



**Figure 7.13.** XRD patterns of  $\text{VO}_x$  nanomaterials after 7 days reflux at (a, b) 130 °C in (a) 0.001 and (b) 0.01  $\text{mol dm}^{-3}$  ethylenediamine, (c,d) 90 °C in (c) 0.01 and (d) 0.1  $\text{mol dm}^{-3}$  ethylenediamine, compared with  $\text{VO}_x$  nanotubes synthesised at 180 °C (e).

From the results in this chapter it appears that formation of  $\text{VO}_x$  nanotubes is very sensitive to the amount of dodecylamine present in the interlayer spaces. Complete scrolling of  $\text{VO}_x$  nanosheets does not occur if the molar ratio of V: amine in the solid products deviates significantly from  $\approx 0.3$ . Upon scrolling, the interlayer spacing in the nanosheets undergoes a slight expansion, which is possibly due to changes in the configuration of the amine molecules in the interlayer spaces, as they adopt a different angle to the surface of the  $\text{VO}_x$  layers (Figure 7.4).

It seems that the presence of ethylenediamine in solution increases not only the growth rate of the  $\text{VO}_x$  nanosheets through recrystallisation (see Figure 7.7), but also increases the rate of dodecylamine removal from the interlayer spaces. This is probably caused by energetically favorable hydrogen-bonded interactions between the  $\text{C}_{12}\text{H}_{25}\text{NH}_2$  and  $(\text{CH}_2\text{NH}_2)_2$  molecules, as well as non-bonded interactions between the non-polar  $-\text{CH}_2$  groups which increase the solubility of dodecylamine in the solvent. From the observed tendency of nanosheets to scroll from the ends (Figure 7.11), it appears likely that

dodecylamine removal proceeds from the ends of the nanosheets. To achieve complete scrolling along the length of the nanosheet to form a nanotube below 180 °C apparently requires careful tuning of both the temperature and the solvent composition, and the correct conditions were unfortunately not found within the timescale of this project.

## 7.5. Conclusions

In the synthesis of amine-intercalated  $\text{VO}_x$  nanotubes from microparticles of  $\text{V}_2\text{O}_5(\text{RNH}_2)_2 \cdot n\text{H}_2\text{O}$ , recrystallisation of solvated vanadium species to form elongated nano-sized  $\text{VO}_x$  sheets, combined with the removal of intercalated amine molecules to form particles with stoichiometry  $\text{VO}_x(\text{RNH}_2)_{\approx 0.27}$  are important steps in nanotube formation. The sequences of SEM and TEM images at different temperatures and ethylenediamine concentrations suggest that thin elongated nanosheets grow in solution via recrystallisation, and once they have achieved sufficient loss of interlayer dodecylamine the nanosheets will begin to scroll, beginning from the ends and eventually forming a complete loop. This looped nanosheet joins at the ends, and continues growth by scrolling parallel to the [110] crystallographic axis to form elongated nanotubes. When the conditions do not allow removal of interlayer amine molecules (temperature too low, or incorrect solvent composition), the nanosheets do not scroll but continue to grow as flat, elongated objects in a crystal direction along the [100] direction (see Figure 7.11b). If too much amine is removed, the interlayer space collapses and rigid exfoliated nanosheets are formed. No evidence was found to indicate that changes in the crystal structure of the  $\text{VO}_x$  sheet were necessary to stimulate scrolling, as suggested in previous work.<sup>[133, 134]</sup>

To form amine-intercalated  $\text{VO}_x$  nanotubes at lower temperatures than 180 °C, further work is required in which the solubility of  $\text{VO}_x$  and the intercalating amine molecules are systematically studied in over a range of temperatures in a variety of  $-\text{NH}_2$  functionalised solvents, to find the appropriate conditions for low-temperature scrolling of  $\text{VO}_x$  nanosheets by achieving  $\approx 1.8 \text{ mmol dm}^{-3}$  solubility of  $\text{V(V)}$  species, and removal of  $\approx 73 \%$  of the intercalated amine molecules to create a stoichiometry of  $\text{VO}_x(\text{RNH}_2)_{\approx 0.27}$ .



## Chapter 8: Hydrogen Adsorption Properties of Metal Oxide Nanotubes

### 8.1. Introduction

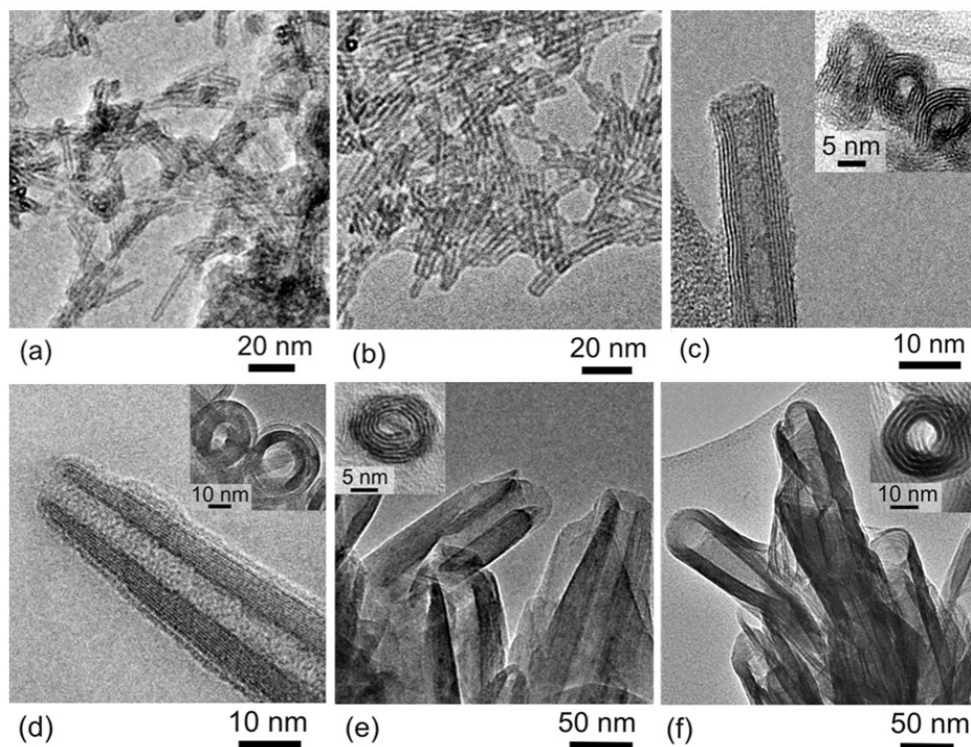
In the future, solid storage of hydrogen may replace liquid or gaseous storage as the means of storing hydrogen for transportation (see literature review Section 2.5). Nanostructured solids, including inorganic nanotubes, are among the materials of interest for hydrogen storage because their large surface area combined with their high porosity makes them promising candidates for storage of hydrogen through physisorption.

The main challenge in this field is to develop an understanding of the structural factors which make materials better or poorer for hydrogen storage applications. A wide range of materials must be studied to interpret how factors such as specific surface area, specific pore volume, pore diameter/shape, and surface heterogeneity affect the gravimetric and volumetric gas storage capacities of materials. Whilst there is a great deal of published literature dealing with the hydrogen storage properties of carbon nanotubes, other inorganic nanotubes have not received the same degree of interest despite the relatively low cost of their synthesis and the ability to scale up the process for large quantities.

This chapter presents the results of hydrogen adsorption experiments performed on the metal oxide nanotubes  $\text{Al}_2\text{GeO}_3(\text{OH})_4$  (germanium imogolite),  $\text{Ni}_3\text{Si}_2\text{O}_5(\text{OH})_4$  (nickel silicate),  $\text{VO}_x$  (vanadium oxide), and halloysite ( $\text{Al}_2\text{Si}_2\text{O}_5(\text{OH})_4$ ) nanotubes, at 77 K, using the volumetric (Sieverts) technique. The experimental conditions (mass, free volume, temperature) were kept as consistent as possible to allow a valid comparison of results. The results for the above metal oxide nanotubes were compared with previous results obtained in this laboratory for titanate nanotubes and their  $\text{Cd}_3[\text{Fe}(\text{CN})_6]_2$  composites, in order to identify the structural factors which improve the hydrogen adsorption properties of nanostructured materials.

## 8.2. Surface area and pore-size distributions of nanotubes

Before collecting the hydrogen adsorption data, the morphology, surface area and pore structures of all the samples were characterised using a combination of transmission electron microscopy and  $N_2$  adsorption. Figure 8.1 shows transmission electron micrographs of the unmodified synthetic germanium imogolite, nickel silicate, titanate nanotubes, and the as-received natural halloysite nanotubes. The synthesis of these nanotubes is detailed in Section 3.1 of the experimental methodology chapter.  $Al_2GeO_3(OH)_4$  nanotubes can be synthesised in two forms, single- or double-walled (see Section 3.1.2, page 50), which have different dimensions (Table 8.1). The  $Ni_3Si_2O_5(OH)_4$  nanotubes used in this chapter were synthesised in a solution with a 1.5 Ni/Si molar ratio and a NaOH concentration of 4 wt %. The titanate nanotubes were synthesised in the previous work of Al-Hajjaj et al. <sup>[215]</sup> The as-synthesised nanotubes were ion-exchanged with  $H^+$  to form the protonated form,  $H_2Ti_nO_{2n+1}$ .



**Figure 8.1.** HRTEM images of (a) single-walled Ge-imogolite, (b) double-walled Ge-imogolite (c) titanate, (d) nickel silicate, (e) halloysite and (f) vanadium oxide nanotubes. The insets in figures (c)-(f) show the end on view of the tube and the multiwalled structure.

Of all the nanotubes shown in Figure 8.1, the  $\text{Al}_2\text{GeO}_3(\text{OH})_4$  nanotubes have the smallest diameters and largest surface areas (see tables 8.1 and 8.2). The other nanotubes increase in both average diameter and length in the order titanates < nickel silicates < halloysite < vanadium oxide. Although it was not possible to observe the interlayer spacing of Ge-imogolite SWNTs directly on the TEM due to rapid movement of the nanotubes in the electron beam, the basal interlayer spacing is assumed to be  $\approx 0.7$  nm similar to titanate, nickel silicate and halloysite nanotubes, because the interlayer bonding is of a similar hydrogen-bonded nature.<sup>[172]</sup> Vanadium oxide nanotubes have a much larger interlayer spacing due to the intercalation of dodecylamine,  $\text{C}_{12}\text{H}_{25}\text{NH}_2$  (=  $\text{RNH}_2$ ).

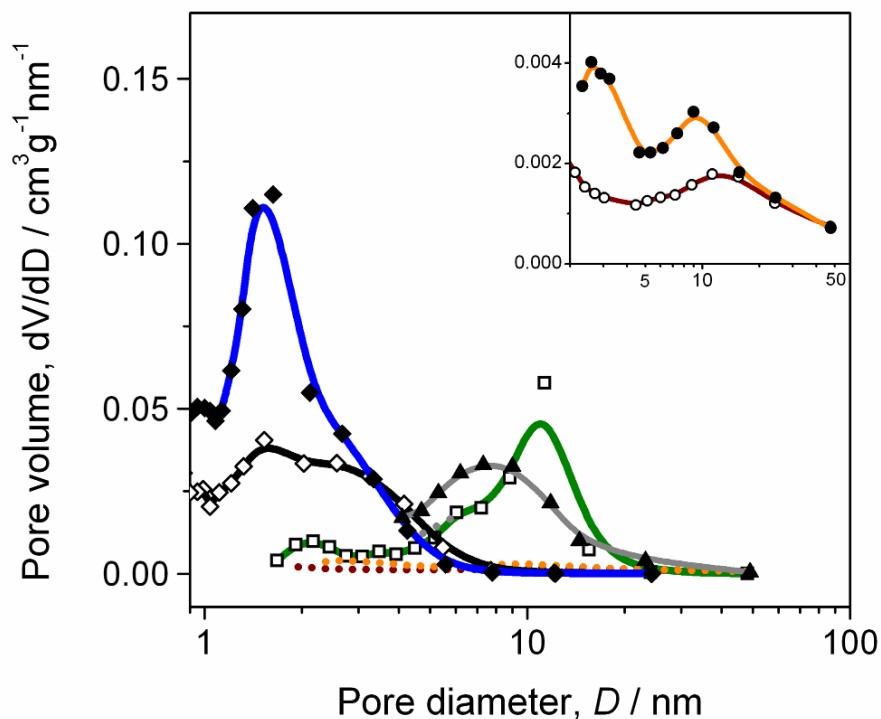
**Table 8.1.** Typical morphology of nanotubes as measured by HRTEM to within  $\pm 0.1$  nm.  $n$  = average number of layers,  $d_s$  = basal interlayer spacing,  $d_o$  = approximate outer diameter,  $d_i$  = approximate inner diameter,  $l$  = approximate average length.

Nanotube	Chemical formula	$n$	$d_s/\text{nm}$	$d_o/\text{nm}$	$d_i/\text{nm}$	$l/\text{nm}$
Ge-imogolite SWNTs	$\text{Al}_2\text{GeO}_3(\text{OH})_4$	1	0	3	2	20-50
Ge-imogolite DWNTs	$\text{Al}_2\text{GeO}_3(\text{OH})_4$	2	-	4	1.5	15-30
Titanate	$\text{H}_2\text{Ti}_n\text{O}_{2n+1}$	4	0.7	10	5	50-100
Nickel silicate	$\text{Ni}_3\text{Si}_2\text{O}_5(\text{OH})_4$	7	0.7	20	10	40-200
Halloysite	$\text{Al}_2\text{Si}_2\text{O}_5(\text{OH})_4$	28	0.7	50	10	$2 \times 10^3$
Vanadium oxide	$\text{VO}_{2.43}(\text{RNH}_2)_{0.27}$	11	2.8	75	30	$5 \times 10^3$

To characterise the surface area and total pore volume of the nanotubes, nitrogen adsorption at 77 K was used. Figure 8.2 shows the pore volume distributions according to pore size, which was calculated from the nitrogen adsorption isotherms using the BJH method.<sup>[72]</sup> The specific BET surface areas and total pore volumes at the saturation pressure ( $P_0$ ) are reported in Table 8.2. From the results it is evident that the titanate, nickel silicate, halloysite and  $\text{VO}_x$  samples are mainly mesoporous (pore size 2 - 50 nm), and the Ge-imogolite samples are mainly microporous (pore size < 2 nm). It should be noted that BJH has a tendency to underestimate small pores sizes < 10 nm,



sometimes by more than 1 nm,<sup>[276]</sup> so the pore diameters given in Table 8.2 should only be taken as a rough guide.



**Figure 8.2.** Pore volume distributions, from nitrogen desorption at 77 K, for (◆) single-walled Ge-imogolite (◇) double-walled Ge-imogolite, (▲) titanate, (□) nickel silicate (●) halloysite, and (○) VO<sub>x</sub> nanotubes (see inset, shown on main graph as dotted lines). The data for titanate nanotubes was obtained from reference<sup>[215]</sup>.

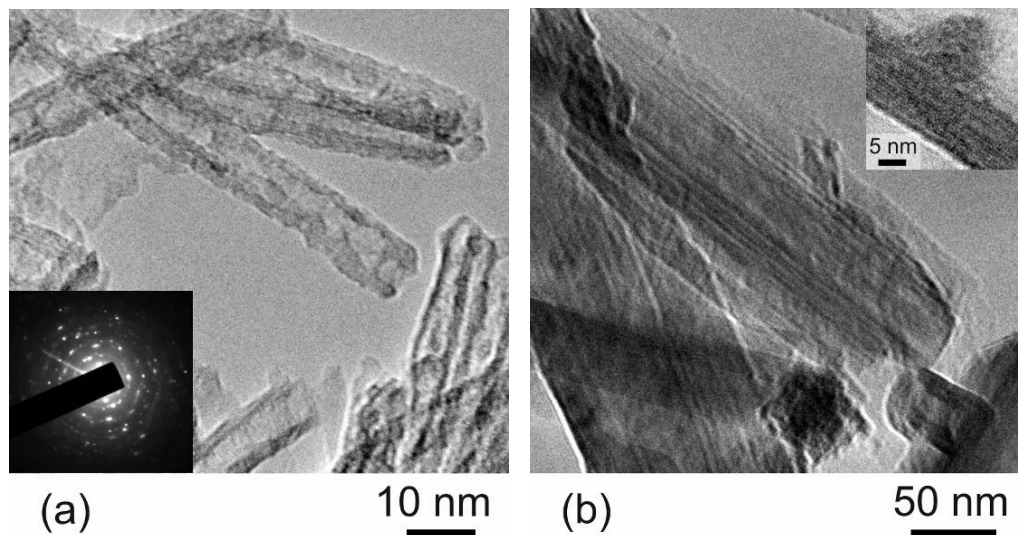
**Table 8.2.** Results of nitrogen adsorption at 77 K on nanotubular samples.  $S_{\text{BET}}$  = specific surface area, calculated using the BET method,  $V_{\text{pores}}$  = specific total pore volume at  $P = P_0$ , and  $d_{\text{pores}}$  = range of diameters in which most (>90 %) of the pore diameters lie, with the peak pore diameters (those with the largest associated pore volumes) shown in brackets.

Nanotube	$S_{\text{BET}} / \text{m}^2 \text{g}^{-1}$	$V_{\text{pores}} / \text{cm}^3 \text{g}^{-1}$	$d_{\text{pores}} / \text{nm}$
Ge-imogolite SWNTs	299	0.200	0.9-3 (0.9, 1.6)
Ge-imogolite DWNTs	194	0.157	0.5-3 (0.9, 1.5)
Titanate	210 <sup>[215]</sup>	0.64 <sup>[215]</sup>	3-11 (7.3)
Nickel silicate	133	0.391	5-17 (11.3)
Halloysite	24.3	0.09	3-25 (2.6, 9.0)
Vanadium oxide	17.8	0.074	3-30 (1.8, 11.3)

For most of the samples, peaks in pore volume at two different pore diameters were observed. The peak at the smallest pore diameter is probably associated with pores between close-packed nanotubes, which would explain the large number of these pores in the Ge-imogolite DWNT sample as this sample shows the closest packing of the nanotubes (Figure 8.1). The peak at the larger pore diameters are probably associated with adsorption in the intra-tubular pores (lumen), and in some of the larger spaces between tubes (see Figure 2.4, page 16). From the relatively small total pore volumes of the samples it appears that access of nitrogen (kinetic diameter 0.364 nm<sup>[292]</sup>) to the interlayer spaces is prevented. The interlayer pores diameters are smaller than the basal spacing of 0.7 nm (see Section 2.2.2.), and access of nitrogen to these pores may be hindered by surface groups such as –OH.

The effect of decorating the nanotube surfaces with Prussian-blue (PB) analogues was also investigated for titanate and natural halloysite nanotubes as these nanotubes can be synthesised/ purchased in large quantities. A composite of titanate nanotubes with Cd<sub>3</sub>[Fe(CN)<sub>6</sub>]<sub>2</sub> was synthesised and characterised in a recent publication,<sup>[215]</sup> and the results are presented here for comparison with a halloysite - Fe<sub>3</sub>[Fe(CN)<sub>6</sub>]<sub>2</sub> composite. Fe<sup>2+</sup> was used instead of Cd<sup>2+</sup> to form the complex in this instance due to concerns about the high toxicity of Cd(II) compounds.<sup>[293]</sup> The halloysite-Fe<sub>3</sub>[Fe(CN)<sub>6</sub>]<sub>2</sub> composite synthesis method is given in Chapter 3.3.

HRTEM images of the two nanotube-PB composites are shown in Figure 8.3. In the titanate-PB composite the Cd<sub>3</sub>[Fe(CN)<sub>6</sub>]<sub>2</sub> formed an almost continuous film on the inner and outer surfaces of the nanotubes, which appear corrugated as a result. In the halloysite-PB composite the Fe<sub>3</sub>[Fe(CN)<sub>6</sub>]<sub>2</sub> appeared partly as a film, but also appeared form occasional spheroidal particles (see inset Figure 8.3b). The SAED pattern for the titanate-PB composite showed reflections for both titanate nanotubes and the cubic Cd<sub>3</sub>[Fe(CN)<sub>6</sub>]<sub>2</sub> lattice.<sup>[215]</sup> A similar pattern could not be obtained for the halloysite-PB composite, possibly because the weight percentage of Fe<sub>3</sub>[Fe(CN)<sub>6</sub>]<sub>2</sub> in the sample was not large enough. However, faint lattice fringes could be seen on the particle in the inset of Figure 8.3b (unfortunately the contrast of this sample is poor), which demonstrate a cubic lattice structure.



**Figure 8.3.** TEM images showing (a) titanate nanotubes decorated with 10 wt %  $\text{Cd}_3[\text{Fe}(\text{CN})_6]_2$  through ion-exchange, <sup>[215]</sup> and (b) halloysite nanotubes decorated with 4.7 wt%  $\text{Fe}_3[\text{Fe}(\text{CN})_6]_2$  through ion exchange. The inset in image (a) shows the SAED pattern of the composite, and the inset in image (b) shows a  $\text{Fe}_3[\text{Fe}(\text{CN})_6]_2$  particle bonded to the inner surface of a halloysite nanotube.

It was estimated through EDX analysis of a  $\approx 1 \mu\text{m}^2$  area of each sample that the titanate nanotube-PB composite contained 10 wt %  $\text{Cd}_3[\text{Fe}(\text{CN})_6]_2$  of the total sample weight, <sup>[215]</sup> and the halloysite nanotube-PB composite contained 4.7 wt %  $\text{Fe}_3[\text{Fe}(\text{CN})_6]_2$  of the total sample weight. The surface area and pore volumes of these composites are given in table 8.4. The microporous PB analogue structure has unit cell dimensions 1.0-1.09 nm, <sup>[294]</sup> which is too small to be analysed using the BJH method.

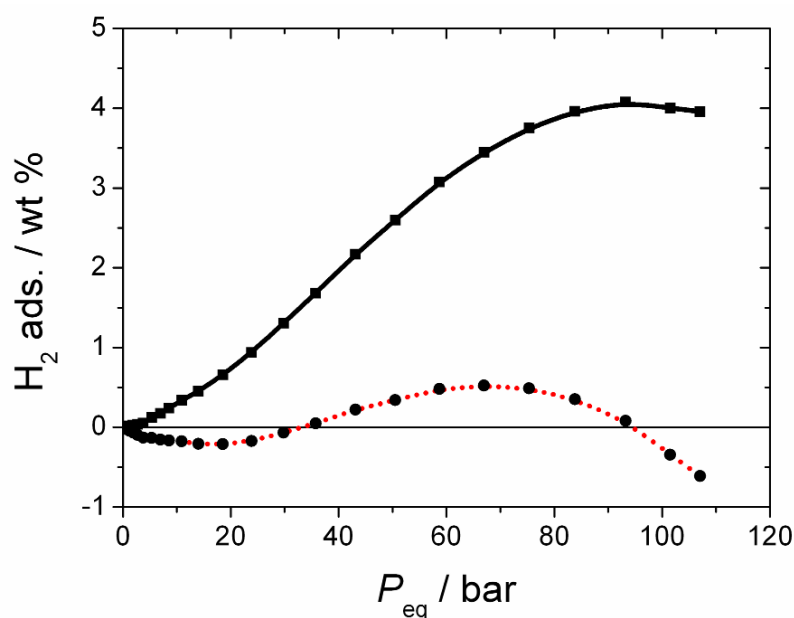
**Table 8.3.** Results of nitrogen adsorption at 77 K on nanotube-PB composites, and bulk  $\text{Fe}_3[\text{Fe}(\text{CN})_6]_2$ .  $S_{\text{BET}}$  = specific surface area,  $V_{\text{pores}}$  = specific total pore volume at  $P = P_0$ .

Composite	$S_{\text{BET}} / \text{m}^2\text{g}^{-1}$	$V_{\text{pores}} / \text{cm}^3\text{g}^{-1}$
Titanate + 10 wt % $\text{Cd}_3[\text{Fe}(\text{CN})_6]_2$	244 <sup>[215]</sup>	0.67 <sup>[215]</sup>
Halloysite + 4.7 wt % $\text{Fe}_3[\text{Fe}(\text{CN})_6]_2$	46.7	0.103
$\text{Cd}_3[\text{Fe}(\text{CN})_6]_2$	556 <sup>[215]</sup>	0.36 <sup>[215]</sup>

### 8.3. Blank testing and temperature correction of data

Before any of the samples could be analysed for hydrogen adsorption, temperature correction of a blank non-adsorbing sample had to be performed using a standardised procedure.<sup>[228]</sup> A linear temperature correction is found from the blank sample, which is then applied to all of the data (see Section 3.7.6). All of the nanotubular samples were kept as similar as possible to the blank quartz wool sample in mass and free volume (0.2671 g and 24.8418 cm<sup>3</sup>), so that the same temperature correction could be applied to all samples.

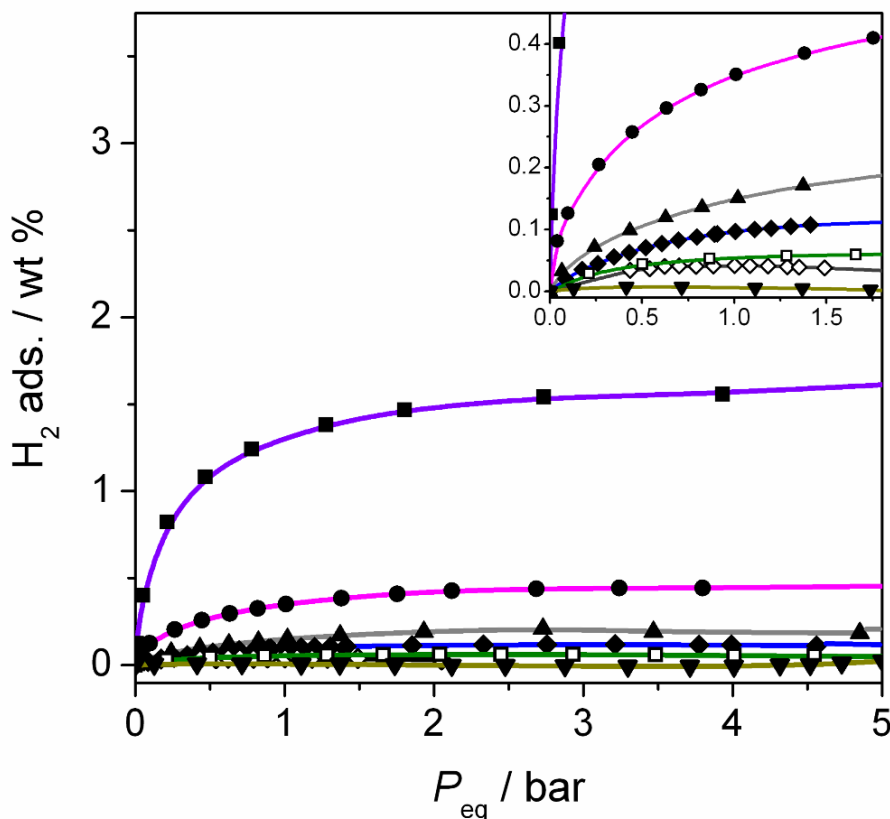
Figure 8.4. shows the uncorrected data for adsorption of the quartz wool blank compared to the temperature-corrected data. A temperature-correction ratio  $T_{ratio} = 0.022$  input into the Igor software macro (see Section 3.7.6), was found to achieve the best correction of the data, where H<sub>2</sub> adsorption was as close as possible to zero over the range 0-100 bar (10 MPa). The data cannot be corrected to exactly zero over the entire pressure range because the compressibility factor,  $Z$ , of hydrogen shows a strong non-linear variation with pressure at 77 K.<sup>[295]</sup>



**Figure 8.4.** Hydrogen adsorption isotherm for non-adsorbing quartz wool sample at 77 K, -(■)- before temperature correction, and ..(●).. after temperature correction.<sup>[228]</sup>

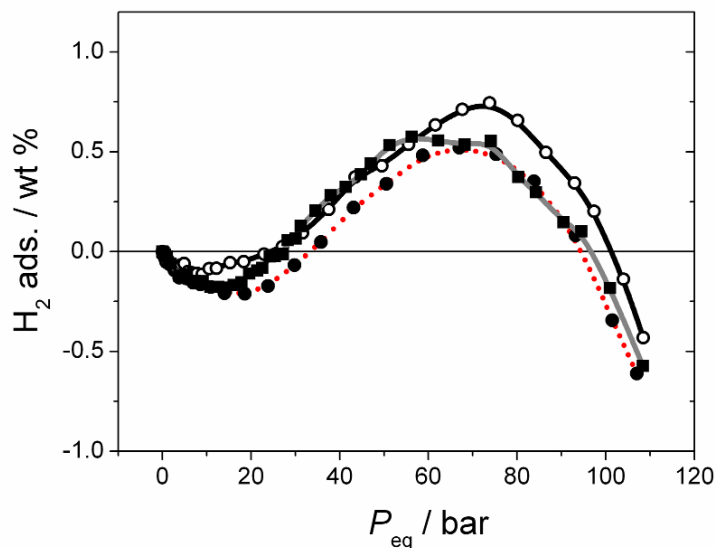
### 8.4. Comparison of hydrogen adsorption data

Hydrogen PCT adsorption isotherms were recorded for all the nanotubular samples and the halloysite-PB composites synthesised in this work. The isotherms were temperature-corrected, and compared with previous data from titanate nanotubes,  $\text{Cd}_3[\text{Fe}(\text{CN})_6]_2$  nanoparticles, and the titanate nanotube composite with 10 wt %  $\text{Cd}_3[\text{Fe}(\text{CN})_6]_2$ . This data had not been temperature-corrected in the original publication, leading to erroneously large measured wt % storage at high pressures.<sup>[215]</sup> In this work, the temperature correction was also applied to these samples. The temperature-corrected isotherms of all the samples are compared in Figure 8.5.



**Figure 8.5.** Temperature-corrected hydrogen excess adsorption isotherms in the range 0-5 bar for (■)  $\text{Cd}_3[\text{Fe}(\text{CN})_6]_2$  (●)  $\text{Cd}_3[\text{Fe}(\text{CN})_6]_2$ -titanate composite, and (▲) titanate (◆) single-walled Ge-imogolite, (◇) double-walled Ge-imogolite, (□) nickel silicate and (▼)  $\text{Fe}_3[\text{Fe}(\text{CN})_6]_2$ -halloysite composite. Data for the first 3 isotherms was taken from reference<sup>[215]</sup> and modified using the temperature correction method. The inset shows the adsorption below 2 bars.

The appearance of the isotherms corresponds to type I adsorption which is typical of the adsorption of supercritical  $H_2$  onto porous materials. <sup>[195]</sup> The isotherms were not observed to have a two-step nature, as was reported by Al-Hajjaj et al. <sup>[215]</sup> Halloysite and vanadium oxide ( $VO_x$ ) nanotubes were found to have zero adsorption compared to the blank sample (Figure 8.6), so were not included in Figure 8.5.



**Figure 8.6.** Hydrogen adsorption isotherms at 77 K for (○) natural halloysite and (■)  $VO_x$  nanotubes compared with ... (●) ... the blank quartz wool sample following temperature correction.

It appears from the adsorption data that the hydrogen adsorption of all unmodified nanotubular samples is poor, with the highest excess adsorption being achieved by titanate nanotubes (0.2 wt % at 2.6 bars). All the other nanotubes adsorb between 0 and 0.2 wt % hydrogen. Such small values, together with the absence of a two-step adsorption process (adsorption in interlayer micropores occurring at a higher pressure than in the mesopores <sup>[213, 215]</sup>) do not support the suggestion that hydrogen can access the interlayer spaces of the nanotubes. This is confirmed by the fact that the Geimogolite single-walled nanotubes have a higher wt % excess adsorption than the double-walled nanotubes, despite the fact that the double-walled nanotubes contain interlayer cavities. The correlation between the higher BET surface area and higher hydrogen adsorption observed for the single-walled nanotubes further indicates that hydrogen is adsorbed only on the pore surfaces and not in the interlayer cavities.

The  $\text{Cd}_3[\text{Fe}(\text{CN})_6]_2$  nanoparticles, with their much higher surface area compared to the nanotubes, have a maximum excess adsorption of 1.67 wt % at 8.1 bars. The  $\text{Cd}_3[\text{Fe}(\text{CN})_6]_2$ -titanate nanotube composite shows a maximum of 0.44 wt % excess adsorption at a pressure of 5.7 bars, which is higher than the 0.35 wt % adsorption that would be expected from a weighted mixture of 10 wt %  $\text{Cd}_3[\text{Fe}(\text{CN})_6]_2$  with 90 wt % titanate nanotubes. Clearly, decorating the  $\text{Cd}_3[\text{Fe}(\text{CN})_6]_2$  onto the titanate surface has an enhancing effect on the adsorption of hydrogen, possibly due to charge transfer between  $\text{K}^+$  ions bonded to the surface  $\text{Ti-O}^-$  groups (resulting from ion exchange with  $\text{K}_3[\text{Fe}(\text{CN})_6]_2$  when the composite was formed) and the  $\text{Cd}_3[\text{Fe}(\text{CN})_6]_2$  lattice structure, as suggested in the previous work on this composite.<sup>[215]</sup> However, because the surface area of the composite is much lower than the bulk  $\text{Cd}_3[\text{Fe}(\text{CN})_6]_2$  (Table 8.3), the adsorption of hydrogen is lower than in the bulk particles. Although decoration with PB-analogues did not produce a large adsorption of hydrogen in this instance, if a metal oxide substrate with a higher surface area than titanate nanotubes were found, the adsorption-enhancing effect of decoration with a PB analogue may be more pronounced.

The isotherms in Figure 8.5 show the excess adsorption, which unlike absolute adsorption does not take the bulk gas phase hydrogen inside the pore volume of the sample into account (see literature review Section 2.5.3.) The next section demonstrates the fitting of excess adsorption isotherms to the Langmuir-Freundlich model, in order to derive properties of the absolute adsorption isotherms, in addition to properties such as surface area and the maximum volume, mass and thickness of the adsorbed hydrogen layer.

### 8.5. Langmuir-Freundlich fitting of isotherms

Fitting of an equation based on the Langmuir-Freundlich (L-F) model to excess adsorption isotherms can be used to estimate surface properties such as the specific surface area of the material for hydrogen adsorption and the maximum volume of the adsorbed layer.<sup>[180]</sup> The thickness of the adsorbed layer can also be obtained from division of the volume by the specific surface area. Other equations based on models such as the Dubinin-Astakhov, Toth, and Unilan models<sup>[180]</sup> can also be used to

estimate these properties, and there is good agreement between these models and the L-F model in terms of the calculated properties.<sup>[180]</sup> It is not yet established which of these models gives the most accurate fitting of the excess adsorption isotherm. For simplicity in comparing data, therefore, only the Langmuir-Freundlich model was used in this work to fit the experimentally measured PCT data, as this model is the easiest to fit to the data using the Origin software.

The equation which was fitted to the isotherms is shown below in equation 8.1. Details of the derivation of this model can be found in reference<sup>[180]</sup> and in Appendix D.

$$m_e = \left( \frac{m_{H_2} S_{H_2}}{A_{H_2} N_A} - \frac{m_{H_2} P V_m}{RT} \right) \left( \frac{K_{LF} P^{1/n_{LF}}}{1 + P^{1/n_{LF}}} \right) \quad (8.1)$$

In this equation the terms are defined:  $m_e$  = excess adsorption, grams hydrogen adsorbed per gram of solid material (g g<sup>-1</sup> units),  $m_{H_2}$  = the relative molecular mass of H<sub>2</sub>,  $P$  = equilibrium pressure, in bar,  $R$  = the universal gas constant,  $8.314 \times 10^{-5}$  m<sup>3</sup> bar K<sup>-1</sup> mol<sup>-1</sup>,  $T$  = temperature, in degrees Kelvin,  $N_A$  = Avogadro constant,  $6.022 \times 10^{23}$  mol<sup>-1</sup>,  $A_{H_2}$  = the surface area occupied by one adsorbed H<sub>2</sub> molecule,  $6.83 \times 10^{-20}$  m<sup>2</sup> assuming a circular area for a H<sub>2</sub> molecule with kinetic diameter 0.29 nm.<sup>[296]</sup> The constants  $K_{LF}$  and  $n_{LF}$  are specific to the L-F model.<sup>[297]</sup> The important properties which can be derived using this equation are the specific surface area for hydrogen adsorption,  $S_{H_2}$ , and the maximum volume of hydrogen adsorbed per unit mass of solid material,  $V_m$ . The value of  $q_m$ , the maximum adsorbed mass of hydrogen at full monolayer coverage per gram of material is given by the term  $\frac{m_{H_2} S_{H_2}}{A_{H_2} N_A}$ . The g g<sup>-1</sup> units

of  $m_e$  and  $q_m$  are converted to wt % by multiplying by a factor of 100.

To derive  $S_{H_2}$ ,  $V_m$  and  $q_m$  from the data, a line with the equation

$$m_e = (a - bP) \frac{cP^d}{1 + cP^d} \quad (8.2)$$

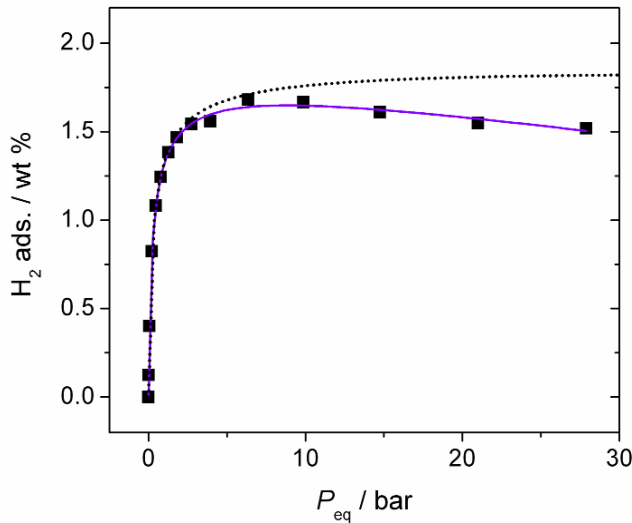
was fitted to the data using a non-linear least-squares method in the Origin 8.1 software. (see reference<sup>[180]</sup>) The properties are then calculated using  $q_m = a$ ,  $V_m = bRT/m_{H_2}$  and  $S_{H_2} = aA_{H_2}N_A/m_{H_2}$ .



The absolute adsorption isotherm is obtained from the excess adsorption isotherm by adding the mass of hydrogen in the bulk gas phase which is present in the total pore volume of the solid materials (see Section 2.5.3). Thus the expression for absolute adsorption is given by:

$$m_t = m_e + V_{pores} \frac{m_{H_2} P}{RT} \quad (8.3)$$

Fitting of the excess adsorption isotherms of the samples shown in Figure 8.5 to the Langmuir-Freundlich model is shown below in Figures 8.7 to 8.10. The absolute adsorption isotherms calculated using Equation (8.3) are shown as dotted lines. The vanadium oxide, halloysite and halloysite nanotube-PB composite samples had very low adsorption capacities and could not be fitted using the L-F model, as negative  $a$  and  $b$  coefficients were generated (see Equation (8.2)).

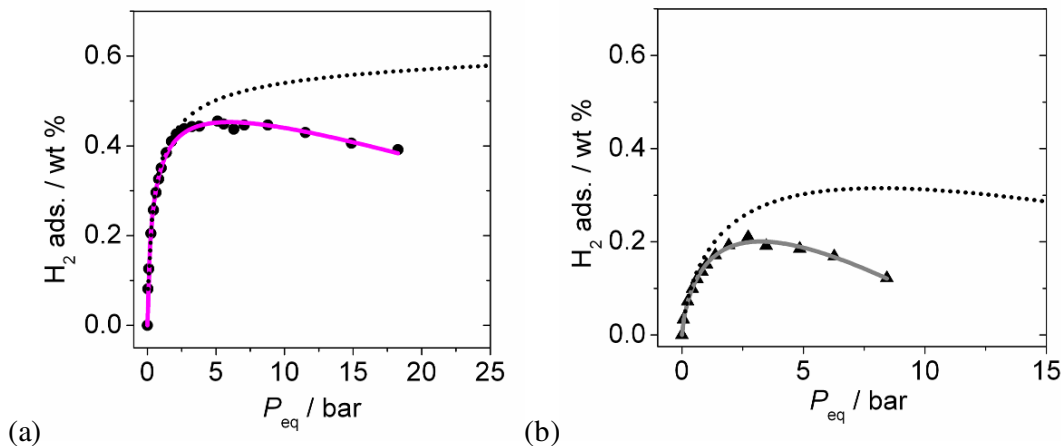


**Figure 8.7.** Langmuir-Freundlich fitting of excess adsorption data for (■) bulk  $\text{Cd}_3[\text{Fe}(\text{CN})_6]_2$  particles at 77 K (solid line), with the calculated absolute adsorption isotherm (dotted line).

Fitting of the excess adsorption isotherm of bulk  $\text{Cd}_3[\text{Fe}(\text{CN})_6]_2$  particles using the L-F model reveals a saturation point of 1.7 wt % excess adsorption at 7 bar pressure. Above this pressure the measured gravimetric excess adsorption falls with increasing pressure, because the surface adsorbed layer  $V_m$  is saturated but the density of the bulk phase gas in the pore volume continues to increase with increasing pressure. The absolute

adsorption isotherm, on the other hand, continues to grow beyond this pressure as the increase in bulk density is included in the isotherm function (Equation (8.3)).

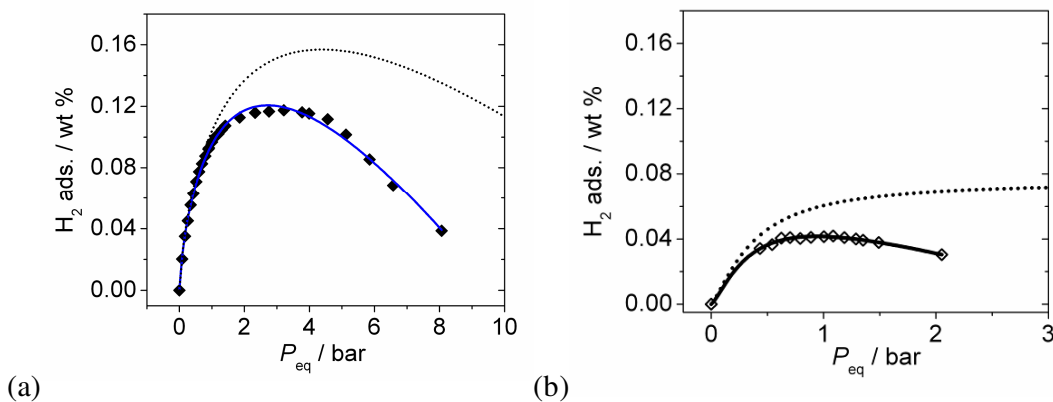
The adsorption data for titanate nanotubes and the  $\text{Cd}_3[\text{Fe}(\text{CN})_6]_2$ -titanate nanotube composite showed a much lower saturation pressure than the bulk  $\text{Cd}_3[\text{Fe}(\text{CN})_6]_2$  particles. In the case of titanate nanotubes (Figure 8.8b), calculation of the absolute adsorption isotherm produced a curve which showed a decrease in adsorption beyond the saturation point. Since this is not typical of absolute adsorption, the measured excess adsorption data from which the absolute adsorption isotherm is derived probably contains errors. The gravimetric adsorption of this sample is so low that small errors in measurement can cause large percentage errors in the results. In this case, errors in the gradient of the negative slope above the saturation point of 3.3 bars may have arisen from differences in pressure measurement  $\geq 5$  bars because of the switchover from the low pressure transducer measurement to the high pressure transducer. The readings of the two transducers may undergo random ‘drift’ relative to each other, even within the short timescale of the experiment.



**Figure 8.8.** Langmuir-Freundlich fitting of excess adsorption data for (a) (▲) titanate nanotubes, and (b) (●)  $\text{Cd}_3[\text{Fe}(\text{CN})_6]_2$ -titanate nanotube composite at 77 K (solid lines), with the calculated absolute adsorption isotherms (dotted lines).

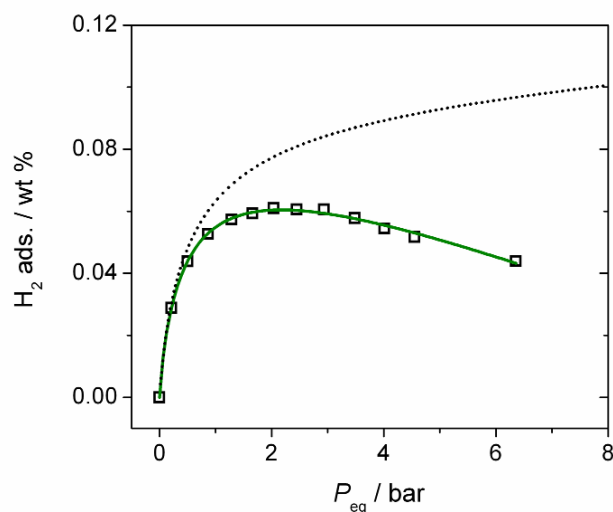
A similar error in the slope of the derived absolute adsorption is observed in the data for Ge-imogolite single-walled nanotubes (Figure 8.9a). This error leads to poor fitting of the L-F function to the data points. To improve the fitting, several (at least 3) identical measurements of the same sample would need to be taken, to produce an average

isotherm, but unfortunately such improvement could not be achieved within the timescale of this project.



**Figure 8.9.** Langmuir-Freundlich fitting of excess adsorption data for (a) (♦) Ge-imogolite single-walled nanotubes, and (b) (◊) Ge-imogolite double-walled nanotubes (solid lines), shown with the calculated absolute adsorption isotherms (dotted lines).

The L-F isotherm fitting for nickel silicate nanotubes (Figure 8.10) indicates a saturation pressure close to 2.2 bars at 0.06 wt % excess adsorption. The slope of the isotherm beyond the saturation point is less negative than the Ge-imogolite SWNT and titanate nanotube samples, giving the absolute adsorption isotherm a more usual shape.



**Figure 8.10.** Langmuir-Freundlich fitting of excess adsorption data for (□) nickel silicate nanotubes (solid lines), with the calculated absolute adsorption isotherm (dotted lines).

The values of  $q_m$ , the maximum mass of hydrogen stored in the adsorption layer derived from the L-F fitting of the curves are displayed in Table 8.4. These values have also been converted from gravimetric adsorption (in  $\text{g g}^{-1}$  units) to volumetric adsorption for each material by multiplying by the bulk density (see table of physical properties in Appendix D). The number of adsorbed hydrogen molecules per unit cell was calculated using the equation

$$n_{H_2} = \frac{q_m \cdot V_{\text{unit cell}} \cdot N_A}{m_{H_2}} \quad (8.4)$$

Where  $q_m$  is the maximum volumetric adsorption, in  $\text{g cm}^{-3}$ , and  $V_{\text{unit cell}}$  is the volume of the unit cell, in  $\text{cm}^{-3}$  (see appendix D).

**Table 8.4.** Gravimetric and volumetric capacities of the nanomaterials, together with the calculated number of  $\text{H}_2$  molecules,  $n_{\text{H}_2}$ , per unit cell.

Nanomaterial	$q_m / \text{wt } \%$	$q_m / \text{g cm}^{-3}$	$n_{\text{H}_2}$ per unit cell
Ge-imogolite SWNT	0.18	$5.96 \times 10^{-3}$	0.6
Ge-imogolite DWNT	0.07	$2.32 \times 10^{-3}$	0.3
Nickel silicate	0.09	$2.54 \times 10^{-3}$	0.2
Titanate	0.47	$14.85 \times 10^{-3}$	2.4
$\text{Cd}_3[\text{Fe}(\text{CN})_6]_2$	1.91	$8.60 \times 10^{-3}$	3.2
Titanate + 10 wt % $\text{Cd}_3[\text{Fe}(\text{CN})_6]_2$ composite	0.58	$16.76 \times 10^{-3}$	2.7

The gravimetric storage capacity of the bulk  $\text{Cd}_3[\text{Fe}(\text{CN})_6]_2$  particles is much greater than any of the nanotubular materials, but because it has a much lower bulk density it does not have the largest volumetric storage capacity. The doping of the titanate nanotube surface with 10 wt %  $\text{Cd}_3[\text{Fe}(\text{CN})_6]_2$  particles increased the maximum gravimetric storage capacity of the nanotubes by a similar amount to that expected for a weighted mixture of the two substances, i.e.  $(0.9 \times 0.47) + (0.1 \times 1.91) = 0.61$ . Thus, the results suggest that chemical bonding between the titanate nanotube surface and the

Prussian blue analogue particles does not enhance the gravimetric adsorption properties of the composite material.

The other metal oxide nanotubes have very low values of  $q_m$ , both gravimetric and volumetric, compared to titanate nanotubes. This cannot be entirely caused by the differences in surface area, because  $q_m$  does not consistently increase as the surface area of the nanotubes increases. The differences in the pore structure and the nature of the nanotube surfaces may be an important factor influencing the value of  $q_m$ . For example, the basal interlayer spacing in most of the nanotubular samples is close to 0.73 nm, but interlayer pores in the titanate nanotubes walls have a zigzag-shaped cross-section, whereas in the Ge-imogolite and nickel silicate nanotubes the pores have a flat cross section. The cross sectional shape of the titanate nanotube surfaces may enhance  $H_2$  adsorption and may even allow some limited access of  $H_2$  to the interlayer spaces, increasing the specific surface area available for hydrogen adsorption (Table 8.5).

**Table 8.5.** Properties of adsorbed hydrogen layer at 77 K calculated from Figures 8.7-8.10, compared with properties of material calculated from nitrogen adsorption (Tables 8.2 and 8.3)  $S_{H_2}$  = specific surface area for hydrogen adsorption,  $V_m$  = maximum volume of adsorbed  $H_2$  layer per gram of material,  $d_{H_2}$  = maximum average thickness of  $H_2$  layer, calculated from  $V_m / S_{H_2}$ , and  $d_{BET}$  = maximum average thickness of  $H_2$  layer, calculated from  $V_m / S_{BET}$ . The diameter of the most common (largest associated volume) pore type in the sample measured by nitrogen adsorption (Table 8.2) is given by  $d_{pores}$ .

Nanomaterial	$S_{H_2} / m^2 g^{-1}$	$S_{BET} / m^2 g^{-1}$	$V_m / cm^3 g^{-1}$	$V_{pores} / cm^3 g^{-1}$	$d_{H_2} / nm$	$d_{BET} / nm$	$d_{pores}$
Ge-imogolite SWNT	85	299	0.11	0.20	1.28	0.36	1.6
Ge-imogolite DWNT	15	194	0.06	0.16	4.06	0.31	1.5
Nickel silicate NT	19	133	0.02	0.39	1.13	0.17	11.3
Titanate NT	97	210 <sup>[215]</sup>	0.12	0.64 <sup>[215]</sup>	1.19	0.55	7.3
$Cd_3[Fe(CN)_6]_2$	393	556 <sup>[215]</sup>	0.40	0.36 <sup>[215]</sup>	1.00	0.71	1.07
Titanate + 10 wt % $Cd_3[Fe(CN)_6]_2$	120	244 <sup>[215]</sup>	0.30	0.67 <sup>[215]</sup>	2.50	1.23	7.3

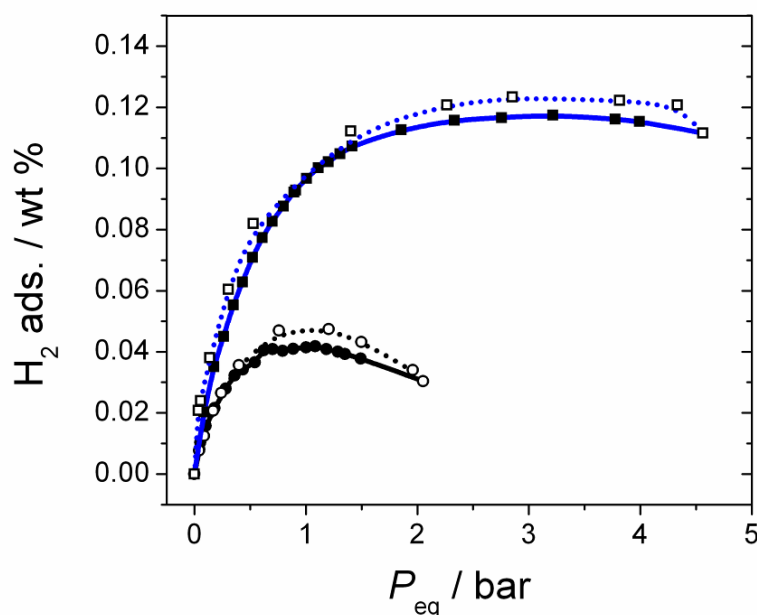
Table 8.5 lists the hydrogen adsorption properties of the materials derived from Langmuir-Freundlich fitting of the adsorption isotherms using Equation (8.1). The specific surface area of hydrogen adsorption ( $S_{H_2}$ ) and the maximum volume of the adsorbed hydrogen layer per gram of material ( $V_m$ ) are shown alongside the equivalent values derived from nitrogen adsorption at 77 K. It is worth drawing attention to a few phenomena in the data, namely that the specific surface area for hydrogen adsorption is much smaller than the specific surface area measured by nitrogen adsorption, and that the maximum volume adsorbed is likewise smaller except in the case of the  $Cd_3[Fe(CN)_6]_2$  bulk particles, which apparently have a slightly higher maximum volume of  $H_2$  adsorption compared to  $N_2$  adsorption.

The volume of hydrogen adsorbed in the pores of any porous material would be expected to be less than the total pore volume estimated from liquid nitrogen at 77 K, since hydrogen is in a supercritical state and cannot undergo condensation inside the pores like nitrogen, it can only form a layer a few molecules thick on the surface (see Table 8.5). The slightly larger  $V_m$  measured for the  $Cd_3[Fe(CN)_6]_2$  bulk particles than the total pore volume  $V_{pores}$  measured by nitrogen adsorption may be due to the degree of uncertainty in both measurements, since it is not possible to adsorb a greater volume of hydrogen than of nitrogen at 77 K.

Dividing  $V_m$  by the specific surface areas  $S_{H_2}$  and  $S_{BET}$  gives  $d_{H_2}$  and  $d_{BET}$ , the thickness of the adsorbed layer of  $H_2$  molecules using the surface areas measured with hydrogen and nitrogen respectively. The accuracy of these results probably suffers from several cumulative errors (from isotherm measurement and isotherm fitting), but they show that the thickness of the adsorbed layer is less than the diameter of the pores measured by nitrogen adsorption ( $d_{pores}$ ) given in Table 8.5, which is the only result physically possible. It would appear from the data that the layer thickness and degree of filling of the pores is greatly enhanced, even doubled, in the titanate nanotubes-  $Cd_3[Fe(CN)_6]_2$  composite compared with the raw titanate nanotubes, but this is only preliminary data and the results need to be reproduced and verified. On the whole, the values of  $d_{BET}$  seem more likely than the values of  $d_{H_2}$ , as they are smaller and represent adsorption of only one or two layers of hydrogen molecules, as would be expected at 77 K which is well above the hydrogen supercritical temperature of 33.2 K. <sup>[298]</sup>

## 8.6. Reversibility of hydrogen adsorption

The reversibility of hydrogen adsorption in the microporous Ge-imogolite samples was evaluated by running a complete adsorption/desorption cycle in which the equilibrium pressure was increased stepwise until it was just above the saturation point of the material, and then decreased stepwise back to zero. The results for both single-walled and double-walled nanotubes are shown in Figure 8.11. The shape of the desorption isotherm demonstrates fully reversible adsorption, with a very narrow hysteresis between the adsorption and desorption curves. The kinetics of both adsorption and desorption were rapid: the adsorption steps reached equilibrium (measured rate of change in adsorption  $< 1 \times 10^{-4}$  wt% min<sup>-1</sup>) within 2 minutes and the desorption steps reached equilibrium within 5 minutes.



**Figure 8.11.** Temperature-corrected isotherms at 77 K showing (■) hydrogen adsorption, (□)...hydrogen desorption in single-walled Ge-imogolite, and (●) hydrogen adsorption, (○)...hydrogen desorption in double-walled Ge-imogolite.

The adsorption/desorption cycle behaviour of the other metal oxide nanotubes was not measured, but they are expected to behave in a similar manner since the binding

between the nanotubes surfaces and  $H_2$  molecules is only described by weak physisorption forces.

## 8.7. Conclusions

Of the metal oxide nanotubes studied in this chapter, titanate nanotubes show the best cryogenic adsorption of hydrogen, with 0.2 wt % excess adsorption at 3 bars pressure, and a calculated maximum surface adsorbed mass of 0.47 wt %. Both the gravimetric and volumetric hydrogen adsorption properties of titanate nanotubes can be increased by doping with 10 wt %  $Cd_3[Fe(CN)_6]_2$  Prussian blue analogue material, although the chemical bonding of the PB analogue to the titanate nanotube surface does not appear to enhance the gravimetric storage over what would be expected for a physical mixture of the two substances (ca. 0.6 wt %). The excess hydrogen adsorption of all the other metal oxide nanotubes is less than 0.2 wt %, and at room temperature the hydrogen adsorption of all the materials was found to be zero.

The isotherms measured in this chapter are only preliminary data and require repetition together with measurement of more points to improve fitting, but the results obtained so far suggest that, without any modifications to increase the surface area or the binding energy of hydrogen to the nanotube surfaces, the metal oxide nanotubes studied here are not useful as hydrogen storage materials.





## Chapter 9: Conclusions and Suggestions for Further Work

### 9.1. Conclusions

The work presented in this thesis was carried out to improve understanding of the hydrothermal synthesis mechanism and hydrogen storage properties of metal oxide nanotubes. Nanotubes composed of the materials  $\text{Al}_2\text{Si}_2\text{O}_5(\text{OH})_4$  (halloysite),  $\text{Ni}_3\text{Si}_2\text{O}_5(\text{OH})_4$  (nickel silicate),  $\text{Al}_2\text{GeO}_3(\text{OH})_4$  (germanium-imogolite),  $\text{VO}_x$  (vanadium oxide) and  $\text{H}_3\text{Ti}_x\text{O}_{2x+1}$  (titanate) formed the basis of this work.

In the first part of this project, a hydrothermal synthesis method at 220 °C for 7 days duration under acid conditions (pH 2) was devised for halloysite nanotubes, which had not yet been synthesised except in very slow processes close to room temperature due to the lesser thermodynamic stability of halloysite nanotubes in relation to the flat nanosheet form of  $\text{Al}_2\text{Si}_2\text{O}_5(\text{OH})_4$ , kaolinite. The synthesis method used in this thesis was inspired by the use of silicon(IV) substitution with germanium(IV) in another type of aluminosilicate nanotubes,  $\text{Al}_2\text{SiO}_3(\text{OH})_4$  (imogolite) to alter the curvature of the nanotubes. It was expected that replacement of  $\text{SiO}_4$  tetrahedra with  $\text{GeO}_4$  tetrahedra in the silicate sheet in the  $\text{Al}_2\text{Si}_2\text{O}_5(\text{OH})_4$  layers would cause an increase in the geometric strain of the layers, promoting bending of the  $\text{Al}_2\text{Si}_2\text{O}_5(\text{OH})_4$  nanosheets into nanotubes.

The synthesis was successful, with an increase in  $\text{Al}_2\text{Si}_2\text{O}_5(\text{OH})_4$  curvature from sheets towards spheres and finally tubes as  $X$ , the mole fraction of Ge(IV) substituted for Si(IV) in the starting materials, was increased from 0 to 0.2. However, the amount of Ge(IV) actually incorporated into the  $\text{Al}_2\text{Si}_2\text{O}_5(\text{OH})_4$  structure was less than expected, the chemical formula of the as-synthesised multiwalled nanotubes estimated using EDX being described by  $\text{Al}_2\text{Si}_{2-x}\text{Ge}_x\text{O}_5(\text{OH})_4$ , where  $x \leq 0.004$ . Calculations for curved halloysite layers producing a nanotube with an inner diameter of 10 nm and an outer

diameter of 50 nm, which were the average dimensions of the synthetic nanotubes, estimated that  $x$  should be equal to approximately 0.34 (i.e. 18 % Ge(IV) substitution) to achieve this degree of curvature. The fact that a much smaller substitution was observed means that the presence of Ge(IV) in the structure has a stronger effect on the  $\text{Al}_2\text{Si}_2\text{O}_5(\text{OH})_4$  that might be expected, either by distorting the interconnected framework of  $\text{SiO}_4$  tetrahedra beyond the neighbours of the  $\text{GeO}_4$  substituted into the layer, or by inducing Si(IV) cation vacancies which enlarge the  $\text{SiO}_4$  sheet due to neighbouring  $\text{O}^-$  -  $\text{O}^-$  repulsion.

When  $X$  is increased further to 0.5, a change is induced in the aluminosilicate structure to form Ge-doped imogolite nanotubes,  $\text{Al}_2\text{Si}_{1-x}\text{Ge}_x\text{O}_3(\text{OH})_4$  where  $x$  is approximately equal to 0.35. The large increase in Ge(IV) substitution apparently favours the imogolite structure over the halloysite structure, whereas in the absence of Ge(IV),  $\text{Al}_2\text{Si}_2\text{O}_5(\text{OH})_4$  is the only aluminosilicate product. The reasons for this change are not yet clear. The substitution of Ge(IV) in the synthesis also generates an increasingly large percentage of amorphous material, in which most of the Ge(IV) from the starting materials is contained: in the  $X = 0.2$  and 0.5 products, only approximately 10 % of the products by mass contain crystalline aluminosilicates.

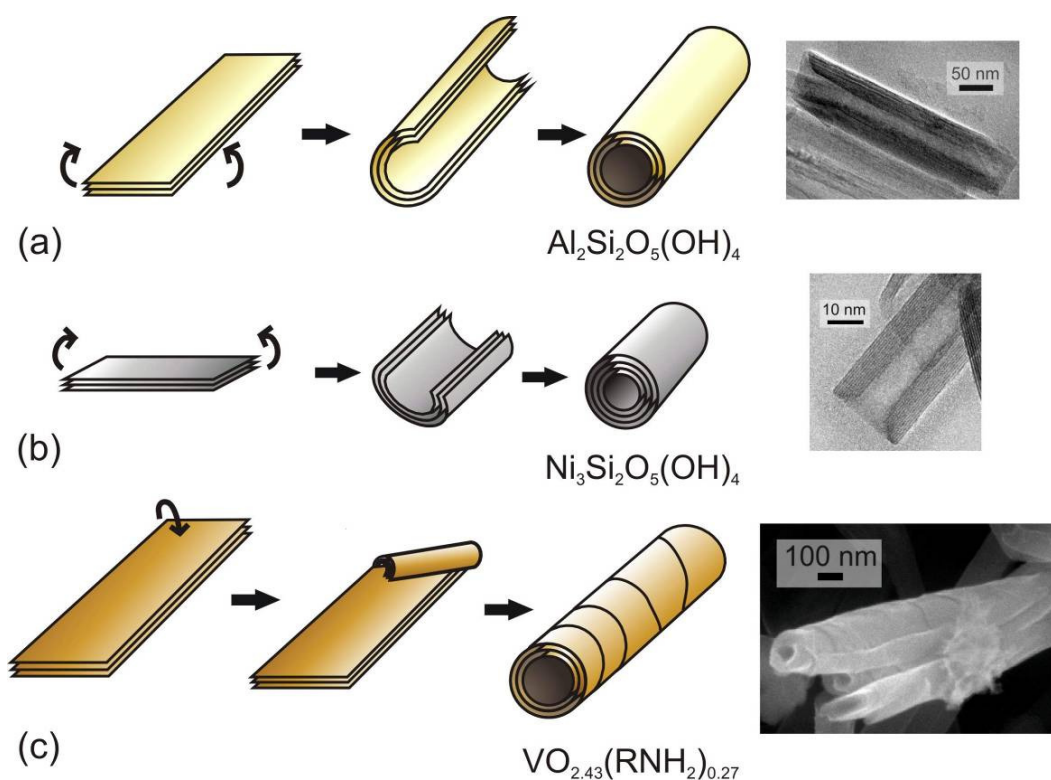
Aging of samples of naturally-occurring halloysite nanotubes in dilute and concentrated acidic and basic solutions revealed that halloysite is kinetically stable in water, and weak organic or dilute ( $1 \text{ mmol dm}^{-3}$ ) inorganic acid and alkaline solutions at room temperature. In concentrated ( $0.01 - 1 \text{ mol dm}^{-3}$ ) solutions of strong acids and bases, extensive acid- or base-catalysed dissolution is initiated at the inner Al-OH surface of the nanotubes, leading to progressive thinning of the tubes from the inside. In solutions of strong acids  $\text{H}_2\text{SO}_4$  and  $\text{HCl}$ , the greater solubility of Al(III) vs. Si(IV) leads to the formation of small  $\text{SiO}_2$  nanoparticles inside the tubes, enhancing the surface area and pore volume of the sample. In  $\text{NaOH}$  solutions the greater solubility of Si(IV) compared to Al(III) leads to the formation of fragmented flaky particles containing layers of  $\text{Al}(\text{OH})_3$  outside the tubes. In  $\text{NaOH}$  the initial rate of the dissolution follows pseudo-first-order reaction kinetics, whereas in  $\text{H}_2\text{SO}_4$  the kinetic curves of dissolution are characterized by an ‘induction’ period of time, indicating a slower mechanism of Al(III) removal in acids compared with bases.

The hydrothermal synthesis experiments for  $\text{Ni}_3\text{Si}_2\text{O}_5(\text{OH})_4$  nanotubes at 195 °C for 2 days duration in NaOH solutions were designed to investigate the effect of the Ni/Si ratio and NaOH concentration in the starting materials on the morphology of the resulting nanotubes, in order to reveal details of the nanotube formation mechanism. An molar Ni/Si ratio of 1.5 and added concentration of NaOH in the range 2 – 10 wt % were found to be the optimum conditions for the formation of nickel silicate nanotubes. The average length of the nanotubes increased as the concentration of added NaOH was increased.

The hydrothermal synthesis experiments for vanadium oxide nanomaterials at a range of temperatures between 90 – 180 °C were designed to increase understanding of the nanotube formation mechanism and to investigate whether this use of the V(V)-coordinating ligand ethylenediamine would stimulate formation of nanotubes at temperatures below 180 °C. At the ethylenediamine concentrations used in this work, nanotubes were not observed to form, although the rate of formation of elongated  $\text{VO}_x$  nanosheets was more than tripled at 90 °C through the addition of 0.1 mol dm<sup>-3</sup> ethylenediamine prior to hydrothermal treatment. The rapid scrolling of these nanosheets under the TEM electron beam was observed, and together with the XRD results this strongly suggests that the nanosheets scroll into tubular shapes because of the removal of intercalated amine molecules during heating.

The studies of metal oxide nanotube synthesis in this thesis have shown that metal oxide nanotubes are formed via the scrolling of elongated nanosheets which grow from precursor materials via recrystallisation. The mechanism of scrolling, however, is specific to each nanotube (Figure 9.1). The scrolling of  $\text{Al}_2\text{Si}_2\text{O}_5(\text{OH})_4$  nanotubes occurs parallel to the [010] nanosheet growth direction (the crystallographic *b*-axis), and must be induced by the presence of doping agents such as Ge(IV) in the synthesis mixture, otherwise flat nanosheets are thermodynamically favoured. The scrolling of nickel silicate ( $\text{Ni}_3\text{Si}_2\text{O}_5(\text{OH})_4$ ) nanotubes, on the other hand, occurs spontaneously in a straightforward stoichiometric mixture (1.5 molar ratio) of  $\text{NiCl}_2$  and  $\text{Na}_2\text{SiO}_3$ . The scrolling of the nanotubes occurs around the *a*-axis, perpendicular to the nanosheet growth direction (*b*-axis). In this way the formation mechanism of nickel silicate nanotubes strongly resembles that of titanate nanotubes (cf. Figure 2.12), although the thermodynamic driving forces for their scrolling are different (see Section 2.3.2).

Vanadium oxide ( $\text{VO}_x$ ) nanotubes form from elongated nanosheets scrolled around the [110] direction. The scrolling commences from the nanosheet ends rather than evenly along the whole nanosheet as occurs with  $\text{Al}_2\text{Si}_2\text{O}_5(\text{OH})_4$  and  $\text{Ni}_3\text{Si}_2\text{O}_5(\text{OH})_4$ , because the driving force for scrolling is the removal of intercalating amine molecules starting from the nanosheet ends. The elongated nanosheets wind around themselves like a piece of flexible tape to form nanotubes, producing uneven tube walls with a variable diameter along their length (see Figure 9.1).



**Figure 9.1.** Scrolling mechanisms of different metal oxide nanotubes proposed in this thesis, (a) halloysite  $\text{Al}_2\text{Si}_2\text{O}_5(\text{OH})_4$ , (b) nickel silicate  $\text{Ni}_3\text{Si}_2\text{O}_5(\text{OH})_4$ , and (c) vanadium oxide  $\text{VO}_{2.43}(\text{RNH}_2)_{0.27}$ . The images on the right are SEM and TEM images of the resulting nanotubes.

In the latter part of this work, the hydrogen storage properties of a range of synthetic metal oxide nanotubes were measured and compared. The results show that metal oxide nanotubes do not strongly physisorb hydrogen even at temperatures as low as 77 K. The best gravimetric adsorption results were achieved with titanate nanotubes, which may adsorb up to 0.47 wt % hydrogen on their surface. This is far short of the DOE 2015

target of 9 wt % storage, indicating that metal oxide nanotubes are not promising as hydrogen storage materials. A small enhancement of hydrogen adsorption can be achieved by doping metal oxide nanotubes with Prussian blue (PB) analogues with the structure  $M_3[Fe(CN)_6]_2$ , but a much higher gravimetric adsorption (above 1.5 wt %) is achievable by simply using bulk PB particles without supporting them on nanotubes. At room temperature, none of the nanotubular or PB particles adsorb hydrogen, therefore the binding energy of hydrogen to the particle surfaces must be small ( $\ll 10 \text{ kJ mol}^{-1}$ ).

## 9.2. Suggestions for Further Work

### 9.2.1. Hydrothermal synthesis of $Al_2Si_2O_5(OH)_4$ (halloysite) nanotubes

Although the work in Chapter 4 is a novel route to producing halloysite nanotubes, which had not previously been synthesised under hydrothermal conditions, the synthesis protocol has some drawbacks for large-scale synthesis of halloysite. These drawbacks are mainly associated with (i) a large mass of unwanted products, initially low at zero  $GeO_2$ -doping but rising to 90 % of the total product mass in the  $X = 0.2$  (20 %  $GeO_2$  substituted) sample in which halloysite nanotubes are formed, and (ii) the 7 day reaction period, which is too long to be of practical large-scale use. With these challenges in mind, the following suggestions for further work are proposed:

- Reduce the quantity of unwanted by-products ( $\gamma$ - $AlOOH$  and amorphous  $aSiO_2 \cdot bGeO_2 \cdot cAl_2O_3$  nanoparticles). The reactions in this thesis were performed at  $pH = 2$ , but  $Al_2Si_2O_5(OH)_4$  can form within a wide pH range (0.5- 7) <sup>[299]</sup> under hydrothermal conditions at 200 - 250 °C. Lowering the pH may increase the solubility of  $Al(III)$  species (see Figure 2.7, page 22), and help dissolve  $\gamma$ - $AlOOH$  particles. Decreasing the pH will almost certainly decrease the mass yield of  $Al_2Si_2O_5(OH)_4$ , and more  $Al(III)$  will remain in solution, but may increase the percentage yield of  $Al_2Si_2O_5(OH)_4$  relative to  $\gamma$ - $AlOOH$ .
- Decrease the duration of the reaction below 7 days. Ligands which bind  $Al(III)$  or  $Si/Ge(IV)$  species (e.g. EDTA) could be used to increase the solubility of the starting materials, increasing the rate of reaction.

- Lower the synthesis temperature (without compromising crystallinity of product). This would be difficult to achieve, because lowering the synthesis temperature would contradict the previous aim of reducing the reaction duration. However, the use of ligands as suggested above may also allow some reduction in the synthesis temperature, if their effect of increasing the reaction rate is strong enough.

### 9.2.2. Long-term solution stability of halloysite nanotubes

The work in Chapter 5 is complete in that it successfully catalogues the rate of dissolution and dissolution mechanism of halloysite nanotubes in  $\text{H}_2\text{SO}_4$ ,  $\text{HCl}$ ,  $\text{CH}_3\text{COOH}$ , and  $\text{NaOH}$  solutions at both high and low acid and base concentrations. It was also established that halloysite nanotubes are very stable in a distilled aqueous solution over a long period of time, with a small release of  $\text{Si(IV)}$  into solution corresponding to less than 4 % of the  $\text{Si(IV)}$  mass in the original halloysite the only indication of any dissolution. There is scope, however, for the work to be extended, particularly in the direction of assessing the long-term stability of halloysite in biological solution environments for the proposed drug-delivery applications of halloysite (see Chapter 1). Therefore, the following extension of this work is suggested:

- Perform controlled aging experiments of halloysite in bio-mimetic solutions, i.e. solutions containing metal salts and buffers such as citrate and phosphate in biologically significant concentrations, to determine whether such solutions have any effect on the structure or properties of halloysite: either by initiating dissolution of the nanotubes walls or by intercalation into the interlayer spaces.

### 9.2.3. Hydrothermal synthesis of $\text{Ni}_3\text{Si}_2\text{O}_5(\text{OH})_4$ nanotubes

In Chapter 6 the effect of varying the nickel(II) to silicon(IV) ratio and sodium hydroxide concentration in the starting materials on the structure of the resulting

nanotubes was fully described. It would be possible to extend this work through investigation of the following:

- Analyse effect of temperature on the synthesis of  $\text{Ni}_3\text{Si}_2\text{O}_5(\text{OH})_4$  nanotubes. Previous work (see Table 2.2 in Chapter 2) suggests that raising the synthesis temperature increases the formation rate of nanotubes such that a lower concentration of NaOH is necessary in the reaction solution. Conversely, if the concentration of NaOH is very high, the synthesis temperature of the nanotubes could possibly be lowered.
- Investigate whether other  $\text{M}^{2+}$  metal species (e.g.  $\text{Fe}^{2+}$ ,  $\text{Co}^{2+}$ ,  $\text{Mn}^{2+}$ ) can be substituted in the  $\text{NiO}_6$  layer of the nanotubes, in order to prepare novel nanotubes with a range of different properties and morphologies.

#### 9.2.4. Hydrothermal synthesis of $\text{VO}_x$ (vanadium oxide) nanotubes

A low temperature route to vanadium oxide nanotubes was not achieved in this work. The following list gives suggestions for the improvement of the synthesis at low temperatures:

- Experiment with using different  $-\text{NH}_2$  containing ligands dissolved in the reaction suspension to increase the solubility of vanadium(V) from the precursor material, and to aid the partial removal of dodecylamine from the interlayer spaces.
- Change the intercalating amine used for  $\text{VO}_x$  nanotube synthesis. Shorter chain amines, such as hexylamine or butylamine, may have faster intercalation and deintercalation rates. This could accelerate the scrolling process.

#### 9.2.5. Hydrogen storage properties of nanotubes

The hydrogen adsorption capacities of the nanotubes measured in this thesis were found to be low ( $\ll 1$  wt %) at cryogenic temperatures, and negligible at room temperature. This challenges previous observations of reasonably high wt % storage in nanotubes



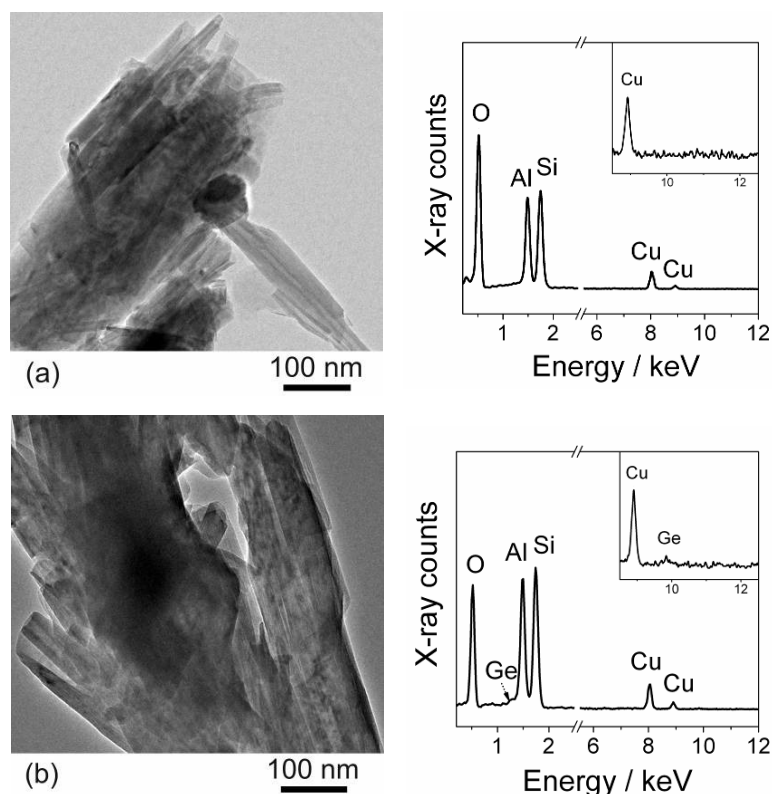
even at room temperature (see Chapter 2). To improve the adsorption capacities of these metal oxide materials, the following areas should be addressed:

- Increase the surface area of the nanotubes. Surface areas above  $1000 \text{ m}^2\text{g}^{-1}$  are necessary to increase both the gravimetric and volumetric storage of hydrogen. The surface areas of metal oxide nanotubes could be significantly increased by acid treatment (as shown with halloysite in Chapter 5).
- Doping the acid-treated nanotubes with materials which have stronger binding energies with  $\text{H}_2$  (for example Pt clusters with a binding energy of  $50\text{-}60 \text{ kJ mol}^{-1}$  [300]) to attempt to create hydrogen ‘spillover’ onto the nanotube surface from the doping material.

## Appendix A: Electron Microscopy EDX and SAED, and XRD Analysis

### A1. Determination of EDX detection limits for Ge(IV) content

In order to identify the lower limit of determination of germanium content in nanotubular aluminosilicates using EDX (on the Jeol 3010 TEM), several samples of naturally-occurring  $\text{Al}_2\text{Si}_2\text{O}_5(\text{OH})_4$  halloysite nanotubes (Sigma Aldrich, cat. number 685445) were impregnated with an aqueous solution of  $\text{Na}_4\text{GeO}_4$  (prepared from a stock solution of  $\text{GeO}_2$  dissolved in  $1 \text{ mol dm}^{-1}$   $\text{NaOH}$ ) followed by evaporation of the solvent using a rotary evaporator (100 rpm), resulting in homogenous deposition of  $\text{Na}_4\text{GeO}_4$  on the surface of the nanotubes.



**Figure A.1.** TEM images and EDX spectra of halloysite nanotubes doped with Ge(IV) at the level of (a) 0.05 wt % and (b) 0.1 wt %. The threshold of Ge(IV) detection appears to be close to 0.1 wt %.

The doping concentration of Ge(IV) was varied in the range from 0.05 to 0.5 wt %  $\text{GeO}_2$  per mass of nanotubes, which is equal to 0.06 – 0.6 % Ge(IV) of the total number of Ge(IV) + Si(IV) atoms, calculated from the molecular masses of  $\text{GeO}_2$  and  $\text{Al}_2\text{Si}_2\text{O}_5(\text{OH})_4$ . More than 10 areas in each sample were analyzed using the electron microscope. Figure A.1 shows characteristic TEM images and EDX spectra taken from the nanotubes doped with germanium. Based on these results, the lower limit of germanium determination can be approximated as 0.1 wt %, or approximately 0.12 % Ge(IV) of the total Ge(IV) + Si(IV) atoms.

## A2. Indexing of reflections of Ge-aluminosilicate SAED patterns

The following table shows measured d-spacings from the crystalline products of Chapter 4 analysed by SAED, compared with d-spacings from published SAED and XRD data.

**Table A.1.** Indexing of crystal reflections in halloysite-type nanotubes synthesised in products with mole fraction  $\text{GeO}_2$  ( $X$ ), in the range 0 – 0.5, by comparison with XRD and SAED data in the literature.

Mole fraction $\text{GeO}_2$	Morphologies examined by SAED	$hkl$	Experimental $d / \text{nm}$	$d / \text{nm}$ , taken from references <sup>[233, 235, 301, 302, 303, 304]</sup>
<b>0</b>	$\text{Al}_2\text{Si}_2\text{O}_5(\text{OH})_4$ NS	020	0.455	0.447
		110	0.439	0.438
		111	0.427	0.418
		021	0.397	0.384
		002	0.334	0.357
<b>0.2</b>	$\text{Al}_2\text{Si}_2\text{O}_5(\text{OH})_4$ MWNT	110	0.441	0.441
		002	0.363	0.372
		131	0.242	0.249
		040	0.221	0.223
		262	0.121	0.125

	$\gamma$ -AlOOH NR/ NS	020	0.603	0.606
		120	0.310	0.310
		031	0.219	0.229
		051	0.172	0.181
		251	0.133	0.132
<b>0.5</b>	Al <sub>2</sub> Si <sub>x</sub> Ge <sub>1-x</sub> O <sub>3</sub> (OH) <sub>4</sub> SWNT	71	0.341-0.351	0.328 – 0.353
		04	0.220	0.208
		06	0.148	0.138

### A3. Indexing of reflections in nickel silicate XRD patterns

The following table shows measured d-spacings from the crystalline products of Chapter 6 analysed by XRD, indexed by comparison with published crystallographic data.<sup>[264, 272]</sup> The FWHM (full width at half maximum) of each reflection peak is given, with the instrumental broadening of 0.085 ° subtracted.

**Table A.2.** Indexing of Ni<sub>3</sub>Si<sub>2</sub>O<sub>5</sub>(OH)<sub>4</sub> and  $\beta$ -Ni(OH)<sub>2</sub> crystal reflection in the XRD patterns of the unmodified nickel silicate products.

Sample wt % NaOH (Ni/Si)	Phase	<i>hkl</i>	2 $\theta$ / °	<i>d</i> / nm	FWHM / °
0 wt % (1.5)	Ni <sub>3</sub> Si <sub>2</sub> O <sub>5</sub> (OH) <sub>4</sub>	(002)	25.8	0.345	1.91
	Ni <sub>3</sub> Si <sub>2</sub> O <sub>5</sub> (OH) <sub>4</sub>	(200)	37.11	0.242	2.488
	Ni <sub>3</sub> Si <sub>2</sub> O <sub>5</sub> (OH) <sub>4</sub>	(030)	60.48	0.153	1.035
4 wt % (1)	Ni <sub>3</sub> Si <sub>2</sub> O <sub>5</sub> (OH) <sub>4</sub>	(001)	12.09	0.731	2.586
	$\beta$ -Ni(OH) <sub>2</sub>	(001)	19.33	0.459	0.913
	Ni <sub>3</sub> Si <sub>2</sub> O <sub>5</sub> (OH) <sub>4</sub>	(002)	24.46	0.364	1.534
	Ni <sub>3</sub> Si <sub>2</sub> O <sub>5</sub> (OH) <sub>4</sub>	(200)	33.93	0.264	0.009
	Ni <sub>3</sub> Si <sub>2</sub> O <sub>5</sub> (OH) <sub>4</sub>	(030)	60.58	0.153	0.434
4 wt % (1.5)	Ni <sub>3</sub> Si <sub>2</sub> O <sub>5</sub> (OH) <sub>4</sub>	(001)	12.1	0.730	0.764

	$\beta$ -Ni(OH) <sub>2</sub>	(001)	19.21	0.462	0.137
	Ni <sub>3</sub> Si <sub>2</sub> O <sub>5</sub> (OH) <sub>4</sub>	(002)	24.36	0.365	0.893
	$\beta$ -Ni(OH) <sub>2</sub>	(100)	33.0	0.261	0.0
	Ni <sub>3</sub> Si <sub>2</sub> O <sub>5</sub> (OH) <sub>4</sub>	(200)	33.86	0.265	0.29
	$\beta$ -Ni(OH) <sub>2</sub>	(101)	38.48	0.234	0.095
	$\beta$ -Ni(OH) <sub>2</sub>	(102)	52.30	0.176	0.024
	$\beta$ -Ni(OH) <sub>2</sub>	(110)	58.96	0.157	0.197
	Ni <sub>3</sub> Si <sub>2</sub> O <sub>5</sub> (OH) <sub>4</sub>	(030)	60.46	0.153	0.433
4 wt % (2)	Ni <sub>3</sub> Si <sub>2</sub> O <sub>5</sub> (OH) <sub>4</sub>	(001)	12.09	0.731	1.005
	$\beta$ -Ni(OH) <sub>2</sub>	(001)	19.33	0.459	0.095
	Ni <sub>3</sub> Si <sub>2</sub> O <sub>5</sub> (OH) <sub>4</sub>	(002)	24.46	0.364	0.853
	$\beta$ -Ni(OH) <sub>2</sub>	(100)	33.04	0.271	0.02
	Ni <sub>3</sub> Si <sub>2</sub> O <sub>5</sub> (OH) <sub>4</sub>	(200)	33.93	0.264	0.226
	$\beta$ -Ni(OH) <sub>2</sub>	(101)	38.53	0.233	0.085
	$\beta$ -Ni(OH) <sub>2</sub>	(102)	52.05	0.176	0.105
	$\beta$ -Ni(OH) <sub>2</sub>	(110)	59.03	0.156	0.063
	Ni <sub>3</sub> Si <sub>2</sub> O <sub>5</sub> (OH) <sub>4</sub>	(030)	60.58	0.153	0.698
	$\beta$ -Ni(OH) <sub>2</sub>	(111)	62.70	0.148	0.171
4 wt % (3)	Ni <sub>3</sub> Si <sub>2</sub> O <sub>5</sub> (OH) <sub>4</sub>	(001)	12.07	0.732	1.005
	$\beta$ -Ni(OH) <sub>2</sub>	(001)	19.25	0.461	0.039
	Ni <sub>3</sub> Si <sub>2</sub> O <sub>5</sub> (OH)	(002)	24.34	0.365	0.53
	$\beta$ -Ni(OH) <sub>2</sub>	(100)	33.03	0.271	0.052
	Ni <sub>3</sub> Si <sub>2</sub> O <sub>5</sub> (OH)	(200)	33.88	0.264	0.102
	$\beta$ -Ni(OH) <sub>2</sub>	(101)	38.54	0.233	0.076
	$\beta$ -Ni(OH) <sub>2</sub>	(102)	52.08	0.175	0.115
	$\beta$ -Ni(OH) <sub>2</sub>	(110)	59.04	0.156	0.053

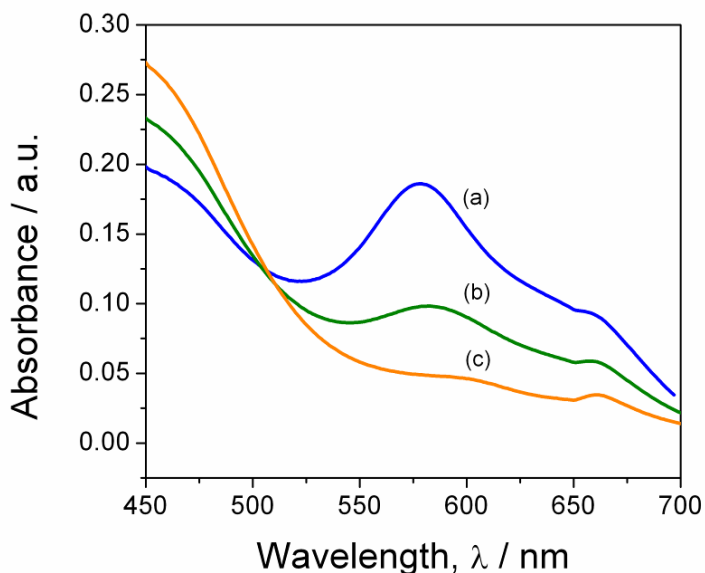
	$\text{Ni}_3\text{Si}_2\text{O}_5(\text{OH})_4$	(030)	60.53	0.152	0.288
	$\beta\text{-Ni}(\text{OH})_2$	(111)	62.68	0.148	0.093
7 wt % (1.5)	$\text{Ni}_3\text{Si}_2\text{O}_5(\text{OH})_4$	(001)	12.02	0.735	0.675
	$\beta\text{-Ni}(\text{OH})_2$	(001)	19.30	0.460	0.022
	$\text{Ni}_3\text{Si}_2\text{O}_5(\text{OH})_4$	(002)	24.35	0.365	0.742
	$\beta\text{-Ni}(\text{OH})_2$	(100)	32.98	0.271	0.042
	$\text{Ni}_3\text{Si}_2\text{O}_5(\text{OH})_4$	(200)	33.98	0.264	0.398
	$\beta\text{-Ni}(\text{OH})_2$	(101)	38.45	0.234	0.067
	$\beta\text{-Ni}(\text{OH})_2$	(102)	52.01	0.175	0.019
	$\beta\text{-Ni}(\text{OH})_2$	(110)	58.97	0.156	0.067
	$\text{Ni}_3\text{Si}_2\text{O}_5(\text{OH})_4$	(030)	60.46	0.153	0.289
10 wt % (1.5)	$\text{Ni}_3\text{Si}_2\text{O}_5(\text{OH})_4$	(001)	12.01	0.749	0.945
	$\beta\text{-Ni}(\text{OH})_2$	(001)	18.96	0.478	0.874
	$\text{Ni}_3\text{Si}_2\text{O}_5(\text{OH})_4$	(002)	24.43	0.365	0.469
	$\beta\text{-Ni}(\text{OH})_2$	(100)	33.05	0.271	0.010
	$\text{Ni}_3\text{Si}_2\text{O}_5(\text{OH})_4$	(200)	34.01	0.265	0.286
	$\beta\text{-Ni}(\text{OH})_2$	(101)	38.50	0.234	0.676
	$\beta\text{-Ni}(\text{OH})_2$	(102)	53.04	0.173	2.166
	$\text{Ni}_3\text{Si}_2\text{O}_5(\text{OH})_4$	(030)	60.15	0.154	1.042
15 wt % (1.5)	$\beta\text{-Ni}(\text{OH})_2$	(001)	19.18	0.462	0.975
	$\beta\text{-Ni}(\text{OH})_2$	(100)	33.33	0.269	0.368
	$\beta\text{-Ni}(\text{OH})_2$	(101)	38.45	0.234	1.401
	$\beta\text{-Ni}(\text{OH})_2$	(102)	51.977	0.176	1.960
	$\beta\text{-Ni}(\text{OH})_2$	(110)	59.18	0.156	0.282
	$\beta\text{-Ni}(\text{OH})_2$	(111)	62.75	0.148	0.681



## Appendix B: Colorimetric Data

### B1. Sample spectra of colorimetric complexes

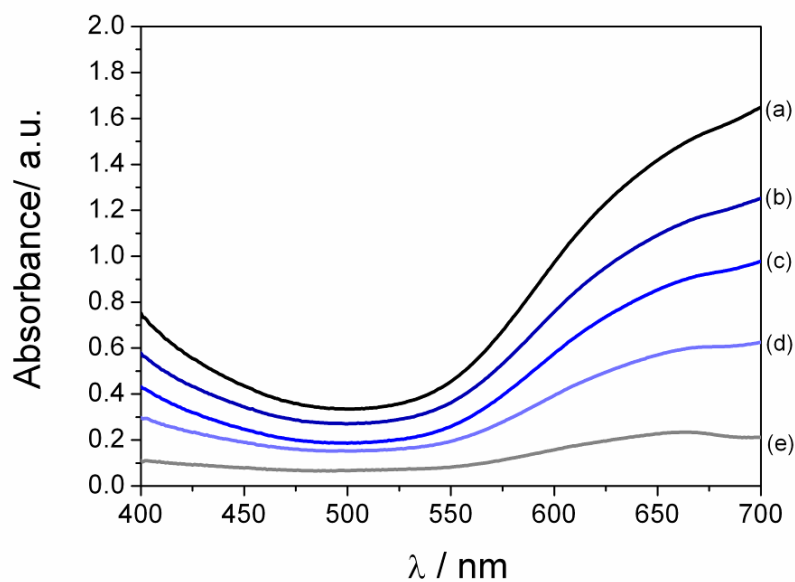
The following graphs are sample spectra collected over the visible range for the colorimetric complexes used in this thesis. Figure B.1 shows the UV-visible spectrum of the blue complex of pyrocatechol violet with  $20 \mu\text{mol dm}^{-3}$  Al(III) compared with the unreacted pyrocatechol violet, which is orange-yellow. At intermediate Al(III) concentrations close to  $10 \mu\text{mol dm}^{-3}$  the solution appears green as it is a mixture of the Al(III) complex and unreacted pyrocatechol violet.



**Figure B.1.** Sample UV-vis. spectra of pyrocatechol violet in the presence of (a) 20 and (b)  $10 \mu\text{mol dm}^{-3}$   $\text{AlCl}_3$  solution, and (c) unreacted pyrocatechol violet.

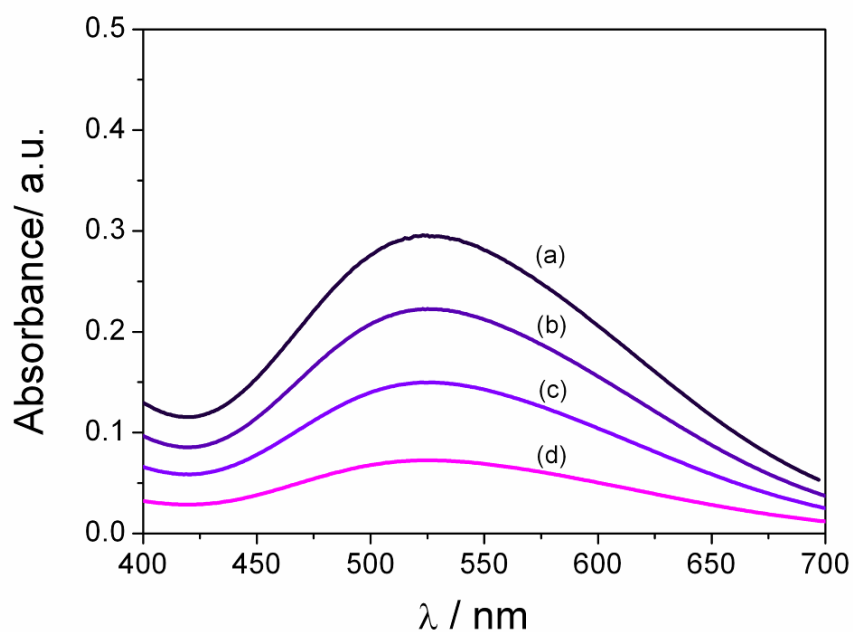
Figure B.2. shows the UV-visible spectrum of the silico-molybdate complex “molybdenum blue”,  $\text{H}_8\text{SiMo}_{12}\text{O}_{40} \cdot 12\text{H}_2\text{O}$ . The blue color intensifies as the solution concentration of Si(IV) increases. In the absence of Si(IV) the solution is colourless.





**Figure B.2.** Sample UV-vis. spectra of Si(IV) molybdenum blue complex at (a) 0.5, (b) 0.4, (c) 0.3, (d) 0.2 and (e) 0.1  $\mu\text{mol dm}^{-3}$  concentrations of dissolved  $\text{SiO}_2$ .

The UV-vis. spectrum of the V(V)-BPHA complex (purple) is shown below in figure B.3.

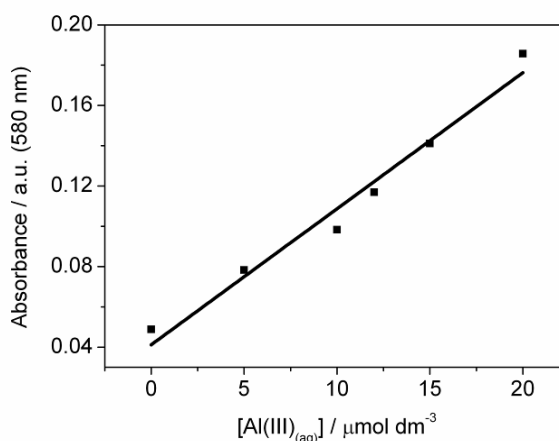


**Figure B.3.** Sample UV- vis. spectra of V(V)-BPHA complex at (a) 40, (b) 30, (c) 20 and (d) 10  $\mu\text{mol dm}^{-3}$  concentrations of dissolved  $\text{V}_2\text{O}_5$ .

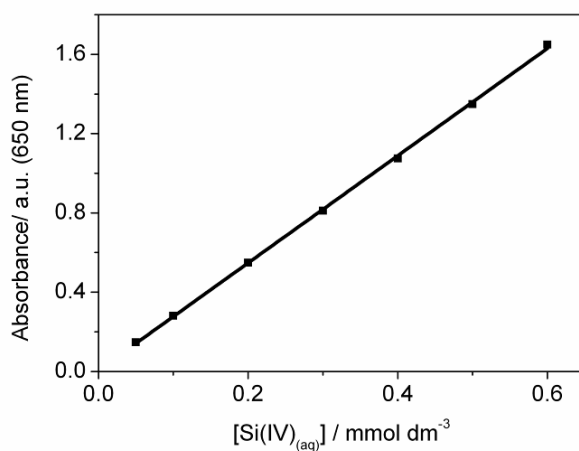
## B2. Typical calibration curves

The calibration curves used to determine the solution concentration of Al(III), Si(IV) and V(V) in chapters 5 and 7 are shown in Figures B.4.-B.5. To produce the calibration curves, stock solutions containing known concentrations of metal ions were used. The stock solution of Al(III) was made by dissolving  $\text{AlCl}_3 \cdot 6\text{H}_2\text{O}$  in distilled water, the stock solution of Si(IV) was made by dissolving  $\text{SiO}_2$  in  $1 \text{ mol dm}^{-3}$  NaOH and diluting with distilled water, and the stock solution of V(V) was made by dissolving  $\text{V}_2\text{O}_5$  in  $1 \text{ mol dm}^{-3}$  HCl and diluting with distilled water. The stock solutions were all  $0.01 \text{ mol dm}^{-3}$  in concentration and had to be diluted by an appropriate amount to produce the points for the calibration curves in this section. The procedure followed to produce the colorimetric complexes from the solutions containing metal ions is detailed in Section 3.6 page 58.

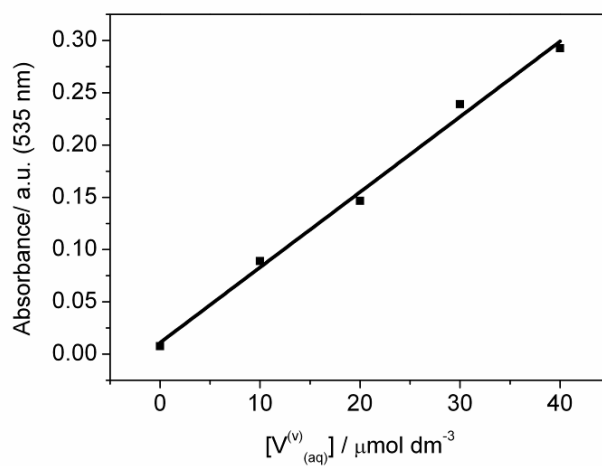
It should be noted that pyrocatechol violet is light-sensitive and decomposes over a few days, so a fresh stock solution had to be made for each analysis, hence Figure B.4. is a single representation of a calibration curve that had to be re-measured for every new stock solution of pyrocatechol violet. For molybdate and BPHA, the same stock solution was used for all analyses, and Figures B.5 and B.6. were used to determine the concentration of all samples analysed for Si(IV) and V(V).



**Figure B.4.** Calibration curve for  $\text{Al(III)}_{(\text{aq})}$  concentration /  $\mu\text{mol dm}^{-3}$  vs. absorbance at 580 nm.



**Figure B.5.** Calibration curve for  $\text{Si(IV)}_{(\text{aq})}$  concentration/  $\text{mmol dm}^{-3}$  vs. absorbance at 650 nm.



**Figure B.6.** Calibration curve for  $\text{V(V)}_{(\text{aq})}$  concentration/  $\mu\text{mol dm}^{-3}$  vs. absorbance at 535 nm.

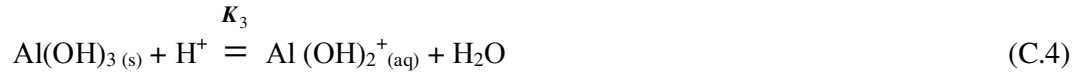
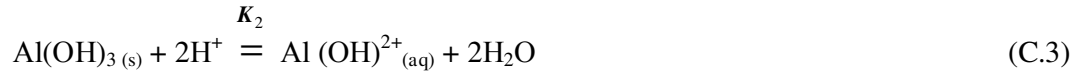
## Appendix C: Calculations for Solubility Diagrams

### C1. Aluminium hydroxide solubility

The total concentration of aluminium (III) in aqueous solution is given by the sum of all hydrolysed species:

$$C_{\text{Al(III)}} = C_{\text{Al}^{3+}} + C_{\text{Al(OH)}^{2+}} + C_{\text{Al(OH)}_2^+} + C_{\text{Al(OH)}_3} + C_{\text{Al(OH)}_4^-} \quad (\text{C.1})$$

The solubility constants of  $\text{Al(OH)}_3$  have been measured over the range 25 – 350 °C by [111, 260]. The solubility constants refer to the reactions:



Consequently, the concentrations of each hydrolysed species can be calculated by the formulae  $C_{\text{Al}^{3+}} = K_1 \cdot [\text{H}^+]^3$ ,  $C_{\text{Al(OH)}^{2+}} = K_2 \cdot [\text{H}^+]^2$  etc. Since the concentration of  $\text{H}^+$  is measured in logarithmic units (i.e.  $\text{pH} = -\log_{10}[\text{H}^+]$ ), it is more convenient to derive an expression that measures the concentration of each Al species in terms of pH and  $\log K_n$  (Equation C.7).

$$C_{\text{Al(III)}} = 10^{(\log K_1 - 3\text{pH})} + 10^{(\log K_2 - 2\text{pH})} + 10^{(\log K_3 - \text{pH})} + 10^{(\log K_4)} + 10^{(\log K_5 + \text{pH})} \quad (\text{C.7})$$

The values of  $\log K_n$  are temperature dependent, causing the shape of the solubility curve to change with temperature. The values of  $\log K_n$  at 25 °C were taken from the experimental  $\text{Al}(\text{OH})_3$  (gibbsite) solubility data of Wesolowski et al.<sup>[260]</sup>, and the values of  $\log K_n$  at 200 °C were taken from the experimental  $\gamma\text{-AlOOH}$  (boehmite) solubility data of Castet et al.<sup>[111]</sup> These constants were substituted into Equation C.7 to produce the solubility plots shown in Sections 2.3.1 and 5.4.

**Table C.1.** Logarithmic solubility constants for aluminium hydroxides. At 25 °C the constants are determined for  $\text{Al}(\text{OH})_3$ , and at 200 °C they are determined for the dehydrated aluminium hydroxide,  $\gamma\text{-AlOOH}$ .

Temperature/ °C	$\log K_1$	$\log K_2$	$\log K_3$	$\log K_4$	$\log K_5$
25	7.74	2.78	-2.80	-9.60	-15.13
200	-0.028	-1.41	-4.00	-6.65	-11.75

## C2. Ni(II) hydroxide solubility

The total concentration of Ni(II) in aqueous solution is given by the sum of all hydrolysed species:

$$C_{\text{Ni(II)}} = C_{\text{Ni}^{2+}} + C_{\text{Ni}(\text{OH})_2} \quad (\text{C.8})$$

Based on the dissolution reactions



$$\beta\text{-Ni (OH)}_2\text{ (s)} \xrightleftharpoons{K_2} \text{Ni(OH)}_2\text{ (aq)} \quad (\text{C.10})$$

The species  $\text{Ni(OH)}^+_{(\text{aq})}$  and  $\text{Ni(OH)}^-_{3(\text{aq})}$  are thought to only exist in negligible amounts.  
<sup>[105]</sup> Thus the expression for the variation in Ni(II) concentration with pH is given by:

$$C_{\text{Ni(II)}} = 10^{(\log K_1 - 2\text{pH})} + 10^{(\log K_2)} \quad (\text{C.11})$$

The temperature dependence equation derived by Palmer et al. <sup>[105]</sup> states that

$$\log_{10} K_1 = -2.71 + (4228.48/T) \quad (\text{C.12})$$

where T is measured in degrees Kelvin. Hence the values of  $\log K_1$  can be derived at 25 °C and 195 °C, which was the synthesis temperature of  $\text{Ni}_3\text{Si}_2\text{O}_5(\text{OH})_4$  nanotubes used in this thesis. To calculate  $\log K_2$ , the second hydrolysis constant  $K_{\text{H2}}$  for the reaction  $\text{Ni}^{2+}_{(\text{aq})} + 2\text{H}_2\text{O} = \text{Ni(OH)}_2\text{ (aq)} + 2\text{H}^+$  was used in conjunction with  $\log K_1$  according to the formula

$$\log K_2 = \log K_1 + \log K_{\text{H2}} \quad (\text{C.12})$$

where  $\log K_{\text{H2}}$  was calculated using the temperature dependence formula <sup>[105]</sup>

$$\log K_{\text{H2}} = 6.09 - (7282.7/T) - 0.009476T \quad (\text{C.13})$$

The results of these calculations are presented below in Table C.2. These values were substituted into equation C.8 to give the solubility plots in Sections 2.4.1 and 6.3.

**Table C.2.** Logarithmic solubility constants for  $\beta\text{-Ni(OH)}_2$ .

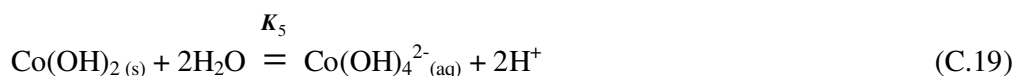
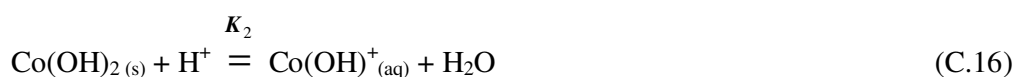
Temperature/ °C	$\log K_1$	$\log K_2$
25	11.48	-18.22
195	6.34	-13.91

### C3. Cobalt (II) hydroxide solubility

The total concentration of Co(II) in aqueous solution is given by the sum of all hydrolysed species:

$$C_{\text{Co(II)}} = C_{\text{Co}^{2+}} + C_{\text{Co(OH)}^+} + C_{\text{Co(OH)}_2} + C_{\text{Co(OH)}_3^-} + C_{\text{Co(OH)}_4^{2-}} \quad (\text{C.14})$$

Which is based on the dissolution reactions



At 25 °C the value of  $\log K_1$  can be derived from the solubility product  $K_{\text{sp}} = 2.5 \times 10^{-16}$

derived by Gayer and Garrett.<sup>[305]</sup> Since  $K_{\text{sp}} = [\text{Co}^{2+}][\text{OH}^-] = [\text{Co}^{2+}] \frac{K_w}{[\text{H}^+]}$ , it follows

that  $\log K_1 = \log K_{\text{sp}} - 2\log K_w$  where  $K_w$  is the dissociation constant of water at 25 °C which is equal to  $1.2 \times 10^{-14}$ . Therefore  $\log K_1 = 12.24$ . Using the published hydrolysis constants determined from experimental results,<sup>[110]</sup> it is possible to calculate values for all  $\log K_n$  at 25 °C. These values, which are shown in Table C.3, were used in equation C.14 to produce the solubility plot in Section 2.4.1.

**Table C.3.** Logarithmic solubility constants for  $\text{Co(OH)}_2$ .

Temperature/ °C	$\log K_1$	$\log K_2$	$\log K_3$	$\log K_4$	$\log K_5$
25	12.24	2.59	-6.56	-19.26	-34.06

### C4. Iron (III) hydroxide solubility

The solvation of iron (III) hydroxide proceeds in much the same way as Al(III) hydroxides, forming similar  $\text{Fe}^{3+}$ ,  $\text{Fe}(\text{OH})^{2+}$ ,  $\text{Fe}(\text{OH})_2^+$ ,  $\text{Fe}(\text{OH})_3$  and  $\text{Fe}(\text{OH})_4^-$  species in solution (see section C1). The solubility constants for these species have been calculated at 25 °C from solubility products and hydrolysis constants derived from experimental data by Liu and Millero,<sup>[109]</sup> and are shown in Table C.4 below.

**Table C.4.** Logarithmic solubility constants for  $\text{Fe}(\text{OH})_3$ .

Temperature/ °C	log $K_1$	log $K_2$	log $K_3$	log $K_4$	log $K_5$
25	4.1	2.0	-2.2	-10.2	-18.2

These constants were then used in an equation identical to equation C.7 to produce the solubility plot in Section 2.4.1.

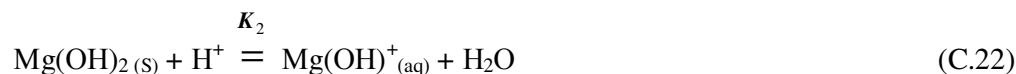
### C5. Magnesium (II) hydroxide solubility

The total concentration of Mg(II) in aqueous solution is given by the sum of all hydrolysed species:

$$C_{\text{Mg(II)}} = C_{\text{Mg}^{2+}} + C_{\text{Mg}(\text{OH})^+} \quad (\text{C.20})$$

Existence of the species  $\text{Mg}(\text{OH})_2(\text{aq})$  and  $\text{Mg}(\text{OH})_3^-(\text{aq})$  has not been confirmed by experimental results.<sup>[108]</sup>

The solubility constants for magnesium hydroxide are defined by the reactions





Based on the experimental results of Brown et al.,<sup>[107]</sup>  $\log K_1$  can be calculated using

$$-\log K_1 = 2.49 - (5847/T) \quad (C.23)$$

where T is in degrees Kelvin. The value of  $\log K_2$  at a given temperature can be calculated using the formula

$$\log K_2 = \log K_1 + \log K_{H1} \quad (C.24)$$

where  $K_{H1}$  is the first hydrolysis constant of  $Mg^{2+}_{(aq)}$ .  $K_{H1}$  can be calculated from the data of Benezeth, Palmer and Wesolowski.<sup>[108]</sup> The calculated values of  $\log K_1$  and  $\log K_2$  are displayed in Table C.5. These values were used in equation C.20 to obtain the solubility plots in Section 2.4.1.

**Table C.5.** Logarithmic solubility constants for  $Mg(OH)_2$ .

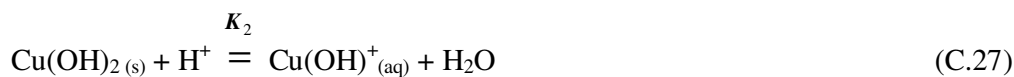
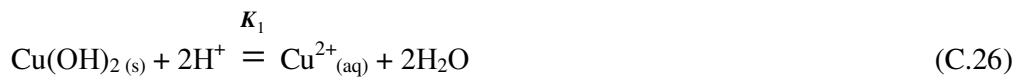
Temperature/ °C	$\log K_1$	$\log K_2$
25	17.13	5.45
200	10.08	2.94

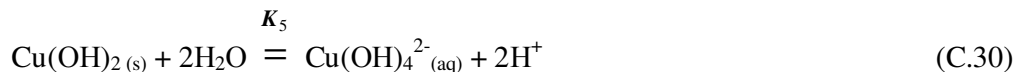
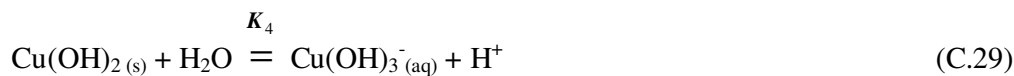
## C6. Copper (II) hydroxide solubility

The total concentration of Cu(II) in aqueous solution is given by the sum of all hydrolysed species:

$$C_{Cu(II)} = C_{Cu^{2+}} + C_{Cu(OH)^+} + C_{Cu(OH)_2} + C_{Cu(OH)_3^-} + C_{Cu(OH)_4^{2-}} \quad (C.25)$$

The solubility constants for  $Cu(OH)_2$  are defined by the reactions





The values for  $\log K_n$  at room temperature were calculated from the values of  $\log K_1$  and the hydrolysis constants recommended in the IUPAC book “Pure & Applied Chemistry, Chemical Speciation of Environmentally Significant Metals”.<sup>[106]</sup> The calculated  $\log K_n$  are shown below in Table C.6, and used to produce the plot in Section 2.4.1.

**Table C.6.** Logarithmic solubility constants for  $\text{Cu(OH)}_2$ .

Temperature/ °C	$\log K_1$	$\log K_2$	$\log K_3$	$\log K_4$	$\log K_5$
25	8.67	0.72	-7.52	-17.93	-31.07

## C7. Silicon (IV) dioxide solubility

Silicon dioxide dissolves to produce neutral or negatively charged species only (except for a small concentration of positively charged polymeric species under acid conditions at low temperature (< 100 °C)). It therefore has low solubility in acid solution and high solubility in strongly alkaline solution. The total Si(IV) concentration in solution is given by the formula

$$C_{\text{Si(IV)}} = C_{\text{H}_4\text{SiO}_4} + C_{\text{H}_3\text{SiO}_4^-} + C_{\text{H}_2\text{SiO}_4^{2-}} \quad (\text{C.31})$$

In figure 5.13, showing the solubility of  $\text{SiO}_2$  at room temperature,  $C_{\text{Si(IV)}}$  is taken from direct measurement at different pH values.<sup>[259]</sup> At 195 and 200 °C, the solubility can be derived using the equations



The value of  $\log K_1$  could be calculated from the experimental results of Gunnarsson and Arnorsson<sup>[112]</sup> relating  $K_1$  to temperature

$$\log K_1 = -8.476 - (485.24/T) - (2.268 \times 10^{-6} \times T^2) + 3.068(\log T) \quad (\text{C.34})$$

Where T is in degrees Kelvin. A value for the first acid dissociation constant,  $K_{H1} = -8.85$  was obtained from the experimental results of Busey and Mesmer.<sup>[277]</sup> The second acid dissociation constant has not yet been obtained experimentally, so a value of  $K_{H2} = -10.89$  was calculated using the data of Robbie et al.<sup>[131]</sup> These acid dissociation constants were used to calculate  $\log K_2$  and  $\log K_3$ , using the method described by equation C.12. The values of all  $\log K_n$  are shown below in Table C.7, and were used to produce the plots in Sections 2.4.1, 5.4 and 6.3.

**Table C.7.** Logarithmic solubility constants for  $\text{SiO}_2$ .

Temperature/ °C	$\log K_1$	$\log K_2$	$\log K_3$
195	-1.76	-10.60	-21.49
200	-1.74	-10.55	-21.47

## Appendix D: Hydrogen Adsorption Calculations

### D1. Derivation of Langmuir-Freundlich model

This derivation can be found with more explanation in reference; <sup>[180]</sup> a summary is presented here.

The absolute mass of hydrogen stored in a porous material is given by the sum of the mass of hydrogen in the adsorbed phase and in the bulk gas phase, i.e.

$$M = M_{H_2(a)} + M_{H_2(g)} \quad (D.1)$$

The mass of hydrogen in the bulk phase is given by:

$$M_{H_2(g)} = \rho_g (V_{pores} - V_a) \quad (D.2)$$

where  $\rho_g$  is the density of the gas phase,  $V_{pores}$  is the total pore (void) volume, and  $V_a$  is the volume of the adsorption layer.

As the solid surface is covered with hydrogen, the surface fractional coverage or occupancy ratio,  $\theta$ , is given by

$$\theta = q_{H_2} / q_m \quad (D.3)$$

where  $q_{H_2}$  is the adsorbed mass of hydrogen, and  $q_m$  is the total adsorbed mass of hydrogen at full surface coverage, both measured per unit mass of solid, i.e.  $q_{H_2} = M_{H_2(a)} / M_s$  where  $M_s$  is the solid mass. Therefore,

$$M_{H_2(a)} = q_m \theta \cdot M_s \quad (D.4)$$

Substituting the definition

$$q_m = \frac{m_{H_2} S}{A_{H_2} \cdot N_A} \quad (D.5)$$

where  $S$  is the specific surface area of full coverage,  $m_{H_2}$  is the mass of  $H_2$  in a.u.,  $A_{H_2}$  is the area occupied by one molecule of hydrogen, and  $N_A$  is Avagadro's number, we obtain

$$M_{H_2(a)} = \frac{m_{H_2} M_s}{A_{H_2} \cdot N_A} S \theta \quad (D.6)$$

Substituting this definition of  $M_{H_2(a)}$  and the definition of  $M_{H_2(g)}$  in equation (D.2) into equation (D.1) gives the expression for the absolute mass of adsorption

$$M = \frac{m_{H_2} M_s}{A_{H_2} \cdot N_A} S \theta + \rho_g (V_{pores} - V_a) \quad (D.7)$$

Assuming ideal gas behavior,  $\rho_g = \frac{m_{H_2} P}{RT}$ . It follows that

$$M = \frac{m_{H_2} M_s}{A_{H_2} \cdot N_A} S \theta + \frac{m_{H_2} P (V_{pores} - V_a)}{RT} \quad (D.8)$$

The excess adsorption of hydrogen,  $M_e$ , is defined by (see figure 2.15)

$$M_e = M - \rho_g V_g = M_{H_2(a)} - \rho_g V_a \quad (D.9)$$

Therefore

$$M_e = m_{H_2} \left( \frac{M_s S \theta}{A_{H_2} \cdot N_A} - \frac{P V_a}{RT} \right) \quad (D.10)$$

$V_a$  can be expressed in terms of the total adsorption volume  $V_m$  at the saturation limit of the adsorbed layer by the expression  $V_a = V_m\theta$ . If we substitute this expression into equation (D.10), and let  $\theta$  be expressed as a function of pressure such that  $\theta = f(P)$ , then

$$M_e = \left( \frac{M_s S}{A_{H_2} \cdot N_A} - \frac{PV_m}{RT} \right) \cdot m_{H_2} f(P) \quad (D.11)$$

To convert this into an expression for the gravimetric excess adsorption,  $m_e$ , defined as the excess adsorption per unit mass, we divide equation (D.11) by  $M_s$ , and redefine the units of  $V_m$  as the total volume of the adsorption layer *per gram of material*. Thus:

$$m_e = \left( \frac{S}{A_{H_2} N_A} - \frac{PV_m}{RT} \right) \cdot m_{H_2} f(P) \quad (D.12)$$

Several different models to describe  $f(P)$  can be substituted into this equation. The model used in this thesis was the Langmuir-Freundlich model, which states that

$$\theta = \frac{K_{LF} P^{1/n_{LF}}}{1 + K_{LF} P^{1/n_{LF}}} \quad (D.13)$$

where  $K_{LF}$  is the temperature-dependent Langmuir-Freundlich affinity constant, and  $n_{LF}$  is a parameter associated with the degree of heterogeneity of the adsorbed gas. <sup>[297]</sup>

## D2. Physical properties of hydrogen storage materials

**Table D.1.** Physical properties of the nanomaterials measured for hydrogen adsorption. The symbol  $\rho_b$  is the bulk density of the material, and  $a$ ,  $b$  and  $c$  are the unit cell parameters. The estimated density of the titanate  $\text{Cd}_3[\text{Fe}(\text{CN})_6]_2$  composite provided here is an average of the densities of titanate nanotubes and bulk  $\text{Cd}_3[\text{Fe}(\text{CN})_6]_2$ , and the unit cell volume for titanate nanotubes is used as an approximation for the composite.

Material	$\rho_b / \text{gcm}^{-3}$	Unit cell / nm	$V_{\text{unit cell}} / \text{cm}^3$	$M_r(\text{unit cell}) / \text{gmol}^{-1}$	Refs.
$\text{Cd}_3[\text{Fe}(\text{CN})_6]_2$	0.45	$a = 1.071$	$1.23 \times 10^{-21}$	761.1	[215, 306]
Titanate $\text{H}_2\text{Ti}_3\text{O}_7$	3.16	$a = 1.602$ $b = 0.375$ $c = 0.919$ $\beta = 101.5^\circ$	$0.54 \times 10^{-21}$	258.1	[62, 307]
Titanate + 10 wt % $\text{Cd}_3[\text{Fe}(\text{CN})_6]_2$	2.89	-	$0.54 \times 10^{-21}$	308.4	-
Ge-imogolite $\text{Al}_2\text{GeO}_3(\text{OH})_4$	$3.31^\ddagger$	$a = 0.490$ $b = 0.846$ $c = 0.872$ $\gamma = 78^\circ$	$0.35 \times 10^{-21}$	242.6	[308, 309]
Nickel silicate $\text{Ni}_3\text{Si}_2\text{O}_5(\text{OH})_4$	2.82	$a = b = 0.563$ $c = 0.738$ $\gamma = 120^\circ$	$0.23 \times 10^{-21}$	380.3	[308, 264]

---

$^\ddagger$  Estimated from the density of  $\text{Al}_2\text{SiO}_3(\text{OH})_4$  [308] using  $M_r(\text{Ge}) = 72.6 \text{ g mol}^{-1}$  and  $M_r(\text{Si}) = 28.1 \text{ g mol}^{-1}$ .

---

## References

---

- [1]. Cao, G., *Nanostructure & Nanomaterials, synthesis, properties & applications*, 2004, Imperial College Press, London, ISBN: 1-86094-415-9.
- [2]. Hornyak, G.L., Tibbals, H.F., Dutta, J., Moore, J.J., *Introduction to Nanoscience and Nanotechnology*, 2008, CRC Press, Taylor and Francis Group, ISBN: 9781420047790.
- [3]. Reibold, M., Paufler, P., Levin, A.A., Kochmann, W., Pätzke, N., and Meyer, D.C., Carbon nanotubes in an ancient Damascus sabre. *Nature*, **444**, p. 286, 2006.
- [4]. Murr, L.E., Nanoparticulate materials in antiquity: the good, the bad and the ugly, *Microscopy and Microanalysis*, 2007, **13**, 1118-1119.
- [5]. Radushkevich, L.V., Lukyanovich, V.M., *Zurn. Fisic. Chem.*, 1952, **111**, 24.
- [6]. Iijima, S., Helical microtubules of graphite carbon, *Nature*, 1991, **354**, 56.
- [7]. Tenne, R., Margulis, L., Genut, M., Hodes, G., Polyhedral and cylindrical structures of tungsten disulfide, *Nature*, 1992, **360**, 6403, 444-446.
- [8]. Kasuga, T., Hiramatsu, M., Hoson, A., Sekino, T., Niihara, K., Formation of titanium oxide nanotube, *Langmuir*, 1998, **14**, 12, 3160-3163.
- [9]. Spahr, M.E., Bitterli, P., Nesper, R., Muller, M., Krumeich, F., Nissen, H.U., Redox-active nanotubes of vanadium oxide, *Angewandte Chemie-International Edition*, 1998, **37**, 9, 1263-1265.
- [10]. Sarangi, D., Hierold, C., Carbon nanotubes over metallic wires and its possible applications, *Fullerenes, Nanotubes, and Carbon Nanostructures*, 2005, **13**, 243-254.
- [11]. Xu, H., Zhang, Q., Yan, W., Chu, W., A composite Sb-doped SnO<sub>2</sub> electrode based on the TiO<sub>2</sub> nanotubes prepared by hydrothermal synthesis, *International Journal of Electrochemical Science*, 2011, **6**, 6639-6652.
- [12]. Nah, Y.C., Paramasivam, I., Schmuki, P., Doped TiO<sub>2</sub> and TiO<sub>2</sub> nanotubes: Synthesis and applications, *ChemPhysChem*, 2010, **11**, 2698-2713.
- [13]. Lvov, Y.M., Shchukin, D.G., Möhwald, H., Price, R., Halloysite clay nanotubes for controlled release of protective agents, *ACS Nano*, 2008, **2**, 5, 814-820.
- [14]. Cai, K., Jiang, F., Luo, Z., Chen, X., Temperature-responsive controlled drug delivery system based on titanium nanotubes, *Advanced Engineering Materials*, 2010, **12**, 9, B565-B570.



- 
- [15]. Chen, X., Chen, H., Tripisciano, C., Jedrzejewska, A., Rummeli, M.H., Klingeler, R., Kalenczuk, R.J., Chu, P.K., Borowiak-Palen, E., Carbon-nanotube-based stimuli-responsive controlled-release system, *Chemistry- A European Journal*, 2011, **17**, 16, 4454-4459.
- [16]. Verago, V., Abullayev, E., Lvov, Y.M., Zeitoin, A., Cingolani, R., Rinaldi, R., Leporatti, S., Cytocompatibility and uptake of halloysite nanotubes, *Biomacromolecules*, 2010, **11**, 3, 820-826.
- [17]. US Department of Energy, *Hydrogen and Fuel Cells*, Fuel Cell Technologies Program, January 2011.  
([http://www1.eere.energy.gov/hydrogenandfuelcells/pdfs/fct\\_h2\\_storage.pdf](http://www1.eere.energy.gov/hydrogenandfuelcells/pdfs/fct_h2_storage.pdf)), accessed 15.08.2012.
- [18]. US Department of Energy, *Targets for Onboard Hydrogen Storage Systems for Light Duty Vehicles*, September 2009,  
([http://www1.eere.energy.gov/hydrogenandfuelcells/storage/pdfs/targets\\_onboard\\_hydro\\_storage\\_explanation.pdf](http://www1.eere.energy.gov/hydrogenandfuelcells/storage/pdfs/targets_onboard_hydro_storage_explanation.pdf)), accessed 15.08.2012.
- [19]. Yudasaka, M., Kikuchi, R., Matsui, T., Ohki, Y., Yoshimura, S., Ota, E., Specific conditions for Ni catalyzed carbon nanotube growth by chemical-vapor-deposition, *Appl. Phys. Lett.*, 1995, **67**, 17, 2477-2479.
- [20]. Loiseau, A., Willaime, F., Demoncy, N., Hug, G., Pascard, H., Boron nitride nanotubes with reduced number of layers synthesized by arc discharge, *Phys. Rev. Lett.*, 1996, **76**, 25, 4737-4740.
- [21]. Gong, D., Grimes, C.A., Varghese, O.K., Hu, W.C., Singh, R.S., Chen, Z., Dickey, E.C., Titanium oxide nanotube arrays prepared by anodic oxidation, *J. Mater. Res.*, 2001, **16**, 12, 3331-3334.
- [22]. Sander, M.S., Gao, H., Aligned arrays of nanotubes and segmented nanotubes on substrates fabricated by electrodeposition onto nanorods, *J. Am. Chem. Soc.*, 2005, **127**, 35, 12158-12159.
- [23]. Hernandez, B.A., Chang, K.S., Fisher, E.R., Sol-gel template synthesis and characterisation of BaTiO<sub>3</sub> and PbTiO<sub>3</sub> nanotubes, *Chem. Mater.*, 2002, **14**, 2, 480-482
- [24]. Bae, C., Yoo, H., Kim, S., Lee, K., Kim, J., Sung, M.A., Shin, H., Template-directed synthesis of oxide nanotubes: fabrication, characterization, and applications, *Chem. Mater.*, 2008, **20**, 3, 756-767.

- 
- [25]. Schaak, R.E., Mallouk, T.E., Prying apart Ruddlesden-Popper phases: exfoliation into sheets and nanotubes for assembly of perovskite thin films, *Chem. Mater.*, 2000, **12**, 11, 3427-3434.
- [26]. Ma, R., Sasaki, T., Conversion of metal oxide nanosheets into nanotubes, in: *Inorganic and Metallic Nanotubular Materials, Topics in Applied Physics*, vol. **117**, pp. 135-146, Kijima, T. (ed.), Springer-Verlag, Berlin.
- [27]. Kijima, T., Introduction to inorganic and metallic nanotubes, in: *Inorganic and Metallic Nanotubular Materials, Topics in Applied Physics*, vol. **117**, pp. 1-13, Kijima, T. (ed.), Springer-Verlag, Berlin.
- [28]. Tenne, R., Inorganic nanotubes and fullerene-like nanoparticles, *Nature Nanotechnology*, **1**, 2, 103-111.
- [29]. Wang, X., Li, Y., Solution-based synthetic strategies for 1-D nanostructures, *Inorganic Chemistry*, 2006, **45**, 7522-7534.
- [30]. Krivovichev, S.V., Nanotubes in minerals and mineral-related systems, in: *Minerals as Advanced Materials*, 2008, Krivovichev, S.V.(ed.), Springer-Verlag, Berlin-Heidelberg.
- [31]. Fang, Y., Xu, A., You, L., Song, R., Yu, J.C., Zhang, H., Li, Q., Liu, H., *Adv. Functional Mater.*, 2003, **13**, 12, 955-960.
- [32]. Xu, A., Fang, Y., You, L., Liu, H., *J. Am. Chem. Soc.*, 2003, **125**, 6, 1494-1495.
- [33]. Tang, C., Bando, Y., Liu, B., Goldberg, D., *Adv. Mater.*, 2005, **17**, 24, 3005-3009.
- [34]. Zhuo, L., Ge, J., Cao, L., Tang, B., *Cryst. Growth Des.*, 2009, **9**, 1, 1-6.
- [35]. Hou, H., Xie, Y., Yang, Q., Guo, Q., Tan, C., *Nanotechnology*, 2005, **16**, 741-745.
- [36]. Bavykin, D.V., Parmon, V.N., Lapkin, A.A., Walsh, F.C., The effect of hydrothermal conditions on the mesoporous structure of TiO<sub>2</sub> nanotubes, *J. Mater. Chem.*, 2004, **14**, 3370.
- [37]. Niederberger, M., Muhr, H.J., Krumeich, F., Bieri, F., Günther, D., Nesper, R., Low cost synthesis of vanadium oxide nanotubes via two novel non-alkoxide routes, *Chem. Mater.*, 2000, **12**, 7, 1995-2000.
- [38]. Wang, X., Li, Y., Thermally stable silicate nanotubes, *Chemistry Letters*, 2004, **33**, 1, 48-49.
- [39]. Sun, Y., Ma, L., Zhou, B., Gao, P., *Int. J. Hydrogen Energy*, 2011, advance web article.

- 
- [40]. Korytkova, E.N., Maslov, A.V., Pivovarova, L.N., Drozdova, A., Gusarov, V.V., Formation of  $\text{Mg}_3\text{Si}_2\text{O}_5(\text{OH})_4$  nanotubes under hydrothermal conditions, *Glass Phys. Chem.*, 2004, **30**, 1, 51-55.
- [41]. Wada, S.I., Eto, A., Wada, K., *J. Soil Sci.*, 1979, **30**, 2, 347-355.
- [42]. Bursill, L.A., Peng, J.L., Bourgeois, L.N., *Philosophical Magazine A*, 2000, **80**, 1, 105-117.
- [43]. La Iglesia, A., Martin Vivaldi, J.L., *Clay Miner.*, 1975, **10**, 401-407.
- [44]. La Iglesia, A., Van Oosterwyck-Gastuche, M.C. *Clays and Clay Minerals*, 1978, **26**, 397-408.
- [45]. Wang, X., Zhuang, J., Chen, J. Zhou, K., Li, Y., *Angewandte Chemie*, 2004, **116**, 2051-2054.
- [46]. Korytkova, E.N., Pivovarova, L.N., *Glass Phys. Chem.*, 2010, **36**, 1, 53-60.
- [47]. Yang, Y., Liang, Q.Q., Li, J., Zhuang, Y. He, Y. Bai, B., Wang X., *Nano Res.*, 2011, **4**, 9, 882-890.
- [48]. Duan, J., Gregory, J., *Advances in Colloid and Interface Science*, 2003, **100-102**, 475-502.
- [49]. Abdin, Z., Matsue, N., Hemmi, T., *Interdisciplinary Studies on Environmental Chemistry- Environmental Research in Asia*, 2009, TERRAPUB, Tokyo, pp. 331-341.
- [50]. Yucelen, G.I., Choudhury, R.P., Vyalikh, A., Scheler, U., Beckham, H.W., Nair, S., *J. Am. Chem. Soc.*, 2011, **133**, 14, 5397-5412.
- [51]. Korytkova, E.N., Pivovarova, L.N., Semenova, O.E., Drozdova, I.A., Povinich, V.F., Gusarov, V.V., *Russian Journal of Inorganic Chemistry*, 2005, **52**, 3, 338-344.
- [52]. Wilson, I.R., Kaolin and halloysite deposits of China, *Clay Miner.*, 2004, **39**, 1, 1-15.
- [53]. Li, H.H., Chen, R.F., Ma, C., Zhang, S.L., An, Z.F., Huang, W., *Acta Physico-Chimica Sinica*, 2011, **27**, 5, 1017-1025.
- [54]. Tenne, R., Redlich, M., *Chem. Soc. Rev.*, 2010, **39**, 5, 1423-1434.
- [55]. Mai, L.Q., Yang, S., Han, C.H., Xu, L. Xu, X., Pi, Y.Q., *Acta Physico-Chimica Sinia*, 2011, **27**, 7, 1551-1559.
- [56]. Jiang, J.A., Li, Y.Y., Liu, J.P., Huang, X.T., *Nanoscale*, 2011, **3**, 1, 45-58.
- [57]. Cheng, F.Y., Chen, J., *J. Mater. Res.*, 2006, **21**, 11, 2744-2757.
- [58]. Lu, Y.Z., Jin, R.T., Chen, W., *Nanoscale*, 2011, **3**, 6, 2476-2480.

- 
- [59]. Yue, Z.G., Wei, W., You, Z.X., Yang, Q.Z., Yue, H., Su, Z.G., Ma, G.H., *Advanced Functional Materials*, 2011, **21**, 18, 3446-3453.
- [60]. Losic, D., Simovic, S., *Expert Opinion on Drug Delivery*, 2009, **6**, 12, 1361-1381.
- [61]. Bhushan, B., in *Springer Handbook of Nanotechnology*, 2003, Springer-Verlag Berlin-Heidelberg-New York, ISBN 3-540-01218-4, p. 792.
- [62]. Bavykin, D.V., Walsh, F.C., Elongated titanate nanostructures and their applications, *European Journal of Inorganic Chemistry*, 2009, 8, 977-997.
- [63]. Putnis, A., *Introduction to Mineral Sciences*, 1992, Cambridge University Press, ISBN 0-521-42947-1, p. 163-165.
- [64]. Mori, M., Kumagai, Y., Matsunaga, K., Tanaka, I., First-principles investigation of atomic structures and stability of proton-exchanged layered sodium titanate, *Phys. Rev. B*, 2009, **79**, 144117.
- [65]. Joussein, E., Petit, S., Churchman, J., Theng, B., Righi, D., Delvaux, B., Halloysite clay minerals- a review, *Clay Miner.*, 2005, **40**, 383-426.
- [66]. Enjalbert, R., Galy, J., *Acta Crystallogr. Sect. C- Cryst. Struct. Commun.*, 1986, **42**, 1467-1469.
- [67]. Bieri, F., Krumeich, F., Muhr, H.J., Nesper, R., *Helvetica Chimica Acta*, 2001, **84**, 10, 3015-3022.
- [68]. Wörle, M., Krumeich, F., Bieri, F., Muhr, H.J., Nesper, R., *Z. Anorg. Allg. Chem.* 2002, **628**, 2778-2784.
- [69]. Bavykin, D.V., Walsh, F.C., Kinetics of metal ion exchange into nanotubular and nanofibrous titanates, *J. Phys. Chem. C*, 2007, **111**, 40, 14644-14651.
- [70]. Konduri, S., Tong, H.M., Chempath, S., Nair, S., Water in single-walled aluminosilicate nanotubes: diffusion and adsorption properties, *J. Phys. Chem. C*, 2008, **112**, 39, 15367-15374.
- [71]. Brunauer, S., Emmett, P.H., Teller, E., Adsorption of gases in multimolecular layers, *J. Am. Chem. Soc.*, 1938, **60**, 2, 309-319.
- [72]. Barrett, E.P., Joyner, L.G., Halenda, P.P., The determination of pore volume and area distributions in porous substances. I. Computations from nitrogen isotherms, *J. Am. Chem. Soc.*, 1951, **73**, 1, 373-380.
- [73]. Breck, D.W., *Zeolite Molecular Sieves: Structure, Chemistry and Use*, 1974, John Wiley, New York.

- 
- [74]. Bavykin, D.V., Cressey, B.A., Light, M.E., Walsh, F.C., *Nanotechnology*, 2008, **19**, 275604.
- [75]. Wei, J., Zhu, Y., Zhang Jing, C., *Chinese Sci. Bulletin*, 2007, **52**, 1920-1924.
- [76]. Spahr, M.E., Stoschitzki-Bitterli, P., Nesper, R., Haas, O., Novak, P., Vanadium oxide nanotubes a new nanostructured redox-active material for the insertion of lithium, *Journal of the Electrochemical Society*, 1999, **146**, 8, 2780-2783.
- [77]. Farmer, V.C., Fraser, A.R., Tait, J.M., Synthesis of imogolite: a tubular aluminium silicate polymer, *J. Chem. Soc. Chem. Commun.*, 1977, 13, 462-463.
- [78]. Ackerman, W.C., Smith, D.M., Huling, C., Kim, Y.W., Bailey, J.K., Brinker, C.J., Gas/vapour adsorption in imogolite: a microporous tubular aluminosilicate, *Langmuir*, 1993, **9**, 1051-1057.
- [79]. Da Silva, S.P., Wander, A.P., Bisatto, R., Galland, G.B., *Nanotechnology*, 2011, **22**, 105701.
- [80]. Malkov, A.A., Korytkova, E.N., Maslennikova, T.P., Shtykhova, A.M., Gusarov, V.V., *Russian Journal of Applied Chemistry*, 2009, **82**, 12, 2079-2086.
- [81]. McDonald, A., Scott, B., Villemure, G., *Microporous Mesoporous Mater.*, 2009, **120**, 3, 263-266.
- [82]. White, R.D., Bavykin D.V., unpublished data.
- [83]. Nakahira, A., Kubo, T., Numako, C., *Inorg. Chem.*, 2010, **49**, 13, 5845-5852.
- [84]. O'Dwyer, C., Navas, D., Lavayen, V., Benavente, E., Santa Ana, M.A., Gonzalez, G., Newcomb, S.B., Torres, C.M.S., *Chem. Mater.*, 2006, **18**, 13, 3016-3022.
- [85]. Bavykin, D.V., Friedrich, J.M., Walsh, F.C., *Adv. Mater.*, 2006, **18**, 21, 2807-2824.
- [86]. Sun, H.T., Chaudhuri, J., Kenik, E.A., Zhu, H., Ma, Y., *Nanoscience and Nanotechnology Letters*, 2011, **3**, 314-318.
- [87]. Wang, X., Li, Y., *Chemistry- A European Journal*, 2003, **9**, 22, 5627-5635.
- [88]. White, R.D., Bavykin, D.V., Walsh, F.C., *J. Phys. Chem. C*, 2012, **116**, 15, 8824-8833.
- [89]. Liu, P., Zhang, H., Liu, H., Wang, Y., Yao, X., Zhu, G., Zhang, S., Zhao, H., *J. Am. Chem. Soc.*, 2011, **133**, 47, 19032-19035.
- [90]. Jancar, B., Suvorov, D., *Nanotechnology*, 2006, **17**, 25-29.

- 
- [91]. Rooth, M., Quinlan, R.A., Widenkvist, E., Lu, J., Grennberg, H., Holloway, B.C., Harsta, A., Jansson, U., *J. Cryst. Growth*, 2009, **311**, 2, 373-377.
- [92]. Li, C.J., Yin, Y.S., Zhu, H.T., *Adv. Mater. Res.*, 2009, **79-82**, 621-624.
- [93]. Chen, W., Guo, X., Zhang, S., Jin, Z., *J. Nanoparticle Res.*, 2007, **9**, 1173-1180.
- [94]. Lu, H., Zhao, J., Li, L., Zheng, J., Zhang, L., Gong, L., Wang, Z., Zhu, Z., *Chem. Phys. Lett.*, 2011, **508**, 4-6, 258-264.
- [95]. Wei, M., Konishi, Y., Zhou, H., Sugihara, H., Arakawa, H., *Solid State Commun.*, 2005, **133**, 8, 493-497.
- [96]. Livage, J., Hydrothermal synthesis of nanostructured vanadium oxides, *Materials*, 2010, **3**, 4175-4195.
- [97]. Bavykin, D.V., Kulak, A.N., Walsh, F.C., *Cryst. Growth Des.*, 2010, **10**, 10, 4421-4427.
- [98]. Gardolinski, J., Lagaly, G., *Clay Min.*, 2005, **40**, 547-556.
- [99]. Kuroda, Y., Ito, K., Itabashi, K. Kuroda, K., *Langmuir* 2011, **27**, 2028-2035.
- [100]. Robertson, D. I. M., Eggleton, R.A., *Clays and Clay Minerals*, 1991, **39**, 113-126.
- [101]. Singh, B., Mackinnon, I.D.R., *Clays and Clay Minerals*, 1996, **44**, 825-834.
- [102]. Ma, R., Bando, Y., Sasaki, T., Directly rolling nanosheets into nanotubes, *J.Phys. Chem. B*, 2004, **108**, 2115-2119.
- [103]. Kovytkova, E.N., Brovkin, A.S., Maslennikova, T.P., Pivovarova, L.N., Drozdova, I.A., *Glass Phys. Chem.*, 2011, **37**, 2, 161-171.
- [104]. Olejnik, S., Posner, A.M., Quirk, J.P., The intercalation of polar organic compounds into kaolinite, *Clay Miner.*, 1970, **8**, 421-434.
- [105]. Palmer, D.A., Gamsjäger, H., *J. Coord. Chem.*, 2010, **63**, 14-16, 2888.
- [106]. Powell, K.J., Brown, P.L., Byrne, R.H., Gajda, T., Hefter, G., Sjöberg, S., Wanner, H., Chemical Speciation of environmentally significant metals with inorganic ligands (IUPAC technical report), *Pure Appl. Chem.*, 2007, **79**, 5, 895-950.
- [107]. Brown, P.L., Drummond, S.E.(Jnr.), Palmer, D.A., *J. Chem. Soc. Dalton Trans.*, 1996, 3071-3075.
- [108]. Benezeth, P., Palmer, D.A., Wesolowski, D.J., *J. Sol. Chem.*, 1997, **26**, 1, 63-84.
- [109]. Liu, X., Millero, F.J., *Geochim. et Cosmochim. Acta*, 1999, **63**, 19-20, 3487-3497.

- 
- [110]. Baes, C.F., Mesmer, R.E., *The Hydrolysis of Cations*, Wiley-Interscience, New York, 1976.
- [111]. Castet, S., Dandurand, J., Schott, J., Gout, R., *Geochim. Et Cosmochim. Acta*, 1993, **57**, 4869-4884.
- [112]. Gunnarson, I., Arnosson, S., *Geochim. et Cosmochim. Acta*, **64**, 13, 2295-2307.
- [113]. Ryu, K.W., Jang, Y.N., Chae, S.C., *Clays and Clay Minerals*, 2010, **58**, 44-51.
- [114]. Murat, M., Amokrane, A., Bastide, J.P., Montanaro, L., Synthesis of zeolites from thermally activated kaolinite. Some observations on nucleation and growth, *Clay Miner.*, 1992, **27**, 119-130.
- [115]. Kahn, Y., Durrani, S.K., Mehmood, M., Jan, A., Abbasi, M.A., *Mater. Chem. Phys.* 2011, **130**, 3, 1169-1174.
- [116]. Fan, W., Sun, S., Song, X., Zhang, W., Yu, H., Tan, X., Cao, G., *J. Solid State Chem.*, 2004, **177**, 7, 2329-2338.
- [117]. Gundiah, G., Mukhopadhyay, S., Tumkurkar, U.G., Givindaraj, A., Maitra, U., Rao, C.N.R., Hydrogel route to nanotubes of metal oxides and sulfates, *J. Mater. Chem.*, 2003, **13**, 9, 2118-2122.
- [118]. Hong, G., Chen, Y.B., Li, P., Zhang, J., *Carbon*, 2012, **50**, 6, 2067-2082.
- [119]. Pauling, L., *Proc. Natl. Acad. Sci. U.S.A.*, 1930, **16**, 578.
- [120]. Wang, Y.Q., Hu, G.Q., Duan, X.F., Sun, H.L., Xue, Q.K., *Chem. Phys. Lett.*, **365**, 5-6, 2002, 427-431.
- [121]. Song, J.M., Lin, Y.Z., Zhan, Y.J., Tian, Y.C., Liu, G., Yu, S.H., *Cryst. Growth & Design*, 2008, **8**, 6, 1902-1908.
- [122]. Levard, C., Rose, J., Masion, A., Doelsch, E., Borschneck, D., Olivi, L., Dominici, C., Grauby, O., Woicik, J.C., Bottero, J.Y., *J. Am. Chem. Soc.*, 2008, **130**, 18, 5862-5863.
- [123]. Seifert, G., Terrones, H., Terrones, M., Jungnickel, G., Frauenheim, T., *Phys. Rev. Lett.*, 2000, **85**, 146-149.
- [124]. Enyashin, A.N., Seifert, G., *Phys. Status Solidi B*, 2005, **242**, 7, 1361-1370.
- [125]. Guimaraes, L., Enyashin, A.N., Seifert, G., Duarte, H.A., *J. Phys. Chem. C*, 2010, **114**, 26, 11358-11363.
- [126]. Lee, S.U., Choi, Y.C., Youm, S.G., Sohn, D., *J. Phys. Chem. C*, 2011, **115**, 13, 5226-5231.

- 
- [127]. Enyashin, A.N., Ivanovskii, A.I., *J.Phys.Chem. C*, 2009, **113**, 20837-20840.
- [128]. D'Arco, P., Noel, Y., Demichelis, R., Dovesi, R., *J. Chem. Phys.*, 2009, **131**, 204701.
- [129]. Radoslovich, E.W., *Amer. Mineralogist*, 1963, **48**, 368-378.
- [130]. Singh, B., *Clays and Clay Minerals*, 1996, **44**, 191-196.
- [131]. Robbie, R.A., Hemingway, B.S., Fisher, J.R., *U.S. Geological Survey Bulletin* 1979, **1452**, p456.
- [132]. Zhang, S., Peng, L.M., Chen, Q., Du, G.H., Dawson, G., Zhou, W.Z., Formation mechanism of  $\text{Ti}_2\text{Ti}_3\text{O}_7$  nanotubes, *Phys. Rev. Lett.*, 2003, **91**, 256103.
- [133]. Petkov, V., Zavalij, P.Y., Lutta, S., Whittingham, M.S., Parvanov, V., Shastri, S., *Phys. Rev. B*, 2004, **69**, 085410.
- [134]. Vera-Robles, L.I., Camparo, A., *J. Phys. Chem. C*, 2008, **112**, 50, 19930-19933.
- [135]. Du, M., Guo, B., Jia, D., Newly emerging applications of halloysite nanotubes: a review, *Polymer International*, 2010, **59**, 5, 574-582.
- [136]. Garcia Garcia, F.J., Garica Rodriguez, S., Kalytta, A., Reller, A., *Zeitschr. Anorg. Allg. Chem.*, 2009, **635**, 4-5, 790-795.
- [137]. MacKenzie, K.J.D., Meinhold, R.H., *American Mineralogist*, 1994, **79**, 43-50.
- [138]. MacKenzie, K.J.D., Bowden M.E., Brown, I.W.M., Meinhold, R.H., *Clays and Clay Minerals*, 1989, **37**, 4, 317-324.
- [139]. Morgado Jr, E., Jardim, P.M., Marinkovic, B.A., Rizzo, F.C., Abreul, M.A.S., Zotin, J.L., Araujo, A.S., *Nanotechnology*, 2007, **18**, 495710.
- [140]. Chen, W., Peng, J., Mai, L., Zhu, Q., Xu, Q., *Materials Letters*, 2004, **58**, 17-18, 2275-2278.
- [141]. Bavykin, D.V., Friedrich, J.M. Lapkin, A.A., Walsh, F.C., *Chem. Mater.*, 2006, **18**, 1124-1129.
- [142]. Zhang, K.F., Guo, D.J., Liu, X., Li, J., Li, H.L., Su, Z.X., *Journal of Power Sources*, 2006, **162**, 2, 1077-1081.
- [143]. Su, C., Harsh, J.B., *Geochim. et Cosmochim. Acta*, 1994, **58**, 6, 1667-1677.
- [144]. Pickrell, J.A., Erickson, L.E., Dhakal, K., Klabunde, K.J., Toxicity of inhaled nanomaterials, in: *Nanoscale Materials in Chemistry*, 2009, Klabunde, K.J., Richards, R.M. (ed.), John Wiley and Sons, New Jersey, ISBN 978-0-470-22270-6, p.732



- 
- [145]. Zhang, Z.B., Peng, J.C., Chen, X.H., Research on the elastic modulus of the carbon nanotubes, *Rare Metal Materials and Engineering*, 2004, **33**, 12, 1233-1237.
- [146]. Löffler, M., Weissker, U., Mühl, T., Gemming, T., Büchner, B., *Ultramicroscopy*, 2011, **11**, 2, 155-158.
- [147]. Krishan, A., Dujardin, E., Ebbesen, T.W., Yianilos, P.N., Treacy, M.M.J., Young's modulus of single-walled nanotubes, *Phys. Rev. B*, 1998, **58**, 20, 14013-14019.
- [148]. Bavykin, D.V., Redmond, K.E., Nias, B.P., Kulak, A.N., Walsh, F.C, *Aust. J. Chem.*, 2010, **63**, 270-275.
- [149]. Bavykin, D.V., Walsh, F.C., *Titanate and Titania Nanotubes: Synthesis, Properties and Applications*, 2009, RSC, London, p. 1 -19.
- [150]. Liu, Y.J., Cowen, J.A., Kaplan, T.A., DeGroot, D.C., Kanatzidis, M.G., *Chem. Mater.*, 1995, **7**, 1616-1624.
- [151]. Sipos, B., Duchamp, M., Magrez, A., Forro, L. Barisic, N., Kis, A., Seo, J.W., Bieri, F., Krumeich, F., Nesper, R., Patzke, G.R., *J. Appl. Phys.*, 2009, **105**, 074317.
- [152]. Roberts, W.L., Campbell, T.J., Rapp, G.R., *Encyclopaedia of Minerals*, 2<sup>nd</sup> Edition, 1990, Ed. Weber, J., ISBN 978-0442268206.
- [153]. Piperno, S., Kaplan-Ashiri, I., Cohen, S.R., Popovitz-Biro, R., Wagner, D., Tenne, R., Foresti, E., Lesci, I.G., Roveri, N., *Adv. Functional Materials*, 2007, **17**, 16, 3332-3338.
- [154]. Lourenco, M.P., de Oliveira, C., Oliveira, A.F., Guimaraes, L., Duarte, H.A., *J. Phys. Chem. C*, 2012, **116**, 17, 9405-9411.
- [155]. Datta, A.K., Bhattacharjee, S., *J. Mater. Sci.*, 1986, **21**, 1041-1045.
- [156]. Karube, J., Abe, Y., *Clays and Clay Minerals*, 1998, **46**, 3, 322-329.
- [157]. Li, L., Xia, Y., Zhao, M., Song, C., Li, J., Liu, X., *Nanotechnology*, 2008, **19**, 175702.
- [158]. Demichelis, R., Noël, Y., D'Arco, P., Maschio, L., Orlando, R., Dovesi, R., *J. Mater. Chem.*, 2010, **20**, 10417-10425.
- [159]. Ma, W., Yah, W.O., Otsuka, H., Takahara, A., *Beilstein J. Nanotechnol.*, 2012, **3**, 82-100.
- [160]. Kralova, D., Neykova, N., Slouf, M., Preparation of titanate nanotubes and their polymer composites, *EMC 14<sup>th</sup> European Microscopy Congress*, September 2008, Aachen, Germany, **M4**, 765-766.

- 
- [161]. Rawtani, D., Agrawal, Y.K., Multifarious applications of halloysite nanotubes: a review, *Reviews on Advanced Materials Science*, 2012, **30**, 3, 282-295.
- [162]. Otsuka, H., Takahara, A., Structure and properties of imogolite nanotubes and their application to polymer nanocomposites, in: *Inorganic and Metallic Nanotubular Materials: Recent Technologies and Applications*, Topics in Applied Physics, 2010, Kijima, T. (Ed.), **117**, 169-190.
- [163]. Yah, W.O., Yamamoto, K., Jiravanichanun, N., Otsuka, H., Takahara, A., Imogolite reinforced nanocomposites: multifaceted green materials, *Materials*, 2010, **3**, 3, 1709-1745.
- [164]. Ma, Y. C., Foster, A. S., Nieminen, R. M., *J. Chem. Phys.*, 2005, **122**, 9.
- [165]. Morgado, E., Marinkovic, B.A., Jardim, P.M., de Abreu, M.A. S., Rocha, M.D.C., Bargiela, P., Studies on Fe-modified nanostructured trititanates, *Mater. Chem. Phys.*, 2011, **126**, 1-2, 118-127.
- [166]. Yuan, P., Southon, P.D., Liu, Z., Green, M.E.R., Hook, J.M., Antill, S.J., Kepert, C.J., *J. Phys. Chem.*, 2008, **112**, 40, 15742-15751.
- [167]. Korytkova, E.N., Maslov, A.V., Pivivarova, L.N., Polegotchenkova, V.Y., Povinich, V.F., Gusarov, V.V., Synthesis of nanotubular  $\text{Mg}_3\text{Si}_2\text{O}_5(\text{OH})_4$ - $\text{Ni}_3\text{Si}_2\text{O}_5(\text{OH})_4$  silicates at elevated temperatures and pressures, *Inorg. Mater.*, 2005, **41**, 7, 743-749.
- [168]. Roveri, N., Falini, G., Foresti, E., Fracasso, G., Lesci, I.G., Sabatino, P., Geoinspired synthetic chrysotile nanotubes, *J. Mater. Res.*, 2006, **21**, 11, 2711-2725.
- [169]. Levard, C., Masion, A., Rose, J., Doelsch, E., Borschneck, D., Olivi, L., Chaurand, P., Dominici, C.; Ziarelli, F., Thill, A., Maillet P., Bottero, J. Y., *Phys. Chem. Chem. Phys.*, 2011, **13**, 14516-14522.
- [170]. Shannon, R.D., *Acta Cryst.*, 1976, **A32**, 751-767.
- [171]. Maillet, P., Levard, C., Larquet, E., Mariet, C., Spalla, O., Menguy, E., Masion, A., Doelsch, E., Rose, J.; Thill, A., *J. Am. Chem. Soc.*, 2010, **132**, 1208-1209.
- [172]. Thill, A., Maillet, P., Guiose, B., Spalla, O., Belloni, L., Chaurrand, P., Auffan, M., Olivi, L., Rose, J., *J. Am. Chem. Soc.*, 2012, **134**, 8, 3780-3786.
- [173]. US Department of Energy, *Properties of Hydrogen*, Technology Validation Manual, December 2001.

---

([http://www1.eere.energy.gov/hydrogenandfuelcells/tech\\_validation/pdfs/fcm01r0.pdf](http://www1.eere.energy.gov/hydrogenandfuelcells/tech_validation/pdfs/fcm01r0.pdf)), accessed 15.08.2012.

[174]. US Department of Energy, *Targets for Onboard Hydrogen Storage Systems for Light Duty Vehicles*, September 2009,  
([http://www1.eere.energy.gov/hydrogenandfuelcells/storage/pdfs/targets\\_onboard\\_hydro\\_storage\\_explanation.pdf](http://www1.eere.energy.gov/hydrogenandfuelcells/storage/pdfs/targets_onboard_hydro_storage_explanation.pdf)), accessed 15.08.2012.

[175]. Niedzwiecki, A., (Quantum Technologies), Proc. Hydrogen Vision Meeting, US DOE, Washington, November 2001.  
([http://www1.eere.energy.gov/hydrogenandfuelcells/pdfs/hv\\_report\\_12-17.pdf](http://www1.eere.energy.gov/hydrogenandfuelcells/pdfs/hv_report_12-17.pdf))

[176]. Broom, D.P., The accuracy of hydrogen sorption measurements on potential storage materials, *Int. Journal of Hydrogen Energy*, 2007, **32**, 4871-4888.

[177]. Checchetto, R. Trettel, G., Miotello, A., *Meas. Sci. Technol.*, 2004, **15**, 127-130.

[178]. Sing, K.S.W, Everett, D.H., Haul, R.A.W., Moscou, L., Pierotti, R.A., Rouquerol, J., Siemieniewska, T., Reporting physisorption data for gas/solid systems with special reference to determination of surface area and porosity, *Pure Appl. Chem*, 1985, **57**, 4, 603-619.

[179]. Zhou, L., Zhou, Y.P., Sun, Y., Studies on the mechanism and capacity of hydrogen uptake by physisorption-based materials, *International Journal of Hydrogen Energy*, 2004, **29**, 319-322.

[180]. Al-Hajjaj, A., Zamora, B, Shah, A.A., Regura, E., Bavykin, D., Walsh, F.C., On the application of standard isotherms to hydrogen adsorption in microporous materials, *International Journal of Hydrogen Energy*, 2011, **36**, 22, 14464-14476.

[181]. Huheey, J.E., Keiter, E.A., Keiter, R.L., *Inorganic Chemistry: Principles of Structure and Reactivity*, 4<sup>th</sup> ed., 1993, Harper-Collins, New York, pp. A25-A33.

[182]. Ding, F., Yakobson, B.I., Challenges in hydrogen adsorptions: from physisorption to chemisorption, *Front. Phys.*, 2011, **6**, 2, 142-150.

[183]. Van der Borg, A.W.C., Arean, C.O., Materials for hydrogen storage: current research trends and perspectives, *Chem. Commun.*, 2008, 668-681.

[184]. Mao, W.L., Mao, H., Goncharov, A.F., Struzhkin, V.V., Guo, Q., Hu, J., Shu, J., Hemley, R.J., Somayazulu, M., Zhao, Y., Hydrogen clusters in clathrate hydrate, *Science*, 2002, **297**, 5590, 2246- 2249.

- 
- [185]. Felderhoff, M., Weidenthaler, C., von Helmolt, R., Eberle, U., Hydrogen storage the remaining scientific and technological challenges, *Phys. Chem. Chem. Phys.*, 2007, **9**, 2643-2653.
- [186]. Binewale, R.B., Rayalu, S., Devotta, S., Ichikawa, M., Chemical hydrides: a solution to high capacity hydrogen storage and supply, *Int. Journal Hydrogen Energy*, 2008, **33**, 360-365.
- [187]. Jain, I. P., Jain P., Jain, A., *Journal of Alloys and Compounds*, 2010, **503**, 2, 303-339.
- [188]. Sandrock, G., A panoramic overview of hydrogen storage alloys from a gas reaction point of view, *Journal of Alloys and Compounds*, 1999, **293-295**, 877-888.
- [189]. Struzhkin, V.V., Militzer, B., Mao, W.L., Mao, H.K., Hemley, R.J., Hydrogen storage in molecular clathrates, *Chemical Reviews*, 2007, **107**, 10, 4133-4151.
- [190]. Wang-Foy, A.G., Matzger, A.J., Yaghi, O.M., Exceptional uptake in microporous metal-organic frameworks, *J. Am. Chem. Soc.*, 2006, **128**, 3494-3495.
- [191]. Du, X., Wu, E., Physisorption of hydrogen in A, X, and ZSM-5 types of zeolites at moderately high pressures, *Chin. J. Chem. Phys.* 2006, **19**, 5, 457-462.
- [192]. Yang, Z., Xia, Y., Mokaya, R., Enhanced hydrogen storage capacity of high surface area zeolite-like carbon materials, *J. Am. Chem. Soc.*, 2007, **129**, 1673-1679.
- [193]. Germain, J., Hradil, J., Frechet, M. J., Svec, F., *Chem. Mater.*, 2006, **18**, 4430-4435.
- [194]. Kaye, S.S., Long, J.R., Hydrogen storage in the dehydrated prussian blue analogues  $M_3[Co(CN)_6]_2$ , *J. Am. Chem. Soc.*, 2005, **127**, 18, 6506-6507.
- [195]. Broom, D.P., *Hydrogen Storage Materials: The Characterisation of their Storage Properties*, 1<sup>st</sup> ed., 2011, Springer-Verlag, London, ISBN: 978-0-85729-220-9.
- [196]. Zhao, Y., Kim, Y.H., Dillon, A.C., Heben, M.J., Zhang, S.B., *Phys. Rev. Lett.*, 2005, **94**, 145554.
- [197]. Yildirim, T., Circi, S., *Phys. Rev. Lett.*, 2005, **94**, 75501.
- [198]. Yildirim, T., Iniguez, J., Ciraci, S., *Phys. Rev. B*, 2005, **72**, 153403.
- [199]. Yoon, M., Yang, S.Y., Hicke, C., Wang, E., Geohegan, D., Zhang, Z.Y., *Phys. Rev. Lett.*, 2008, **100**, 20, 206806.
- [200]. Yoon, M., Yang, S.Y., Wang, E., Zhang, Z.Y., *Nano Lett.*, 2007, **7**, 9, 2578.
- [201]. Wang, S.C., Senbetu, L., Woo, C., *J. Low Temp. Phys.*, 1980, **41**, 5-6, 611.

- 
- [202]. Huang, W.Z., Zhang, X.B., Kong, F.Z., Tu, J.P., Ma, J.X., Chen, C.P., Ning, Y.S., Sun, Y.L., Hydrogen storages capacity of potassium-doped multi-walled carbon nanotubes, *Chinese Journal of Chemical Physics*, 2002, **15**, 1, 51-55.
- [203]. Wang, Y., Li, A., Wang, K., Guan, C., Deng, W., Li, C., Wang, X., Reversible hydrogen storage of multi-wall carbon nanotubes doped wit atomically dispersed lithium, *J. Mater. Chem.*, 2010, **20**, 31, 6490-6494.
- [204]. Wu, X., Yang, J., Hou, J.G., Zhu, Q., Defects-enhanced dissociation of H<sub>2</sub> on boron nitride nanotubes, *J. Chem. Phys.*, 2006, **124**, 054706.
- [205]. Shevlin, S.A., Guo, Z.X., Hydrogen sorption in defective hexagonal BN sheets and BN nanotubes, *Phys. Rev. B*, 2007, **76**, 024104.
- [206]. Huda, M.N., Kleinman, L., Hydrogen adsorption and dissociation on small platinum clusters: An electronic structure density functional study, *Phys. Rev. B*, 2006, **74**, 195407.
- [207]. Ritschel, M. , Uhlemann, M., Gutfleisch, O., Leonhardt, A., Graff, A., Täschner, Ch., Fink, J., Hydrogen storage in different carbon nanostructures, *Appl. Phys. Lett.*, 2002, **80**, 16, 2985-2987.
- [208]. Jordá-Beneyto, M., Suarez-Garcia, F., Lozano-Castello, D., Cazorla-Amoros, D., Linares-Solano, A., Hydrogen storage on chemically activated carbon and carbon nanomaterials at high pressure, *Carbon*, 2006, **45**, 2, 293-303.
- [209]. Ma, R., Bando, Y., Zhu, H., Sato, T., Xu, C., Wu, D., Hydrogen uptake in boron nitride nanotubes at room temperature, *J. Am. Chem. Soc.*, 2002, **124**, 26, 7672-7673.
- [210]. Chen, J., Li, S.L., Tao, Z.L., Shen, Y.T., Cui, C.X., Titanium disulfide nanotubes as hydrogen-storage materials, *J. Am. Chem. Soc.*, 2003, **125**, 18, 5284-5285.
- [211]. Hu, J., Chen, J., Chen, H., Song, Y., Sun, Y., Zou, R., Ni, J., Dierre, B., Sekiguchi, T., Golberg, D., Bando, Y., Single-crystal MgS nanotubes: synthesis and properties, *Cryst. Eng. Comm.*, 2010, **12**, 1286-1289.
- [212]. Chang, Z., Liu, J., Sun, X., Liu, J., Derivated titanate nanotubes and their hydrogen storage properties, *Front. Chem. China*, 2010, **5**, 1, 71-75.
- [213]. Bavykin, D.V., Lapkin, A.A., Plucinski, P.K., Friedrich, J.M., Walsh, F.C., Reversible storage of molecular hydrogen by sorption into multilayered TiO<sub>2</sub> nanotubes, *J. Phys. Chem. B*, 2005, **109**, 41, 19422-19427.

- 
- [214]. Kim, D.H., Jang, J.S., Goo, N.H., Kwon, M.S., Lee, J.W., Choi, S.H., Shin, D.W., Kim, S.J., Lee, K.S., Structural characterization and effect of hydrogen on the Ni-doped titanate nanotubes, *Catalysis Today*, 2009, **146**, 1-2, 230-233.
- [215]. Al-Hajjaj, A.A., Zamora, B., Bavykin, D.V., Shah, A.A., Walsh, F.C., Reguera, E., Sorption of hydrogen onto titanate nanotubes decorated with a nanostructured  $\text{Cd}_3[\text{Fe}(\text{CN})_6]_2$  Prussian blue analogue, *International Journal of Hydrogen Energy*, 2012, **37**, 1, 318-326.
- [216]. Lee, J.B., Lee, S.C., Lee, S.M., Kim, H.J., Hydrogen adsorption characteristics of Li-dispersed silica nanotubes, *Chem. Phys. Lett.*, 2007, **436**, 162-166.
- [217]. Jung, J.H., Rim, J.A., Lee, S.J., Sung, J.C., Kim, S.Y., Kang, J.K., Kim, Y.M., Kim, Y.J., Pd-doped double-walled silica nanotubes as hydrogen storage material at room temperature, *J. Phys. Chem. C*, 2007, **111**, 6, 2679-2682.
- [218]. Zhang, Z.W., Zheng, W.T., Jiang, Q., Hydrogen adsorption on Ce/ BNNT systems: A DFT study, *International Journal of Hydrogen Energy*, 2012, **37**, 5090-5099.
- [219]. Al-Ghamdi, A.A., Shalaan, E., Al-Hazmi, F.S., Faidah, A.S., Al-Heniti, S., Husain, M., Adsorption sites of hydrogen atom on pure and Mg-doped multi-walled carbon nanotubes, *Journal of Nanomaterials*, 2012, **2012**, 484692.
- [220]. Li, Y.W., Yang, R.T., Hydrogen storage in metal-organic frameworks by bridged hydrogen spillover, *J. Am. Chem. Soc.*, 2006, **128**, 25, 8136-8137.
- [221]. Bhowmick, R., Rajasekaran, S., Friebe, D., Beasley, C., Jiao, L., Ogasawara, H., Dai, H., Clemens, B., Nilsson, A., Hydrogen Spillover in Pt-single-walled carbon nanotubes composites: formation of stable bonds, *J. Am. Chem. Soc.*, 2011m **133**, 14, 5580-5586.
- [222]. Ahadi, Z., Shadman, M., Yegangi, S., Asgari, F., Hydrogen adsorption capacities of multi-walled boron nitride nanotube arrays: a grand canonical Monte Carlo study, *Journal of Molecular Modelling*, 2012, **18**, 2981-2991.
- [223]. Satokawa, S.; Osaki, Y.; Samejima, S.; Miyawaki, R.; Tomura, S.; Shibasaki, Y.; Sugahara, Y. *Clays and Clay Minerals*, **1994**, *42*, 288-297.
- [224]. British Standard, 1995, *British Standards Online*, BS 6068-2.49.
- [225]. International Standard, 2007 , *British Standards Online*, ISO 21587-2.
- [226]. International Standard, 2006, *British Standards Online*, ISO 9683-1.

- 
- [227]. Wada, K., Yoshinaga, N., *The American Mineralogist*, 1969, **54**, 50-71.
- [228]. Gross, K.J., Carrington, K.R., *Recommended Best Practices for the Characterization of Storage Properties of Hydrogen Storage Materials*, Report, H2 Technology Consulting, 2008.  
[http://www1.eere.energy.gov/hydrogenandfuelcells/pdfs/bestpractices\\_h2\\_storage\\_materials.pdf](http://www1.eere.energy.gov/hydrogenandfuelcells/pdfs/bestpractices_h2_storage_materials.pdf).
- [229]. Huertas, F.J., Fiore, S., Linares. J., *Clay Miner.*, 2004, **39**, 423-431.
- [230]. Tomura, S., Shibasaki, Y., Mizuta, H., Kitamura M., *Clays and Clay Minerals*, 1985, **33**, 200-206.
- [231]. Bobos, I., *Clays and Clay Minerals*, 2001, **49**, 596-607.
- [232]. Mukherjee, S., Kim, K., Nair, S., *J. Am. Chem. Soc.*, 2007, **129**, 6820-6826.
- [233]. Wada, S., Wada, K., *Clays and Clay Minerals*, 1982, **30**, 123-128.
- [234]. Farmer, V.C., Smith, B.F.L., Tait, J.M., The stability, free energy and heat of formation of imogolite, *Clay Miner.*, 1979, **14**, 103-107.
- [235]. Mishra, D., Anans, S., Panda, R.K., Das, R.P., *Mater. Lett.*, 2000, **42**, 38-45.
- [236]. He, T., Xiang, L., Zhu, S., *Cryst. Eng. Comm.*, 2009, **11**, 1338-1342.
- [237]. Levard, C., Rose, J., Thill, A., Masion, A., Doelsch, E., Maillet, P., Spalla, O., Olivi, L., Cognigni, A., Ziarelli, F., Bottero, J.Y., *Chem. Mater.*, 2010, **22**, 2466-2473.
- [238]. Bac, B.H., Song, Y., Kim, M.H., Lee, Y.B., Kang, I.M., *Inorg. Chem. Commun.*, 2009, **12**, 1045-1048.
- [239]. Miller, J.G., *J. Phys. Chem.*, 1961, **65**, 800-804.
- [240]. Kosslick, H., Tuan, V.A., Fricke, R., *J. Phys. Chem.*, 1993, **97**, 5678.
- [241]. Kolesova, V.A., Sher, E.S., *Inorg. Mater.*, 1973, **9**, 909-911.
- [242]. Clauws, P., de Gryse, O., Vanmeerbeek, P., Vanhellemont, J., *Physica B*, 2006, **376-377**, 113-116.
- [243]. Cradwick, P.D.G., Farmer, V.C., Russell, J.D., Masson, C.R., Wada, K., Yoshinaga, N., *Nature*, 1972, **240**, 187-189.
- [244]. Wilson, M. A., Lee, G.S.H., Taylor, R.C., *Journal of Non-crystalline Solids*, 2001, **296**, 172-181.

- 
- [245]. Frost, R.L., Shurvell, H.F., *Clay Clay Min.*, 1997, **45**, 68-72.
- [246]. Temuujin, J., Okada, K., MacKenzie, K.J.D., *Appl. Clay Sci.*, 2002, **21**, 125-131.
- [247]. Ruan, H.D., Frost, R.L., Klopogge, J.T., *J. Raman Spectrosc.*, 2001, **32**, 745-50.
- [248]. Meunier, A., *Clays*; Springer Verlag, Berlin, Heidelberg, 2005, p 4-5.
- [249]. Chakraborty, S., *Annual Review of Earth and Planetary Sciences*, 2008, **36**, 153-190.
- [250]. Kukovecz, A., Hodos, M., Horvath, E., Radnoczi, G., Konya, Z., Kiricsi, I., *J. Phys. Chem. B*, 2005, **109**, 17781.
- [251]. Johnson, S. L., Guggenheim, S., Vangross, A. F. K., *Clays and Clay Minerals*, 1990, **38** 477-484.
- [252]. Yelleswarapu, C. S., Gu, G., Abdullayev, E., Lvov, Y., Rao, D. V.G. L. N., *Opt. Commun.*, 2010, **283**, 438-441.
- [253]. Barrientos-Ramírez, S., Ramos-Fernández, E. V., Silvestre-Albero, J., Sepúlveda-Escribano, A., Pastor-Blas, M. M., González-Montiel, A. *Microporous Mesoporous Mater.*, 2009, **120**, 132-140.
- [254]. Wang, A., Kang, F., Huang, Z., Guo, Z. Chuan, X. *Microporous Mesoporous Mater.*, 2008, **108**, 318-324.
- [255]. Shchukin, D. G., Sukhorukov, G. B., Price, R. R., Lvov, Y. M. *Small*, 2005, **1**, 510-513.
- [256]. Cheng, H., Frost, R. L., Yang, J., Liu, Q., He, J., *Spectrochim. Acta Part A*, 2010, **77**, 1014-1020.
- [257]. Dubikova, M., Cambier, P., Sucha, V., Caplovicova, M., *Appl. Geochem.*, 2002, **17**, 245-257.
- [258]. Brindley, G. W., *Crystal Structures of Clay Minerals and their X-ray identification*, 1980, ed. G. W. Brindley and G. Brown (London: Mineralogical Society) pp 125-196.
- [259]. Alexander, G.B., Heston, W.M., Iler, R.K., *J. Phys. Chem.*, 1954, **58**, 6, 453-455.
- [260]. Wesolowski, D.J., Palmer, D.A., *Geochim. et Cosmochim. Acta*, 1994, **58**, 14, 2947-2969.
- [261]. Guo, Z., Du, F., Li, G., Cui, Z., *Chem. Commun.*, 2008, **25**, 2911-2913.



- 
- [262]. Fang, Q., Xuan, S., Jiang, W., Gong, X., *Adv. Functional Mater.*, 2011, **21**, 10, 1902-1909.
- [263]. Zhang, X.P., Jiang, W.Q., Zhou, Y.F., Xuan, S.H., Peng, C., Zong, L.H., Gong, X.L., *Nanotechnology*, 2011, **22**, 37, 375701.
- [264]. Alvarez-Ramirez, F., Toledo-Antonio, J.A., Angeles-Chavez, C., Guerrero-Abreo, J.H., Lopez-Salinas, E., *J. Phys. Chem. C*, 2011, **115**, 23, 11442-11446.
- [265]. Liu, Y., Yukawa, H., Morinaga, M., *Advances in Quantum Chemistry*, 2003, **42**, 315-330.
- [266]. Tibbetts, K., Miranda, C.R., Meng, Y.S., Ceder, G., *Chem. Mater.*, 2007, **19**, 5302-5308.
- [267]. Zhao, M., Xia, Y., Mei, L., *Phys. Rev. B*, 2005, **71**, 16, 165413.
- [268]. Li, J., Wan, W., Zhu, F., Li, Q., Zhou, H., Li, J., Xu, D., *Chem. Commun.*, 2012, **48**, 389-391.
- [269]. Chen, H.M., Lu, X.H., Deng, C.H., Yan, X.M., *J. Phys. Chem. C*, 2009, **113**, 50, 21068-21073.
- [270]. Wang, Y.Q., Wang, G.Z., Wang, H.Q., Cai, W.P., Zhang, L.D., *Chem. Commun.*, 2008, **48**, 6555-6557.
- [271]. Wang, Y., Tang, C., Deng, Q., Liang, C., Ng, D.H.L., Kwong, F., Wang, H., Cai, W., Zhang, L., Wang, G., *Langmuir*, 2010, **26**, 18, 14830-14834.
- [272]. Zhao, Y., Song, X.C., *Micro & Nano Letters*, 2011, **6**, 12, 995-997.
- [273]. M. Fathima Parveen, S. Umapathy, V. Dhanalakshmi and R. Anbarasan, *J. Mater. Sci.*, 2009, **44**, 21, 5852-5860.
- [274]. Scherrer, P., *Göttinger Nachrichten Gesell.*, 1918, **2**, 98.
- [275]. Zhang, Z., Zhou, F., Lavernia, E.J., *Metallurgical and Minerals Trans. A-Physical Metallurgy and Materials Science*, **34A**, 1349-1355.
- [276]. Lowell, S. Shields, J.E. Thomas, M.A., Thommes, M., *Characterisation of Porous Solids and Powders: Surface Area, Pore Size and Density*, 2004, Kluwer Academic Publishers, Dordrecht, The Netherlands, ISBN: 1-4020-2302-2, p.116.
- [277]. Busey, R.H., Mesmer, R.E., *Inorg. Chem.*, 1977, **16**, 10, 2444-2450.
- [278]. Chen, W., Guo, X., Zhang, S., Jin, Z., *J. Nanoparticle Res.*, 2007, **9**, 1173-1180.
- [279]. Lu, H., Zhao, J., Li, L., Zheng, J., Zhang, L., Gong, L., Wang, Z., Zhu, Z., *Chem. Phys. Lett.*, 2011, **508**, 4-6, 258-264.

- 
- [280]. Wei, M., Konishi, Y., Zhou, H., Sugihara, H., Arakawa, H., *Solid State Commun.*, 2005, **133**, 8, 493-497.
- [281]. Kukovecz, A., Hodos, M., Horvath, E., Radnoczi, G., Konya, Z., Kiricsi, I., *J. Phys. Chem. B*, 2005, **109**, 17781.
- [282]. Palmer, D.A., Benezeth, P., Xia, C., Wesolowski, D.J., Anovitz, L.M., *J. Solution Chem.*, 2011, **40**, 680-702.
- [283]. De Yoreo, J.J., Vekilov, P.G., *Principles of Crystal Nucleation and Growth, Reviews in Mineralogy and Geochemistry*, 2003, **54**, 1, 57-93.
- [284]. Horvath, E., Kukovecz, A., Konya, Z., Kiricsi, I., *Chem. Mater.*, 2007, **19**, 927-931.
- [285]. Bavykin, D.V., Cressey, B.A., Walsh, F.C., *Australian Journal of Chemistry*, 2007, **60**, 2, 95-98.
- [286]. Cheng, S., Hwang, H.D., Maciel, G.E., *J. Molecular Struct.*, 1998, **470**, 135-149.
- [287]. Chen, Z.Y., Guo, X.P., Zhang, Q., Qu, J.E., *J. Mater. Sci.*, 2006, **41**, 5033-5035.
- [288]. Livage, J., *Chem. Mater.*, 1991, **3**, 578-593.
- [289]. Reinoso, J.M., Muhr, H.J., Krumeich, F., Bieri, F., Nesper, R., *Helvetica Chimica Acta*, 2000, **83**, 1724-1733.
- [290]. Ningyi, Y., Jinhua, L., Chenglu, L., *Appl. Surface Sci.*, 2002, **191**, 1-4, 176-180.
- [291]. Irving, H., Williams, R.J.P., *J. Chem. Soc.*, 1953, **637**, 3192-3210.
- [292]. Arnor, J.N., *Separation Technology*, 1994, Ed. Vansat, E.F., Elsevier Science, Amsterdam, p. 163.
- [293]. Naja, G.M., Volesky, B., Toxicity and sources of Pb, Cd, Hg, As, and radionuclides in the environment, in: *Advances in Industrial and Hazardous Waste Treatment*, 2009, Ed. Wang, L.K., Chen, J.P., Hung, Y.T., Shammas, N.K., CRC Press, ISBN: 9-7814-2007-3164.
- [294]. Ludi, A., Güdel, H.U., Structural chemistry of polynuclear transition metal cyanides, *Structure and Bonding*, 1973, **14**, 1-21.
- [295]. Zhou, L., Yaping, Z., Determination of compressibility factor and fugacity coefficient of hydrogen in studies of adsorptive storage, *International Journal of Hydrogen Energy*, 2001, **26**, 597-601.
- [296]. Biro, L.P., Bernado, A., Tibbetts, G.G., Lambin, P., Hydrogen storage in carbon nanotubes, in: *Carbon filaments and nanotubes: common origins, differing applications*,

---

NATO Science Series E: Applied Sciences, Vol. 372, Kluwer Academic Publishers, the Netherlands, ISBN 0-7923-6907-6, pp. 42

[297]. Do, D.D., Adsorption analysis: equilibria and kinetics, in: *Series on Chemical Engineering*, Vol. 2, 1998, Imperial College Press, London, ISBN 1-86094-130-3, pp. 57.

[298]. Hirscher, M., *Handbook of Hydrogen Storage*, 1<sup>st</sup> ed., 2010, Wiley-VCH, Weinheim, ISBN 978-3-527-32273-2, pp. 9.

[299]. Fialips, C.A., Petit, S., Deccareau, A., Beaufort, D., *Clays and Clay Minerals*, 2000, **48**, 2, 173-184.

[300]. Szarek, P., Urakami, K., Zhou, C., Cheng, H., Tachibana, A., On reversible bonding of hydrogen molecules on platinum clusters, *J. Chem. Phys.*, 2009, **130**, 8, 084111.

[301]. Sachan, A., Penumadu, D., *Geotech. Geol. Eng.* 2007, **25**, 603-616.

[302]. Bish, D. L., Von Dreele, R. B., *Clays and Clay Minerals*, 1989, **37**, 289-296.

[303]. Mehmehl, M., *Zeitschrift für Kristallographie*, 1935, **90**, 35-43.

[304]. Tettendorst, R.T., *Clays and Clay Minerals*, 1988, **36**, 2, 181-183.

[305]. Gayer, K.H., Garrett, A.B., *J. Am. Chem. Soc.*, 1950, **72**, 9, 3921-3923.

[306]. Balmaseda, J., Reguera, E., Gomez, A., Diaz, B., Autie, M., *Microporous and Mesoporous Materials*, 2002, **54**, 285-292.

[307]. Morgado Jr., E., de Abreu, M.A.S., Moure, G.T., Marinkovic, B.A., Jardim, P.M., Araujo, A.S., *Chem. Mater.*, 2007, **19**, 665-676.

[308]. Roberts, W.L., Campbell, T.J., Rapp, Jr. G.R.R., *Encyclopedia of Minerals*, 2<sup>nd</sup> ed., 1990, Chapman & Hall, ISBN: 978-0442276812.

[309]. Alvarez-Ramirez, F. *Phys. Rev. B*, 2007, **76**, 125421.

---

## Bibliography

- [1]. Cao, G., *Nanostructure & Nanomaterials, synthesis, properties & applications*, 2004, Imperial College Press, London, ISBN: 1-86094-415-9.
- [2]. Hornyak, G.L., Tibbals, H.F., Dutta, J., Moore, J.J., *Introduction to Nanoscience and Nanotechnology*, 2008, CRC Press, Taylor and Francis Group, ISBN: 9781420047790.
- [3]. Kijima, T. *Inorganic and Metallic Nanotubular Materials, Topics in Applied Physics*, 2010, vol. 117, Springer-Verlag, Berlin.
- [4]. Krivovichev, S.V., *Minerals as Advanced Materials*, 2008, Springer-Verlag, Berlin-Heidelberg.
- [5]. Abidin, Z., Matsue, N., Hemmi, T., *Interdisciplinary Studies on Environmental Chemistry- Environmental Research in Asia*, 2009, TERRAPUB, Tokyo.
- [6]. Bhushan, B., *Springer Handbook of Nanotechnology*, 2003, Springer-Verlag Berlin-Heidelberg-New York, ISBN 3-540-01218-4.
- [7]. Putnis, A., *Introduction to Mineral Sciences*, 1992, Cambridge University Press, ISBN 0-521-42947-1.
- [8]. Breck, D.W., *Zeolite Molecular Sieves: Structure, Chemistry and Use*, 1974, John Wiley, New York.
- [9]. Klabunde, K.J., Richards, R.M., *Nanoscale Materials in Chemistry*, 2009, John Wiley and Sons, New Jersey, ISBN 978-0-470-22270-6.
- [10]. Bavykin, D.V., Walsh, F.C., *Titanate and Titania Nanotubes: Synthesis, Properties and Applications*, 2009, RSC, London.
- [11]. Weber, J., *Encyclopaedia of Minerals, 2<sup>nd</sup> Edition*, 1990, Chapman & Hall, ISBN: 978-0442276812.
- [12]. Huheey, J.E., Keiter, E.A., Keiter, R.L., *Inorganic Chemistry: Principles of Structure and Reactivity*, 4<sup>th</sup> ed., 1993, Harper-Collins, New York.
- [13]. Broom, D.P., *Hydrogen Storage Materials: The Characterisation of their Storage Properties*, 1<sup>st</sup> ed., 2011, Springer-Verlag, London, ISBN: 978-0-85729-220-9.
- [14]. Meunier, A., *Clays*, Springer Verlag, Berlin, Heidelberg, 2005.

---

## Bibliography (cont'd)

- [15]. Brindley, G. W., Brown, G. *Crystal Structures of Clay Minerals and their X-ray identification*, 1980, London Mineralogical Society.
- [16]. Lowell, S., Shields, J.E., Thomas, M.A., Thommes, M., *Characterisation of Porous Solids and Powders: Surface Area, Pore Size and Density*, 2004, Kluwer Academic Publishers, Dordrecht, The Netherlands, ISBN: 1-4020-2302-2.
- [17]. Wang, L.K., Chen, J.P., Hung, Y.T., Shammash, N.K., *Advances in Industrial and Hazardous Waste Treatment*, 2009, CRC Press, ISBN: 9-7814-2007-3164.
- [18]. Biro, L.P., Bernado, A., Tibbetts, G.G., Lambin, P., *Carbon filaments and nanotubes: common origins, differing applications*, NATO Science Series E: Applied Sciences, Vol. 372, Kluwer Academic Publishers, the Netherlands, ISBN 0-7923-6907-6.
- [19]. Do, D.D., *Adsorption analysis: equilibria and kinetics, Series on Chemical Engineering*, Vol. 2, 1998, Imperial College Press, London, ISBN 1-86094-130-3.
- [20]. Hirscher, M., *Handbook of Hydrogen Storage*, 1<sup>st</sup> ed., 2010, Wiley-VCH, Weinheim, ISBN 978-3-527-32273-2.